


<b>Title</b>	Floating wave energy converters: wave measurement & analysis techniques
<b>Author(s)</b>	Barrett, Seán Noel
<b>Publication date</b>	2015
<b>Original citation</b>	Barrett, S .N, 2015. Floating wave energy converters: wave measurement & analysis techniques. PhD Thesis, University College Cork.
<b>Type of publication</b>	Doctoral thesis
<b>Rights</b>	© 2015, Seán Noel Barrett. <a href="http://creativecommons.org/licenses/by-nc-nd/3.0/">http://creativecommons.org/licenses/by-nc-nd/3.0/</a> 
<b>Embargo information</b>	No embargo required
<b>Item downloaded from</b>	<a href="http://hdl.handle.net/10468/3372">http://hdl.handle.net/10468/3372</a>

Downloaded on 2018-08-23T18:03:25Z



**UCC**

University College Cork, Ireland  
Coláiste na hOllscoile Corcaigh

**Ionad Taighde Hiodráilice agus Mara,  
Rionn na hInnealtóireachta Sibhialta agus Timpleallachta,  
Coláiste na hOllscoile Corcaigh,  
Éire.**



**UCC**

**Coláiste na hOllscoile Corcaigh, Éire  
University College Cork, Ireland**

# **FLOATING WAVE ENERGY CONVERTERS**

## ***Wave Measurement & Analysis Techniques***

**A thesis submitted for the Degree of Doctor of Philosophy**

**In the Faculty of Engineering**

**National University of Ireland, Cork**

**By**

**Seán Noel BARRETT, B.E., M.Eng.Sc.**

**Supervisor: Prof. Anthony Lewis,**

**Hydraulics & Maritime Research Centre,**

**Dept. Civil & Environmental Engineering,**

**University College Cork,**

**Ireland.**

**Head of Department: Prof. G. Kiely**

## CONTENTS

Declaration .....	v
Abstract .....	vi
Acknowledgements .....	vii
Abbreviations .....	viii
Nomenclature .....	x
1. INTRODUCTION .....	1
1.1. Device Development Procedures .....	2
1.2. Physical Similarity & Scaling Laws .....	4
1.3. Wave Energy Converter .....	6
1.4. Wave Energy Test Sites .....	12
1.4.1. Galway Bay Quarter Scale Test Site .....	14
1.4.1.1. Benign Site Numerical Model .....	18
1.4.2. Loop Head Exposed Site .....	22
1.5. Work Objectives .....	23
2. OCEAN WAVE MEASUREMENT .....	25
2.1. Wave Measurement Methods .....	25
2.1.1. Visual Observation .....	26
2.1.2. Wave Staff/Probe .....	27
2.1.3. Pressure & Acoustic .....	28
2.1.4. Radar/Satellite .....	29
2.1.5. Surface Buoys .....	31
2.1.6. Eulerian vs. Lagrangian Measurement .....	34
2.2. Surface Following Data Buoys .....	35
2.2.1. Non-directional Buoy .....	36
2.2.2. Directional Buoy .....	38
2.2.3. Buoy Calibration .....	39
2.2.4. Datawell Buoy Mooring .....	41
2.3. Buoy Data Transmission & Preparation .....	43
2.3.1. Data Preparation & Processing .....	44

2.3.1.1.	Loop Head Data Set.....	44
2.3.1.2.	Galway Bay Data Set.....	46
2.3.2.	Buoy Output Files .....	48
2.3.3.	Data Quality Check & Analysis Procedures .....	51
3.	ANALYSIS TECHNIQUES.....	55
3.1.	Time Domain.....	56
3.1.1.	Statistical Distributions .....	57
3.1.1.1.	Gaussian Distribution .....	57
3.1.1.2.	Rayleigh Distribution.....	57
3.1.2.	Time Domain Summary Statistics .....	58
3.2.	Frequency Domain .....	59
3.2.1.	Frequency Domain Analysis .....	59
3.2.1.1.	Fast Fourier Transform .....	61
3.2.1.	Frequency Domain Summary Statistics .....	62
3.2.1.1.	Wave Power.....	64
3.2.3.	Fourier Analysis of Ocean Waves.....	65
3.2.4.	Leakage, Aliasing, Smoothing and Degrees of Freedom.....	68
3.2.4.1.	Leakage.....	68
3.2.4.2.	Aliasing.....	69
3.2.4.3.	Tapering.....	71
3.2.4.4.	Spectral Degrees of Freedom.....	73
3.2.4.5.	Segmenting .....	74
3.2.5.	Directional Analysis.....	76
3.2.5.1.	Cross Spectral Analysis .....	78
3.2.5.2.	Maximum Likelihood Method.....	80
3.2.5.3.	Maximum Entropy Method .....	81
3.3.	Empirical Studies .....	82
3.3.1.	Pierson-Moskowitz .....	83
3.3.2.	Bretschneider.....	84
3.3.3.	JONSWAP .....	85
3.4.	Spectral Bimodality .....	89
3.4.1.	Bimodal Identification Studies.....	90
3.4.2.	Bimodal Identification Techniques .....	91

3.4.2.1.	Parametric Identification Models.....	92
3.4.2.2.	Wang and Hwang Steepness Function.....	93
3.4.3.	Bimodal Modelling Techniques.....	95
3.4.3.1.	Ochi & Hubble, 1976.....	95
3.4.3.2.	Guedes Soares, 1984.....	98
3.4.3.3.	Torsethaugen & Haver, 2004.....	99
3.4.4	Directional Spectra Partition Methods.....	102
3.4.4.1.	Gerling, 1992.....	102
3.4.4.2.	Aarnes & Krogstad Review, 2001.....	104
4.	OCEAN WAVE SPECTRA.....	106
4.1.	Time Domain Analysis.....	107
4.1.1.	Validation of Empirical Results.....	107
4.1.2.	Statistical Distributions.....	108
4.2.	Frequency Domain Analysis.....	111
4.3.	Buoy Measured Summary Statistics.....	114
4.3.1.	Temporal Variations.....	119
4.3.1.1.	Monthly Average Trend.....	120
4.3.1.2.	Winter/Spring Average Spectrum.....	122
4.3.1.3.	Seasonal Average Spectra.....	127
4.3.1.4.	Monthly, Weekly & Daily Spectral Averages.....	129
4.3.1.5.	Daily & Hourly Spectral Averages.....	131
4.4.	Storm Growth & Decay.....	133
4.4.1.	Iso-Height and Iso-Period.....	133
4.4.2.	Iso-Steepness.....	136
4.4.3.	Storm Progression.....	138
4.5.	Spatial Variations.....	140
4.5.1.	Concurrent Summary Statistics.....	141
4.5.2.	Regression Analysis.....	144
4.6.	Bimodal Spectra Identification.....	146
4.6.1.	Application of Separation Methods.....	146
4.6.1.1.	Constant Separation Frequency.....	146
4.6.1.2.	Parametric Separation Method.....	148
4.6.1.3.	Wang & Hwang Bimodal Identification Method.....	152

---

4.6.2. Consequences of Bimodal Spectra.....	154
4.7. Directional Spectra .....	159
5. SITE SCALING & WEC INTERACTION .....	165
5.1. Benign Site Scaling .....	166
5.1.1. Scalability.....	166
5.2. Wave Energy Device Interaction .....	170
5.2.1. Wave Excitation .....	171
5.2.2. Device Power Response .....	173
5.2.3. Long Period Excitation .....	187
6. DISCUSSION & CONCLUSION .....	189
6.1. Discussion .....	189
6.2. Conclusion.....	191
REFERENCES.....	194
APPENDIX A: Datawell Output Files.....	199
APPENDIX B: Published Papers.....	210

**Declaration**

I hereby declare that this thesis is my own work and effort and that it has not been submitted either at University College Cork or elsewhere for any award.

Where other sources of information have been used, they have been acknowledged.

Signature: 

Date: 20/4/14

## **Abstract**

The wave energy industry is entering a new phase of pre-commercial and commercial deployments of full-scale devices, so better understanding of seaway variability is critical to the successful operation of devices. The response of Wave Energy Converter to incident waves govern their operational performance and for many devices, this is highly dependent on spectral shape due to their resonant properties. Various methods of wave measurement are presented, along with analysis techniques and empirical models. Resource assessments, device performance predictions and monitoring of operational devices will often be based on summary statistics and assume a standard spectral shape such as Pierson-Moskowitz or JONSWAP. Furthermore, these are typically derived from the closest available wave data, frequently separated from the site on scales in the order of 1km. Therefore, variability of seaways from standard spectral shapes and spatial inconsistency between the measurement point and the device site will cause inaccuracies in the performance assessment.

This thesis categorises time and frequency domain analysis techniques that can be used to identify changes in a sea state from record to record. Device specific issues such as dimensional scaling of sea states and power output are discussed along with potential differences that arise in estimated and actual output power of a WEC due to spectral shape variation. This is investigated using measured data from various phases of device development.



## **Acknowledgements**

I wish to thank Prof. Tony Lewis for his informative supervision throughout the course of this thesis, his immeasurable knowledge, constant support and his addictive enthusiasm for wave energy. I would also like to thank Prof. Lars Bergdahl of Chalmers University, Sweden and Dr. Gareth Thomas of University College Cork, as the external examiners.

Prof. J. Philip O’Kane, Prof. Gerard Kiely and Dr. Michael Creed for affording me the facilities of the Civil and Environmental Engineering Department, University College Cork to undertake this study.

I am hugely grateful to Mr. Brian Holmes, for encouraging me to pursue this path and for his time, guidance, and suggestions, along with greatly needed distractions from time to time!

To all the staff of the HMRC, past and present, who have been a great support throughout the duration of my time there, both technically and socially.

I gratefully acknowledge the funding support of the Marine Institute through the Blue Power Initiative, funded by the Irish Government under the National Development Plan, 2007-2013.

I would like to thank Mike Whelan, Ocean Energy Ltd, Pat McCullen, ESBI and Caitriona Nic Aonghusa, Marine Institute for the provision of the various datasets and permission for their use throughout this study.

To my friends, home and abroad, and my fellow students in the offshore engineering community for their support and comradeship.

To my family, whose belief and patience have made the years invested in this journey all the more worthwhile.

Finally, to Nuala, whose unwavering encouragement and confidence was both the anchor and the guiding light, thank you.

## Abbreviations

ADCP	Acoustic Doppler Current Profiler
COLOS	Coastal Oceanographic Line Of Sight
DBCP	Data Buoy Cooperation Panel
DECC	Dept. Energy and Climate Change
DFT	Discrete Fourier Transform
DIA	Discrete Interaction Approximation
DIWAR	Digital Waverider Receiver
DNV	Det Norske Veritas
DOS	Disk Operating System
DSF	Directional Spreading Function
DTI	Dept. Trade and Industry, UK
ECMWF	European Centre for Medium Range Weather Forecasts
ECN	Ecole Centrale de Nantes
EMEC	European Marine Energy Centre
ENVISAT	Environmental Satellite
ERS	European Remote Sensing Satellite
ESBI	Electricity Supply Board International
FFT	Fast Fourier Transform
GPS	Global Positioning System
GSM	Global System for Mobile or Groupe Spécial Mobile
GTS	Global Telecommunication System
HF	High Frequency
HMRC	Hydraulics and Maritime Research Centre
IAHR	International Association for Hydraulic Research
IEA-OES	International Energy Agency – Ocean Energy Systems
IMLM	Iterative Maximum Likelihood Method
INFOMAR	Integrated Mapping For the Sustainable Development of Ireland’s Marine Resource
IOC	Intergovernmental Oceanographic Commission
ITTC	International Towing Tank Conference
JCOMM	Joint WMO-IOC Technical Commission for Oceanography and Marine Meteorology
JONSWAP	Joint North Sea Wave Program
LEWEX	Labrador Extreme Waves Experiment
MAWS	Marine Automatic Weather Station
MEM	Maximum Entropy Method
MLM	Maximum Likelihood Method
NASA	National Aeronautics and Space Administration
NOAA	National Oceanic and Atmospheric Association
NOMAD	Navy Oceanographic Meteorological Automatic Device
ODAS	Ocean Data Acquisition System
OWC	Oscillating Water Column
PA	Pruning Algorithm
PADIWA	Package for Directional Wave Analysis
PDF	Probability Distribution Function
PEA	Pattern Recognition Algorithm
PTO	Power Take Off
QC	Quality Control
RAO	Response Amplitude Operator
RAW	Raw Elevation file (Datawell Waverider Directional Buoy)
REFIT	Renewable Energy Feed In Tariff
RW	Raw Elevation file (Datawell Waverider Non-directional Buoy)
SAR	Synthetic Aperture Radar
SP	Wave Spectrum file (Datawell Waverider Non-directional Buoy)
SPA	Spectral Partitioning Algorithm
SPT	Wave Spectrum file (Datawell Waverider Directional Buoy)
SWAN	Simulating Waves Nearshore
TOPEX	Ocean Topography Experiment
TRL	Technology Readiness Level

UNESCO	United Nations educational, Scientific and Cultural Organisation
VOS	Voluntary Observing Ship
WAM	Wave Model
WEC	Wave Energy Converter
WMO	World Meteorological Organisation
WV	Wave statistics file (Datawell Non-directional Waverider Buoy)
WVS	Wave statistics file (Datawell Directional Waverider Buoy)

## Nomenclature

### Chapter 1. INTRODUCTION

$a$	acceleration	[m/s <sup>2</sup> ]
$f$	frequency of a sinusoidal wave component	[Hz]
$F_g$	gravity force	[N]
$F_i$	inertia force	[N]
$F_r$	Froude number	[-]
$g$	acceleration due to gravity	[m/s <sup>2</sup> ]
$H_{m0}$	significant wave height derived from the zeroth moment of variance density spectrum	[m]
$L$	length	[m]
$M$	mass	[kg]
$N$	number of harmonics in spectrum	[-]
$Re$	Reynolds number	[-]
$T$	time	[s]
$T_p$	peak wave period	[s]
$T_{02}$	average wave period derived from spectral moments	[s]
$u$	velocity	[m/s]
$\Delta f$	frequency resolution of variance density spectrum	[Hz]
$\Delta\theta$	directional resolution	[°]
$\rho$	mass density	[kg/m <sup>3</sup> ]
$\lambda$	scale factor	[-]

### Chapter 2. OCEAN WAVE MEASUREMENT

$a$	wave amplitude	[m]
$A$	vertical acceleration (Eq. 2.3)	[m/s <sup>2</sup> ]
$A_v$	acceleration along vertical axis	[m/s <sup>2</sup> ]
$A_x$	acceleration along x axis	[m/s <sup>2</sup> ]
$A_y$	acceleration along y axis	[m/s <sup>2</sup> ]
$c$	wave phase velocity	[m/s]
$h$	horizontal excursion of buoy swing	[m]
$H_{max}$	maximum wave height in time series	[m]
$H_s$	significant wave height	[m]
$H_x$	magnetic field strength along x axis	[T]
$H_y$	magnetic field strength along y axis	[T]
$H_z$	magnetic field strength along vertical axis	[T]
$k$	wave number	[m <sup>-1</sup> ]
$L$	wave length	[m]
$L_p$	pendulum length	[m]
$L_R$	distance from suspension point to accelerometer	[m]
$S(f_i)$	variance density spectral ordinate	[m <sup>2</sup> /Hz]
$T$	natural period of a pendulum	[s]
$T_E$	Eulerian wave period	[s]
$T_L$	Lagrangian wave period	[s]
$U$	drift velocity	[m/s]
$\lambda$	wave length	[m]

### Chapter 3. ANALYSIS TECHNIQUES

$A, B$	Fourier coefficients	[-]
$c_g$	wave group velocity	[m/s]
$c_p$	wave phase velocity	[m/s]
$c_s$	phase velocity of wave component with frequency equal to separation frequency	[m/s]
$c_0$	offset of a Fourier series	[m]
$D(\theta)$	directional spreading function	[-]
$E[]$	expected value	[-]
$E_p$	Potential energy	[J]
$f_m$	peak of the Wang and Hwang steepness function	[Hz]

$f_{\max}$	maximum frequency in the frequency range	[Hz]
$f_{Nq}$	Nyquist frequency	[Hz]
$f_p$	peak frequency	[Hz]
$f_s$	sampling frequency	[Hz]
$f_s$	separation frequency (Eq. 3.43)	[Hz]
$h$	water depth	[m]
$H$	zero crossing wave height	[m]
$\bar{H}$	mean wave height of surface elevation time series	[m]
$H_{1/3}$	mean of the highest one third of zero crossing waves in time series	[m]
$H_R$	ratio of wind to swell significant wave height	
$H_{ss}$	swell component significant wave height	[m]
$H_{sw}$	wind component significant wave height	[m]
$H_{var}$	significant wave height derived from the variance of a time series	[m]
$K_R$	ratio of estimated to theoretical spectral ordinates	[-]
$m_n$	spectral moment of the $n^{\text{th}}$ power	[m <sup>2</sup> Hz <sup>n</sup> ]
$m_0$	zero moment of variance density spectrum	[m <sup>2</sup> ]
$N$	population size (Eq. 3.4)	[-]
$P$	probability distribution	[-]
$s$	spreading parameter	[-]
$s_s$	significant steepness	[-]
$S(f, \theta)$	directional spectral ordinate	[m <sup>2</sup> Hz/ <sup>o</sup> ]
$S_R$	ratio of wind to swell spectral peaks	[-]
$S^*(\omega)$	unit spectrum	[s/rad]
$T$	total duration of a time series	[s]
$T_e$	energy wave period	[s]
$T_{H\max}$	Period corresponding to the maximum wave in the record	[s]
$T_I$	integral wave period	[s]
$T_{\max}$	maximum wave period in a record	[s]
$T_{ms}$	swell component mean period	[s]
$T_{mw}$	wind component mean period	[s]
$T_{pf}$	peak wave period of an equivalent fully developed sea state	[s]
$T_R$	ratio of wind to swell mean period	[-]
$T_z$	average period of all zero crossing periods	[s]
$U$	wind speed	[m/s]
$U_{10}$	wind speed measured 10m above sea level	[m/s]
$u^*$	wind friction velocity	[m/s]
$x$	ratio of individual wave height to mean wave height	[-]
$X_n$	complex amplitude	
$X_{-n}$	complex conjugate	
$\alpha$	effective spectral degree of freedom	[-]
$\alpha$	Phillips constant (Eq. 3.37)	[-]
$\alpha(f^*)$	Wang and Hwang steepness function	[-]
$\gamma$	JONSWAP peak enhancement factor	[-]
$\Delta t$	time step of a sampled time series	[s]
$\eta$	surface elevation of time series	[m]
$\bar{\eta}$	mean of surface elevation of time series	[m]
$\theta_m$	mean direction	[ <sup>o</sup> ]
$\theta_n$	phase of a sinusoidal component	[ <sup>o</sup> ]
$\nu$	spectral degree of freedom	[-]
$\sigma$	standard deviation of a time varying signal	[m]
$\sigma_{a,b}$	JONSWAP peak width factor (Eq. 3.40)	[-]
$\sigma^2$	variance of a time varying signal	[m <sup>2</sup> ]
$\omega_n$	angular frequency	[rad/s]
$\Gamma$	Gamma probability function	[-]
$\mathbb{P}_w$	incident wave power per meter wave crest	[W/m]

**Chapter 4. OCEAN WAVE SPECTRA**

$T$	wave period	[s]
$R$	correlation coefficient	[-]

**Chapter 5. SITE SCALING & WEC INTERACTION**

a	orifice area	[m <sup>2</sup> ]
C <sub>d</sub>	coefficient of discharge	[-]
Q	volume flow rate	[m <sup>3</sup> /s]
Δp	change in air pressure	[Pa]
P <sub>p</sub>	Device pneumatic power derived from measured pressure	[W]

## 1. INTRODUCTION

The oceans cover 71% of the Earth's surface, providing mankind with navigation routes, food sources and the possibility of an energy resource. The need for knowledge of the sea's surface is important on many levels. Safety is the primary factor that drives the demand for knowledge of the marine environment. Ocean crossing and passenger safety has led to the establishment of many methods of sea surface observation from direct manual record keeping to satellite telemetry. Stewart (2005) gives an historical account of sea observations, from the early explorers to the latest technology, including the development of the theory behind physical oceanography.

Natural disasters have led to the need to develop a greater understanding of the processes involved in storm generation and prediction. To prevent further loss of life such as that caused by the North Sea Flood of 1953 in which over two thousand people died both in the southern United Kingdom, the Netherlands and at sea, methods were needed to predict such catastrophic events. These predictions require a better understanding of the physics involved and an improved accuracy of the measurement technology. In fact, it was an outcome of the need for greater accuracy and knowledge of the sea state in the aftermath of the 1953 storm surge that the buoy instrumentation company Datawell, was formally founded in 1961.

These floods not only necessitated the need to understand wave excitation and the elevation of the ocean surface, but also tidal effects. This knowledge was then used for the design of dykes, barriers, dams and other coastal defences, the Delta Works in the Netherlands, which are not only dictated by the water level but also the height of the largest waves that may arise in any given storm event. These measurements can then be incorporated into sophisticated numerical prediction software packages for the early warning of significant meteorological events. Accurate measurement leads to a more accurate prediction, thereby reducing the risk of structural damage and loss of life.

Now that there are many instrument types that provide accurate measurements of the ocean's surface, there is the possibility that these instruments can be used in other fields of engineering. One such application is in the assimilation of wave data for wave energy generation. Wave Energy Converter (WEC) need precise time and frequency domain information for a number of reasons. These include the assessment of the ability of

devices to harness wave energy to produce electricity, identification and quantification of the resource potential of a site and its suitability as a wave energy park, prediction of annual productivity or yield, and real-time control where applicable.

The Det Norske Veritas (DNV 2008) certification document does not refer to wave measurement specifically, while the WaveNet subsection on safety recommends the detailed analysis of the wave climate (Bergdahl and McCullen 2003). The Department of Trade & Industry (DTI) preliminary performance protocol also includes a section on resource measurement. In this document and its supporting commentary, (Smith and Taylor 2007) the authors on behalf of DTI, make several recommendations on wave measurement and instrument placement. These recommendations include that a time series of 30 minutes is recorded and analysed to produce the summary seaway statistics and that the wave measuring instrument should be placed at least 100m from the maximum excursion of the device in the seaward direction and the measurement device is no more than 1 km from the wave convertor.

To successfully navigate the development path of a wave energy device from the initial concept to the commercial prototype, a system of enhanced testing stages have been proposed by several European bodies to reduce the risks involved, both technically and financially. The more successful devices that are operating today have followed similar deployment schedules, and this has been encouraged by state funding agencies with the provision of funds and recognised test sites.

### **1.1. Device Development Procedures**

To date there are no recognised standards in place that are widely adopted by the wave energy industry for device development, deployment and monitoring; however there have been several published documents which act as guidelines in this regard. One of the first to be published introduced the phased development concept of the technology readiness level, which was a cost and time efficient means to develop a technology concept through varying stages or test scales, loosely based on the NASA Technology Readiness Level (TRL) protocol. This protocol described the steps required to develop the initial small-scale concept verification model in a laboratory tank to a full-scale prototype device in real sea conditions (Holmes 2003). Subsequent to this, government and statutory bodies



devised similar documents to enable a consistent device development and comparison, and as a tool to audit the widely varying technologies in terms of appropriate funding levels, commercial viability and market readiness.

The TRL process is cyclical in nature, allowing the developer to return to any previous phase of testing, if further investigation or major modification of the concept is required. The staged development concept is broadly divided by the relevant similitude scales of the device models, defined by the Froude scaling parameter  $\lambda$ . Physical testing is conducted in parallel with various mathematical and numerical models, where the results of the physical trials are used to calibrate the numerical models, and in turn, the numerical models are used to predict future output.

It is recommended that the first two phases of testing are conducted under controlled conditions in a wave flume or basin, where the device concept is realised physically and a simplified power take-off (PTO) is used or a method is incorporated into the model so the characteristics of the chosen PTO can be modelled effectively. Phase 1 is described as small scale testing. A physical model of the concept would be approximately 1/50<sup>th</sup> the size of the full-scale representation of the device, therefore the Froude scale is  $\lambda \approx 1:50$ . Phase 2 is intermediate scale testing ( $\lambda \approx 1:15$ ), and conducted at a large tank facility, such as Marin or Ecole Centrale de Nantes (ECN), France. In Phase 3 ( $\lambda \approx 1:4$ ), due to the size of the quarter scale model, testing would usually be carried out at a real sea test site. At this stage, not only do device and PTO adhere to Froude scaling laws, but the real sea waves must also comply. These locations are usually found in fetch limited bays and harbours, such as Galway Bay in Ireland or Nissum Bredning, Denmark.

Phase 4 is the deployment of a single pre-commercial demonstration unit, approximate in size to the full-scale device ( $\lambda \approx 1:1 - 2$ ), at which stage there should be very little alterations to be considered and the production and quality of electricity to the grid is a priority along with device survival and instil investor confidence. Full-scale test sites such as the European Marine Energy Centre (EMEC) in Scotland or the many proposed sites in Ireland, France, Portugal or Spain, will then be utilised for Phase 4 pilot scale commercial demonstration. This phase also allows for the identification of any issues with the manufacturing of the device and a more realistic idea of the costs involved. Finally, when the commercially viable device reaches Phase 5, it is expected that a small array of

devices can be grid connected. This stage of testing is used to prove the technical and economical viability at full-scale while dealing with issues such as multi-device manufacture, economies of scale, electrical and quality grid connection, array interaction and the implementation of operation and maintenance strategies. A schematic of the five-phased Irish Ocean Energy Strategy can be seen in Figure 1.1.

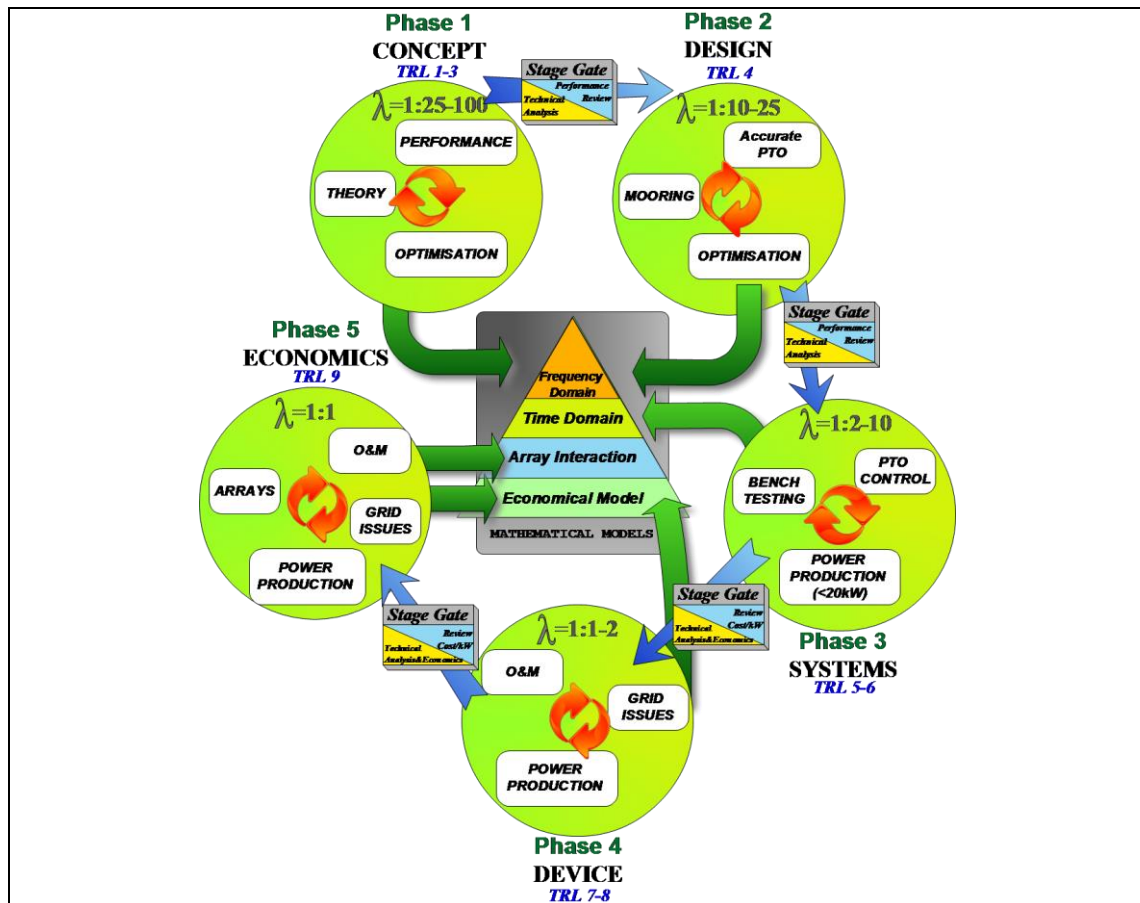


Figure 1.1. Ocean Energy Development Strategy.

### 1.2. Physical Similarity & Scaling Laws

The laws of similarity allow for a replica of a prototype to be tested at a different scale to the prototype and furnish similar results. For the comparison of the results to be valid, the circumstances of the testing need to be physically similar. Two systems are said to be physically similar in respect to certain specified physical quantities when the ratio of corresponding magnitudes of these quantities between the two systems is everywhere the same (Massey 1998).

There exist several types of similarity. Geometric similarity relates to the ratio of the corresponding physical lengths between the model and the prototype. This is the scale

factor  $\lambda$ , which is dimensionless. Kinematic similarity relates to the similarity of motion and requires the similarity of both length and time intervals. Due to these quantities being at fixed ratios, kinematic similarity also includes similarity of velocity and acceleration of corresponding particles. Thermal similarity requires a fixed ratio of temperature difference between model and prototype and chemical similarity is the fixed ratio of concentrations of reactants at corresponding points.

Similarity of forces is known as dynamic similarity, when the magnitude of forces at similarly located points in the systems are in a fixed ratio or the magnitude ratio of any two forces in each system are the same and acting in the same direction. There are many requirements for perfect dynamic similarity due to the types of forces in action such as viscosity, gravitation, difference of pressure, surface tension, elasticity, etc. In all cases there will exist the force required to bring the acceleration of a particle to a stop, the inertia force. Therefore, perfect dynamic similarity is usually impossible to achieve, however, in most cases either some of these forces do not apply, such as surface tension in a completely flooded pipe, or their effect is negligible and can be neglected. It is then possible to concentrate on the more important force contributions. In cases where the gravity force can be neglected, the primary forces are usually, inertia and net viscous forces. The ratio of these forces gives the Reynolds Number,  $Re$ , an indicator of the flow type being laminar, transitional or turbulent.

In cases where free surface flows are present and surface tension is negligible, such as ocean waves; gravity, pressure and inertia forces are dominant and viscous forces can be disregarded. Dynamic similarity requires that the magnitude ratio of inertia to gravity forces should be the same at corresponding points. This ratio is known as the Froude number,  $F_r$ . This relationship is presented in Equation 1.1. Froude scaling is characterised by a scaling parameter, and its relationship to length, time and mass is given in Table 1.1.

$$F_r = \frac{F_i}{F_g} = \frac{Ma}{Mg} = \frac{\rho u^2 L^2}{\rho L^3 g} = \frac{u^2}{Lg} \equiv \frac{u}{\sqrt{Lg}} \quad (1.1)$$

where the subscripts  $i$  and  $g$  denote inertia and gravity respectively,  $M$  is the mass of the fluid,  $a$  is acceleration of the fluid particle,  $\rho$  is the density of the fluid,  $u$  is velocity, and  $L$  is a dimension of length.

Characteristic	Unit	Dimension	Froude Scale
Length	[m]	[L]	$\lambda$
Area	[m <sup>2</sup> ]	[L <sup>2</sup> ]	$\lambda^2$
Volume	[m <sup>3</sup> ]	[L <sup>3</sup> ]	$\lambda^3$
Time	[s]	[T]	$\sqrt{\lambda}$
Velocity	[m/s]	[LT <sup>-1</sup> ]	$\sqrt{\lambda}$
Volume Flow	[m <sup>3</sup> /s]	[L <sup>3</sup> T <sup>-1</sup> ]	$\lambda^{5/2}$
Mass	[kg]	[M]	$\lambda^3$
Force	[N]	[MLT <sup>-2</sup> ]	$\lambda^3$
Pressure	[Pa]	[ML <sup>-1</sup> T <sup>-2</sup> ]	$\lambda$
Power	[W]	[ML <sup>2</sup> T <sup>-3</sup> ]	$\lambda^{7/2}$

Table 1.1. Froude Scaling Ratios

Scaled model testing is used to carry out the phased development and allow an inter-comparison of the results derived from phase to phase. There are numerous justifications for carrying out scaled model testing. Small scale testing is quick and inexpensive, the model is easily altered if required and the testing can be carried out at a controlled level with instrumentation that is highly sensitive in the laboratory environment.

### 1.3. Wave Energy Converter

A wave energy converter (WEC) is a device that can convert the potential and kinetic energy in ocean waves to electrical or hydraulic energy. This conversion of energy takes place from the wave motion acting on the device itself or on a volume of water enclosed by the device. It is beneficial for the purposes of energy extraction to match the resonant properties of the device to the dominant frequency components in the wave field. This can be achieved in numerous ways, indicated by the large number of WEC in development around the world.

WEC are generally devices that respond to the frequency component of the incident wave field in a resonant manner. To understand the device characteristics fully, knowledge of the frequency makeup of the sea state is required for the evaluation of a number of aspects of the device performance along with survival and seaworthiness. Most WEC devices have a narrow frequency response curve, operating at an optimum level or above only periodically when the incident wave conditions match the resonant excitation criteria. To

maximise the power production of a device one method is to carefully assess the wave climate at the proposed deployment zone and suitably size the device so that its inherent resonant properties are excited at the most occurring sea states so that the greatest amount of power is produced on a yearly basis. Another approach is to broadening the frequency response curve by enhancing the frequency response off resonance through elaborate control strategies that rely on wave-by-wave information. The supply of this information relies on the accurate representation of the sea state by wave measurement instruments, which have an important function to play.

Wave energy devices can be categorised by their location or mooring technique, with several of the latest generation devices being either floating, bottom standing or fixed at the shoreline. The power extraction mechanism is the secondary method to define a wave energy convertor and includes systems such as the oscillating water column (OWC), overtopping into a reservoir, mechanical body referential difference or surging pivoted flap.

The OWC method has been incorporated into all of the structure types listed in Table 1.2. Shoreline based OWC (e.g. LIMPET) are considered to be economically unviable and environmentally unpopular at present and other than government subsidised projects which incorporate OWC into breakwaters (e.g. Mutriku, Spain), the technology is being applied to floating structures such as Ocean Energy Ltd's OE Buoy and Oceanlinx' blueWAVE device.

Overtopping devices are designed to enhance wave run-up. The water accumulates within a reservoir creating a hydraulic pressure head that supplies a steady flow to a set of turbines. An example of one such over topping device is the Danish Wave Dragon. Referential devices use the relative mechanical motion between two bodies to produce power. This motion is due to inertia and the reference bodies can be two bodies within the device (e.g. Wavebob) activated by the wave motion or the relative motion between the device and its anchor point on the seabed (e.g. CETO). Finally, the surge motion of waves are used by pivoted flaps to pump a hydraulic system. A hinged flap device can be fixed to the sea floor and submerged (e.g. WaveRoller) or surface piercing (e.g. Aquamarine's Oyster) for operation in the nearshore environment but also positioned on a floating platform for deep-sea locations (e.g. Langlee).

Table 1.2 lists a small selection of current wave energy devices that have been deployed in the real sea environment categorised by structure type and power extraction method. Historically, the shoreline devices were used as proving devices to promote confidence in the fledgling industry and to understand the aerodynamic properties of bi-directional air turbines, which are the corner stone of OWC devices. Many of the other devices in this table have, as a minimum, conducted medium scale testing (Phase 3) in real sea conditions at approximately a quarter scale of the proposed prototype device, and some have continued to full-scale with single, grid connected devices (Phase 4) or small arrays (Phase 5).

<i>Power Mech.</i> <i>Structure Type</i>	<b>OWC</b>	<b>Overtopping</b>	<b>Referential</b>	<b>Surge Flap</b>
<b>Floating</b>	OE Buoy Oceanlinx	Wave Dragon Waveplane	Pelamis Wavebob OPT Aquabuoy Oceantec	
<b>Bottom Standing</b>	Mutriku Breakwater		AWS MkI CETO Seabased Fobox Wave Star	Oyster Wave Roller
<b>Shoreline</b>	LIMPET Pico Plant			

**Table 1.2. Categorisation of wave energy converter (Phase 3 minimum requirement).**

Several device developers have reached the full-scale deployment stage so far, where their devices are moored in the sea to experience real conditions, initially at a sheltered site with a medium scale model and ultimately with a full-scale grid connected prototype at an exposed site. Figure 1.2 shows some examples of devices that have been deployed at medium and full-scale. The top row shows the AWS device which was grid connected and deployed off the Portuguese coast in 2004, the current full-scale version of the Pelamis, the P2, which follows the array testing at the Agucadoura wave farm, Portugal, and Aquamarine’s Oyster device before its deployment at the European Marine Energy Centre.

The second row of Figure 1.2 shows a selection of devices that are at the intermediate stage of testing where the size of the device is approximately a quarter scale of the proposed prototype in Froude scaling terms. These medium sized devices are also tested at specified locations where the sea states are a quarter scale of either the North Sea or

Atlantic Ocean conditions. Usually these devices are not grid connected, due to their low power output, but they are an operational replica of the full-scale device. The Wave Dragon was deployed at the Nissum Bredning site in Denmark for 6 years from 2003. The Oceantec device was deployed off the Northern coast of Spain, while the Wavebob device was stationed at the Galway Bay Wave Energy Test Site, Ireland for approximately two years.

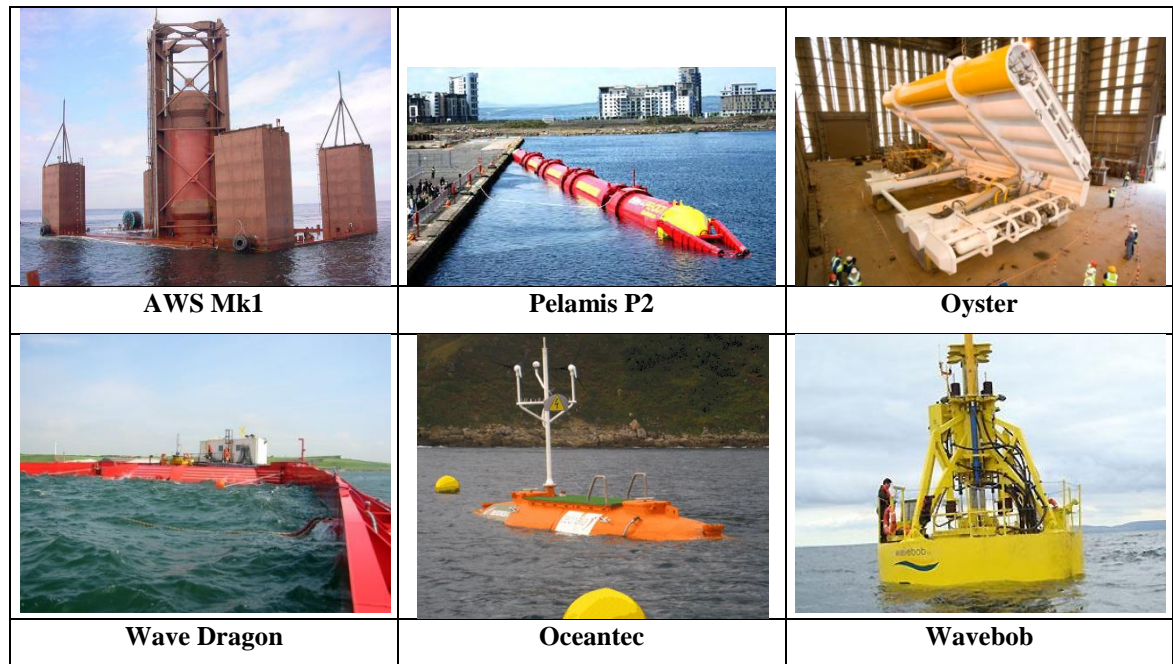


Figure 1.2. Selection of wave energy devices that have undergone real sea trials.

In a recent study for the European project WAVEPLAM, 16 devices were identified that had followed the development protocol and had reached a stage where scaled testing in real sea conditions had been conducted. A further ten were also noted to be at a stage of development where they will be deploying their devices in the marine environment in the near future (Holmes 2009). This state-of-the-art study, which focused exclusively on wave energy, gives a good indication of the current position of the wave energy community. To accommodate the introduction of these devices into regulated offshore environments, several test sites have been established with many more due to come on stream in the near future. Many of these sites aim to remove the legislative workload and associated consenting costs from the developers by providing pre-licensed test berths, most with a grid connection. Along with well-established safety and grid connection regulations, the resource measurement and reporting procedures are less well defined.

The Ocean Energy Systems group of the International Energy Association (IEA-OES) published a document on the development status of ocean energy technologies worldwide (Khan and Bhuyan 2009). This report lists 77 wave energy technologies at various degrees of development with 7% at the initial concept design stage. It is reported that 37% of the listed technologies are in Phase 1 & 2, 32% are at Phase 3, 17% are undertaking Phase 4 full-scale trials and only 7% are at the pre-commercial stage of Phase 5. However, some of the devices listed such as the Salter Duck and the Kvaener Brug OWC are pioneering devices where development has stopped indefinitely due to economic factors, device failures or technology barriers.

An independent but parallel report was produced by Garrad Hassan (Cruz and Elkinton 2009). This study identified 73 wave energy devices and 75 tidal energy devices. This list was reduced to 22 wave energy devices that were participating in at least one of the five development phases of the protocol, the results of which closely agree with the WAVEPLAM report.

An Irish company, Ocean Energy Ltd. have been developing a wave energy device using the structured development plan. This device is the OE Buoy, a floating backward bent OWC device, which uses a Wells turbine as the power take-off mechanism. The incident waves outside the plenum chamber induce an oscillation in the internal water column. This combined with the motion of the device causes the internal water column to act as a piston, with the air flowing to and from the plenum chamber. A Wells turbine converts this bi-directional airflow into uni-directional rotation that generates electricity. This device has been extensively tested in the first three stages of the development protocol.

Phase 1 was conducted in the wave basin at the Hydraulics and Maritime Research Centre (HMRC), at University College Cork, Ireland with a  $\lambda = 1:50$  scale model for concept validation (Barrett 2005). Phase 2 was then conducted in the large ocean basin at ECN, France with a  $\lambda = 1:15$  scale device. Both of these models are shown in Figure 1.3. The model tested at HMRC had a width of 300mm while the model that was tested at the Nantes facilities was three times larger with a width of 1m. An extensive set of monochromatic and panchromatic trials were conducted during these two stages. The panchromatic trials consisted of idealised Bretschneider spectra as input to the wave



paddle generation software. These sea states were of varying wave heights and periods, chosen to represent all areas of a scatter diagram.

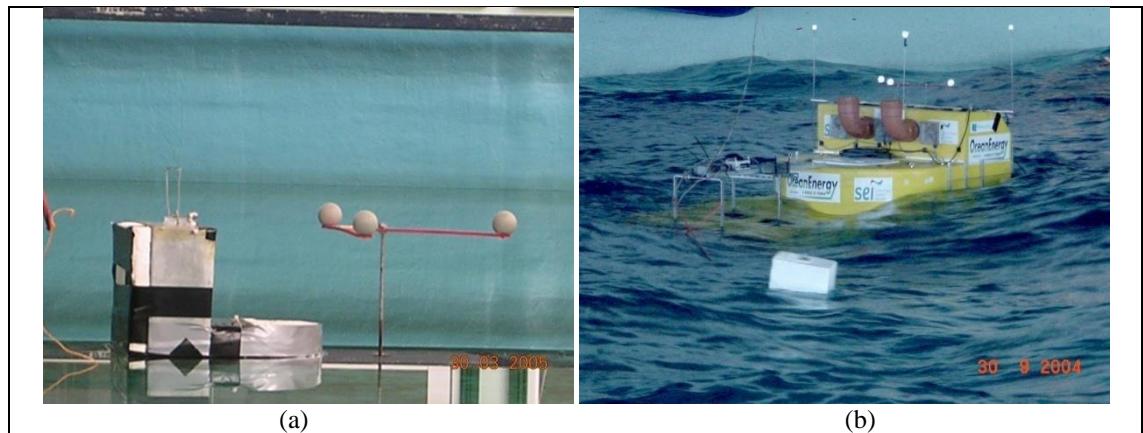


Figure 1.3. (a) Phase 1  $\lambda = 1: 50$  and (b) Phase 2  $\lambda = 1: 15$  OE Buoy models.

In August 2009, Ocean Energy Ltd. finished two years of testing their device, the OE Buoy at the benign test site in Galway Bay. This stage, Phase 3, presents developers with the final opportunity to be acquainted quickly and inexpensively with their device in real sea conditions. It can also be used as a guide on the complexities of manufacture and as a yardstick for survivability, which if successful will instil confidence in the device. By implementing Froude scaling, a model of the concept at this scale ( $\lambda \approx 1: 4$ ) can be built relatively cheaply in comparison to the prototype, and does not require large operational vessels for towing, installation and access. For this phase, Ocean Energy Ltd designed a scaled version of the Wells turbine, as the power take-off mechanism. However, for the first six month deployment in Galway Bay an orifice plate was used to mimic the characteristics of the power conversion mechanism and it is the data from this testing phase that will be analysed later in this thesis. The orifice plate is indicated in Figure 1.4a and Figure 1.4b shows the device on site in Galway Bay.



Figure 1.4. (a) Phase 3 OE Buoy with orifice plate to model PTO and (b) on site in Galway Bay.

### 1.4. Wave Energy Test Sites

The wave energy industry is now at the stage where devices are emerging from the laboratory setting and being deployed in the real sea environment for the first time at varying scales. This follows the adoption of development protocols by the leading developers in this new marine industry. The currently existing and future test sites around Europe can be seen in Figure 1.5. The first test site made available to developers who wished to pursue a medium scale device in benign sea conditions was Nissum Bredning in Denmark (See Figure 1.5). Before this, developers deployed their devices on a pioneering basis without focused state support. These sites were chosen primarily because of a suitable wave regime but also for the projects goals and requirements, such as Queens University 75kW shoreline OWC constructed on the island of Islay off the west coast of Scotland in 1991. This predated the 500kW LIMPET installation at a different location on the same island.

The Nissum Bredning site provides developers with a deployment jetty, control cabin and a low power grid connection. Two devices that have spent a considerable amount of time at the Danish test site are Wave Dragon and Wave Star, two of Denmark’s leading wave energy companies.

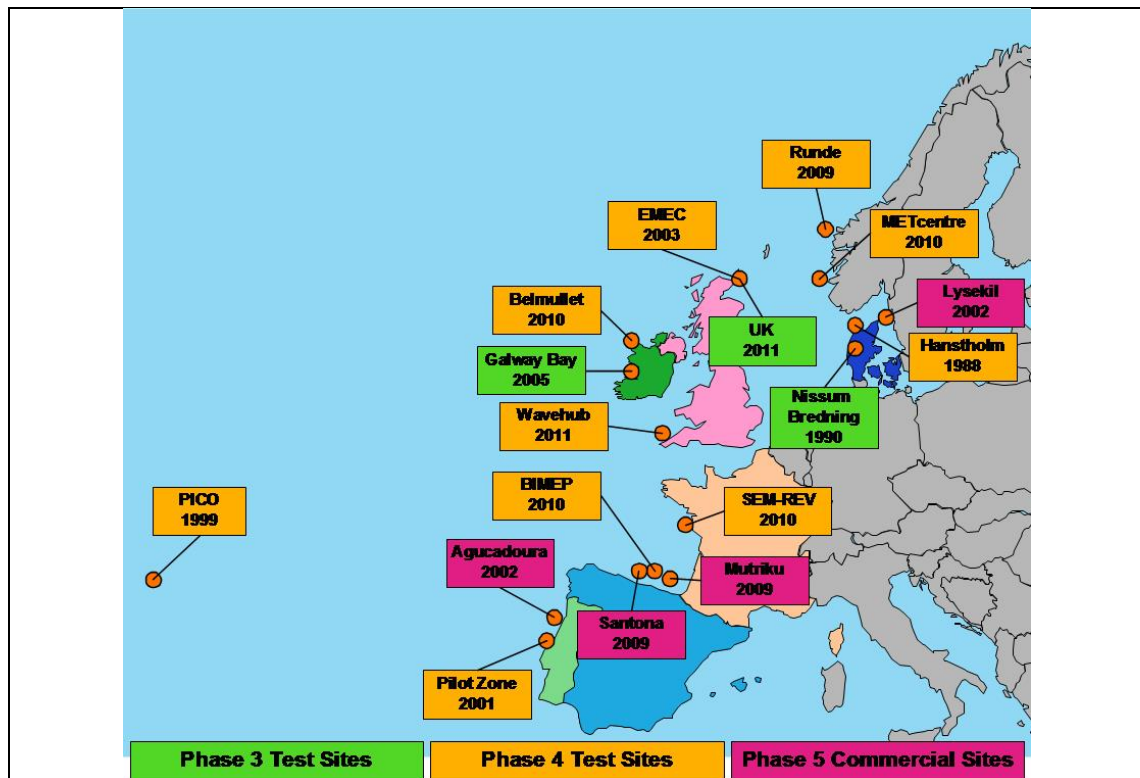


Figure 1.5. European wave energy test sites.

Numerous full-scale regulated test sites subsequently followed, especially around Europe, the best supported being the European Marine Energy Centre (EMEC) in Scotland. Portugal has also been an early developer of test facilities with the Pico project on the Azores Archipelago and the deployment of the AWS device off the Portuguese coast at Agucadoura. This site was later used for the first wave energy device array, installed by Pelamis Wave Power in September 2008 (Pelamis Wave Power 2008). This first array consisted of three full size 750kW Pelamis P1 converter connected to the grid through a 5km long subsea cable. Utility led investment and the introduction of feed-in tariffs for grid connected marine energy converter has put Portugal and Spain to the fore with five sites for the investigation of full-scale prototype wave energy devices. Pelamis developed the P1 attenuator device through a phased research programme, similar to the test schedules envisaged by the current device development protocols and the prototype was tested extensively at the EMEC facility in Scotland before deployment in Portugal.

However, only the Nissum Bredning site accommodated developers who wished to adopt the development protocol and test their device at medium scales in a benign sea environment before risking a huge investment by going straight from the laboratory to a full-scale prototype device. The British Dept. of Energy and Climate Change (DECC) have awarded £8 million in funding to EMEC to investigate and establish medium scale test sites for both wave and tidal devices to fill the gap between laboratory testing and EMEC own full-scale wave and tidal sites (EMEC 2009).

In 2005, the Irish government launched the Galway Bay Quarter Scale Wave Energy test site as an alternative to the Danish test facility. Using the Froude scaling laws mentioned previously, the sea states experienced at the Galway Bay site were proposed to be a quarter scale of North Atlantic sea states. A licensed and instrumented area in a semi-enclosed bay on the west coast of Ireland was provided and availed of by two Irish companies, Ocean Energy Ltd and Wavebob Ltd. Both companies deployed quarter scale devices in the test zone. Although the site and device is termed a quarter scale, the test site is not benign in relation to the device, therefore it would be expected that the device will experience extreme storm seas during the winter months. This was the first time that both companies had experienced the unpredictable and unforgiving nature of the marine environment with their devices, and hence the importance of marine measurement was realised in terms of device performance, maintenance scheduling and survival strategies.

In 2008, a funding package of over €26 million in targeted projects from 2008 to 2011, as part of Phase 2 of the Ocean Energy Strategy for Ireland was announced by the Irish Government (Dept. Communications Marine & Natural Resources 2005). Part of the funding initiative announced includes a full-scale grid connected wave energy test site at an exposed location off the west coast of Ireland, making landfall near Belmullet, Co. Mayo.

The wave data collected, collated and used in this work for analysis and investigation is from two sites, the primary site being the benign wave energy test site in Galway Bay and the second site is positioned off Loop Head on the western seaboard. These sites are shown in Figure 1.6 along with the Marine Institute data buoys that are located at various positions around the coast of Ireland in open sea locations and another source of summary data provided by the North American NDBC buoys. Summary data is only available from these buoys, therefore their data will be used in an analysis of the summary statistics in a later section. In the present context of this work, Galway Bay is a Phase 3 site and Loop Head could be considered as a Phase 4 or 5 test site for a device development team in the future.

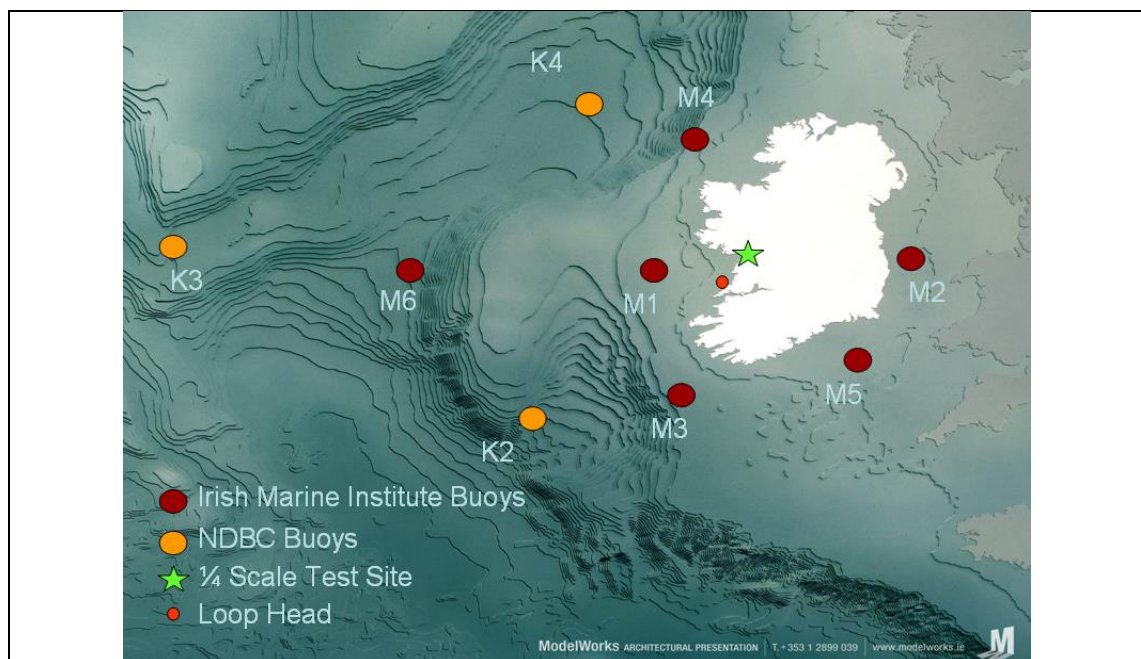


**Figure 1.6. Data buoy network around the Irish Coast.**

#### ***1.4.1. Galway Bay Quarter Scale Test Site***

The Galway Bay Wave Energy Test Site was established jointly by the Marine Institute and Sustainable Energy Ireland under Phase 1 of the Ocean Strategy for Ireland, which

focuses on development by supporting product R&D and research facilities (Dept. Communications Marine & Natural Resources 2005). This Development Strategy was submitted to government to ensure that ocean energy will be in a strong position to be part of the renewable energy mix in the future. One of the main benefits of this is the development of Irish expertise and technologies so that a leading export industry for ocean energy devices can be established.

The Marine Institute, a national agency responsible for marine research, technology development and innovation in Ireland, and the Sustainable Energy Authority of Ireland, formally Sustainable Energy Ireland, a statutory agency of the Irish Government Department of Communications and Natural Resources, are the two primary government level bodies responsible for the development of ocean energy in Ireland. These bodies obtained a foreshore license for a 37 hectare site defined by four navigational buoys, 2.4km off the Spiddle coast in Galway Bay. The site has a minimum water depth of 21m, with a spring tidal range of 4.5m and a neap tidal range of 1.9m. Both the flood and ebb tidal stream is approximately 0.5 m/s in an east west direction (United Kingdom Hydrographic Office 1980). This provides developers with an instrumented, legal test site and the prospect to progress to Phase 3 of the Development and Evaluation Protocol for Ocean Energy Devices with a device in the region of a ¼ scale of the full-scale prototype. This phase of the protocol presents developers with the final opportunity to quickly and inexpensively acquaint themselves with their device in real sea conditions.

The benign quarter scale test site in Galway Bay has had a non-directional surface following buoy on location since the site's inception in 2005. This produced hourly, twenty-minute records of the surface elevation and subsequent spectra and summary statistics. In 2008, the equipment at the site was upgraded with a new receiving station at the Marine Institute Headquarters in Rinville, Oranmore and over a period of four months from April to July of that year, a directional buoy was included on site for a parallel deployment with a spatial separation of 200m where simultaneous measurements were recorded. The data buoys used were Datawell non-directional and directional Waverider buoys. The data sets contained 30 minute surface elevation records from both buoys, although at different sampling rates. The files generated concurrently were analysed in both the frequency and time domain, the results of which are presented in a later section.

The Galway Bay test site is a benign location, and it is usual to scale the measured waves by a quarter according to Froude scaling laws to represent full-scale conditions in the Atlantic Ocean. However, the wave energy test berth is located in a semi-enclosed bay, therefore full-scale swell approaches the site from the west and south west, to mix with the quarter scale fetch limited conditions. The consequences of this aspect of scaling at an intermediate test site are also discussed. A map of the site is shown in Figure 1.7 and the Waverider buoy locations and coordinates are shown in Figure 1.8.

The nature of the bathymetry of Galway Bay can be seen from Figure 1.9. The survey information is from the Integrated Mapping For the Sustainable Development of Irelands Marine Resource (INFOMAR) project, a joint venture between the Marine Institute and the Geological Survey of Ireland (Marine Institute 2009). Due to shoaling effects in such conditions, the theory suggests that the wave height will change as the waves approach the coastline from the Atlantic. As the wave propagates into shallower water, the phase speed approaches the group velocity and the waves become less and less dispersive. Such variations in group velocity cause variations in wave energy and hence amplitude (Holthuijsen 2007).

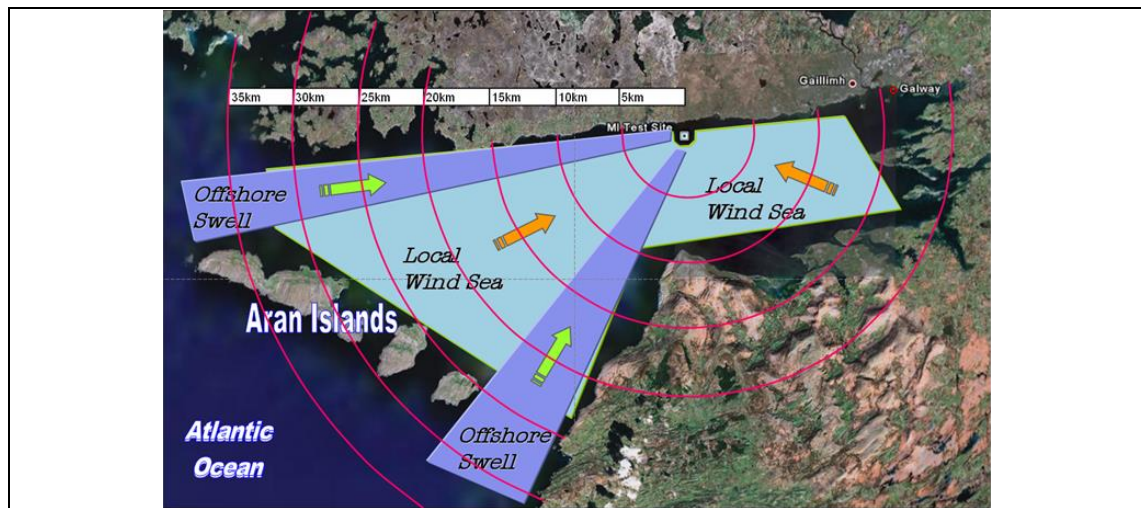


Figure 1.7. Galway Bay benign wave energy test site map.

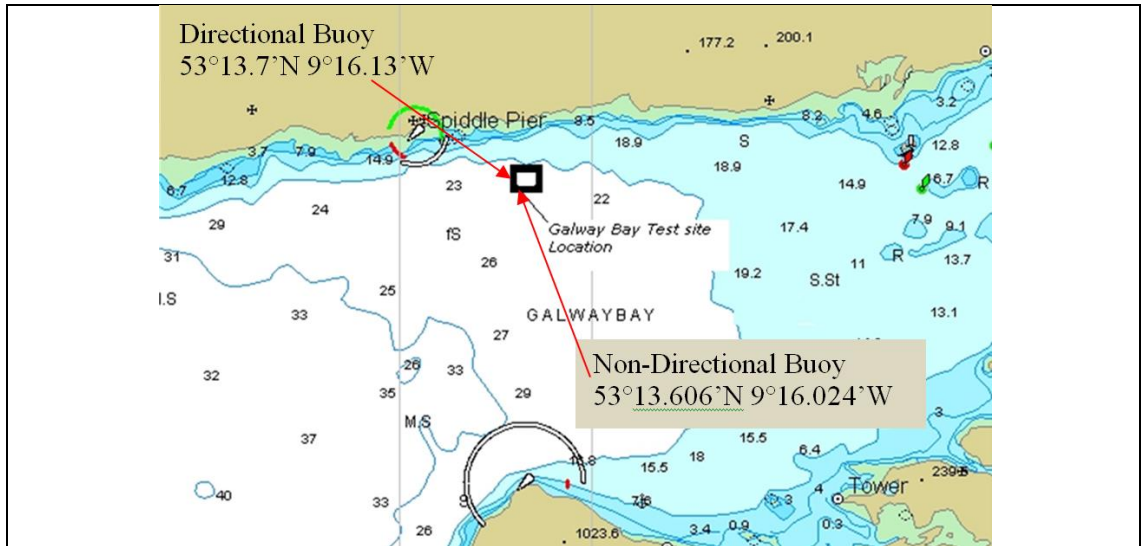


Figure 1.8. Data buoy locations in Galway Bay.

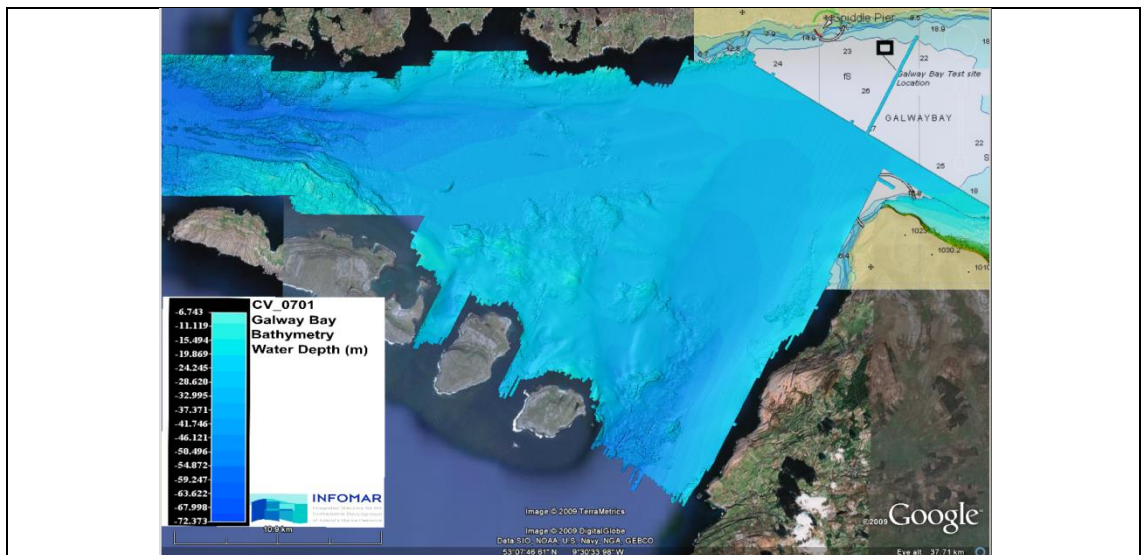


Figure 1.9. Galway Bay bathymetry.



Figure 1.10. Fetch lengths for Galway Bay.

Figure 1.10 shows the primary fetch distances in Galway Bay from the wave energy test site. The Aran Islands to the southwest protect the test site from the full force of the North Atlantic, however, long period swell does approach the test site through the north and south channel around the Aran Islands. These short distances of fetch make the location of the Galway Bay site suitable to medium scale testing of wave energy devices.

Figure 1.11 shows two quarter scale devices, OE Buoy and Wavebob, on site in Galway Bay with the town of Spiddie to the left in the background. This is the location of the nearest pier and berthing facilities, although the industrial port of Galway City is 17 km to the east. The device power output of the OE Buoy and the concurrent wave record were used to perform a comparison of the input wave spectral shape to the produced power output of the device, the results of which are presented in a later section. These results showed that the spectral shape of the input wave field can have a significant effect on the device power output, even though the summary statistics of the incident wave field may not vary too much.

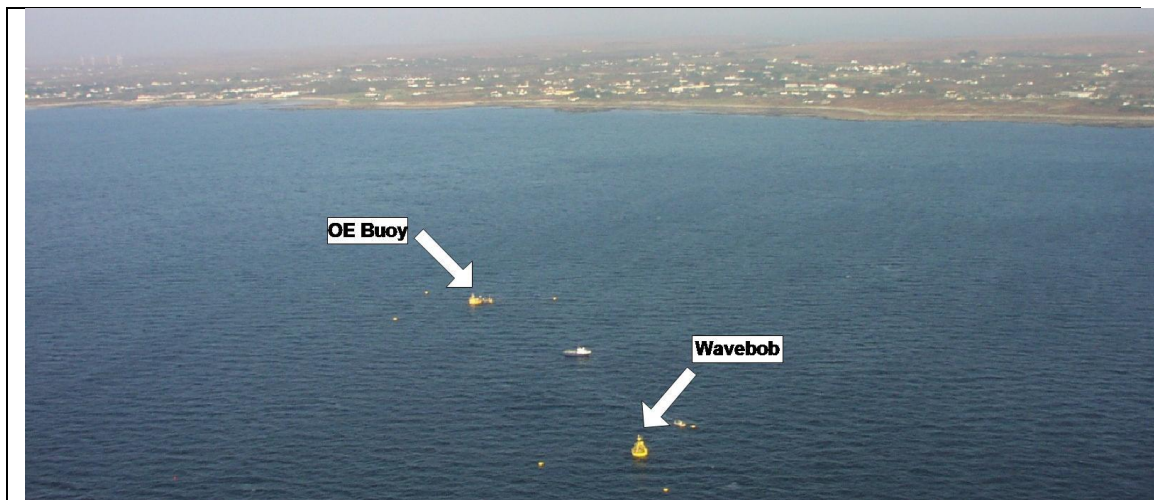


Figure 1.11. Devices and work vessel on site at benign wave energy test site, Galway Bay.

#### 1.4.1.1. Benign Site Numerical Model

To investigate the wave conditions and the sites' suitability as a wave energy test site, the Marine Institute implemented a numerical wave model to obtain a full year's hindcast data for the year 2000. The results of the model were made available to the HMRC for further study. The computer model used to obtain the hindcast data for the test site was SWAN (Simulating WAVes Nearshore), which is a package developed at Delft University (Booij, Ris and Holthuijsen 1999). SWAN predicts wave conditions, primarily in shallow



water coastal areas, lakes or estuaries from user-defined wind, bottom and current conditions. SWAN is a free, open source, wave model based on the energy balance equation. Variable resolution grids and boundary fitted grids are accommodated by the model, which included nested grids of finer resolution. Phenomena such as bottom and current induced shoaling, reflections and dissipation by white-capping, wave breaking and bottom friction are all represented in the SWAN model. However, refraction is modelled in a restricted sense, limiting the effect to a few wavelengths and diffraction is only approximated (Holthuijsen 2007).

The SWAN package is a third generation model, which calculates the non-linear energy transfers explicitly, although it is necessary to make both analytical and numerical approximations to accelerate the calculations. This energy balance equation describes the surface gravity wave field in time and space. On the left hand side of the equation are terms describing the two-dimensional wave spectrum, dependent on frequency and direction. On the right hand side is the net source function, which describes the energy input by the wind, propagation, non-linear wave-wave interactions and dissipation. The essence of the model is to solve this equation.

The definition of the generation of the model is based on the calculation or approximation of the quadruplet wave-wave interactions. This phenomenon occurs in deep water when two pairs of wave components (i.e. four frequencies and directions) interact and resonate. In this case, energy is transferred among the four components involved. However, the computation of this phenomenon in models such as SWAN is substantial as it is required for each wave frequency and direction considered. Hasselmann (1985) derived a method, called discrete interaction approximation (DIA), which found approximations that would reduce the computational effort but retain the basic characteristics of the quadruplet wave-wave interactions. The explicit calculation of these interactions are what distinguish third generation models from those of first or second generation, where the wave-wave interactions are absent or severely parameterised (Holthuijsen 2007).

The Galway Bay SWAN model is based on a spatial grid that extends west from Oranmore, Galway at  $8^{\circ}54'W$  to  $10^{\circ}56'W$  and from Liscannor Bay, Co. Clare at  $52^{\circ}49'N$  to Slyne Head, Co Galway at  $53^{\circ}28'N$ . This area covers approximately 2,774 square nautical miles or 9,500 square kilometres,  $600\text{km}^2$  of which consists of Galway

Bay. The grid units are in kilometres with grid nodes at 2km spacing (See Figure 1.12). The focus of interest is the Wave Energy Test Site at a local grid location of (112.530, 46.037). The test site falls within the bounds of four grid nodes of the SWAN model and so the output data is interpolated from these grid nodes.

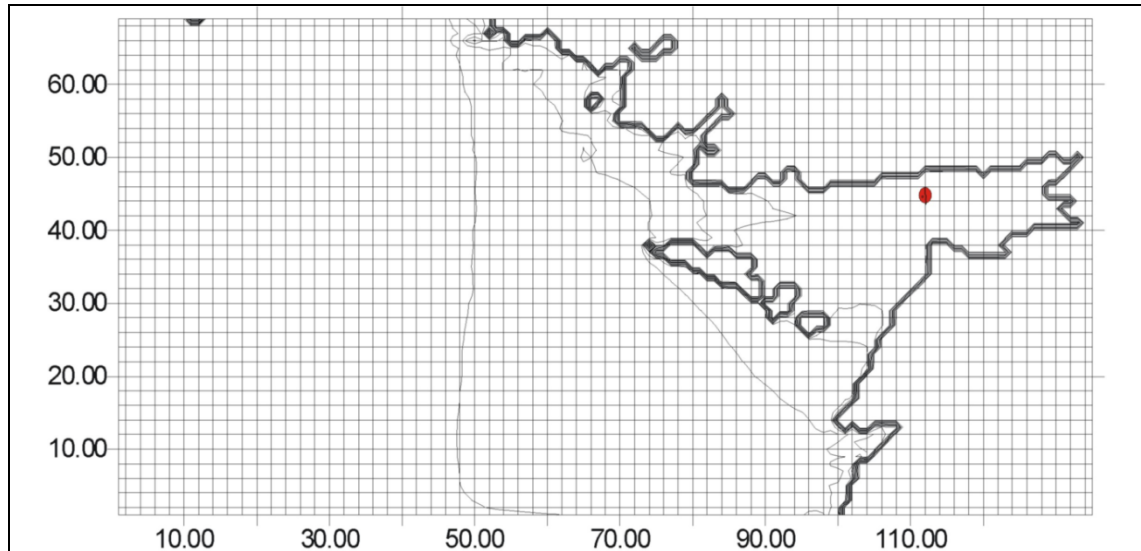


Figure 1.12. Extent of SWAN model.

It was possible to analyse the output data of the SWAN model in two forms, the summary statistics comprising of significant wave height ( $H_{m0}$ ), spectral peak period ( $T_p$ ), spectral mean period ( $T_{02}$ ) and the mean direction of propagation of the waves in degrees. This data is provided for the twelve months of the year 2000 at 12-hour intervals for midnight and noon. The second output file is the two-dimensional non-stationary coordinate file from the SWAN model. This file contains the two-dimensional variance density spectrum, every three hours for the entire year at the interpolated grid point. This file comprises information on the coordinate system employed, either Cartesian or spherical, whether the computations are stationary or non-stationary with respect to time, and the location coordinates of the point of interest in the spatial grid. Following this header data, the 32 frequencies bins, 36 directional bins and corresponding variance densities are supplied.

The variance densities are truncated by SWAN to integer values. A factor is provided for each data set to obtain the correct values of the variance densities. The unit of the variance density is then [ $m^2/Hz/^\circ$ ]. By integration across the frequencies the one-dimensional variance spectrum may be obtained. The spectrum in the model is segregated with a constant directional resolution ( $\Delta\theta = 10^\circ$ ) and a constant relative frequency resolution

( $\Delta f/f = 0.1$ ). The directional resolution can be defined by the user as the number of subdivisions of the  $360^\circ$  of a circle. The frequency resolution is defined by the high and low discrete frequencies and the number of frequency bins in this range, where  $N$  is the number of frequencies in Equation 1.2 and the frequency step is given by Equation 1.3. This method of discretisation results in a frequency range from 0.0521 Hz to 1 Hz.

$$\Delta f = \left( \left( \frac{f_{high}}{f_{low}} \right)^{1/N-1} - 1 \right) f \tag{1.2}$$

$$f_{i+1} = 1.1f_i \tag{1.3}$$

The convention for the Cartesian coordinate system in SWAN is as follows. The direction is the angle between the wave propagation vector and the positive  $x$ -axis, measured counter clockwise. This vector indicates the direction in which the waves are travelling to as shown in Figure 1.13 indicated by the innermost circle, *SWAN Orientation*. The orientation of the positive  $x$ -axis is chosen arbitrarily by the user and in this case is geographic East. For ease of understanding, use, and application of the results the SWAN wave directions have been converted to meteorological convention. By adopting this conversion system a SWAN wave vector of  $90^\circ$  would be defined geographically as approaching from the South. The analysis of the data from this model will be dealt with in a later section.

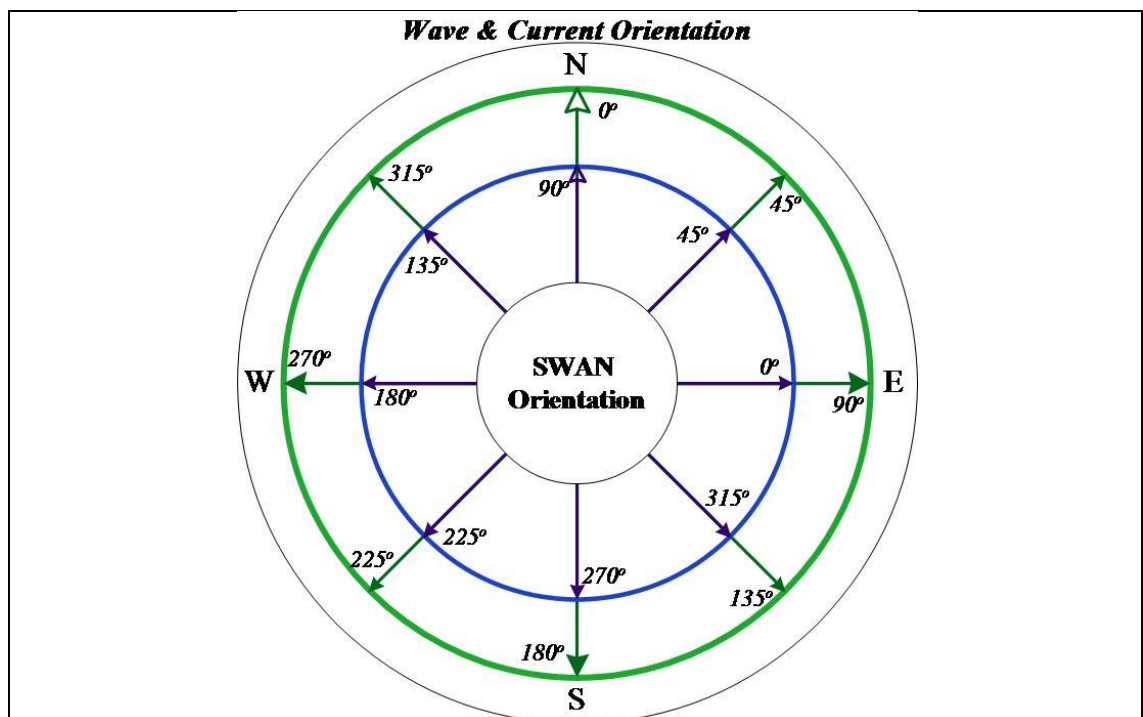


Figure 1.13. SWAN direction orientation.

#### ***1.4.2. Loop Head Exposed Site***

The second site that data has been measured at is an exposed Atlantic Ocean location that would be suitable for the deployment of a wave energy convertor at the full-scale demonstration or prototype phase of development. The mean water depth at this location is approximately 50m and the site is fully exposed to the prevailing wave systems of the North Atlantic Ocean. A non-directional wave measurement buoy was deployed at the site 2km from shore, from the end of 2003 up to the summer of 2005. The site was chosen for an investigation of the spectral output of the WAM wave forecasting numerical package output spectra compared to measured spectra (Holmes 2007), however, in this work its data will be used as a full-scale comparison to the benign test site in Galway Bay and for other seasonal analyses.

Although there are similarities in the in the basic scientific philosophy of the SWAN and WAM models, SWAN contains some additional formulations primarily for shallow water and the numerical techniques are very different. The application of the WAM model is more suited to large scale global models encompassing offshore deep water. In this way, SWAN can be nested within a global WAM model as long as the boundary conditions of the nested SWAN model is not influenced by shallow water effects.

A non-directional surface following buoy was located at this site for data retrieval. The buoy was the same model as the original buoy at the Galway Bay test site. The data set from this site comprised of two consecutive sets of six month winter/spring seasons from December to May. The location of the Datawell Waverider buoy off Loop Head is  $52^{\circ}39'N$ ,  $9^{\circ}47'W$  and can be seen in Figure 1.14.

The buoy records acceleration which is converted into surface elevation with a sampling frequency of 2.56 Hz, and the raw elevation profile comprised 3,072 data points that resulted in a 20 minute time series, stored by the receiver onshore at Loop Head. These surface elevation and spectral files were general logged hourly, however there is a bias towards storm seas due to over measurement when the significant wave height exceeded a given threshold. This was due to an onboard procedural routine. This bias has been removed from the data set used here.

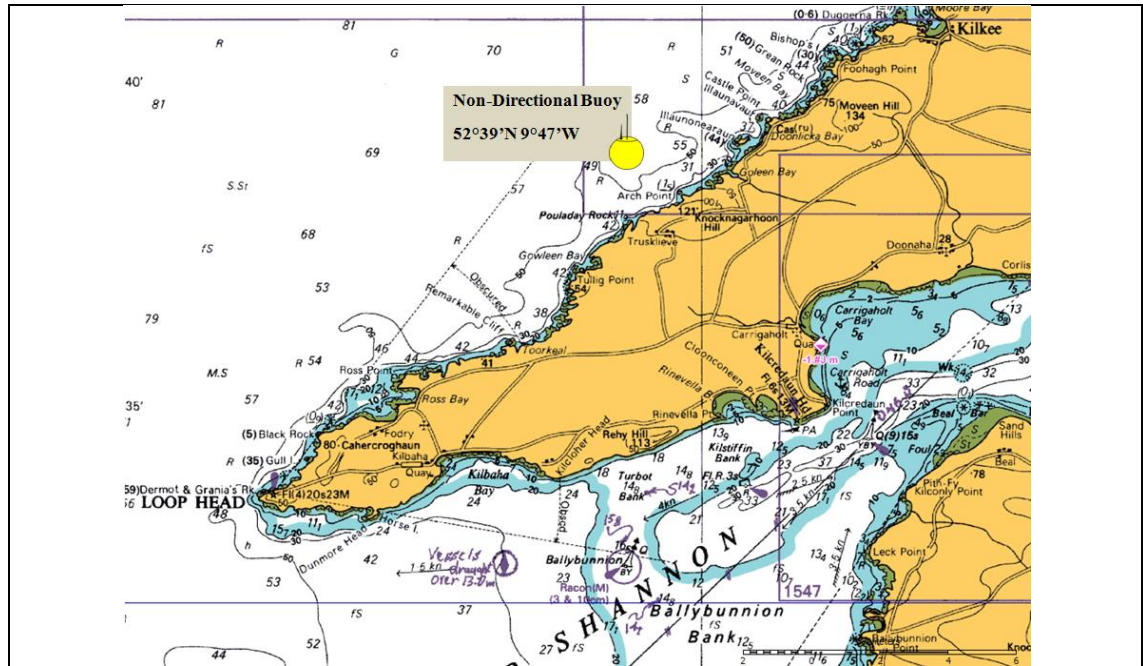


Figure 1.14. Location of non-directional buoy off Loop Head.

**1.5. Work Objectives**

The previous sections have shown that there are many wave energy devices being developed worldwide, with a lot of these concepts in a position to be deployed in the real sea environment for the first time. The luxury of having the ability to run required sea states at a testing facility is no longer available and so device developers have to accommodate the incident wave field to its fullest extent.

It is proposed to introduce the various instruments that are available to a developer of a wave energy device for the purpose of wave measurement. Specifically, surface following buoys are introduced but other instruments and measurement methods are discussed. The data files and internal processing methodology of the surface following buoys are given along with the implementation of analysis methods, measurement schemes and data quality check procedures that were carried out for the data sets from the Loop Head and Galway Bay sites.

The various tools available in the time and frequency domains, for analysing time varying signals are discussed in detail and applied to the wave data sets. The results of this analysis are compared to empirically derived studies, especially the more commonly used spectral profile equations such as Pierson-Moskowitz, JONSWAP and Bretschneider. By investigating the spectra that are used to compile bi-variate scatter diagrams, various

comparisons are introduced and the variation of the ensemble averaged spectra across the scatter diagram is discussed and compared to the more ideal profiles of the empirical studies. The ensemble averaging at various time scales is also investigated and discussed.

The study of the variation of wave spectra is developed further by investigating various methods to analyse and separate bimodal wave spectra and the suitability of these methods for application to the data sets from Galway Bay and Loop Head including a comparison to the findings of previous studies.

Finally, the methods investigated in the preceding sections are applied to the investigation and analysis of the OE Buoy wave energy convertor and sea state data from the Galway Bay test site. Initially, it is determined whether the benign test site is a suitable quarter scale test site by using Froude scaling laws and comparing the results to those of the more exposed open Atlantic site at Loop Head. The measured sea states at Galway Bay are then presented concurrently with device power output data from the device with the simplified orifice PTO to show the influence that variations in the incident wave spectral profile can have on a device's power output while comparing the power output levels to those estimated from previous phases of testing. A new concept of a Power RAO is introduced as a means of identifying a suitable incident wave spectrum in terms of the required spectral profile for optimum device power conversion.

The overall theme of this work is to encourage detailed wave measurement in the wave energy industry by highlighting the various measurement instruments available and their limitations along with the tools to conduct extensive analysis of the incident wave field. The importance of obtaining a measured wave spectrum is shown to eliminate the assumptions that can be made of the spectral profile from summary statistic data, and the impact this can have on device assessment and development.

## 2. OCEAN WAVE MEASUREMENT

The increased sophistication of wave data analysis techniques have coincided with the advancement of measurement instrumentation and equipment to record the surface elevation and wave direction with the computer technology and power to perform the analysis onboard and in near real time. Visual observation from ocean shipping was the primary source of met-ocean data until the introduction of ship borne measurement technology. This has advanced from floating buoys that can be deployed for years on end to remote sensing techniques such as radar and satellite observational methods.

The next phase in the evolution of wave measurement comes from the requirement of detailed information for wave energy device assessment. Knowledge is required at several different time scales. The shortest time scale being seconds required for wave-by-wave measurement for real time control of the power take-off mechanism of the device. The power production from sea state to sea state has a time scale of approximately 30 minutes to a few hours and the subsequent forecasting of electricity sales for grid monitoring and compliance would be 12-24 hours. A longer-term assessment of the prevailing conditions so that operation and maintenance activities can be scheduled and performed in an efficient and cost effective manner would be taken from forecasts of a number of days.

### 2.1. Wave Measurement Methods

Apart from surface following buoys, there are many different systems available for obtaining information from the sea. These options, of course, depend on the information needed, and on the scale of the application. Wave measurement apparatus can be categorised as either *in situ* or remote sensing. *In situ* measurement apparatus incorporates surface following buoys, sub-surface instruments such as ADCPs and pressure transducers, and surface piercing mechanisms such as wave poles (Holthuijsen 2007). As technology and accuracy improves, the data recovered is more expansive leading to better capabilities in terms of prediction and assessment.

Data recovery, storage and transmission also influence the type of measurement instrument requirements for a given task. Remote devices require either telemetry by satellite or onboard storage with scheduled retrieval. Coastal projects will be able to incorporate shoreline-based systems such as radar or cabled ADCPs while surface

following buoys can incorporate HF radio antennas or utilise the GSM mobile phone network for data transmission. Measurement systems closer to shore can also provide a greater abundance of information to the user as a direct cable link can incorporate larger data packets in the transmission and negate battery requirements in comparison to remote systems.

### 2.1.1. Visual Observation

With the popularity of commercial trans-Atlantic shipping and the advent of radio communication at the start of the twentieth century, a system was devised that incorporated observations from ships which relayed sea conditions and other meteorological details to ships in the vicinity and back to meteorological offices ashore.

The World Meteorological Organisation's (WMO) Voluntary Observing Ship (VOS) scheme is an international system incorporating nearly 5,000 ships across the world. These ships are divided into three categories: Selected, Supplementary and Auxiliary ships with decreasing meteorological instrumentation onboard, respectively. Of these ships, only the Selected store information on direction, period and height of waves. The equipment is supplied and installed on these ships by WMO who also cover the cost of transmission via satellite or radio four times daily.

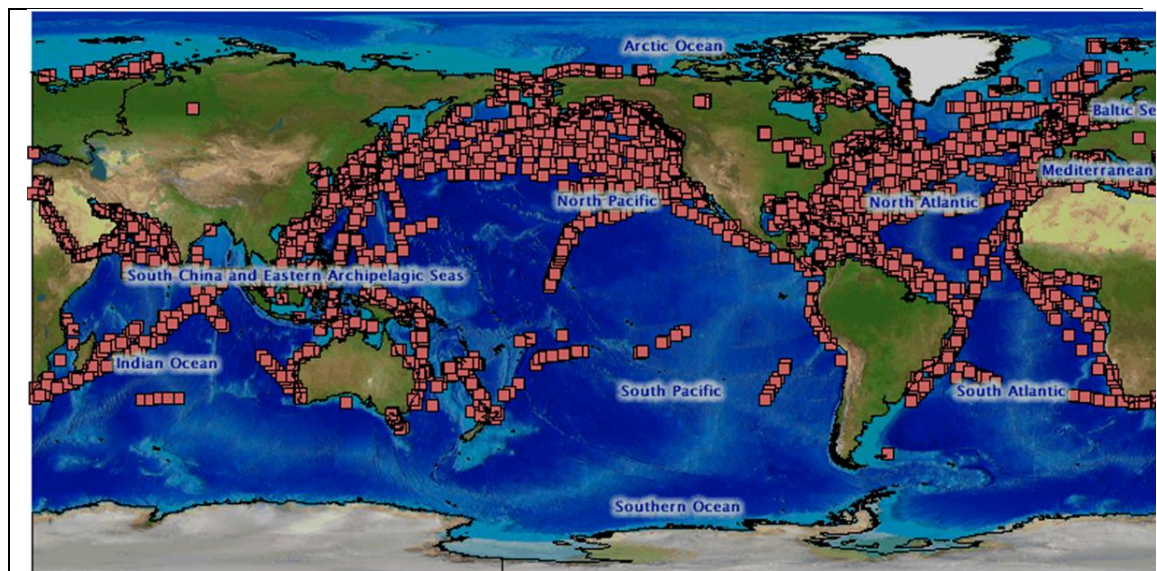


Figure 2.1. Visual observing ship worldwide coverage (JCOMM).

In studies that have been conducted with both onboard wave measurement instruments and visual observation, it has been shown that waves are reported steeper than recorded



by instruments due to shorter, steeper waves dominating the observer's perception of wavelength. However, wave height is reported reasonably accurately as the ship size can be used as a scale ((Draper 1986), (Liu and Kessenich 1976)). Visually observed wave data is abundant for the north Atlantic and Pacific as the northern hemisphere has experienced much more sea traffic than the southern hemisphere, where there are large areas of the southern oceans bereft of visual wave data (Figure 2.1).

It has been found however, that visual observations can be subject to fair weather bias, especially during the winter months of the northern and southern hemispheres. In a study that compared global VOS observations to satellite altimeter data, the significant wave height determined from the altimeter data was higher than those from VOS in areas of high waves and smaller in areas of low to moderate waves. Positive differences, where VOS observations are greater than altimeter data, occurred during the northern and southern hemisphere summer months. This trend was independent on the sampling density, implying a fair weather bias in all observations (Gulev et al. 2003).

### **2.1.2. Wave Staff/Probe**

One of the simplest forms of surface elevation measurement is that of a vertical pole or gauge that measures displacement by a change in resistance or capacitance over an electrical circuit as the water level rises and falls. This is the approach adopted in most wave basins and flumes at hydraulic facilities to measure the surface elevation, but it can also be adopted in real conditions at a larger scale. Resistive and capacitive probes are twin wire electrical probes that pierce the surface. Elevation is measured by the change in conductance between two parallel wires. The conductance and hence immersion can be measured by applying a potential difference between the wires and measuring the current that flows. This change in voltage is linearly proportional to the water surface displacement. As the conductance in water can change, the probe must be calibrated regularly.

The measurement method of a wave staff or capacitive/resistive probe is described as Eulerian. This is the measurement of the displacement or velocity of the fluid at a point in the fluid at every instant of time. This mathematical theory also relates to measured fluid flow and can be described graphically with vectors.

In the field, this configuration is surface piercing and requires a support frame or structure, therefore the accuracy of the reading can be contaminated by reflections. One probe is enough for non-directional measurement, however at least three probes are required to obtain directional information, although the use of more wire gauges give better accuracy and there are many configurations available, e.g. PADIWA (Frigaard, Brorsen and Kofoed 1997).

### **2.1.3. Pressure & Acoustic**

Pressure sensing modules work on the principle that the induced pressure of surface waves decay with depth and the nature of the decay is dependent on the water depth and wavelength. To capture information on those waves of interest in wave energy (wind and swell waves), this limits the deployment of pressure gauges to a depth limit of between 10-20m due to attenuation of the measured waves caused by wave period and pressure at the seabed. They must also be fixed-mounted so that the only variation being measured is that of the sea surface. The reading of a pressure sensor can be degraded by air entrainment near the water surface, turbidity and fouling.

An Acoustic Doppler Current Profiler (ADCP) is a common method for measuring the current profile along a column of water. The support frame incorporating the ADCP can be anchored to the seabed, quay wall or to the keel of a ship. High frequency sound waves are transmitted from the ADCP, which when reflected by particles in the water will return to the ADCP as an echo with a slight change in frequency. This frequency difference is the Doppler shift and can be used to calculate the velocity of the water particle and its direction. The reflected sound wave will have a higher frequency than the transmitted wave if the particle is moving toward the instrument and a lower frequency if the particle is moving away from the instrument. By measuring the time it takes for a sound wave to return as an echo, the current profile at various positions along the water column can be obtained. Added to this setup, a pressure sensor or echo sounder can be used to determine the wave as well as the current profile.

As with the pressure sensor, for accurate measurements it is important to prevent fouling of the transmitters/transducers. Marine life and air entrainment can also cause miscalculations of the current.

#### **2.1.4. Radar/Satellite**

Wave measurement from the shoreline or over great distances (i.e. from space) is achievable by using electromagnetic waves to measure the disturbance of the water surface. This method of remote sensing allows for measurement without disturbing the water surface. These instruments can be positioned on a tower at the shoreline, on the deck of an offshore platform or onboard a ship.

Several ground-based systems are available that use a variety of techniques, however there are two general operation modes, near vertical and low grazing. These techniques are combined with either HF radio, infrared or microwave signals to obtain the required ocean data. The selection of the electromagnetic wave type corresponds to the range over which the measurements are to be taken and the accuracy required. The signal from a microwave antenna is dispersive, therefore range limited. However, infrared radar is non-dispersive.

Near vertical radars measure the water surface by the change in the echo of the transmitted wave, however the measurement can be contaminated by reflections of the supporting structure, as they tend to have a large footprint. A single unit will give a point measurement, although similar to wave gauges, three or more in a geometrical configuration can reveal directional details. For ship based systems, accelerometers are used to compensate for the ship motion. The low grazing mode of operation relies on surface ripples. The echo is generated by Bragg scatter, hence Bragg waves (surface ripple) must be present. The backscatter signal is modified by tilting, hydrodynamic interaction, and the shadowing of the surface ripple by larger gravity waves.

Laser altimeters (infrared) produce a narrow high frequency pulsed beam with a small footprint, although it is prone to natural sources of infrared interference such as fog or water spray. Microwave radar is not affected by fog or spray and can be used day or night, however a large antenna is required to produce a narrow beam. High frequency radar can operate at distances from 30km to 100km, in bad weather and it can be used to measure both wave and current conditions. There is no colour associated with radar images because of the use of a single frequency.

The first satellite system designed specifically for remote sensing of the Earth's oceans, Seasat, and managed by the NASA Jet Propulsion Laboratory was launched on the 28<sup>th</sup> June 1978 however lasted just over 100 days. Since then there have been several other satellites, from Europe and America, put into orbit for the purpose of ocean wave and wind measurement. These satellites are in orbits of between 700km and 1400km, depending on the return period and density of the measurements. For example, the current European Space Agency satellite Envisat has a return period of 35 days at an orbit of 790km, whereas the American Jason-2 satellite has a cycle of ten days at an orbit of 1330km. The difference in orbital distance and return period is a compromise towards density of measurement points around the globe as the distance of the orbit dictates the ground track separation. Two examples of the ground track spacing around the British Isles is shown in Figure 2.2 for the European ERS-2 satellite, which preceded Envisat, and the TOPEX/Poseidon satellite which preceded the Jason satellites. The spacing of the measurement tracks for the ERS-2 satellite is much closer than that for the TOPEX satellite as the altitude of the ERS-2 orbit is lower at 790km than for the TOPEX which orbits at the an altitude of 1330km.

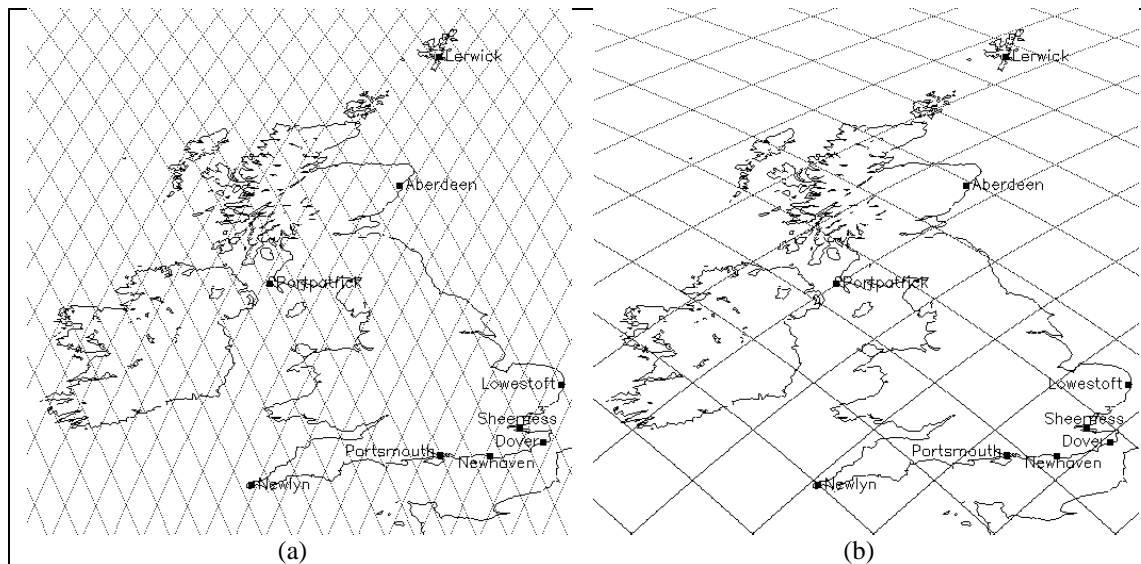


**Figure 2.2. Satellite ground tracks for (a) ERS-2 and (b) TOPEX.**

The main instruments onboard these satellites are radar altimeter, microwave scatterometer, and synthetic aperture radar (SAR). The vertical pointing altimeter transmits a pulsed radio signal. The backscatter of the pulse is influenced by the roughness of the sea surface and the amount of distortion is related to the significant wave height over the footprint, the accuracy of which can be comparable to wave buoys. Wind speed

can be derived from the strength of the backscatter signal, although the microwave scatterometer is specifically designed to measure the near surface wind speed and direction. The synthetic aperture radar tracks the phase and amplitude of a returned signal as the satellite moves along a track. These observations are combined to form high-resolution images, from which algorithms are determined to estimate the wave crest length, direction and subsequently the primary summary statistics.

### **2.1.5. Surface Buoys**

Surface following buoys are the most common method of obtaining information from the ocean's surface. These buoys can vary in size and form, from spherical buoys of less than a meter diameter to ship hull shaped floating platforms and discus buoys up to 12m in diameter. An important aspect of these buoys is their mooring, which is designed to keep the buoy on station without influencing the measurements.

Ocean Data Acquisition Systems (ODAS) are defined as follows (Meindl 1996):

*“ODAS means a structure, platform, installation, buoy, or other device, not being a ship, together with its appurtenant equipment, deployed at sea essentially for the purpose of collecting, storing or transmitting samples or data relating to the marine environment or the atmosphere or the uses thereof”*

These buoys were initially developed by government funded agencies, whose remit it was to provide data from isolated locations around the coast. Initially these buoys transmitted the data over HF radio, but now most transmit via satellite systems.

Data buoys not only have wave measurement instrumentation onboard, but may also have atmospheric observational sensors such as barometers and wind anemometers. Weather buoys are the first indication of severe weather systems approaching an area. Due to the value of this data, some countries have dedicated buoy monitoring networks such as Marine Automatic Weather Station (MAWS) in the UK and the Irish Marine Weather Buoy Network. The data includes readings of the water and air temperature, wind speed and direction, wave height and period, and atmospheric pressure. This data is produced hourly and transmitted to the European Centre for Medium Range Weather Forecasts (ECMWF) for further dissemination and incorporation into environmental numerical models for calibration and to give ground truth measurements for weather forecasting.

The design of a buoy hull has to adapt to the changing sea state and weather conditions as quickly as possible while negating the likelihood of capsizing in severe seas or damage to the instrumentation. There have been various forms of hulls proposed, mostly developed from research. The American National Oceanic and Atmospheric Association (NOAA) have developed six buoy designs detailed as follows and shown in Figure 2.3:

- 12m diameter discus hull (Fig. 2.3a)
- 10m diameter discus hull (Fig. 2.3b)
- 6m NOMAD (Navy Oceanographic Meteorological Automatic Device) (Fig. 2.3c)
- 3m diameter discus hull (Fig. 2.3d)
- 2.4m diameter Coastal Buoy (Fig. 2.3e)
- 1.5m COLOS (Coastal Oceanographic Line Of Sight) (Fig. 2.3f)

Other groups from around the world who operate an observational buoy network have developed their own buoy hulls due to practical and financial reasons. Primarily the environmental variables to be measured dictate the design, along with water depth and mooring system. The M and K buoys deployed off around the Irish coast referred to in Section 1.4 are of the type depicted in Figure 2.3d.

For commercial projects, smaller buoys of approximately one-meter diameter, which can be deployed by hand from small vessels, are more suitable. These buoys are primarily designed to follow the displacement of the ocean's surface and derive wave height and period from the relevant motions of the buoy through spectral analysis techniques. The basic version consists of a heave sensor, an accelerometer on the vertical axis, to measure the near vertical surface displacement. Analysis in the time and frequency domain reveals the summary statistics such as wave height and period. This concept is then expanded to the horizontal axes for derivation of the directional spectrum.



Figure 2.3. ODAS hull types.

There are a number of companies who manufacture and supply such data buoys, with two of the technology leaders being Datawell BV, based in the Netherlands, and AXYS Technologies in Canada. Examples of their directional buoys are shown in Figure 2.4.

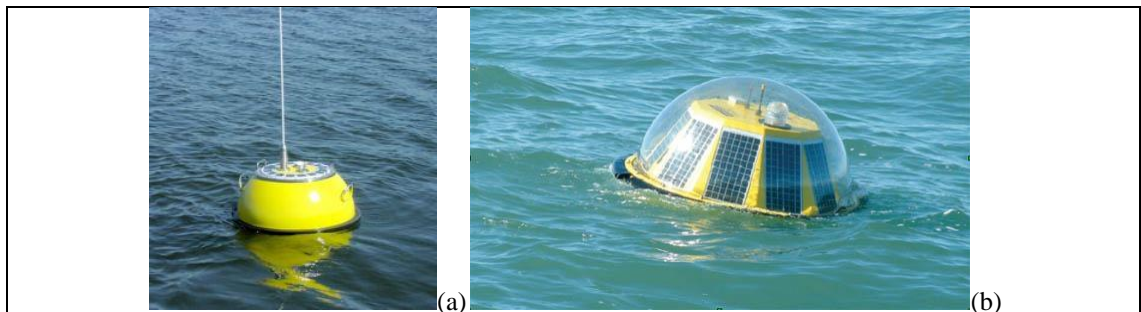


Figure 2.4. (a) Datawell BV and (b) AXYS Technologies directional buoys.

It is shown in Figure 2.4 that both buoy hulls incorporate solar panels. This prolongs the battery life for floating buoys, however latitude and hours of sunlight will have an impact on the power budget of these buoys. Both of these buoys use accelerometers on three axes

as well as gyroscopes and a compass to measure the surface elevation and direction in ocean waves. The AXYS Technologies buoy uses solid state accelerometers and rate gyros with a fluxgate compass (Axys Technologies Inc. 2005), whereas the Datawell buoy is based on a stabilised platform that remains horizontal. The acceleration measurements are integrated to produce velocity or displacement as required. In the case of directional measurements, there are various methods to determine the directional spectrum, which will be discussed in more detail in a later section.

The mathematical description used for surface following buoys is that described by Lagrangian methods. In essence, the buoy follows a portion of fluid along its path, specifying when each particle reaches each point in its path. Graphically this can be described by streamlines.

#### ***2.1.6. Eulerian vs. Lagrangian Measurement***

Eulerian and Lagrangian measurements are described briefly in their respective measurement mode sections. The measurement of the surface elevation of the sea at a point in space by a wave staff or probe is said to be an Eulerian measurement. By placing an accelerometer in a floating buoy and double integrating the instruments measurement, the resultant vertical surface displacement is said to be Lagrangian. The measurements from these two methods are assumed equivalent for low amplitude irrotational waves. However, in a paper by Longuet-Higgins (1986), it was shown by calculation and physical trials that there can be a marked difference in the measurement of steep waves in deep water.

The first difference in the two methods that this paper addresses is the difference in the measured period for trochoidal waves. Trochoidal wave theory is a simplified method to describe the motion of wave particles but it does not account for the forward motion of these particles, as is the case in reality. A trochoidal path is one traced by a point within the circumference of a circle as it rolls along a line, differing slightly to a sine wave.

For the Eulerian case, the wave period is simply the wavelength divided by the wave speed. However, the Lagrangian case has to take into account the Stokes drift, therefore the wave period is then the wavelength divided by the difference between the wave speed ( $c$ ) and the drift velocity ( $U$ ). The difference between the Eulerian wave period ( $T_E =$



$\lambda/c$ ) and the Lagrangian wave period ( $T_L = \lambda/(c - U)$ ) is then due to a Doppler shift. By approximating the surface profile of a wave by the arc of a pendulum swing, where the chord of the arc is equivalent to the side of an equilateral triangle, the mean speed of advance of the surface particle ( $U/c$ ) is calculated and the following relationship is observed (Equation 2.1).

$$\frac{T_L - T_E}{T_E} = 0.38 \tag{2.1}$$

The consequence of this is that the frequency spectrum may tend to deviate towards the lower frequencies in the Lagrangian case compared to the equivalent Eulerian measurement case.

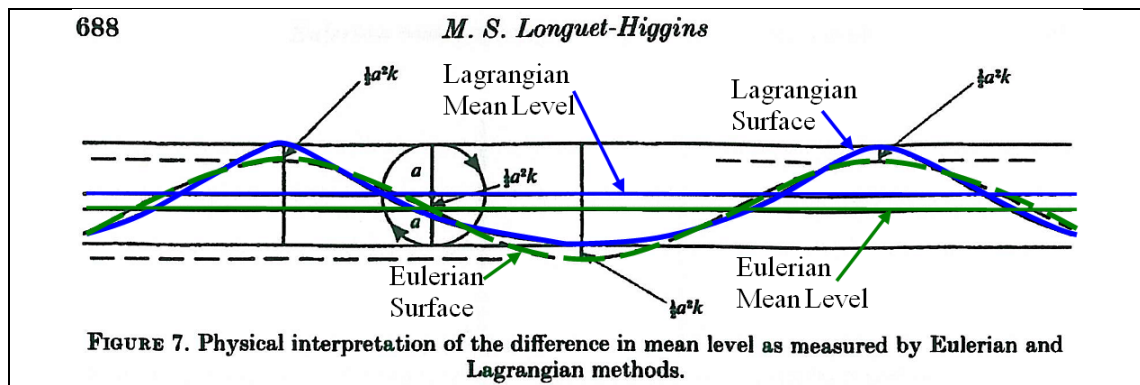


Figure 2.5. Definition of Lagrangian and Eulerian Path, after (Longuet-Higgins 1986) [where  $a$  is wave amplitude and  $k$  is wave number]

Another consideration highlighted by Longuet-Higgins and shown in Figure 2.5 is that the mean of the surface displacement tends to be higher for a Lagrangian measurement than for an Eulerian measurement. This has implications for satellite measurement as the difference in mean level could be in the order of 1% of the dominant wavelength (Longuet-Higgins 1986).

## 2.2. Surface Following Data Buoys

The most common method of measuring the ocean’s waves is by placing a floating body, tethered to the seabed, at the surface and allowing it trace the undulations that occur. There are many forms of wave measuring buoys available of various sizes and shapes, and equipped with a variety of instruments for not only oceanographic information recovery but also meteorological information cataloguing. Some of the data that is used

in the following analysis is from the ODAS meteorological buoys deployed by the Marine Institute around the coast of Ireland. These buoys do not transmit the surface elevation record, but only the hourly summary statistics.

The two pieces of equipment that were deployed at the chosen sites are both from the Datawell company. The largest data set is provided by the Waverider Buoy, a non-directional spherical buoy. Two of these buoys were deployed at the exposed Atlantic coast location and as the initial monitoring buoy at the wave energy test site in Galway Bay. This measurement platform is based on the original buoy developed by Datawell that was launched in 1968. The primary element of this buoy is the stabilised platform that provides an artificial horizon so that vertical accelerations are measured and doubly integrated to obtain the surface elevation. This combined with an anchoring system combining bungee cord and chain, allows the buoy to follow the surface waves closely with a natural period of 40s, an acceptable upper limit for surface gravity waves.

The second buoy deployed at the Galway Bay test site is a directional version of the Datawell Waverider. The directional measurement system is a further development of the stabilised platform of the non-directional buoy. A 0.9m diameter spherical stainless steel hull directional buoy was launched to market by Datawell in 1988 (Datawell BV 2001). The most modern version of this was deployed by the Marine Institute at the benign wave energy test site in March 2007.

Several transmission options are available for the buoys, although they are equipped with onboard logging for remote deployment. The most common method is to transmit the data via high frequency radio to an onshore receiving station. It is with this option that the quoted battery life occurs. However, although satellite based transmission systems (e.g. Argos or Iridium) are available, these are more battery intensive. GPS position monitoring is available on the Datawell directional buoy only.

### ***2.2.1. Non-directional Buoy***

The Datawell Waverider non-directional buoy is one of the most common types of wave measuring buoys in the world. This type of buoy was used at both the Galway Bay and Loop Head site. Weighing at just less than 100kg, with a diameter of 0.7m, it can be easily deployed from a small boat. The majority of the volume of the hull consists of 26

Leclanché cells, which give a battery life of approximately 12 months. There is also the option to supplement these batteries with an additional solar panel unit. The solar panels are connected to capacitors that are charged by solar energy. In the case of no sunlight and empty capacitors, the power from the batteries is utilised. It should be noted however, that these battery cells are not rechargeable due to floating voltage issues and the possibility of gas production within the pressurised hull, thus creating an explosive risk when brought in for servicing. With the addition of the solar cell hatch cover, the life of the buoy can extend to 36 months for the 0.7m diameter hull. These hybrid power hatch covers are available for all the present Datawell buoys.

The vertical measurements of the buoy are obtained from an accelerometer placed on a stabilised platform, which is located within an aluminium canister toward the base of the buoy hull. The sensitive axis of this accelerometer is pointed in the vertical direction. The stabilised platform consists of a disk suspended in a fluid of similar specific gravity. A very small mass is placed at the base of the platform to make it sensitive to gravity. The large mass of the fluid in combination with the small force of the metal weight makes a pendulum with a natural period of 40s, corresponding to a pendulum length of 400m. This makes the direction of the heave measurement insensitive to horizontal accelerations. Four gold wires support the stabilised platform in the fluid, which is housed within a Perspex sphere as shown in Figure 2.6.



**Figure 2.6. Datawell stabilised platform unit.**

Due to these gold wires, it is not recommended that the buoy be twisted or rotated excessively, as the wires can become entangled. Excessive rotation is defined by Datawell as being spun faster than one turn in 10 seconds. In this case, it is required that the buoy is returned to the manufacturers. To minimise this risk, a triangular frame can be fitted to the hull of the buoy to ensure that it does not spin when a boat or vessel comes into contact with the buoy. The stabilised platform remains vertical within a few degrees, keeping the sensitivity of horizontal accelerations below 3%. When the stabilised platform ensemble becomes entangled, it can be identified in the wave record as deviations of the zero line with a period of 40s due to oscillations of the platform (Datawell BV 1992).

### **2.2.2. Directional Buoy**

The Datawell Directional Waverider buoy is very similar to the non-directional buoy, although it is larger and has the added capability of directional measurement. This was installed later at the Galway Bay test site. The directional buoy is over twice the weight of the non-directional version, with a mass of approximately 225kg. The majority of this weight can be attributed to the 45 batteries that give the buoy a life span of 3 years, which can be extended with the use of an optional solar panel hatch cover up to 5 years. The directional buoys are also fitted with GPS telemetry, which is used as a warning system if the buoy moves off station, to give the data files a timestamp, and to locate the buoy in the event of mooring failure.

The directional buoy determines the surface elevation in the same way as the non-directional buoy. In addition to the stabilised platform with vertical accelerometer, the directional buoy is also fitted with two accelerometers on the horizontal plane at an angle of  $90^\circ$ , two pairs of pitch-roll coils and a fluxgate compass (Figure 2.7a). The horizontal accelerometers are housed in a stainless steel canister above the stabilised platform in a similar fluid to aid stability. When the buoy is in the upright position, the accelerometers aligned along X and Y in the horizontal plane, measure the horizontal buoy motion. As this is rarely the case in real sea conditions, when the buoy is tilted, the Helmholtz coil pairs are used to determine the pitch and roll angles by sensing the electromagnetic coupling with a coil on the stabilised platform. The set-up of one pair (pitch) of the coils can be seen in Figure 2.7b. The second pair (roll) is orientated at  $90^\circ$  to the pitch coil pairs surrounding the stabilised platform sphere. Helmholtz coils are defined by the distance between the coils being equal to the radius of the coils. This generates a near uniform

magnetic field at its centre. This magnetic field is then disturbed by a coil on the platform. With knowledge of the angle of tilt of the buoy, the reading from the accelerometers can be converted to real horizontal accelerations.

The fluxgate compass consists of an aluminium cube with three holes in three mutually perpendicular directions. A magnetic field sensor in each of the holes determines the magnetic inclination, which is a phenomenon of the buoys location, and the orientation of the reference axis of the buoy, indicated by the serial number label on the buoy hull, to magnetic north. By incorporating the fluxgate compass, the accelerations in buoy coordinates can be transferred to north-west coordinates. The elegant combination of the Helmholtz coils with the fluxgate compass negates the need to incorporate the vertical accelerations, ensuring that the best quality surface profile is obtained (Datawell BV 2007). Due to the utilisation of the compass all materials used are non-ferromagnetic, such as stainless steel, aluminium, and Perspex. All the sensors are electronic, therefore there is no need for analogue to digital converter, which can deteriorate the signal quality.

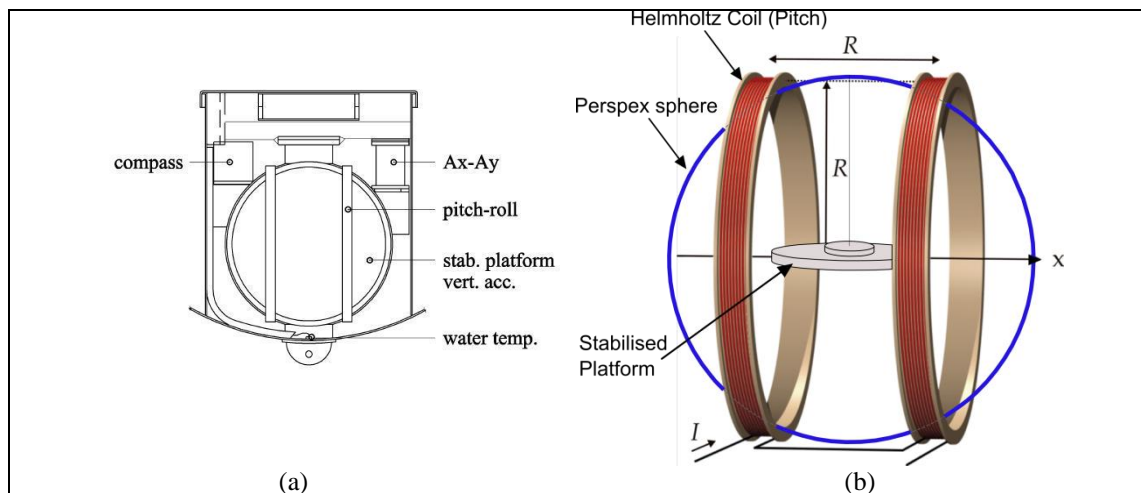


Figure 2.7. (a) Canister layout and (b) Helmholtz Coil pitch/roll sensor.

### 2.2.3. Buoy Calibration

Datawell recommend several ways to calibrate the buoys before deployment to ensure that none of the sensors have become damaged during manufacturer or shipment. At the Datawell facility in Haarlem, Netherlands, there is a certified calibration rig to test all buoys before sale or deployment. This rig is shown in Figure 2.8a. Operated by an electrical motor, it places the buoy at the end of the arm in a circular orbit with constant velocity, mimicking the circular orbit of ocean wave particles. The calibration rig can

simulate waves with a height of 1.8m and periods from three seconds to several minutes. Through this procedure, the validity of the vertical accelerations are verified.

The sensors onboard the directional buoy measure eight signals, three accelerations,  $A_x$ ,  $A_y$ ,  $A_v$ , three magnetic field strengths,  $H_x$ ,  $H_y$ ,  $H_z$ , pitch and roll. The positive direction of these measurements can be seen in Figure 2.8b. It is general practice to point the serial number label on the buoy hull towards North. This will yield a positive magnetic field strength,  $H_x$ , with a zero orientation and a positive acceleration in the  $X$  direction. Double integration of the accelerometers would then provide north, west and vertical motion. For the horizontal axis of the buoy, the magnetic field strength,  $H_x$  is fixed to the buoy hull orientation; however, the vertical axis of the accelerometer,  $A_v$ , is always near vertical and fixed to the stabilised platform.

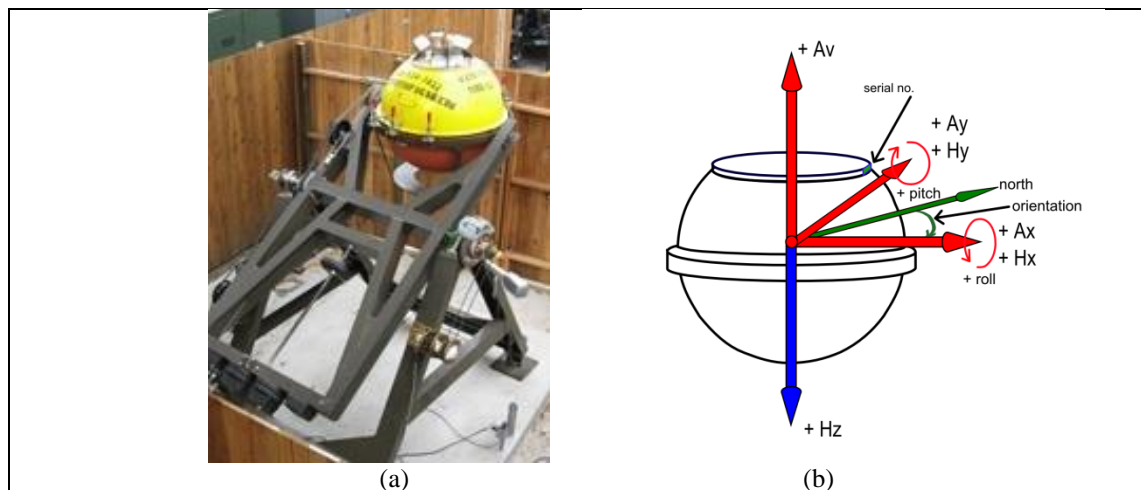


Figure 2.8. (a) Datawell calibration rig and (b) axes orientation.

To test the natural period of the buoy in the field before deployment, the Waverider is suspended with ropes from a sufficient height. The natural period of a pendulum,  $T$  is defined by Equation 2.2 where  $L_P$  is the length of the system and  $g$  is the acceleration due to gravity:

$$T = 2\pi \sqrt{\frac{L_P}{g}} \tag{2.2}$$

To determine the natural period of the system, we need to determine the effective length of the stabilised system. The length from the suspension point to the accelerometer is denoted  $L_R$  and as the buoy swings, the suspension line makes an angle of  $h/L_R$  [radians],

where  $h$  is the horizontal excursion of the buoy from rest. The horizontal excursion of the buoy is a sinusoidal function of time and its square averages to  $\frac{1}{2}h^2$ . Therefore, the shift in vertical acceleration becomes (Equation 2.3):

$$A = \frac{gh^2}{2L_R L_P} \quad (2.3)$$

By rearranging Equation 2.3, the length of the system can be obtained. Over the course of 25 oscillations of the pendulum, the shift of the zero position of the accelerometer reading is 20cm, which leads to an average shift in acceleration,  $A = 0.008 \text{ m/s}^2$ . The length of rope,  $L_R$ , is 1.7m and the horizontal distance of the swing of the buoy,  $h$ , is 1m. This gives a length of the pendulum system,  $L_P$ , of 360.66m. Putting this into the natural period formulae gives a period of 38.09s, which is very close to the reported natural period of 40s for the Waverider buoys (Gerritzen 1993).

#### 2.2.4. *Datawell Buoy Mooring*

Datawell buoys use a combination of rubber cord, rope, floats and sinkers, anchored with chain, for mooring in water depths from 8m to water depths greater than 200m. Natural rather than synthetic rubber is used due to its superior tear strength, low tear propagation and creep properties. Natural rubber has a characteristic stress-strain curve of a linear Gaussian regime with a sharp upturn. The elasticity of the rubber also allows the buoy to follow the orbital path of the water particles more closely, while the rope, which has a specific weight close to water, minimises the downward submerging force on the buoy due to the mooring configuration. Parallel to the rubber section of the mooring, a safety rope is fitted, which has a length of 4 times the length of rubber cord. The diameter of the rubber cord is conditional on the diameter of the Waverider buoy, 27mm for the 0.7m diameter buoy, or 35mm for the 0.9m diameter buoy.

The connections used in the mooring configuration along with the ballast chain and terminals are all either stainless steel, similar to the buoy hull, or aluminium. This ensures the longevity of both the buoy and the mooring in such a corrosive environment. Floats are also incorporated into the mooring line. A 0.2m diameter float with 3kg of buoyancy is used to keep the polypropylene rope free from the seabed, while the larger 0.3m diameter float has a buoyancy of 10kg, which is needed to lift the heavier rubber cord and terminals. The mooring configuration for both the directional and non-directional buoy is

shown in Figure 2.9 as recommended by Datawell for the water depth at the Galway Bay test site, which is approximately 25m. This gives a total mooring length for the non-directional buoy of 50m and 60m for the directional Waverider buoy.

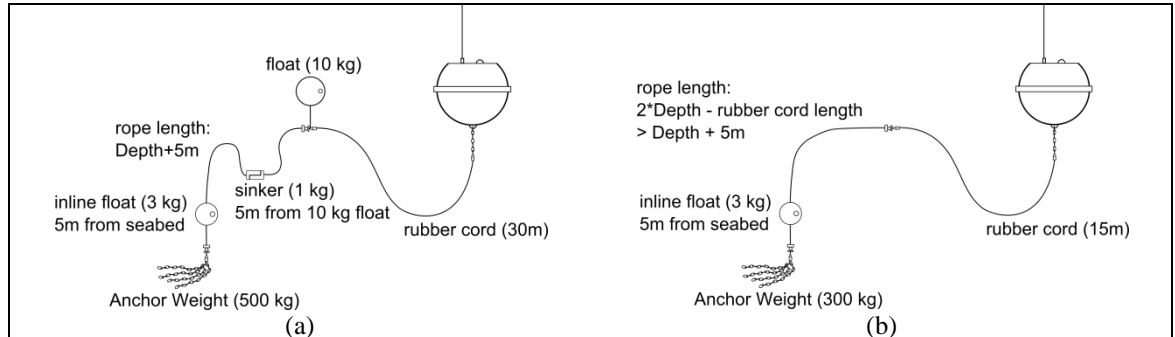


Figure 2.9. Mooring configuration for (a) directional and (b) non-directional buoy.

In the case of the directional buoy, the mooring consists of 30m of 35mm diameter rubber cord with 30m of polypropylene rope. The safety rope parallel to the rubber cord will then have a length of 120m, that is four times the length of the rubber cord. The non-directional buoy will have a 27mm diameter rubber cord, which is 15m in length attached to a rope of length 35m. The extra length in the directional buoy mooring is to allow the buoy to follow the direction of wave travel as closely as possible (Joosten 2006). Figure 2.10 shows the mooring configuration of the non-directional buoy for the deeper, more exposed location off the western seaboard. The water depth at the Loop Head site is approximately 50m, therefore the combined length of the mooring is 100m, 85m of which is polypropylene rope.

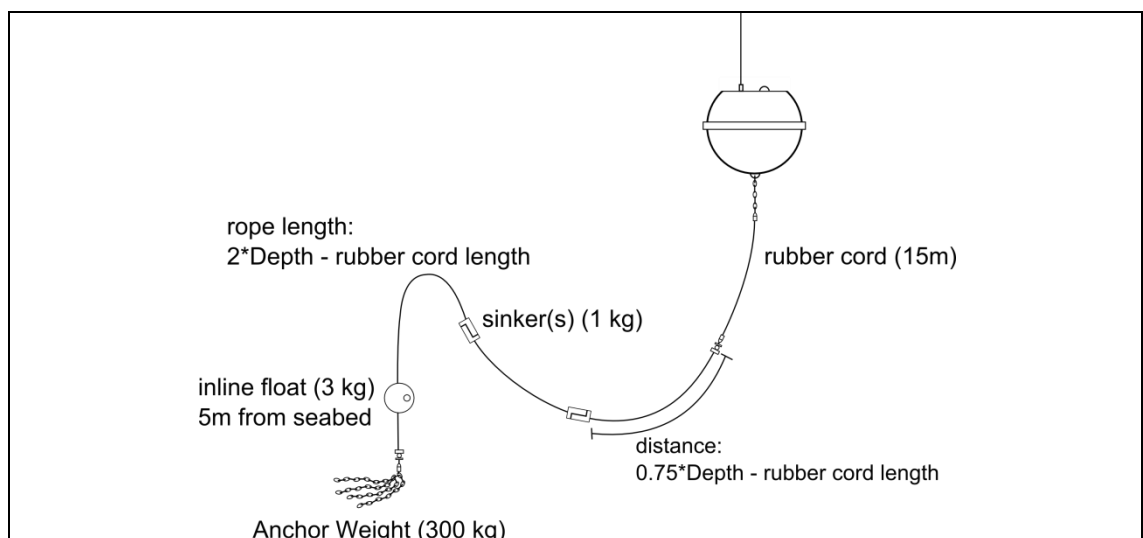


Figure 2.10. Datawell mooring configuration for non-directional buoy in 50m water depth.



At the base of both Datawell buoys, 5kg of ballast chain with a thickness of 20mm is attached to aid stability and prevent excessive pitch and roll motions that could damage the internal stabilised platform. A swivel at the end of this chain prevents the buoy from spinning due to the mooring. Attached to this ballast chain are sacrificial aluminium anodes to prevent corrosion risk to the buoy hull. In the water, a galvanic current path is formed between the anodes and the hull through the chain and back to the seawater. The sacrificial anodes have an expected lifetime of 3 years.

### **2.3. Buoy Data Transmission & Preparation**

All the Datawell buoys used in this project, the directional and non-directional buoys deployed in Galway Bay and the non-directional buoy deployed off Loop Head, transmit the data by high frequency radio. The transmitter is a two-stage crystal controlled transmitter suitable for the 27-40 MHz band with a range of 50km over water. A receiving antenna is positioned on the roof of the Marine Institute headquarters in Rinville, on the edge of Galway Bay and a receiving station was installed just onshore from the Loop Head buoy deployment. Initially, the Galway Bay non-directional buoy was deployed at the test site in November 2005. From that time until February 2008, the Datawell Digital Waverider Receiver (DIWAR) system was utilised to receive and organise the data transmitted by the buoy. The DIWAR receiver is a DOS based system and for use with the non-directional buoy only. With the addition of the directional buoy, a new receiving system, the rfBuoy module, was installed. The antenna length for the non-directional buoy is 1645mm and the resulting frequency at which the Waverider buoy transmits is a function of the length of the antenna, as shown in Figure 2.11.

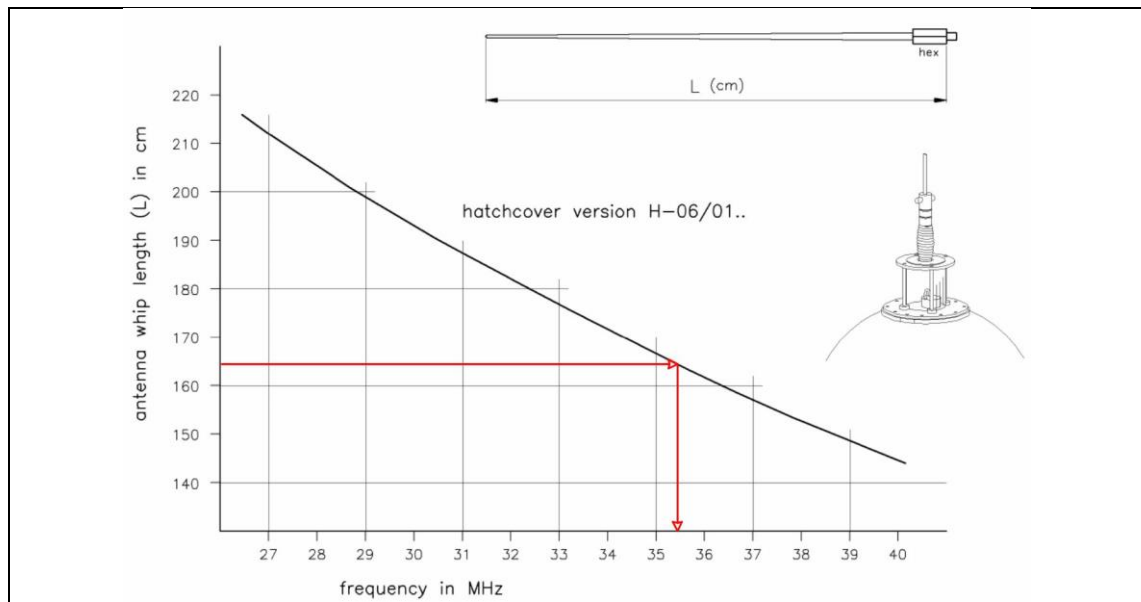


**Figure 2.11. Antenna whip length as a function of transmission frequency for Datawell non-directional buoy.**

### 2.3.1. Data Preparation & Processing

Due to two different receiving systems for the buoys, DIWAR and rfBuoy, two data preparation methods have been used during the course of this project. The majority of the data for the Galway Bay test site has been received from the non-directional buoy through the DIWAR system, which is the same system used for the Loop Head deployment. All that is measured onboard the non-directional buoy is the near vertical accelerations from the stabilised platform. The accelerometer onboard the buoy is, in electronic terms, effectively a potentiometer. The voltage signal from this accelerometer is sampled at a rate of 10.24 Hz. Although no analogue filtering takes place, digital filtering is applied, where a low pass filter has a cut-off frequency of 2 Hz and a high pass filter has a cut-off frequency of 0.0416 Hz. The sampling rate is then converted to 2.56 Hz. Double integration of the vertical acceleration is performed, resulting in the wave height signal that is continuously transmitted at a frequency of 2.56 Hz.

#### 2.3.1.1. Loop Head Data Set

A Datawell non-directional buoy was deployed at the Loop Head location as shown in Figure 1.14 in November 2003. This buoy was the property of ESBI who provided the data to HMRC for analysis in the Sea & Swell Spectra Project (Holmes and Barrett 2007). This data buoy was moored in approximately 50m of water depth and stayed on station until the end of June 2004, when the signal was lost and an unsuccessful attempt to recover and subsequently locate the buoy failed. A new replacement buoy was obtained

by ESBI and deployed on the same site in early September 2004. This buoy remained on site until the beginning of July 2005. This buoy recorded as a minimum the near vertical surface displacement of the sea surface for 20 minutes every hour for the duration of deployment stated above.

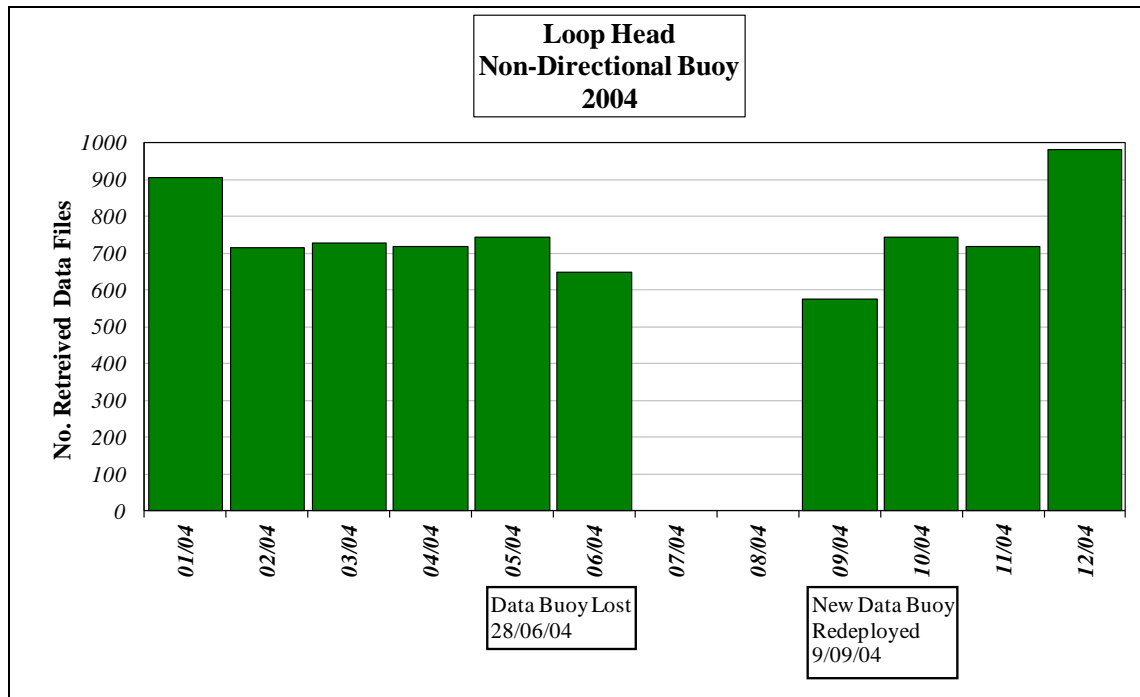


Figure 2.12. Number of elevation files recovered from the non-directional buoy deployed at the Loop Head site in 2004.

Figure 2.12 shows the number of wave elevation data files that was recovered from the Waverider buoy deployed at the Loop Head location. A typical 31 day month would return 744 hourly data files. Note that for some of the months, especially in winter, this number of files is greatly exceeded. This is due to a threshold setting for wave height in the DIWAR system. Once this predefined significant wave height setting has been exceeded in measurement, the DIWAR receiver will process and store every twenty minute record continuously; however there will be some overhead between each twenty minute record due to the processing of the spectra and relevant files. As the wave height recedes below the user set threshold value, the DIWAR system reverts to the hourly processing and storage method.

### 2.3.1.2. Galway Bay Data Set

The Marine Institute deployed a Datawell non-directional surface following buoy at the southwest corner of the wave energy test site at the coordinates given in Figure 1.8. The buoy was deployed in November 2005, and the data was supplied intermittently to the HMRC by email until an FTP server was installed at the receiving station at the Marine Institute Headquarters in Rinville, on the shores of Galway Bay. This then allowed HMRC staff near real time access to the buoy transmitted data. The same 20 minute recording scheme was used in Galway Bay as had been used at the Loop Head site.

Various problems with the DIWAR receiver and receiving antenna at the Marine Institute have meant that a less than favourable amount of data was captured in the first year of deployment. To compound this problem the batteries exhausted on the 12th July 2006. The buoy was recovered from Galway Bay for repair and redeployed on the 19th October 2006. Since that time there has been close to maximum hourly data retrieval. The non-directional buoy was decommissioned at the Galway Bay test site in November 2008. The number of retrieved wave elevation data files from the Galway Bay test site can be seen in Figure 2.13.

With the installation of the directional buoy at the Galway Bay test site, a more sophisticated receiver and software package was required. The Datawell RX-D receiver along with the rfBuoy module of the Datawell visualisation software Waves21 is used to receive the HF radio signal from the directional buoy and process the data stream. The RX-D receiver is a fixed frequency receiver due to its tuneable crystal. For more than one directional buoy, the RX-C receiver is recommended, which can host up to eight directional buoys. The rfBuoy module has also changed the way the data from both buoys is treated. The raw displacement files from both buoys are now of 30 minute duration and stored every half hour, although the respective sampling frequency of the buoys are retained. Again, there is a slight overhead between the files, therefore the data is not exactly continuous. The receivers for both Datawell buoys can be seen in Figure 2.14, with the DIWAR on the left and the RX-C on the right.

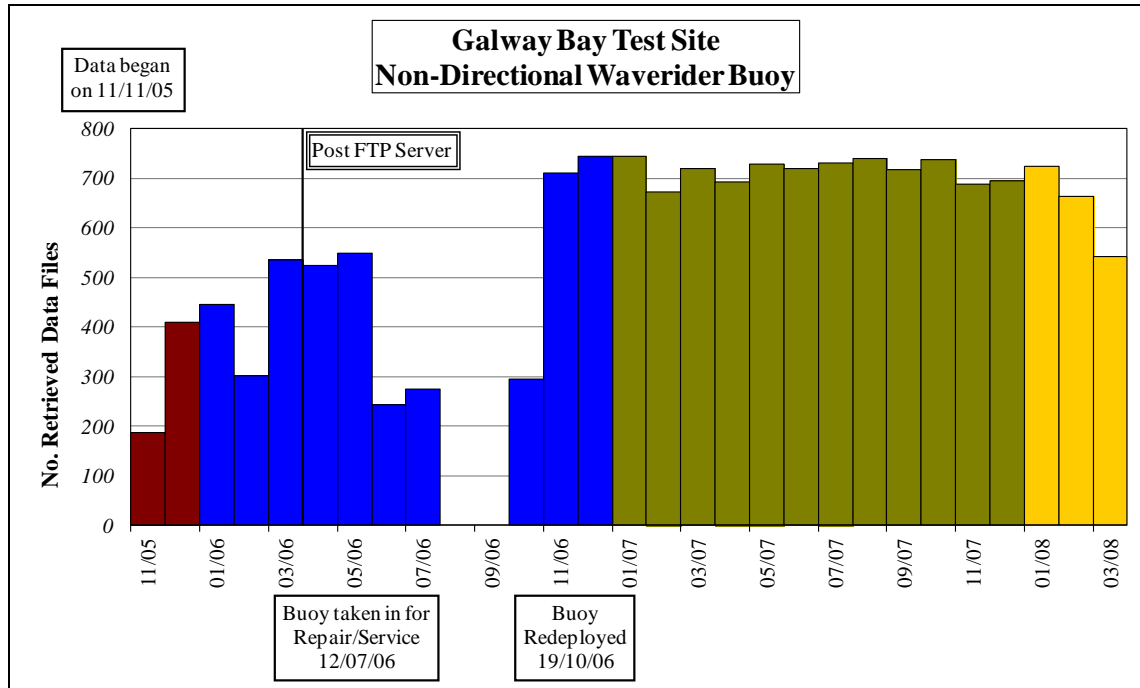


Figure 2.13. Number of retrieved data files from the non-directional buoy data from Galway Bay.

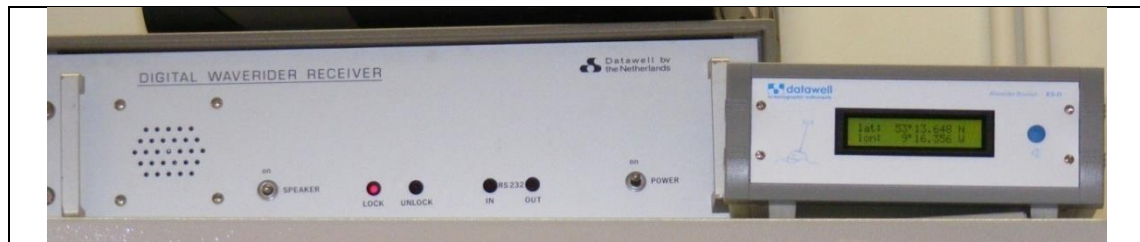


Figure 2.14. Datowell waverider buoy receivers, DIWAR (left) and RX-D (right).

The directional buoy is equipped with an onboard logger that stores the raw displacements, spectral data and an event log, and it can store up to 3 years worth of data before it selectively over-writes data files, starting with files corresponding to the lowest significant wave height first. The data that is transmitted by the directional buoy is in the form of hexadecimal 64-bit vectors at a frequency of 1.28 Hz. This in turn is translated by the rfBuoy module into its constituent files. The transmitted displacements are the twice integrated accelerations of north, west and vertical. To limit the effect of noise on the accelerometer sensors, the analogue sensor outputs are first filtered by a low-pass filter with a cut-off frequency of 1.5 Hz. The sensor outputs are then transformed to a sampling rate of 3.84 Hz. At low frequencies, the accelerations become small and are lost in the sensor noise. A high pass filter with a cut-off frequency of 0.033 Hz is applied to the samples. The sensor outputs are finally re-sampled to a frequency of 1.28 Hz for transmission.

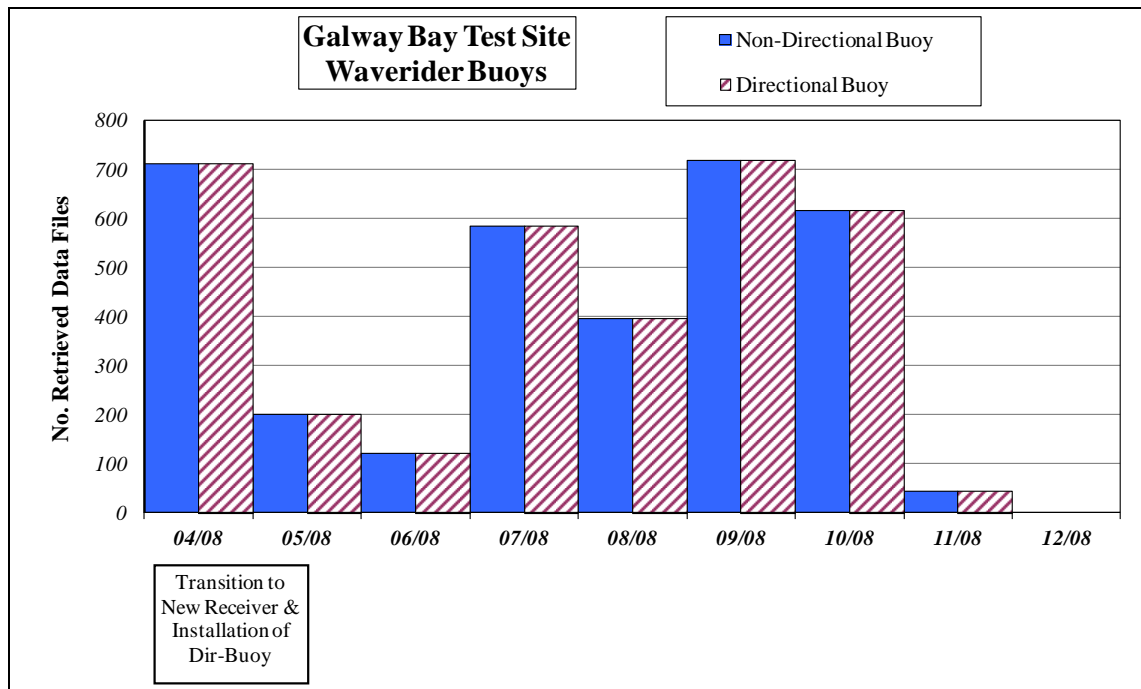


Figure 2.15. Number of retrieved data files from both the directional and non-directional buoys in Galway Bay for 2008.

The number of retrieved wave elevation data files after the addition of the directional buoy and the RX-D receiver is shown in Figure 2.15. For the first few months of the concurrent deployment, the receiving station at the Marine Institute Headquarters was switched between the non-directional and directional buoy, therefore neither buoy could achieve full data recovery for those months. Then in August 2008, a problem was discovered with the hybrid hatch cover of the directional buoy, which was subsequently returned to Datawell. Due to this, the directional buoy was recovered from the test site, thus prolonging the installation of the non-directional Waverider at the Galway Bay site. In November 2008, a new hybrid hatch cover was supplied by Datawell and the non-directional buoy was finally replaced by the directional Waverider buoy.

### 2.3.2. Buoy Output Files

For all the Loop Head data set and the first block of the Galway Bay non-directional data set (November 2005-March 2008), the DIWAR receiving system starts recording and processing the data for twenty minutes at the start of each hour. This results in a wave elevation file of 3,072 data points that are saved to a file denoted by the extension 'RW'. These elevations are processed while being received. Spectra are produced from six sequential blocks of 512 surface elevation data points, and the summary statistics are obtained from the average of these spectra. This averaged spectrum is saved with the file

extension of 'SP' and has a frequency range of 0.04 Hz to 0.6 Hz (1.66-25s) with a frequency step of 0.01 Hz. Then, a time series analysis is performed on the surface elevation file, the results of which are saved to a file with the extension 'WV'. All these files have as a filename the time stamp of the last data point in the wave elevation sequence.

The second block of the Galway Bay data set (post April 2008) starts with the addition of the RX-D receiver, the DIWAR receiver is still used for the non-directional buoy, but all the files are now processed by the rfBuoy module. This has increased the duration of surface elevation files to 30 minutes, however, the same sampling frequency is retained with respect to the directional and non-directional buoys. The non-directional files also retain their naming file extensions. This results in a raw elevation file of over 4,608 data points. A feature of the Datawell rfBuoy system is that, in the case of the non-directional buoy, only the short-term sequential spectra are now filed and stored, whereas for the directional data the 30 minute representative spectrum is also filed and saved.

Due to the increased complexity of the measurement systems onboard the directional Waverider buoy, and the increased number of variables being measured, the output files are consequently more complex than in the case of the non-directional buoy. However, there are some similarities. In the case of the surface elevation, both buoys are treated in the same manner. As explained in the previous section, the data stream transmitted by the directional buoy is in hexadecimal format and converted by the rfBuoy module. The makeup of the 30 minute record is shown schematically in Figure 2.16. The vector block is transmitted at a frequency of 1.28 Hz. It consists of 64 bits of data that comprise the three accelerometer displacements, cyclical data that contain spectral information, and parity bits which are used to encode the transmitted data packet and to check the data integrity. Eighteen vectors form a block of data, which includes the spectral and directional information spectrum for four frequencies. In turn, sixteen sequential blocks are assembled to create a full wave spectrum file of 64 frequencies. This spectrum file is the analysis of 200 seconds of displacement data. Finally, eight spectral files are transmitted over the course of 30 minutes. These eight spectra are averaged to produce an equivalent half hour spectrum, although its calculation has only been computed over 1,600 seconds, instead of the correct 1,800 seconds. It is also important to note that the spectral files transmitted with the displacement data, are the spectra of the elevation data

that was transmitted in the previous 30 minutes. The time stamp of these segmented spectral files will be between 3 and 30 minutes approximately after the displacement data from which they have be processed.

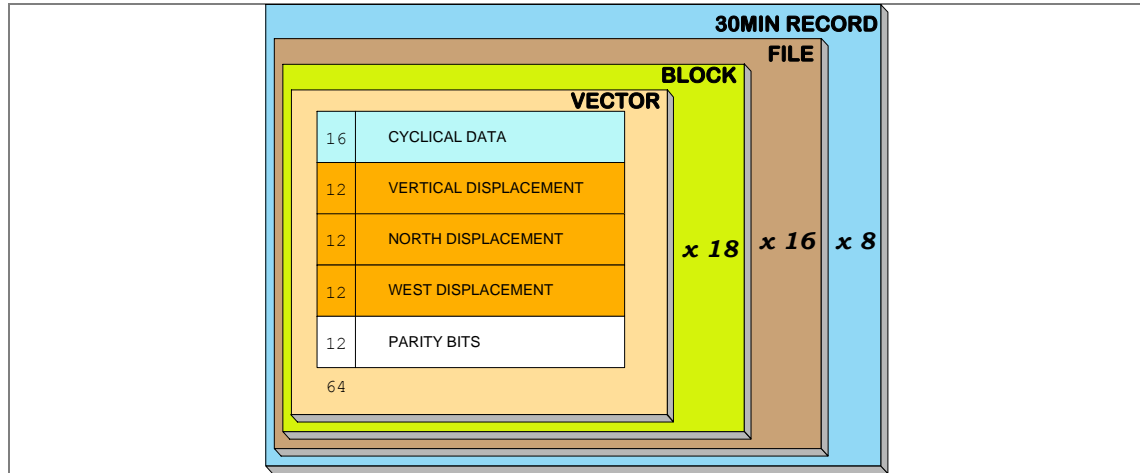


Figure 2.16. Data composition of a directional buoy 30 minute record.

The directional displacements are stored in a file with the ‘RAW’ extension and the file is named with a timestamp corresponding to the first data point received. This file comprises four columns of data, the first being the status indicator of the quality of the data. The subsequent three columns are in the following order; Heave, North and West. The spectra are saved in files denoted with the extension ‘SPT’, however the eight component spectra are distinguishable by the inclusion of a dollar sign (\$) in the file name. The start of each of these files includes various summary and indicative data. Along with a normalised spectrum, they also contain information on the direction, spread, skewness and kurtosis at each frequency. It should be noted, however, that the directional spectrum is not transmitted by the buoy, but only computed through the proprietary Datawell Waves21 software or through another software package by the user. As with the non-directional data, time domain analysis is performed on the heave displacement, the results of which are stored in a file with the following extension, ‘WVS’. Further information on the contents of these files is available in Appendix A.

The analysis system on board the Datawell buoys computes the Fourier coefficients of each file shown in Figure 2.16. The non-directional buoy elevation file has twice as many data points as the directional file due to the sampling frequency, therefore only the even displacements are analysed onboard the non-directional buoy so the same spectral routines can be used on either buoy. These 200s elevation files are also cosine tapered



over the first and last 32 data points, which is 25% of the data. At this point for the non-directional spectral data, the individual 200 s spectral files are transmitted. One further processing step is carried out for the directional buoy data. After the spectral routine has been carried out, the spectral file has a frequency range of 0.05 Hz to 0.64 Hz and the spectral ordinates are smoothed with the routine given in Equation 2.4. For frequencies higher than 0.1 Hz, every other smoothed spectral component is retained in the spectral file (Datawell 2007).

$$S(f_i) = \frac{1}{4}S(f_{i-1}) + \frac{1}{2}S(f_i) + \frac{1}{4}S(f_{i+1}) \quad (2.4)$$

where  $S(f_i)$  is the spectral ordinate at a frequency  $f_i$ .

### 2.3.3. Data Quality Check & Analysis Procedures

Several methods have been developed and ratified as suggested quality control techniques by various bodies around the world. The World Meteorological Organisation (WMO) have ratified several documents on wave observation, processing and transmission through the Data Buoy Cooperation Panel (DBCP) and the Joint WMO-IOC Technical Commission for Oceanography and Marine Meteorology (JCOMM) which is a joint partnership between the WMO and the Intergovernmental Oceanographic Commission (IOC) of UNESCO. These documents are primarily based on the dissemination of oceanographic data over the Global Telecommunication System (GTS).

The International Association for Hydraulic Research (IAHR) have established a set of standards for the measurement and interpretation of wave data (IAHR 1986). The International Towing Tank Conference (ITTC) Symbols and Terminology Group have also compiled a list of standard definitions, most of which have been adopted from the IAHR list (ITTC 1999). These set of standards are specifically aimed at the interpretation and definition of measurements taken at sea and in hydraulic laboratories to assist in the transparency of scientific research in this field. It is based on these guidelines that the following data quality procedures were implemented on the data retrieved from the wave buoys.

The Datawell rfBuoy processing system at the Marine Institute, which incorporates both the directional and non-directional buoy, has its own data quality check and correction procedures in place. Primarily, the data quality checks and analysis applied here were implemented on the vertical displacements provided by the non-directional buoy received

through the DIWAR system before the new system was implemented. A work flow diagram of the Quality Check and Analysis Procedure is shown in Figure 2.17.

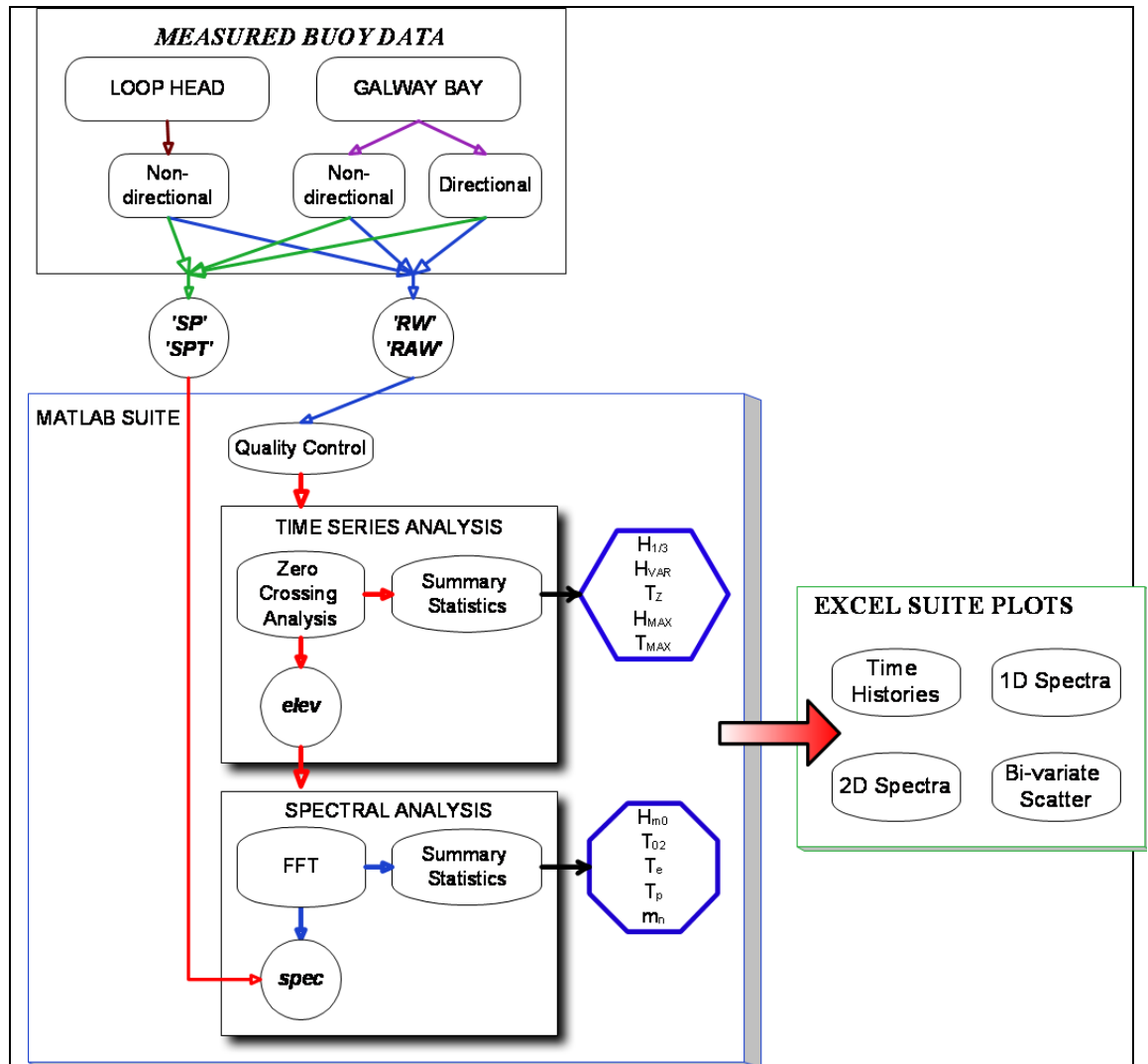


Figure 2.17. Work flow diagram depicting the quality check and analysis procedures for the data sets.

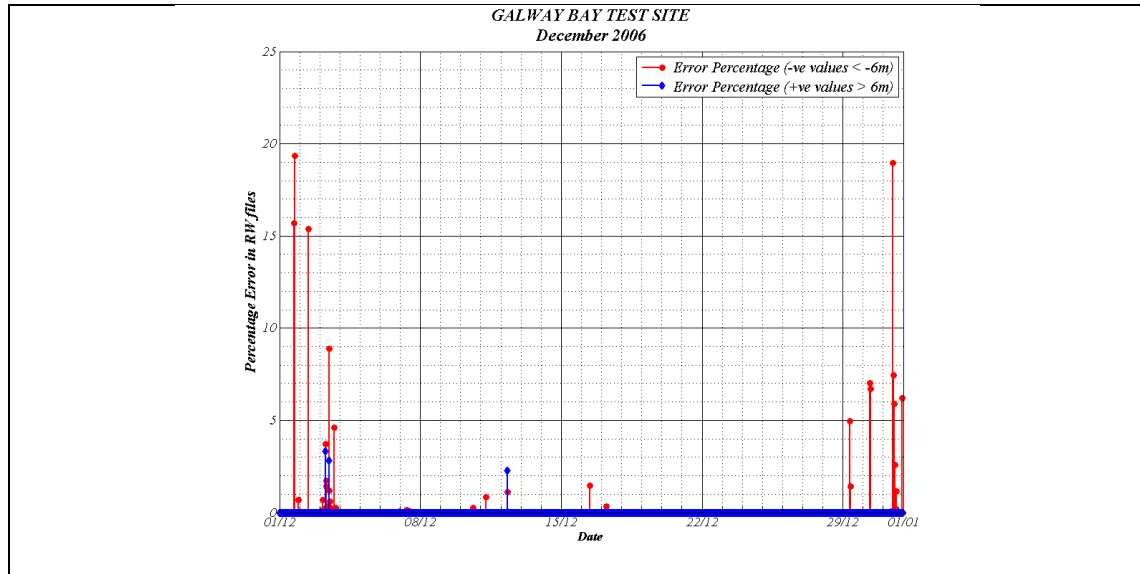


Figure 2.18. Percentage error of spurious data within RW files.

Spurious data was a common occurrence in the ‘RW’ files along with the inclusion of a default value of  $-2048\text{ cm}$ . This occurred when the signal transmitted by the buoy was lost due direct line of sight because of large wave crests or radio interference at the receiving antenna. It is primarily the ‘RW’ files containing the surface elevation data that is processed by the QC procedure. As the water depth at the Galway Bay site is approximately 25m, as a first check for spurious data, a data point in the ‘RW’ elevation file outside a range of  $\pm 6\text{m}$  is flagged as an erroneous entry. This is based on the reasonable assumption that any sea generated in the Galway Bay area over a period of 20 minutes will have a significant wave height,  $H_s$  of less than 6m containing a maximum wave height,  $H_{max} = 12\text{ m}$ . Therefore, any raw elevation file with a value outside of this range is identified. The number of suspicious data points falling outside this range is counted and for each ‘RW’ file, the percentage of the total number of data points (3,072) is plotted for the complete data set of the month in question. From visual inspection of these plots, similar to that shown in Figure 2.18, those files with an error count greater than 10% are discarded from the usable data set and those with percentage error values greater than 5% are visually inspected for accuracy.

Once those RW files with the largest proportion of erroneous elements and associated SP and WV, are quarantined the quality check procedure attempts to correct the spurious elevations contained within the remaining files that have been flagged in the previous step. Each RW file is examined and averages and standard deviations are recorded for portions of the file that contain legitimate data. This initial mean value of the RW file is

used to replace the spurious data points. The mean trend is removed from all *RW* files so that they now oscillate about a zero level and again the mean and standard deviation is calculated for the now corrected files. A further elevation check is imposed on the *RW* files. If a point is outside the range of five times the standard deviation, it is replaced with the mean of the data file, which now has a value of zero. These modified surface elevation files are then used to determine various statistics in later stages of the analysis scheme.

Once the surface elevation file has been qualified for further analysis, various methods are applied to garner as much useful information as possible. Using both time and frequency domain tools, various comparisons can be made to qualify the measured data further. The subsequent output data of the MatLab<sup>®</sup> routines are processed further in Excel to form informative plots. The analysis processes and summary statistical outputs that are shown in Figure 2.17 are explained in more detail in the following sections.

### 3. ANALYSIS TECHNIQUES

The previous section has shown that there are many diverse ways of obtaining a record of the elevation of the sea surface. Presented here are many ways in which to derive the necessary information through different analysis techniques, both in the time and frequency domains. Although it is easy to apply these methods and get some sort of measurement, it is important that the derived results are both qualified and quantified, to ensure false values or interpretations are not obtained.

The length of the time series to be recorded by the instruments is generally recommended to be between 20-30 minutes if possible. This length of record gives a satisfactory standard error of 0.1 for a record of 30 minutes, which would have approximately 180-200 zero crossing waves (Draper 1963). Records of this length can be regarded as a Gaussian stochastic process, which allow for certain assumptions and definitions. That is, the mean of the process does not vary (stationary), the temporal mean at any point and the spatial mean at any instant are equal (ergodic), and the surface elevation follows a Gaussian distribution.

The larger ODAS buoys generally do not provide the surface elevation or spectral information. The record of the acceleration or velocity of the near vertical motion of the platform is spectrally analysed to obtain the summary statistics. For battery conservation strategies, these statistics are then either averaged over the hour or simply computed once within the hour and broadcast to the receiving station. The smaller surface following buoys are capable of storing the surface profile onboard, while also transmitting both the surface elevation and the spectral ordinates ashore for further analysis and quality checking, due to a shorter deployment life than the larger ODAS buoys.

Once the wave elevation record has been obtained from the surface following buoys, there are a number of analysis methods available, depending on the information that is required by the user. The primary analysis techniques available are based in the time and frequency domains. Time domain analysis would be considered the more stable approach as there have been clearly defined methods to ascertain the summary statistics from the time series of the ocean surface although based on widely accepted assumptions of the wave field being measured. Frequency domain analysis is less well defined as there are many variants of the techniques used to transform a wave signal from the time domain to the

frequency domain. Frequency domain analysis is traditionally based on the Fourier transform of the signal, which provides as output the amplitudes and phase of the component sinusoidal waves. Through various smoothing techniques, the distribution of the energy of the wave signal in the frequency domain can be presented.

### 3.1. Time Domain

It is logical to begin the analysis by initial assessment of the surface elevation that has been measured by the chosen instrument. With due consideration for the length of the signal, taking into account any variation in the signals mean due to tide level changes, the mean should be approximately equal to the zero point that the signal oscillates around. The next step is to define the zero crossing type. This can be done by identifying where the surface elevation crosses the mean of the signal, either as it rises from a trough to a crest, known as zero up-crossing, or as the water level falls from the crest to the trough, known as zero down-crossing. It is important to note that these two analysis procedures will produce different values for individual wave height and period because the midpoint of zero up crossing defined wave is the starting point of a zero down crossing wave. A small fraction of the information in the signal is lost due to these definitions.

The time domain analysis techniques define clearly the individual wave periods and heights. The variance of the signal can be used to define the energy within the record and can be equated to the zeroth moment of the frequency domain spectrum. The average of the largest 1/3 of the wave heights is defined as the significant wave height, and the average of all the periods of the waves in the record is defined as the zero-crossing period. Both these time domain quantities can be related to frequency domain equivalents under the assumption that the record is a Gaussian stochastic process. Another quantity of importance is that of the maximum wave within the time series. This is the largest elevation difference from trough to successive wave crest using the zero up-crossing analysis definition.

Certain checks can be performed on the time history to qualify it as a stochastic process. These include the assumption that the significant wave height will be approximately half the maximum wave height, the distribution of the water surface elevation about its mean level will be Gaussian or Normal and that the distribution of all wave heights within the

time series will follow a Rayleigh distribution, a continuous probability distribution for positive-valued random variables.

### 3.1.1. Statistical Distributions

The primary assumption that is applied to the surface elevation record of ocean waves is that the seaway is the superposition of a large number of harmonic sinusoidal waves of constant amplitude and random phase (Tucker and Pitt 2001). These waves have been generated independently and travel independently of each other according to the linear approximation of waves as described by Airy in 1845, which is used for the approximation of waves in deep water. There are other higher order theories available such as Stokes (1847) and Dean (1965) but these describe steep waves in shallow water, whose profile does not conform to a sinusoidal shape.

#### 3.1.1.1. Gaussian Distribution

One of the main assumptions applied to a measured seaway is that it is a Gaussian process. This is a special case of a stochastic process, and in a statistical sense, the elevation of the seaway being measured has a certain distribution, which can be described by the Normal or Gaussian distribution. When a signal is Gaussian distributed, it is equally proportioned about its mean. Both the Galway Bay and Loop Head data has been conditioned to have a zero mean, which simplifies the resulting equation of the distribution (Equation 3.1).

$$P(\eta) = \frac{1}{\sigma\sqrt{2\pi}} \exp\left(-\frac{(\eta - \bar{\eta})^2}{2\sigma^2}\right) \quad (3.1)$$

where  $\eta$  is the surface elevation time series,  $\sigma$  standard deviation of the time series and  $\bar{\eta}$  is the mean of the time series

#### 3.1.1.2. Rayleigh Distribution

The second statistical assumption applied to seaway statistics is that the distribution of the individual wave heights generally follow a Rayleigh distribution for a narrow spectrum. Longuet-Higgins (1952) showed that if the sea surface is assumed to be the sum of many sinusoidal waves in random phase, and if the frequency spectrum is sufficiently narrow, then the wave heights are distributed according to a Rayleigh distribution. This type of distribution has only one parameter, the variance of the signal,  $\sigma^2$ , which is also equal to the zero order moment of the variance density spectrum,  $m_0$  (Holthuijsen 2007). The Rayleigh distribution is given in Equation 3.2, where  $x$  is the

quantity to be distributed, in this case the ratio of the zero crossing wave height to the mean of the wave height.

$$P(x) = \frac{\pi}{2} x \exp\left(-\frac{\pi}{4} x^2\right) \tag{3.2}$$

where  $x = \frac{H}{\bar{H}}$ ,  $H$  is the individual wave height and  $\bar{H}$  is the mean wave height.

Other variations of this equation are given by Tucker and Pitt (2001) and by Holthuijsen (2007), which is shown in Equation 3.3.

$$P(H) = \left(\frac{H}{4\sigma^2}\right) \exp\left(-\frac{H^2}{8\sigma^2}\right) \tag{3.3}$$

where  $\sigma^2$  is the variance of the surface elevation record.

**3.1.2. Time Domain Summary Statistics**

One of the primary definitions in time domain analysis is that of the zero-crossing wave. This is the point in the irregular wave record where the surface elevation crosses the mean level in either an upward or a downward direction. The zero down-crossing point is the method suggested for use by the International Association for Hydraulic Research (IAHR 1986) however, both up and down crossing methods are widely found in literature. By locating these points in the record, the number of waves can be determined, as it is one less than the number of zero crossing points. This is shown in the illustration in Figure 3.1.

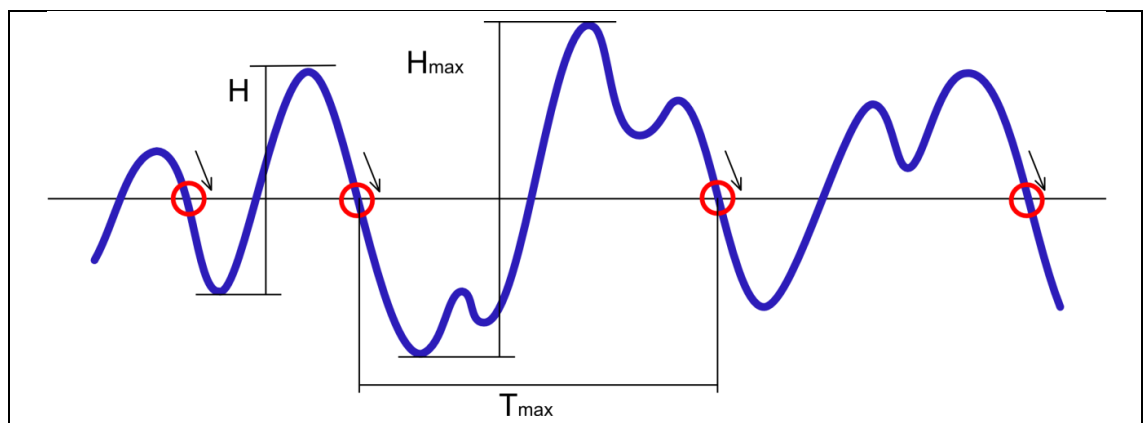


**Figure 3.1. IAHR recommended zero down crossing method.**

The most characteristic measure of a seaway is the significant wave height, which can be measured in a number of ways. Primarily, it is taken as the mean of the largest  $\frac{1}{3}$  waves and denoted by  $H_{1/3}$ . The characteristic period of note is the mean period of all the waves identified by the zero crossing method and denoted accordingly as the zero crossing



period,  $T_z$ . Another pair of important parameters that can be derived from the time domain analysis of the wave record is the maximum wave height,  $H_{max}$  and its corresponding period,  $T_{max}$ . It should be noted however, that  $T_{max}$  may not be the longest wave period in the record and its correct notation should be as follows,  $T_{H_{max}}$ .

The variance of the irregular signal can also be used to derive the significant wave height. The variance of a signal, is the average of the squares of the distance that each value is from the mean and is the standard deviation ( $\sigma$ ) of the signal raised to the power of two, which can be calculated as follows (Equation 3.4):

$$\sigma^2 = \frac{1}{N-1} \sum_{i=1}^N (\eta_i - \bar{\eta})^2 \quad (3.4)$$

From this, the significant wave height can be derived from Equation 3.5.

$$H_s \approx H_{var} = 4\sqrt{\sigma^2} \quad (3.5)$$

## 3.2. Frequency Domain

A complimentary set of analysis techniques can be carried out in the frequency domain. It is a long held view that the irregular nature of a wind driven gravity wave surface elevation can be approximated by the linear super-position of an infinite number of sinusoidal waves of distributed amplitude and random phase. By sampling the wave time series at a high frequency, it is possible to approximate this continuous spectrum into discrete frequencies called harmonics. Using Fourier series expansion through an efficient computer algorithm such as the Fast Fourier Transform (FFT) an estimate of the phase and amplitude of the discrete harmonics can be derived. In general, the phase of these elemental sinusoidal waves are random, therefore of no great importance and discarded. One reason for this is that the derived Fourier series is periodic with a period equal to the length of the signal, which of course ocean waves are not. The amplitude or variance spectrum is used to derive numerous important quantities.

### 3.2.1. Frequency Domain Analysis

A schematic of the frequency analysis process is presented in Figure 3.2. The sampled surface elevation file, along with its sampling frequency is passed to a computational routine which conducts a Fast Fourier Transform. For most FFT algorithms, the signal

has to have a required number of data points which is a factor of 2 raised to a real power, i.e.  $N = 2^n$ . The primary output of the FFT algorithm is a complex number series with values for each data point of the irregular signal and the frequency range is the number of data points divided by the sampling frequency. The angle of the complex number is equal to the phase of the sinusoidal components that make up the signal and the absolute of the complex number is a magnitude of the sinusoidal components. The magnitude of the complex number is modified, depending on the FFT algorithm used, to first obtain an amplitude spectrum. This amplitude spectrum presents the amplitude of the sinusoidal components that make up the irregular signal at their respective frequency harmonics. This amplitude spectrum can then be modified further to obtain a variance density spectrum which represents the energy contained in the irregular signal.

The steps involved in analysing a polychromatic signal to obtain the variance density spectrum is explained in more detail in the following sections.

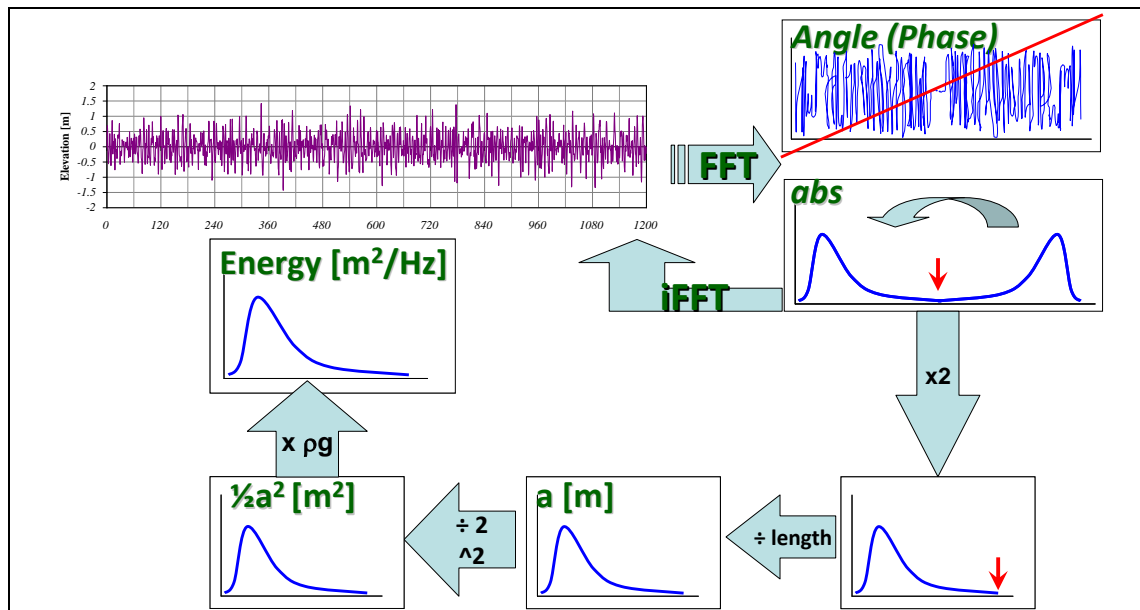


Figure 3.2. The FFT process from irregular signal to variance density spectrum.

The frequency domain approach to wave data analysis involves decomposing the surface elevation signals into constituent parts. The output of spectral analysis is primarily the spectrum, which in general holds information regarding the energy distribution within the harmonic frequencies of an irregular signal, but this can also be developed to indicate the directional distribution of the energy. The most common tool for the treatment of an irregular signal is the Fast Fourier Transform (FFT), however there are other methods

available. The Hilbert-Huang spectral method is proposed for the analysis of non-linear and non-stationary wave data (Hwang *et al.* 2003), while the Wavelet transform can provide a time varying spectral estimate of the surface record (Massel 2001).

3.2.1.1. *Fast Fourier Transform*

The Fast Fourier Transform (FFT) is an efficient numerical algorithm for carrying out the Discrete Fourier Transform (DFT), and was first reported by Cooley and Tukey in 1965. The FFTs strength lies in the fact that the calculation of the coefficients of the DFT are carried out iteratively. There is a requirement that a time series represents a continuous waveform when the sampling interval is at least a few times the highest frequency present in the waveform. When the samples of this waveform are evenly spaced, as is usually the case, the DFT is closely related to the Fourier transform. Preceding the FFT method, to determine the Fourier coefficients of a waveform with  $N = 2^n$  samples,  $N^2$  operations were required. This reduces to  $2N \log_2 N$  arithmetic operations by using the Fast Fourier Transform. This procedure greatly reduces calculations and computational time (Cochran *et al.* 1967).

The functionality of the FFT can be thought of as the factorisation of a transform matrix. Take for example a waveform with  $N = 4$  data points, the DFT can be written as two transforms by separating the even and odd numbers as follows (Equation 3.6):

$$\begin{aligned} \{4 \ 3 \ 2 \ 1\} &= \{4 \ 0 \ 2 \ 0\} + \{0 \ 3 \ 0 \ 1\} \\ \{4 \ 2\} &\supset \{A \ B\} \\ \{4 \ 0 \ 2 \ 0\} &\supset \frac{1}{2}\{A \ B \ A \ B\} \end{aligned} \tag{3.6}$$

likewise for the odd elements of the sequence:

$$\{0 \ 3 \ 0 \ 1\} \supset \frac{1}{2}\{P \ Q \ P \ Q\}$$

A shift is applied to this transform, and multiplication by  $W$  means rotation by one  $N^{th}$  of a revolution in the complex plane, so the effect of a shift is to apply a phase delay that increases progressively along the sequence of elements (Equation 3.7).

$$\{0 \ 3 \ 0 \ 1\} \supset \frac{1}{2}\{P \ WQ \ W^2P \ W^3Q\}, \tag{3.7}$$

where  $W = e^{-\frac{i2\pi}{N}}$  and  $W^N = 1$ .

Addition of the right hand side of Equation 3.6 and Equation 3.7 gives the DFT of the longer sequence. Figure 3.3 represents this diagrammatically. The reduction of the

computational effort required to perform the DFT is shown as the breakdown of the DFT into two element DFTs of  $M = 2$  which require  $M^2$  computations each, therefore the transition leads to a computational saving of 50%, i.e.  $2M^2$  as opposed to  $N^2$ . The solid lines depict addition and the broken lines describe multiplication by the denoted factors. This method can further be reduced to single multiplications and additions. This method relies on the fact that the sequence being analysed is comprised of  $2^n$  elements. Transforms do exist where this criteria are not met, though they are not quite as fast (Bracewell 1999).

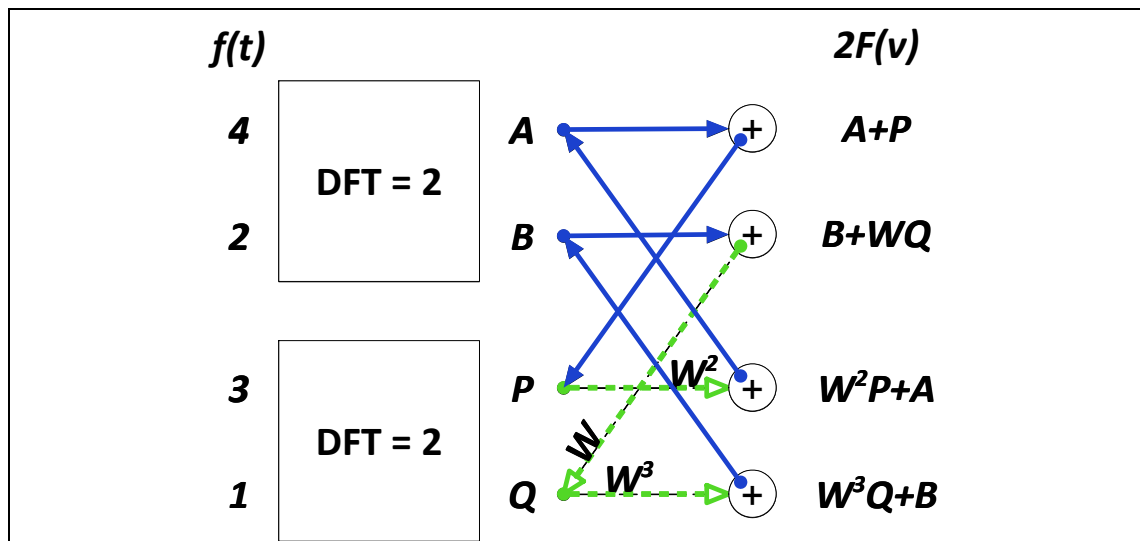


Figure 3.3. Depiction of DFT Reduction

### 3.2.1. Frequency Domain Summary Statistics

Regardless of the presented spectral shapes or equations adopted, various statistical properties can be calculated by deriving the spectral moments in the frequency domain. The area of the variance density spectrum is proportional to the significant wave height, and under certain assumptions, this is also approximately equal to the significant wave height derived from zero-crossing methods in the time domain. The peak period,  $T_p$ , is simply the inverse of the frequency at which the spectral ordinate is a maximum. There are various other temporal periods that can be derived, however, the two most commonly used and understood are the energy period,  $T_e$ , and the average period,  $T_{02}$ . Like the significant wave height, the average period is also equivalent to the zero-crossing period calculated from the time domain analysis,  $T_z$ , again under certain assumptions. The equations to calculate these parameters, along with their units are given in Table 3.1.

<i>Description</i>	<i>Definitions</i>	<i>Units</i>
Spectral moment, $m_n = \int_{f_{min}}^{f_{max}} S(f) f^n df$	$m_n$ spectral moment	$[m^2 Hz^n]$
	$S(f)$ spectral ordinate	$[m^2 / Hz]$
	$f$ frequency	$[Hz]$
	$df$ frequency step	$[Hz]$
Significant Wave Height, $H_{m0} = 4\sqrt{m_0}$	$H_{m0}$ Sig. Wave Height	$[m]$
	$m_0$ zero moment	$[m^2]$
Average Period, $T_{02} = \sqrt{\frac{m_0}{m_2}}$	$T_{02}$ average period	$[s]$
	$m_2$ second moment	$[m^2 Hz^2]$
Energy Period, $T_e = \frac{m_{-1}}{m_0}$	$T_e$ energy period	$[s]$
	$m_{-1}$ first negative moment	$[m^2 / Hz]$
Peak Period, $T_p = \frac{1}{f_p}$	$T_p$ peak period	$[s]$
	$f_p$ peak frequency	$[Hz]$

**Table 3.1. Parameters derived from a Variance Density Spectrum.**

Longuet-Higgins (1980) determined that, firstly from the Wiener-Khinchin theorem which states that the variance density spectrum is the Fourier transform of the corresponding autocorrelation function, that the variance of the surface elevation time series,  $\bar{\eta}^2$ , is equal to the zeroth moment of the frequency spectrum,  $m_0$ . It then follows that,  $H_{var}$  is equal to the significant wave height determined from the variance density spectrum,  $H_{m0}$ . Using data from a storm event in the Gulf of Mexico from Forristall (1978), Longuet-Higgins (1980) found that the data fitted equally well to the relationship presented in Equation 3.8.

$$H_{var} = 0.925H_{m0} \tag{3.8}$$

By applying a relationship to the width of the spectrum, Longuet-Higgins (1980) found for a Pierson-Moskowitz spectrum that the relationship in Equation 3.9 held true.

$$H_{var} = 0.931H_{m0} \tag{3.9}$$

The fact that this observation of the equality of significant wave heights is not unity is described in the conclusion of the paper that it is caused by the presence of free background noise in the spectrum, outside the dominant peak. Holthuijsen (2007) presents two more examples, where a similar relationship (95%) is presented from work by Goda (1988) and from a set of data measured in the southern North Sea in 2003 by the Royal Netherlands Meteorological Institute. It was found that for this data, a subsequent least squares fit determined a percentage of 92.7%.

When using the variance spectrum, the area enclosed is equal to the variance of the time series when plotted in the frequency domain. Other moments of the spectrum are combined to determine periods such as the energy period,  $T_e$  and an equivalent period to the zero-crossing period,  $T_{02}$ . The resolution of the harmonics are dictated by the sampling frequency and time series duration. This is an important aspect especially if knowledge of longer periods is a concern. To get an accurate estimate of the spectrum various methods are available to reduce the errors that are fundamentally part of the Fourier analysis of sea surface time series such as leakage and aliasing. These include tapering or segmentation of the original signal. These methods and others will be discussed in a later section.

### 3.2.1.1. Wave Power

Wave power is the energy that exists in a unit width of wave crest as it approaches the shore. It can be determined from the summary statistics of significant wave height and the energy period in the following way.

The potential energy of a column of water of unit area whose surface is raised by  $a$ , the amplitude of a sinusoidal wave, then:

$$E_p = \frac{1}{2} \rho g a^2 \quad (3.10)$$

The potential energy is equal to the kinetic energy, therefore the power being transported per unit crest length is:

$$\mathbb{P}_w = \frac{1}{2} \rho g a^2 c_g \quad (3.11)$$

where  $c_g$  is the group velocity, for deep water,  $c_g = g/4\pi f$ , where  $f$  is the wave frequency of the sinusoidal wave. Therefore:

$$\mathbb{P}_w = \frac{\rho g a^2}{8\pi f} \quad (3.12)$$

The spectral definition of  $S(f)$  is:

$$S(f)\Delta f = \sum_1^n \frac{1}{2} a_n^2 \quad (3.13)$$

and the total energy of the spectrum is:

$$E = \rho g \int S(f) \delta f = \rho g m_0 \quad (3.14)$$

Therefore, the power transported per meter of wave crest is:

$$\begin{aligned} \mathbb{P}_w &= \rho g \int c_g(f) S(f) \delta f \\ \therefore \mathbb{P}_w &= \frac{\rho g^2}{4\pi} \int f^{-1} S(f) \delta f \\ \therefore \mathbb{P}_w &= \frac{\rho g^2}{4\pi} m_{-1} \end{aligned} \quad (3.15)$$

Now to introduce the significant wave height,  $m_0 = \frac{H_{m0}^2}{16}$ ,

$$\begin{aligned} \mathbb{P}_w &= \frac{\rho g^2}{4\pi} \left( \frac{m_{-1}}{m_0} \right) m_0 \\ \mathbb{P}_w &= \frac{\rho g^2}{64\pi} H_{m0}^2 T_e \end{aligned} \quad (3.16)$$

The units of the equation for wave power presented above is Watts per meter wave crest.

### 3.2.3. Fourier Analysis of Ocean Waves

By assuming that the sampled waveform is the superposition of an infinite number of sinusoidal waves of amplitude,  $a_n$  and random phase  $\theta_n$ , an equation for the surface elevation can be expressed as a discrete Fourier series for the case of a time series of  $N$  data points sampled at regular intervals  $\Delta t = \frac{T}{N}$ , as follows (Equation 3.17):

$$\eta(t) = \frac{1}{2} c_0 + \sum_{n=1}^N a_n \cos\left(\frac{2\pi n t}{T} + \theta_n\right) \quad (3.17)$$

where  $c_0$  is the offset or mean of the waveform and for simplicity is taken as zero, and  $\omega_n = \frac{2\pi n}{T}$ ,  $\frac{n}{T} = f_n$ ,  $\therefore \omega_n = 2\pi f_n$ .

Using trigonometric identities of addition formulae, Equation 3.17 can be converted to Equation 3.18 as follows:

$$\begin{aligned} \eta(t) &= \sum_{n=1}^N a_n [\cos(\omega_n t) \cos(\theta_n) - \sin(\omega_n t) \sin(\theta_n)] \\ \eta(t) &= \sum_{n=1}^N A_n \cos(\omega_n t) + B_n \sin(\omega_n t) \end{aligned} \quad (3.18)$$

where  $A_n = a_n \cos \theta_n$  and  $B_n = -a_n \sin \theta_n$ .

$A_n$  and  $B_n$  are the Fourier coefficients used to determine the amplitude and phase of the sinusoidal components that make up the irregular surface elevation, as shown by Equation 3.19:

$$a_n = \sqrt{A_n^2 + B_n^2} \text{ and } \tan \theta_n = -B_n/A_n \quad (3.1)$$

Due to the relationships derived from Equation 3.12 for the amplitude  $a_n$ , and phase angle  $\theta_n$ , of the individual wave components, the equation for the surface elevation as offered in Equation 3.18 can also be represented in complex form through the following relationships in Equation 3.20:

$$\begin{aligned} X_n &= \frac{1}{2}(A_n - iB_n) \\ X_{-n} &= \frac{1}{2}(A_n + iB_n) = X_n^* \end{aligned} \quad (3.20)$$

where  $X_n$  is a complex amplitude and  $X_{-n}$  is its complex conjugate.

By using Euler's formula in Equation 3.21, then addition in Equation 3.22 gives Equation 3.23, which is equivalent to Equation 3.18:

$$e^{i\omega_n t} = \cos \omega_n t + i \sin \omega_n t \quad (3.21)$$

$$X_n e^{i\omega_n t} + X_{-n} e^{i(-\omega_n)t} = A_n \cos \omega_n t + B_n \sin \omega_n t \quad (3.22)$$

$$\therefore \eta(t) = \sum_{n=-N/2}^{N/2} X_n e^{i\omega_n t} \quad (3.23)$$

The Fast Fourier Transform provides  $N$  coefficients that can be used to describe the amplitude and phase of the sinusoidal components that due to the theory of superposition can be added together to form an exact replica of the measured signal. However, this replicated signal will have a periodic cycle of  $T$ . To derive a spectrum, in most cases the phase angle information is discarded. Rayleigh (1880) showed that the phase of the sinusoidal components that make up an irregular time series are random, and therefore carry no information about the original signal (Tucker 1957). Retaining this information is only useful when the phase difference between simultaneously measured records is required, such as the motion of a floating body and the incident wave elevation exciting it.

Although  $N$  Fourier coefficients are derived from the Fourier Transform method, the second half of these are repeated, therefore the Fourier coefficients with frequencies from



$\Delta f = \frac{1}{T}$  to the Nyquist frequency,  $f_{Nq} = \frac{f_s}{2}$ , are retained and all other coefficients can be discarded as there are only  $\frac{N}{2}$  legitimate frequencies for a record containing  $N$  real values. This is due to the Nyquist Shannon sampling theorem, which states that if a function does not have any frequencies higher than  $B$  Hz, it can be completely determined by giving its ordinates at a sampling frequency of  $2B$  Hz. Following this, the Nyquist criterion is a set of inequalities stating that to reconstruct a function from its samples, the sampling frequency,  $f_s$  has to be greater than twice the highest frequency in the signal,  $B$  which is the Nyquist Rate and that the highest frequency in the signal,  $B$  is less than half the sampling frequency  $\frac{f_s}{2}$ , the Nyquist frequency,  $f_{Nq}$ .

The Fourier Transform of the record contains  $N$  complex values, although the Fourier Transform at the discrete frequencies  $\Delta f$  and  $f_{Nq}$  the imaginary part equals zero. The second half of the complex numbers are in fact complex conjugates of the first half of frequencies. To determine the amplitude information from the legitimate half of complex numbers, their modulus is calculated. These values are doubled to incorporate the second portion of the spectrum contained in the frequencies beyond the Nyquist frequency. In some cases the FFT algorithm does not scale the FFT as a function of the length of the record, for example the MatLab<sup>®</sup> FFT routine (MatLab Support 2008). To correct for this, the modulus of the complex numbers are divided by  $N$ , the number of Fourier Transform complex numbers, which is also the number of real values in the record being analysed. At this stage of the calculation process, the derivation of the amplitude spectrum is complete, although the amplitude spectrum is not additive due to the differing phase angles at each discrete frequency. More information is gained by deriving the variance density spectrum.

To determine the variance density spectrum, the amplitudes at the discrete frequencies are converted to energy parameters and the ordinates of the spectral densities are derived as follows (Equation 3.24):

$$S(f_i) = \frac{1}{2}a_i^2 [m^2] \tag{3.24}$$

The area bounded by these spectral ordinates in the frequency domain is equal to the energy contained in the seaway, which is also the variance of the irregular waveform with

a zero mean. Higher order spectral moments are calculated to describe various parameters of the waveform, which will be dealt with in a later section.

### 3.2.4. Leakage, Aliasing, Smoothing and Degrees of Freedom

Although the theory of the DFT is precise, the method is still only an approximation as it describes discrete frequencies of a continuous process. These discrete frequencies are harmonics and are integer multiples of the fundamental frequency,  $\Delta f$ . In fact, this fundamental frequency can have no relationship with the original frequency content of the sampled signal, as it is purely dictated by the duration of the waveform. This leads to some inherent errors associated with discrete Fourier analysis.

The first rule of spectral analysis is to sample at a frequency that is a few times higher than the expected highest frequency in the record. At this point, the highest frequency in the signal is unknown, therefore setting the sampling frequency high enough to ensure that the Nyquist frequency is captured will limit the effects of aliasing, explained further below. In time, this will become known by experience or multiple measurements of the same process. The frequency resolution is a consequence of the sampling frequency,  $f_s$  and the duration of the record,  $N$ . This can only be improved by taking a longer duration of the wave record. The actual duration is therefore always a compromise. On the one hand, it should be sufficiently short that the assumption of a stationary process is reasonable, on the other hand it should be sufficiently long that the frequency resolution is adequate. In addition, it should be long enough to obtain statistically reliable estimates. This decision also affects the effective degrees of freedom of the spectral estimates.

#### 3.2.4.1. Leakage

An irregular signal is the superposition of a number of sinusoidal waves, therefore taking one sine wave and examining the errors associated with its Fourier analysis is indicative of the errors associated with the spectral analysis of an irregular signal. Figure 3.4 shows a sample sinusoidal waveform and its corresponding amplitude spectrum. The sample wave form has an amplitude of 1 m and a frequency of 5 Hz. This sinusoidal signal was sampled for  $T = 2.56$  s at a frequency of  $f_s = 100$  Hz, giving  $N = 256$  samples. Due to the Nyquist criterion, the resulting spectrum therefore has 128 harmonics up to the folding frequency of  $f_{Nq} = 50$  Hz. By inspection, these details are evident in Figure 3.4.

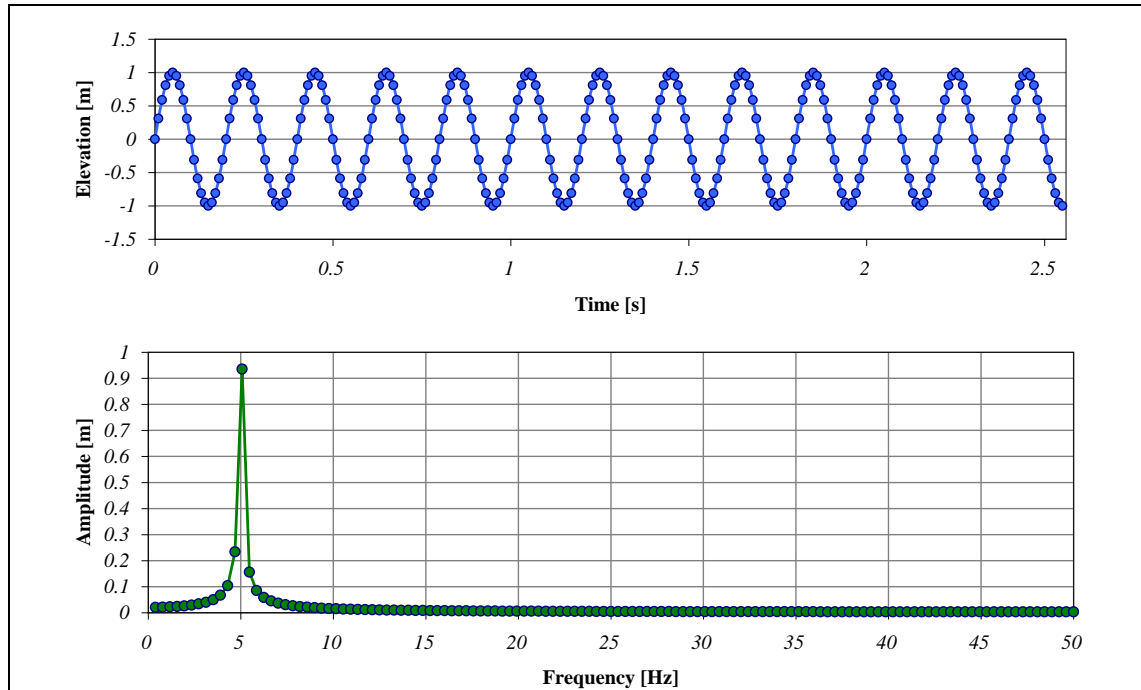


Figure 3.4. Sinusoidal waveform and corresponding frequency spectrum.

Further inspection of Figure 3.4 indicates the existence of a number of errors. Firstly, the peak of the spectrum is not of the correct magnitude as some of the energy is distributed among adjacent harmonics. This phenomenon, known as leakage, is due to the last data point of the sampled waveform being at a different phase to the starting data point. In the continuous case, leakage is not a source of error however, it is usual to sample for a known  $2^n$  number in the discrete case, and to accept the errors associated with leakage. Although not as noticeable, the peak of the spectrum does not occur at exactly 5 Hz. This is due to the fundamental frequency and subsequent harmonics of the spectrum. The frequency of the sinusoidal wave, 5 Hz is not an integer multiple of the frequency resolution,  $\Delta f = 1/2.56 = 0.390625 \text{ Hz}$ , therefore resulting in the peak frequency occurring at the 13<sup>th</sup> harmonic of the spectrum, i.e.  $f = 5.078 \text{ Hz}$ .

#### 3.2.4.2. Aliasing

Aliasing is another error associated with spectral analysis. This phenomenon occurs when the sampling frequency,  $f_s$  is not of the required duration and in the resultant spectrum, frequencies exist of sufficient energy above the Nyquist frequency. In this case, the energy at these higher frequencies,  $f > f_{Nq}$  are incorporated into the spectrum at  $f_s - f$ , leading to an erroneous estimate of the variance as it appears when the energy outside the Nyquist frequency is folded back into the spectrum. This can be minimised by ensuring that the Nyquist Shannon sampling theorem is applied. The elements that may exist above

the Nyquist frequency are in general of minimal energy and their addition to the spectrum causes little error. Aliasing error can be dealt with through experience and examination of the record.

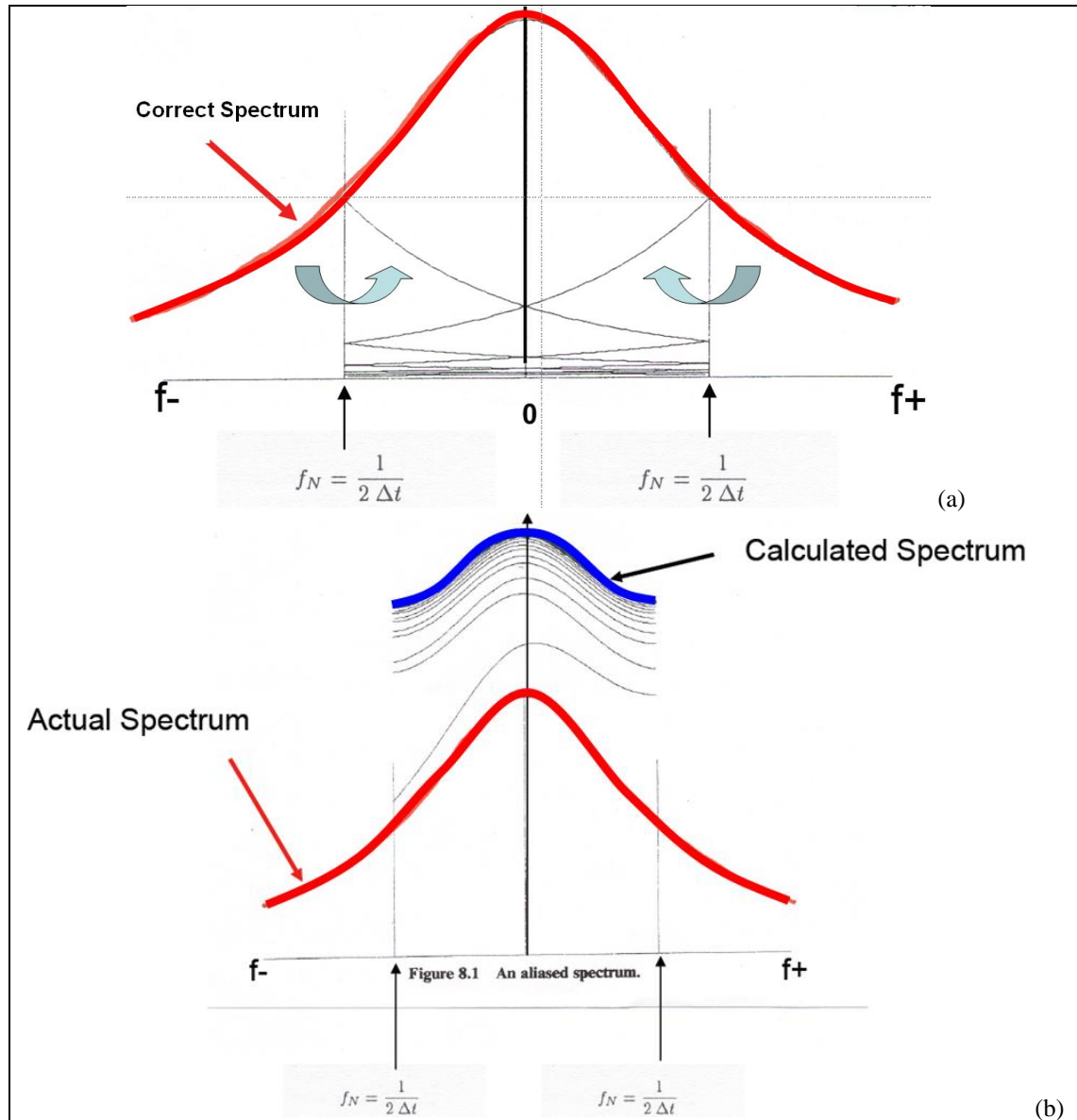


Figure 3.5. Aliasing effect on spectrum.

An exaggerated example of aliasing is shown in Figure 3.5 when the sampling frequency, and therefore the Nyquist frequency, is set too low. Part (a) of this figure shows that there is a considerable amount of energy outside the Nyquist frequency, which will be folded inward and added to the rest of the energy in the spectrum within the legitimate frequency range. This folding will continue until all the energy outside the Nyquist frequencies have been assigned to frequencies within the legitimate frequency range. The calculated spectrum in Figure 3.5b is a result of the summation of the extra energy that existed

outside the Nyquist frequency. It is clear that this is an overestimate of the variance of the correct spectrum.

When the sampling frequency is set high enough so that there is as little energy as possible at frequencies greater than the Nyquist frequency, the effect of erroneous addition of energy due to folding will be minimised.

#### 3.2.4.3. *Tapering*

The general approach to minimising errors associated with spectral analysis is to smooth either the input signal or the spectral ordinates by various means. Two methods are examined here, although others do exist. The first method applies a taper window to the time series of interest. This taper window applies a weighting function to the signal, which reduces some portion of the start and end of the waveform to zero. This method minimises leakage as the signal starts and finishes at the same phase, although there is a reduction of the variance that needs to be accounted for. The second method segments the waveform into short sections that are individually Fourier analysed and the resultant spectral ordinates are averaged to produce a smooth spectrum.

Tapering is not only used for spectral analysis but also for filter design. The MatLab<sup>®</sup> matrix analysis suite makes 16 windows available to the user, however only the most common will be introduced here. A taper window is a weighting function with values from zero to one, and when multiplied by the signal of interest produces a modified waveform for further analysis. Some taper windows do not reach a level of unity until the midpoint of the signal, while others allow the user to define the percentage of unmodified data. In essence, the tapering operation emphasises the middle portion of the time trace, and de-emphasises the start and finish. A selection of these taper forms can be seen in Figure 3.6 and their equations are presented in Table 3.2.

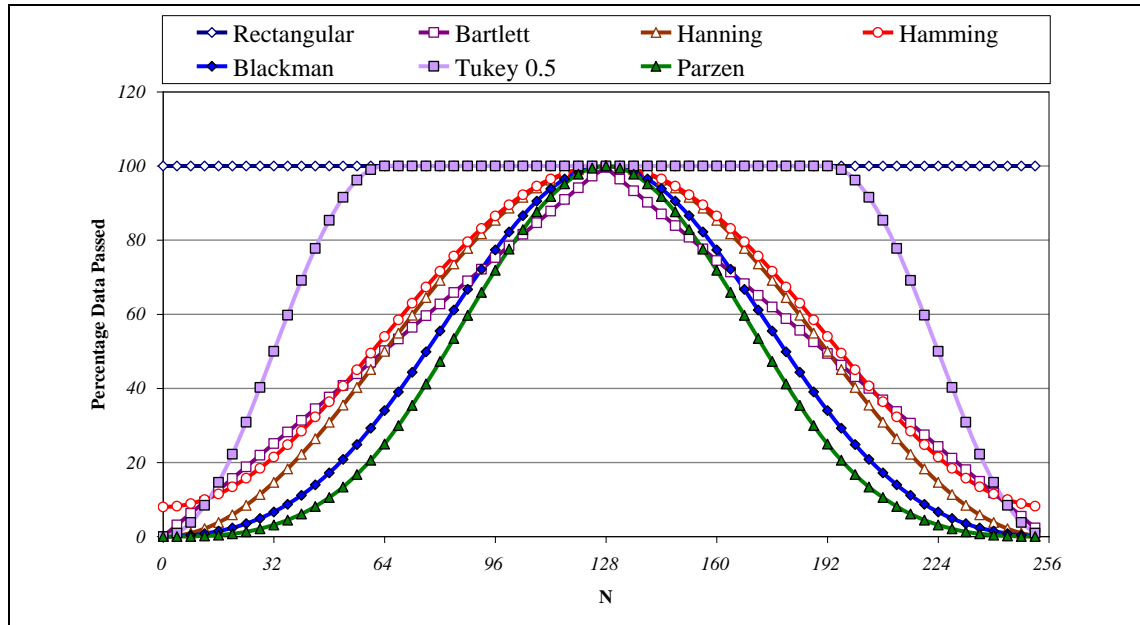


Figure 3.6. Graphical representation of various taper windows.

Taper	Base Form	Description/Equation
Rectangular	Linear	1 for $0 \leq n < N$ .
Bartlett	Triangular	$\frac{2n}{N-1}$ for $0 \leq n < \frac{N}{2}$ , $2 - (\frac{2n}{N-1})$ for $\frac{N}{2} \leq n < N$ .
Hanning	Cosine	$\frac{1}{2} - \frac{1}{2} \cos(\frac{2\pi n}{N})$ for $0 \leq n < N$ .
Hamming	Cosine	$0.54 - 0.46 \cos(\frac{2\pi n}{N})$ for $0 \leq n < N$ .
Blackman	Cosine	$0.42 - 0.5 \cos(\frac{2\pi n}{N}) + 0.08 \cos(\frac{4\pi n}{N})$ for $0 \leq n < N$ .
Tukey	Cosine	$\frac{1}{2} \left[ 1 + \cos\left(\frac{\pi}{\alpha/2} \left(\frac{n}{N} - \frac{\alpha}{2}\right)\right) \right]$ for $0 \leq n \leq \alpha \frac{N}{2}$ , 1 for $\alpha \frac{N}{2} < n < N - \alpha \frac{N}{2}$ , $\frac{1}{2} \left[ 1 + \cos\left(\frac{\pi}{\alpha/2} \left(\frac{N-n}{N} - \frac{\alpha}{2}\right)\right) \right]$ for $\alpha \frac{N}{2} < n < N$ .
Parzen	Gaussian	$2 \left( 1 - \frac{ n - \frac{N}{2} }{\frac{N}{2}} \right)^3$ for $0 \leq n \leq \frac{N}{4}$ , $1 - 6 \left( \frac{ n - \frac{N}{2} }{\frac{N}{2}} \right)^2 + 6 \left( \frac{ n - \frac{N}{2} }{\frac{N}{2}} \right)^3$ for $\frac{N}{4} > n < \frac{3N}{4}$ , $2 \left( 1 - \frac{n - \frac{N}{2}}{\frac{N}{2}} \right)^3$ for $\frac{3N}{4} \geq n < N$ .

Table 3.2. Various taper windows and their equations.

#### 3.2.4.4. Spectral Degrees of Freedom

The methods involved in producing a variance density spectrum all incorporate some degree of smoothing. If an FFT is applied to the entirety of a time series, then the resultant spectrum would be termed “raw”. This spectrum will have ordinates that have a large variance and follow a chi-squared distribution with  $\nu = 2$  degrees of freedom (Donelan and Pierson 1983).

The next step may be to introduce a moving average to the raw spectrum with a band width of  $2m + 1$  frequencies to reduce the variability of the spectral ordinates. In this case, the smoothed estimates have a chi-squared distribution with  $\nu = 2(2m + 1)$  degrees of freedom.

An alternative to applying an averaging technique to the raw spectrum of the entire time series of  $N$  elements, is to segment the wave form into smaller, non-overlapping segments,  $K$ , with an equal number of  $M$  elements, compute the respective spectra, and average the ordinates. The relationship between these segments and the overall waveform is then  $N = KM$ . The average of the spectral ordinate in this case is applied to the same frequency for  $M$  elements and has  $\nu = 2K$  degrees of freedom.

This method can be expanded by allowing the segments to overlap by a certain fraction  $S$ . In this case, the computed estimations of the spectral ordinates have  $\nu = \frac{2(N-S)}{M-S}$  degrees of freedom. This also holds true if a taper window is applied to each segment before the spectra are ensemble averaged.

The above summary by Rodriguez, Guedes Soares and Machado (1999) is for the degrees of freedom of the spectral estimators. However, Elgar (1987) reported that the effective number of degrees of freedom for the total spectrum is not simply the sum of the number of degrees of freedom for each spectral estimate but is a weighted sum that is spectral shape dependent. The effective number of degrees of freedom,  $\alpha$  can be calculated as follows (Equation 3.25):

$$\alpha = \frac{m_0^2}{\Delta f \int S^2(f) df} \quad (3.2)$$

For a raw spectrum where it has been shown that  $\nu = 2$ , the expected value of  $\alpha$ ,  $E[\alpha] = \frac{\alpha}{2}$ . For the case where there is some sort of ensemble averaging being conducted, the expected value of  $\alpha$  is shown in Equation 3.26:

$$E[\alpha] = \frac{1}{1 + \frac{2}{\nu}} \alpha \quad (3.26)$$

The mean value of estimates of the effective of degrees of freedom is biased low when the spectra is under smoothed while over smoothing spectra biases  $\alpha$  high (Elgar 1987).

#### 3.2.4.5. *Segmenting*

Finally, the method adopted in this thesis to produce a smooth spectral variance density is the Welch windowing method. Developed in 1967, the method involves sectioning the record, performing an FFT routine on these subsets of data and then averaging the resultant spectra to produce a smooth spectrum (Welch 1967). Although the method described by Welch applies a taper window to each of the wave record subseries, this extra layer of smoothing is not applied in the analysis carried out for the body of work presented here due to the loss of variance of the record.

The size of the elevation subseries is generally a smaller  $2^n$  number than the total record, and is dictated by the frequency resolution requirement. Care should be taken when adopting this approach, especially if, for example, the work involves the examination of long period RAOs. In this case, the frequency resolution can greatly affect the data spacing at long periods. These subseries can also overlap, but usually only up to 50%. In this instance, a smoother spectrum is derived, but with a loss of some variance.

Figure 3.7 shows the Welch segmenting method adopted for the analysis of the data files used in the analysis presented in this thesis. Figure 3.7a is the segmenting routine applied to the 20 minute surface elevation files, from both the Loop Head and Galway Bay non-directional buoys. The 3,072 data point time series is split into six equal divisions of elevation consisting of 512 data points. Each is analysed using a Fast Fourier Transform routine to produce individual spectra that are then ensemble averaged to calculate the overall variance density spectrum for the elevation record. No taper window is applied to the subseries elevation segments. This results in a frequency spectrum of 128 equally spaced frequency bins from 0.03 Hz to 0.665 Hz with a frequency resolution of 0.005 Hz



and  $\nu = 12$  degrees of freedom. Figure 3.7b shows the analysis method adopted for the directional buoy on site in Galway Bay, which has a sampling frequency of 1.28 Hz and a surface elevation record of 30 minutes. Figure 3.7c shows the application of the Welch segmenting method to the 30 minute surface elevation files from the non-directional buoy in Galway Bay after the installation of the new receiver and the conversion to 30 minute data files. The Galway Bay buoy directional elevation file has 2304 data points, which are divided into nine segments of 256 data points and spectrally analysed. Upper and lower frequency bands are imposed on the spectra and the frequency resolution is given by Equation 3.27 where  $f_s$ , is the sampling frequency and  $N$ , is the length of the data segment.

$$\Delta f = \frac{f_s}{N} \tag{3.3}$$

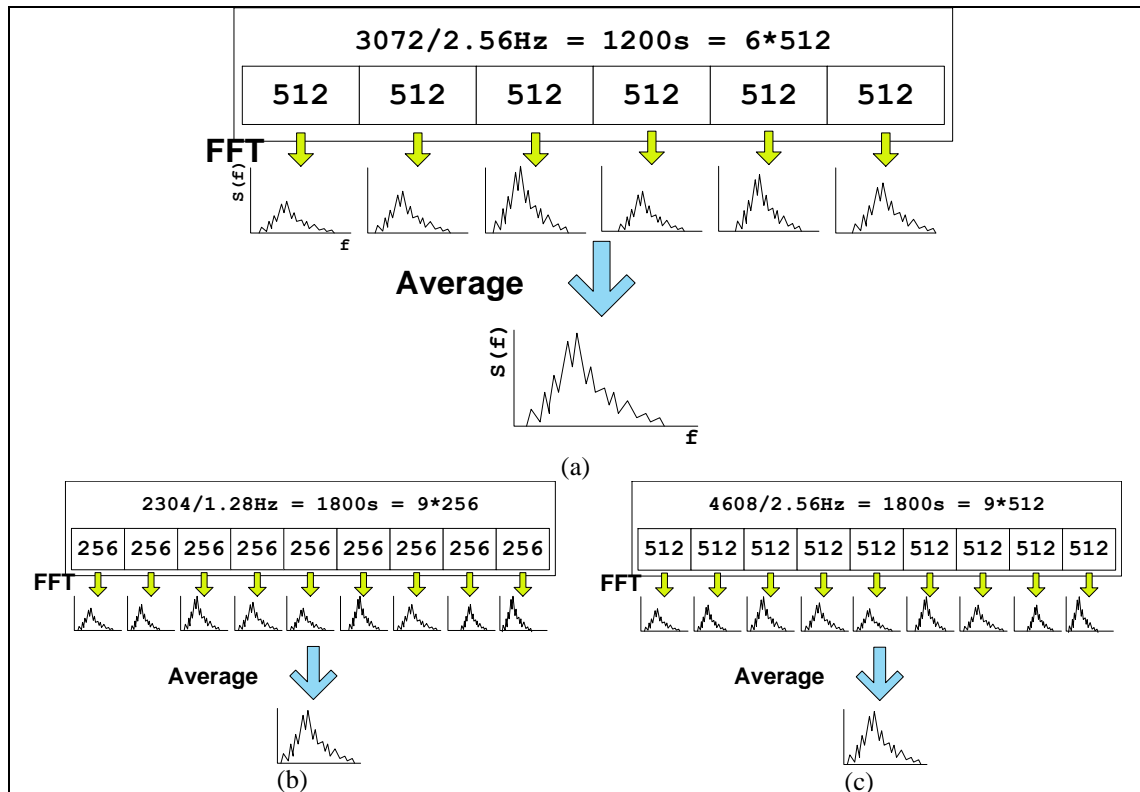


Figure 3.7. Spectral analysis methodology for (a) the 20 minute non-directional buoy at Loop Head and Galway Bay, (b) the 30 minute directional and (c) non-directional buoy at Galway Bay.

For both buoys in Galway Bay, the frequency resolution of the spectra is then  $\Delta f = 0.005 \text{ Hz}$ , with a frequency range of  $0.025 \text{ Hz} - 0.635 \text{ Hz}$ . Both of these spectra have  $\nu = 18$  degrees of freedom. The size of the segmenting was chosen so that all subsequent spectra would have a frequency resolution of  $0.005 \text{ Hz}$ . This allows for a direct comparison of the spectral ordinates, which will be discussed later.

### 3.2.5. Directional Analysis

Directional analysis is an extension of the frequency domain analysis described above. Various techniques are used to determine the directional characteristics of ocean waves. Due to the dispersive nature of sea waves, the sinusoidal components that make up an irregular sea state have frequencies that travel independently of each other. The first wave frequencies to reach the coast from distant storms have long wavelengths, a sea state referred to as swell. An increase in wind speed or change in direction of a local wind in conjunction with swell produces a confused sea state of multiple frequency concentrations and directions.

Directional buoys not only measure the vertical displacement of the surface but also some measure of the perpendicular axes on the horizontal plane. This can be slope, accelerations, velocities or headings and displacements. These simultaneous readings of the buoy displacement in three axes can be spectrally analysed through many different methods and this system is referred to as single point measurement. Where a non-directional spectrum is analogous to an area equivalent to the energy in the measured sea state, the directional spectrum can be thought of as a volume. This volume of energy is determined by applying a directional distribution to the non-directional spectrum. Integration across the frequency bins result in the Directional Spreading Function, while integrating across the directional bins gives the energy spectrum.

There are various methods available to determine this directional distribution. The more common techniques are based on the stochastic approach, as the Directional Spreading Function (DSF) can be treated in the same way as the Probability Distribution Function (PDF) in statistics, as like the PDF it is always positive and its integral equals unity. However, there are other methods available in the deterministic and time domain.

One of the main principles of the stochastic approach to directional spectral analysis is the assumption that the phase is random with a normal distribution. Therefore, the phase information intrinsic to the data can be disregarded, as it is not needed during the analysis scheme. The other important tool in the stochastic approach is the use of cross-spectra.

A cross-power spectrum defines the relationship between two variables. The variables relationship can be determined from the outcome, zero if the variables are completely

independent and the ordinary power spectrum if the variables are identical. For single point measuring systems such as data buoys, directional analysis programs will usually have three signals as input. These signals can be correlated to similar units through the use of transfer functions. That is if all three signals to be analysed are displacements then the transfer function is simply unity.

In the more general case of a system with  $N$  signals, the cross-power spectral approach forms an  $N \times N$  matrix from these signals. However, only  $N(N + 1)/2$  need to be computed, as the diagonal of the matrix is the power spectrum of the three signals and the triangular portion are the cross spectra and complex conjugates. Of the calculated cross spectra  $N(N - 1)/2$  are actual cross spectra in complex form with the real part called coincident spectral density functions or co-spectra, and the imaginary parts are labelled quadrature spectral density functions or quad-spectra. Once the cross-power spectra have been determined, various numerical methods are available to produce the directional spectrum. At present there is no definitive method for this as each approach has its own merits and caveats.

The directional spectrum is a development of the variance density spectrum by applying a spreading function to the frequency components. When modelling of the ocean surface is required, it is usual to apply a parametric spreading function such as Equation 3.28 to the linear theory, which adequately describes the directional spectrum as a product of two functions, adhering to the relationship in Equation 3.29.

$$S(f, \theta) = S(f)D(\theta) [m^2/Hz/\theta] \tag{3.28}$$

$$D(\theta) = F(s) \cos^{2s} \frac{1}{2}(\theta - \theta_M) \tag{3.29}$$

where  $\theta_M$  is the mean direction,  $s$  is the spreading function and  $F(s)$  ensures that  $D(\theta) = 1$ .

For integer values of  $s$ , Equation 3.29 applies as used by D.E. Cartwright (1963) (Tucker and Pitt 2001).

$$F(s) = F(s - 1) \frac{s}{s - 0.5} \tag{3.30}$$

$$F(1) = \frac{1}{\pi}$$

$$\int_0^\infty \int_{-\pi}^\pi S(f)D(\theta) d\theta df = \int_0^\infty S(f) df \tag{3.31}$$

The double integral of Equation 3.31 can easily be considered as a volume of energy, which is equivalent to the area of a non-directional variance density spectrum. Increasing the value of the spreading function  $s$ , thereby increasing the power of the cosine, causes  $D(\theta)$  to narrow (Figure 3.8) and the sea state becomes more long crested. Swell generally has a narrow directional spread.

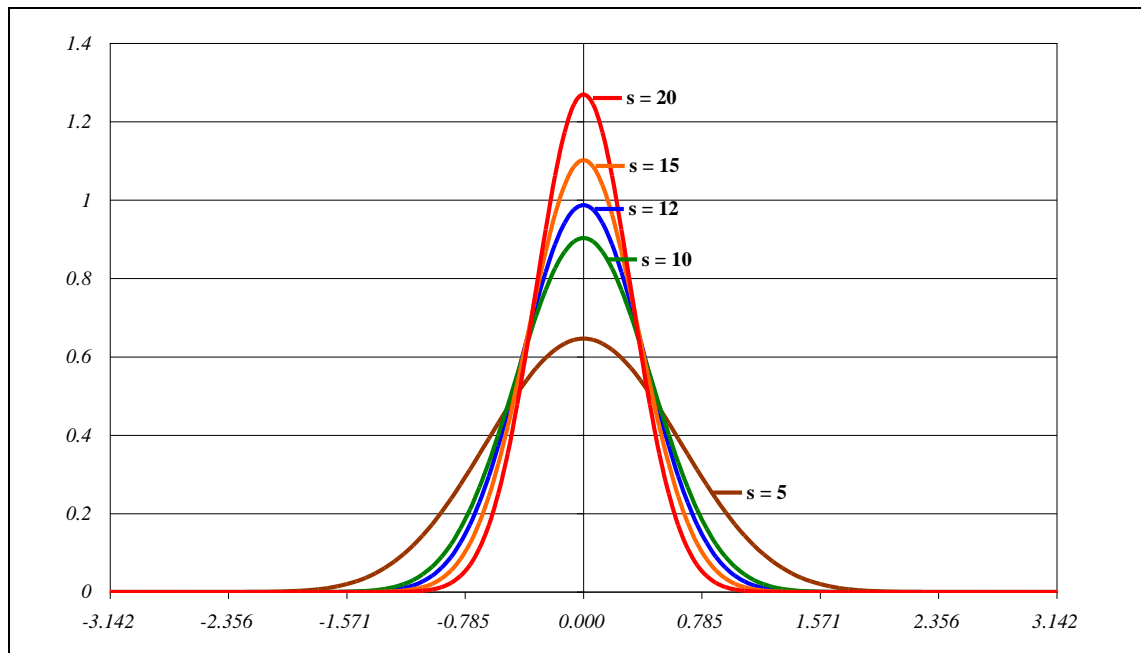


Figure 3.8. Directional spreading function.

Various methods exist to estimate the directional spread and some depend on the recording method, such as spatial arrays, floating buoys and remote sensing techniques. The measurement devices used will provide input data in different forms and therefore some methods are expandable while others are unique to the instrument involved. A Datawell Directional Waverider was used to measure Cartesian displacements at the Galway Bay test site and so techniques for the determination of the directional spectrum from single point systems will be considered here.

3.2.5.1. Cross Spectral Analysis

Stochastic models assume that linear wave theory applies and the phase of the individual sinusoidal components are random. The conclusion of this assumption is that the information of the phase distribution can be disregarded and that these models are not suitable for the analysis of waves in the vicinity of a reflecting structure.

The directional spectrum is obtained from the cross power spectrum of the various concurrent outputs of the measurement system. The Datawell directional Waverider buoy outputs the displacement of the three Cartesian axes. Therefore the three measured signals ( $N = 3$ ), allow for the analysis of the correlation between each pair of signals in the frequency domain by estimation of the cross-covariance spectral densities. The total number of complex cross spectra computed for a device with  $N$  signals is given by Equation 3.32.

$$\frac{N(N + 1)}{2} \tag{3.32}$$

Although this cross spectral analysis produces an  $N \times N$  matrix, in the case of the Datawell buoy, only six of the nine cross spectra need to be evaluated as the other three are complex conjugates as indicated by the apostrophe:

$$\begin{bmatrix} C_{11} & C_{12} & C_{13} \\ C_{21} = C_{12}' & C_{22} & C_{23} \\ C_{31} = C_{13}' & C_{32} = C_{23}' & C_{33} \end{bmatrix}$$

$$C_{11} = S(f)_{heave}, C_{22} = S(f)_{north}, C_{33} = S(f)_{west}$$

These complex cross spectra have real parts called coincident spectral density functions, or co-spectra ( $C_{ij}$ ) and the imaginary parts are known as quadrature spectral density functions, or quad-spectra ( $Q_{ij}$ ). Of the six computed cross spectra in this case,  $\frac{N(N-1)}{2}$  are equivalent to the FFT of the individual input signals and their quad-spectra are equal to zero. These real spectra reside along the diagonal of the matrix where  $i = j$  for  $C_{ij}$ . This follows the cross power rule that if two variables are completely independent then the cross power spectrum is zero and if the variables are identical, you get the normal power spectrum (Tucker and Pitt 2001).

The result of this cross spectral analysis is that only five independent coefficients can be computed for each frequency and one of these is devoted to the estimate of the variance density spectrum. This can be written in terms of the Fourier coefficients as shown in Equation 3.33.

$$a_n = \int_0^{2\pi} D(f, \theta) \cos(n\theta) d\theta \text{ and } b_n = \int_0^{2\pi} D(f, \theta) \sin(n\theta) d\theta \tag{3.33}$$

Fourier Coefficient	$a_1(f)$	$b_1(f)$	$a_2(f)$	$b_2(f)$
Cross Spectral Components	$\frac{Q_{11}}{\sqrt{C_{11}(C_{22} + C_{33})}}$	$\frac{Q_{13}}{\sqrt{C_{11}(C_{22} + C_{33})}}$	$\frac{C_{22} - C_{33}}{C_{22} + C_{33}}$	$\frac{2C_{23}}{C_{22} + C_{33}}$

**Table 3.3. Fourier Coefficients derived from Cross spectra.**

Table 3.3 presents the equations to derive the four Fourier coefficients from the cross spectral analysis for a buoy recording the displacements along three axes presented by Benoit, Frigaard and Schaffer (1997).

Several computational methods and algorithms are available that implement the results from the cross spectra matrix to determine the Directional Spreading function. These involve stochastic, deterministic and time domain analysis methods. For wave data analysis and especially, for the implementation of data from surface following buoys, the stochastic methods are the most popular. These include various Fourier analysis techniques such as the Truncated Fourier Series Decomposition and Weighted Fourier Series Decomposition, Parametrical Fitting models, Maximum Likelihood Method, Maximum Entropy Method and finally the Bayesian Directional Method. These analysis processes are listed in increasing order of complexity, but only the more commonly implemented methods such as the Maximum Likelihood Method and the Maximum Entropy Method are discussed further. Michel Benoit has conducted extensive comparative investigation of the available directional analysis methods, and information on the other methods are available in those publications (Benoit *et al.* 1997).

### 3.2.5.2. Maximum Likelihood Method

A directional analysis method adopted and extended by Isobe (1984), from the original work on seismic arrays by Capon in 1967, the Maximum Likelihood Method (*MLM*) is based on the assumption that the estimate of the Directional Spreading function may be expressed as a linear combination of the cross spectra. The best estimate to the actual Directional Spreading Function involves the inverse of the cross spectral matrix and a check that the *MLM* estimate integrates to unity over the range 0 to  $2\pi$ . For single point measurement systems such as data buoys, the dimension of the cross spectral matrix is three, therefore it can be inverted analytically. This results in computationally efficient routines.

However, the cross spectra computed from the resultant *MLM* tend not to be the same as the cross spectra computed from the wave data and so an Iterative Maximum Likelihood Method (*IMLM*) was developed to obtain a consistent estimate. Two algorithms were developed, the first (*IMLM1*) by Pawka (1983) and the second (*IMLM2*) by Oltman-Shay and Guza (1984). The iterations are stopped after a fixed number of steps or a convergence criteria is met. Tests on these methods have found that the second method, *IMLM2*, although increasing computational time, is a significant improvement on the *MLM* method. It was found that the *MLM* method usually represents the directional spectrum with broader peaks and is intolerant of errors in the input data.

Benoit (1992) analysed three numerical directional spectra of the following form; uni-modal broad spreading function, uni-modal thin spreading function and bi-modal spreading function with the *MLM* and found that it produced rather good estimates for all three cases, and was very computationally efficient.

#### 3.2.5.3. *Maximum Entropy Method*

The Directional Spreading function can be treated in the same way as a Probability Density function, as its integrated value is equal to one and a positive function. In one sense, the Directional Spreading function is the Probability Density function of wave energy over the directions of propagation. This function is then maximised under the constraints given by the cross spectra. In this case, the entropy is in effect the integral of the directional distribution.

Two methods exist to define the function. Lygre and Krogstad (1986) developed the first method (*MEM1*) which maximises the entropy and whose first two harmonics are identical to those from the measured cross spectral analysis. The maximum entropy method estimate is always consistent with the cross spectral data and it is found to be highly efficient computationally. However, it tends to over estimate the magnitude of the spectral peak, and in some cases produce bi-modal distributions of measured uni-modal directional seas. Earle, Steel and Wang (1999) also studied various methods of directional spectrum resolving for both numerical data and measured data and found that *MEM1* provided a better resolution than *IMLM2* but also found similar findings to Benoit of the false occurrence of bi-modal distributions.

The second method (*MEM2*), Nwogu, Mansard, Miles and Isaacson (1987) found to be clearly superior, although the computation times are the highest of all methods and it is more complicated to implement, especially for wave probe arrays but it is recommended by Benoit for precise and reliable directional analysis.

Both Benoit (1992) and Earle *et al* (1999) recommend the *MEM* method for directional spectral analysis, but due to the computational effort involved some of the more basic methods should be implemented as a first estimate or indication of the directional properties of the sea state under investigation.

### 3.3. Empirical Studies

Several studies have been conducted to derive a standardised method of describing the measured sea states. These generally involved the measurement of thousands of surface elevation and associated wind records, calculating the variance density spectrum and applying fitting techniques, to produce equations of varying input parameters and complexity.

Several spectral distribution equations exist, but the more commonly applied to deepwater applications are the Bretschneider Spectrum, also known as the modified Pierson-Moskowitz Spectrum, the one-parameter Pierson-Moskowitz formula, and finally the JONSWAP spectrum, derived from fetch limited seas in the North Sea. The Pierson-Moskowitz spectrum will be dealt with first, as there is a natural progression in the definition of the spectra from this to Bretschneider to JONSWAP.

Phillips (1958) introduced the concept of the equilibrium range, which states that for wind blowing for a long time over a long fetch, the wave energy for a given frequency reaches an upper limit. This describes the energy balance between the input energy from the wind and the losses of the energy to other frequencies and by phenomenon such as wave breaking. Equation 3.34 describes this equilibrium range, which is also the high frequency side of the spectrum.

$$S(f) \approx \left( \frac{\alpha g^2}{(2\pi)^4 f^5} \right) \quad (3.34)$$

where  $\alpha = 0.00074$ .



This was used by Pierson and Moskowitz (1964) as a model for their spectrum and Hasselmann *et al* (1973) used it for the spectrum derived from the Joint North Sea Wave Analysis Project. In 1985, Phillips found that the range should have a frequency tail of  $f^{-4}$ , as shown in Equation 3.35 (Phillips, 1985). For measured spectra this range seems to vary between 4 and 5. This can be an effect of the measuring technique, bottom effects, effects of ocean currents, etc.

$$S(f) \approx \left( \frac{u^* g}{(2\pi f)^4} \right) \quad (3.35)$$

where  $u^*$  is the wind friction velocity.

### 3.3.1. Pierson-Moskowitz

The Pierson-Moskowitz spectrum was first proposed in a paper by the Pierson and Moskowitz (1964). The work was based on the application of a proposed similarity method to data collected by Moskowitz for fully developed sea states with wind speeds from 20 to 40 knots. In work referenced in the paper, a hypothesis was tested that when variance density spectra are plotted in a certain non-dimensional way, they become the same shape. By applying this theory to the measured seas of Moskowitz, they found that of the important range of frequencies, the non-dimensional spectrum is nearly the same for all wind speeds.

The similarity theorem of Kitaigorodskii, used for the analysis, stated that the variance density spectrum of wind generated seas is proportional to only four variables, which are frequency, gravity, friction velocity and fetch. He then proposed a dimensionless spectrum as a function of dimensionless frequency and dimensionless fetch. It was reported in this paper that the spectrum of Bretschneider was one of the few currently proposed at the time that agreed with this analysis. The data of Moskowitz was selected so that it only contained a growing wind sea that is, stronger winds and swell eliminated some spectra in the low wind measurements and wind shifts and rapid variation in speeds eliminated spectra for the high wind speeds. However, it was found that the measured spectra were a good fit to the proposed form when plotted in the above mentioned dimensionless way.

The fitted curve of the non-dimensional spectrum is in fact a form proposed by Bretschneider (1963), although the authors of the paper recommended another form so that the dimensionless form could be determined with greater precision. The Pierson-

Moskowitz spectrum as published in its original form in the paper is presented in Equation 3.36.

$$S(\omega)d\omega = \left(\frac{\alpha g^2}{\omega^5}\right) e^{-\beta\left(\frac{\omega_0}{\omega}\right)^4} d\omega \tag{3.36}$$

where  $\alpha = 0.0081$ ,  $\beta = 0.74$ , and  $\omega_0 = \frac{2\pi g}{U}$ ,  $U$  is the wind speed, and  $\omega = 2\pi f$ .

The only input to this spectrum is the wind speed, and it is that wind speed measured at 19.5m above sea level. However, it can also be expressed in terms of the peak frequency,  $f_p$ , of the spectrum as shown in Equation 3.37 (Tucker and Pitt 2001).

$$S(f) = \left(\frac{\alpha g^2}{2\pi^4 f^5}\right) e^{-\frac{5}{4}\left(\frac{f_p}{f}\right)^4} \tag{3.37}$$

where  $\alpha$  is as in Equation 3.29,  $f_p = \sqrt[4]{\frac{4\beta}{5}} f_0$ , and  $f_0 = \frac{g}{2\pi U}$ .

The consequence of the peak frequency being the only input parameter is that the resultant spectrum will always have a constant significant steepness of 0.0508, and so it can only represent those sea states in a bi-variate scatter diagram that fall on the  $s_s = 1/20$  fully developed steepness line. To allow for the input of the significant wave height to the spectral shape, Bretschneider derived the following spectrum.

### 3.3.2. Bretschneider

In a report to the Beach Erosion Board of the US Army Corps of Engineers, Bretschneider (1959) proposed a spectral form that incorporated both the wave height and period of the sea state. This had the form as shown in Equation 3.38.

$$S(f) = A f^{-5} e^{-B f^{-4}} \tag{3.38}$$

where  $A = \frac{\alpha g^2}{(2\pi)^4}$  and  $B = \frac{5}{4} f_p^4$ .

The coefficient  $B$  is proportional to the wave period and a combination of  $A$  and  $B$  are proportional to the significant wave height. The results of the derivation of the wave height and periods are shown in Table 3.4 (Carter 1982).

<b>Total Variance Density</b>	$m_0 = \frac{A}{4B}$
<b>Significant Wave Height</b>	$H_s = 2 \sqrt{\frac{A}{B}}$
<b>Integral Period</b>	$T_I = 0.8161B^{-\frac{1}{4}}$
<b>Zero-crossing Period</b>	$T_z = 0.7511B^{-\frac{1}{4}}$
<b>Peak Period</b>	$T_p = 1.0574B^{-\frac{1}{4}}$

**Table 3.4. Wave Summary Statistics in Terms of Bretschneider Variables.**

The Bretschneider spectrum in its most usable form is presented in Equation 3.39. It utilises the input significant wave height,  $H_s$  and the inverse of the peak period,  $f_p$ .

$$S(f) = \frac{5}{16} \frac{H_s^2}{f} \left(\frac{f_p}{f}\right)^4 e^{-\frac{5}{4}\left(\frac{f_p}{f}\right)^4} \tag{3.39}$$

When the steepness of the Bretschneider spectrum equals the fully developed case, the spectrum is equivalent to the Pierson-Moskowitz spectrum of Equation 3.37. By incorporating the significant wave height and wave period into the definition of the spectral equation, all the sea states of the bi-variate scatter diagram can be defined by the Bretschneider spectral equation.

**3.3.3. JONSWAP**

The JONSWAP spectrum is a product of a measurement project in the North Sea. Measurements were obtained at one point from thirteen stations over a ten-week period in 1968 and 1969. These measurements took place along a 160m path in water depths extending from the 5m contour out to a water depth of 50m. The goal of the experiment was to determine the structure of the source function governing the energy balance of the wave spectrum, with particular emphasis on wave growth under stationary offshore wind conditions and the attenuation of swell in water of finite depth. The JONSWAP concept was conceived as a cooperative venture by a number of scientists in England, the Netherlands, United States and Germany to obtain wave spectral data of sufficient extent and density to determine the structure of the source function empirically.

The JONSWAP spectrum was devised from a least square fit of the fetch dependent frequency spectrum. A uniform good fit was achieved for nearly all the spectra observed during ideal generation conditions by the spectral form in Equation 3.40.

$$S(f) = \left[ \left( \frac{\alpha g^2}{2\pi^4 f^5} \right) e^{-\frac{5}{4} \left( \frac{f_p}{f} \right)^4} \right] \gamma e^{-\frac{(f-f_p)^2}{2\sigma^2 f_p^2}} \tag{3.40}$$

where:  $\gamma$  is the ratio of the maximal spectral energy to the maximum of the corresponding Pierson-Moskowitz spectrum,  $\sigma$  defines the width on either side of spectral peak,  $\sigma_a$  for  $f \leq f_p$  and  $\sigma_b$  for  $f \geq f_p$ .

This spectrum is the Pierson-Moskowitz spectrum of Equation 3.37 multiplied by an enhancement function and the overall spectrum incorporates five input parameters; peak frequency  $f_p$ , peak enhancement factor  $\gamma$ , Phillips constant  $\alpha$ , and the peak width factors,  $\sigma_a$  and  $\sigma_b$ . From the JONSWAP results, the peak enhancement factor, and the two width factors were highly scattered when plotted against the dimensionless fetch of Kitaigorodskii. It is indicated in the report that at first the scatter could not be explained and therefore was due to some physical process. This has been attributed to small-scale inhomogeneities of the wind field. The following average values have been suggested for the descriptive peak parameters in Table 3.5 (Hasselmann *et al.* 1973).

Peak Enhancement Factor	Peak Width: $\sigma_a$ for $f \leq f_p$	Peak Width: $\sigma_b$ for $f \geq f_p$
$\gamma = 3.3$	$\sigma_a = 0.07$	$\sigma_b = 0.09$

**Table 3.5. Average parameter values for JONSWAP spectrum.**

The consequence of multiplying the Pierson-Moskowitz spectrum by the peak enhancement factor is that the resultant spectral shape has the following characteristics. The significant wave height derived from the JONSWAP spectrum is greater than calculated from the spectral moment of the Pierson-Moskowitz spectrum depending on the peak enhancement factor as shown in Figure 3.9, and this enhanced energy contribution is focused about the peak of the JONSWAP spectrum. The range of the peak enhancement factor lies from 1, when the JONSWAP spectrum is equivalent to the Pierson-Moskowitz spectrum, to 7. Detailed analysis of these values by Ochi and Hubble (1976) showed that they have a standard deviation of 0.79 with a normal distribution about the mean,  $\gamma = 3.3$  (Carter 1982).

By replacing the Pierson-Moskowitz equation in the JONSWAP equation with the Bretschneider equation, it is possible to replicate the more peaked spectra throughout the

bi-variate scatter diagram, and the same percentage increase in significant wave height is experienced for the peak enhancement factors as plotted in Figure 3.9.

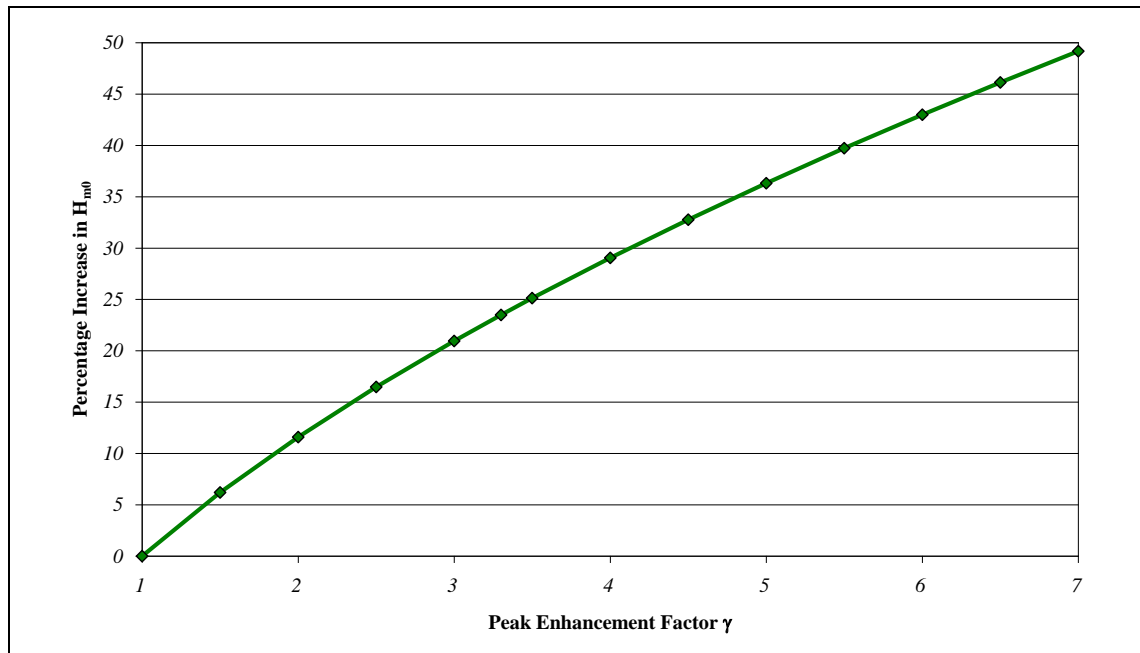


Figure 3.9. Percentage increase of significant wave height due to peak enhancement factor.

Figure 3.10 shows graphically the comparison of a Bretschneider spectrum to a JONSWAP spectrum for the same significant wave height and peak period. This shows the narrowness of the JONSWAP spectrum and the effect of the peak enhancement factor and the side slopes, the values of which are the same as Table 3.5.

Hasselmann *et al* (1973) found that the measured sea states of the JONSWAP project were unaffected by the water depth if the wavelength of the period associated with the peak of the spectrum was greater than 4 times the depth of water, as in Equation 3.41, in terms of the peak period (Carter 1982).

$$h > \frac{gT_p^2}{8\pi} \tag{3.41}$$

It was stated previously that the Bretschneider spectrum is equivalent to the Pierson-Moskowitz spectrum when the significant steepness is equal to 0.0508. The significant steepness can be calculated from the following equation (Equation 3.42). Outside of this, the shape is similar but the total variance, and therefore the steepness can differ.

$$S_s = \frac{2\pi H_{m0}}{gT_{02}^2} \tag{3.42}$$

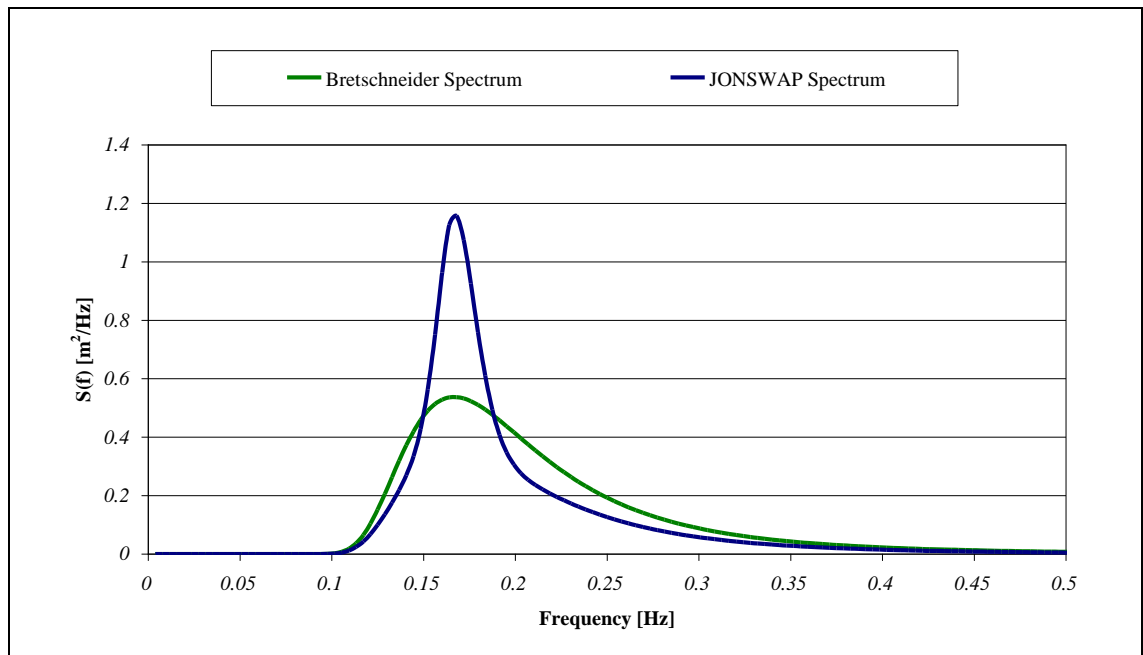


Figure 3.10. Bretschneider and JONSWAP spectrum,  $H_{m0} = 1\text{ m}$ ,  $T_p = 6\text{ s}$ .

The primary input to these spectral shapes is the frequency of the peak of the spectrum, which is the inverse of the peak period,  $T_p$ . For both the Bretschneider and Pierson-Moskowitz spectra the relationship of the peak period to the other periods are a constant and given in Table 3.6. This is contrasted in Figure 3.11 for the JONSWAP spectrum as the ratio changes depending on the peak enhancement factor being used. When the peak enhancement factor,  $\gamma = 1$ , the JONSWAP spectrum is equivalent to the Bretschneider form and the ratio of the periods is as given in Table 3.6. As the peak enhancement factor increases, the JONSWAP spectrum becomes narrower, and the ratio of the periods approach one.

$T_p/T_{02}$	$T_e/T_{02}$	$T_p/T_e$
1.406	1.205	1.167

Table 3.6. Period ratios for Bretschneider and Pierson-Moskowitz spectra.

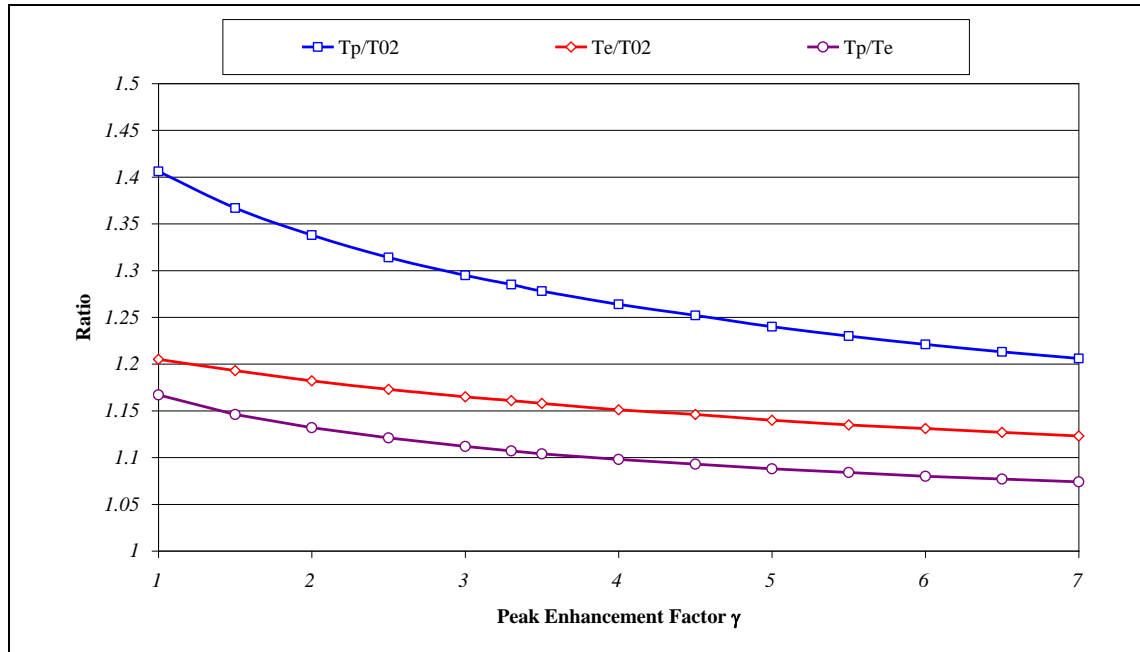


Figure 3.11. Period ratios for JONSWAP spectrum due to peak enhancement factor.

Three spectral models have been presented here, although others for more specific uses are available. Torsethaugen and Haver (2004) and Ochi and Hubble (1976), present spectral forms for modelling spectra that have two separate concentrations of energy to represent bi-modal wind and swell sea conditions, but these will be presented in more detail in a later section.

Another spectral form that may be of interest to those working in shallow waters of between 5m and 40m is the proposed TMA spectrum which gets its name from the source of the data it was fitted to, Texel, MARSEN and ARSLOE. The data used was measured for several projects, MARSEN in the North Sea, Texel off the coast of the Netherlands and ARSLOE off the coast of North Carolina, United States (Bouws *et al.* 1985). Bergdahl (2009) showed that the TMA spectrum was the best at representing measured spectra at shallow water locations.

### 3.4. Spectral Bimodality

Another important indicator of spectral variation is the occurrence of multi-modal sea states. These sea states are classified into two independent frequency concentrations of energy, where in one case the double peaked spectrum is dominated by a high frequency, short period peak. Such a spectrum could have been generated by a low frequency, long

period, swell system that had travelled a considerable distance losing much energy, entering an area consisting of a local wind wave system. This would be classified as a wind dominated spectrum. Spectra dominated by a low frequency, long period swell peak may have been generated by a refreshing wind or by a change in wind direction which creates a system of short period waves coexistent with the “old” wave system. When the wind does not drive the old system any longer, the wave components become uncoupled and the wave system turns into swell. This type of bimodal spectrum is known as a swell dominated spectrum. At an exposed site, it is reasonable to expect swell dominated spectra to occur more often than wind dominated spectra, since wind speed and direction show a larger variability creating a new wave system, each time it changes direction or intensity.

This phenomenon has a significant effect at the Galway Bay test site, as the encroaching swell can be considered to be at full-scale, while the local fetch limited sea states are considered to be at quarter scale. The site characteristics were originally determined from a hindcast model using the 3rd generation wave model SWAN for the year 2000, and a non-directional wave recording buoy *in situ* since the test site’s inception in late 2005. Analysis of this data has shown that there are high occurrences of twin peak spectra, comprising a local fetch limited wind sea and a long period swell which approaches the site around the Aran Islands from offshore. Therefore, the swell components of the spectra are more dominant than would be expected at a more exposed site. A thorough investigation of the spectral shapes of the measured sea states at Galway Bay and the more exposed Loop Head site was conducted to quantify the existence of double peaked spectra. The findings of similar investigations reported in literature for both open ocean and coastal sites in the North Atlantic have found various degrees of influence of double peaked spectra. The method that identifies and separates these multi-modal wave generation systems into their constituent processes will also be presented. Through the application of this method the wind and swell sea components will be presented in various forms to engender a thorough knowledge of the conditions at the test site.

#### **3.4.1. Bimodal Identification Studies**

Guedes Soares (1984) reports that an overall average of 22% of bimodal spectra occur in the North Atlantic. This is averaged across all occurring wave heights and ranged from 34% at low significant wave heights (1-2 m) to 3.4% with  $H_s$  greater than 10m. Later



work by the same author (Guedes Soares 1991), which dealt with an even greater catalogue of data, including measurements from the North Sea, confirmed the findings of the previous 1984 paper and stated on average a 16% double peaked spectral occurrence for the North Sea, again for all significant wave heights that occurred.

Guedes Soares and Nolasco (1992) also investigated bimodal identification techniques with measured spectra from the Atlantic coast of Portugal, off Figueira da Foz in 100m of water depth. In this study, he applied five methods of double peaked qualification to a data set that comprised of over 2,400, twenty-minute surface elevation records. The conclusion was that four of the five schemes identified between 23% and 26% double peaked spectra, which agreed well with the lead author's previous work.

Other authors have found similar percentage occurrences for other areas of the North Atlantic. Cummings, Bale and Gentile (1981) presented some of the first results from a study of hindcast data for the North Atlantic and concluded that approximately 25% of the spectra indicated multiple wave systems. Aranuvachapun (1987), in a paper with the aim of fitting the JONSWAP spectrum to measured spectra, concluded that 24% of the 159 spectra, recorded during two storm events, were double peaked. This data was from a buoy at an exposed site off the Scilly Isles in 100m of water depth, on the south-west coast of England.

### **3.4.2. Bimodal Identification Techniques**

To quantify the influence of bimodal sea states at a site of interest, the spectral shape is required for inspection, as the energy distribution in the frequency or directional domain is lost within the summary statistics. In order to separate the differing wave generation systems, several methods are available for the identification and quantification of multi-peaked sea states. Most are based on defining a legitimate secondary peak by ensuring that there is a required frequency separation between the primary and secondary peak and that the valley between the two peaks is of a sufficiently low energy level.

The wave age criterion can also be used to determine the separation frequency of wind and swell seas. This method is based on knowledge of the wind speed and the peak wave phase speed. Pierson and Moskowitz (1964) determined that the ratio of the phase speed at a peak frequency  $c_p$ , to the wind speed measured at a height of 10m above the water

surface  $U_{10}$ , can indicate if the spectrum is either wind or swell dominated. This approach is used in the WAM forecasting model, such that if  $\frac{c_p}{U_{10}} < 1.2$ , then the energy associated with that peak is wind dominated, and where the ratio is greater than 1.2, it is swell dominated (Hanson and Phillips 1999). However, for use with Waverider data, where there is no instrumentation to measure the wind speed, this method will not be considered further.

#### 3.4.2.1. Parametric Identification Models

In an early paper by Guedes Soares (1984), a simplified method was adopted to qualify a spectrum as double peaked from a collection of data sets of measured sea states from around the North Atlantic and the North Sea. A minimum frequency difference of 0.03 Hz between the peaks, combined with the criterion that the trough between the two peaks should be lower than the 90% confidence limit of the magnitude of the primary peak ordinate. The choice of 0.03 Hz was an arbitrary one, resulting from visual inspection of the spectra of interest.

Houmb and Due (1978), in a report to the Norwegian Institute of Technology, stated that the minimum difference in frequency between two peaks must be at least 6.4 times the bandwidth of the estimates, where the number of degrees of freedom must be  $\nu \geq 16$ . In addition, they required that the lower 90% confidence limits of the two peaks represent a higher variance density than the trough between them (Rodriguez and Guedes Soares 1999).

Guedes Soares and Nolasco (1992), suggested five different criteria to identify more than one legitimate peak. Two of these are based on confidence intervals. The first of these impose as necessary the condition to consider a spectrum being two peaked when the 90% confidence limit of the primary peak is higher than the upper limit of the 90% confidence interval of the adjacent minimum. The second test imposes the condition that the minimum between the two peaks should be below the lower limit of the confidence interval of the secondary peak. An additional condition requires that for a peak to be considered as accountable, the secondary peak is greater than 15% of the primary peak.

The logarithmic transformation of the spectral estimates is often suggested to stabilise the variance of spectral estimates. Although the confidence interval of the original spectrum

varies with frequency, it remains constant over all frequencies for the log spectrum. When implementing the algorithm, it is necessary as a first step to identify the global minima and maxima, and then to compare the vertical distance between them with the confidence interval width. Nevertheless, this kind of problem disappears as the number of degrees of freedom increases and the confidence interval decreases. It was found that a value for the degrees of freedom of  $\nu = 40$  is recommended as adequate in terms of smoothness and bias. For low secondary peaks in the original variance spectrum, they appear quite visible in the log spectrum (Rodriguez and Guedes Soares 1999).

#### 3.4.2.2. Wang and Hwang Steepness Function

Wang and Hwang (2001) presented a method to identify the separation frequency based on the significant steepness of the associated frequency. Assuming the separation frequency is linearly related to the spectral peak of the wind sea, an empirical relationship between the separation frequency and the local wind speed based on the Pierson-Moskowitz equation exists (Equation 3.43):

$$f_s = \frac{\beta}{U} \tag{3.43}$$

The previous peak identification methods presented here require *a priori* knowledge of the degree of freedom of spectral data and have to inefficiently examine every local maximum. The empirical peak identification method also lacks physical basis of wind wave generation and can easily result in misidentification of wind sea and swell peaks, especially for spectra with multiple strong swell peaks. The purpose of the Wang and Hwang study is to develop a physics based method to separate energies of wind and swell without the need of wind and directional wave information.

The Wang and Hwang steepness method is based on the ratio between the wave height and wavelength at that frequency. When that frequency is the minimum frequency of the spectral range, the wave height is  $H_{m0}$  and the period, which is proportional to the wavelength is  $T_{02}$ . The steepness function can be expressed as Equation 3.44:

$$\alpha(f_*) = \frac{8\pi \left[ \int_{f_*}^{f_{max}} f^2 S(f) df \right]}{g \left[ \int_{f_*}^{f_{max}} S(f) df \right]^{0.5}} \tag{3.4}$$

where  $\alpha(f_*)$  is that portion of the spectrum from  $f_*$  to  $f_{max}$

Compared to the spectral peak,  $f_p$ , the peak of the steepness function,  $f_m$  is less affected by spectral irregularities due to the square of the frequency in the function. Using the Pierson-Moskowitz spectrum, a relationship is derived between the peak of the steepness function,  $f_m$  and the wind speed using regression analysis. The maximum frequency used for this relationship is  $f_{max} = 0.5 \text{ Hz}$ , however, maximum frequencies up to 1.0 Hz are investigated. Most surface following buoy systems have a maximum frequency of 0.4-0.6 Hz. In this range, the variation of the peak frequency of the steepness function  $f_m$  with respect to  $f_m$  at a  $f_{max}$  of 0.5 Hz is less than 10%.

Considering that local wind generated waves should have phase velocity  $c$  less than wind speed  $U$ , the separation frequency of wind and swell is the frequency  $f_s$  with its phase velocity  $c_s$  satisfying the relation  $c_s = U$ . Using the deep water phase velocity,  $c_s = g/2\pi f$ , the separation frequency is related to wind speed and so a relationship (Equation 3.45) can be obtained between the separation frequency,  $f_s$  and the peak of the steepness function,  $f_m$  which allows for the determination of the separation frequency without the knowledge of the wind speed.

$$f_s = A(f_m)^B \quad (3.45)$$

where  $A = 4.112$  and  $B = 1.746$ .

A plot of Equation 3.45 against the peak frequency of the steepness function,  $f_m$  in terms of the multiplication factor of  $f_m$  to  $f_s$  can be seen in Figure 3.12. This graph indicates that at peak frequencies less than 0.15 Hz of the steepness function, the separation frequency will be less than  $f_m$  and that for frequencies where  $f_m > 0.15 \text{ Hz}$ , the frequency of the separation frequency quickly increases.

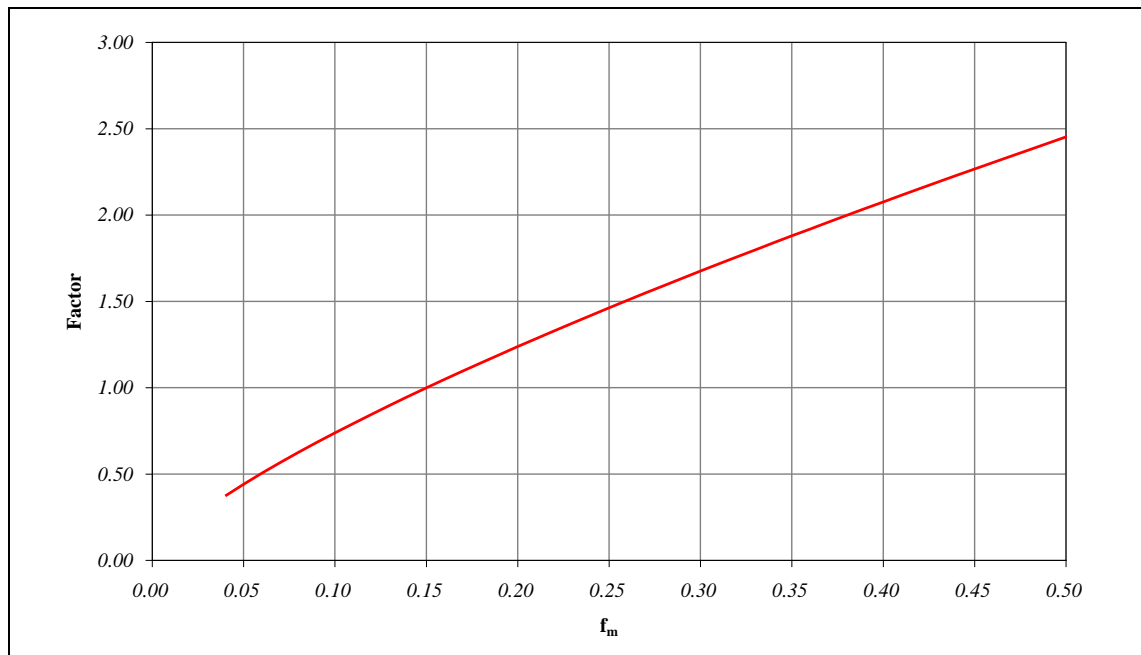


Figure 3.12. Multiplication factor of  $f_m$  due to Equation 3.45.

### 3.4.3. Bimodal Modelling Techniques

To enable the modelling of multi-modal spectra, there are also several methods available. In general, these approaches contain some form of applying the empirically derived spectral equations to each portion of the separated wind and swell peaks. Ochi and Hubble (1976) derived 10 families of representative spectra from a large data set of measured spectra and proceeded to fit a Bretschneider spectra to the wind and swell components. A fitting method developed by Guedes Soares (1984) fits the JONSWAP spectra separately to the wind and swell component of the double peaked spectrum. This method is derived from the analysis of measured spectra from the North Atlantic and the North Sea. Torsethaugen and Haver (2004) developed a similar method using JONSWAP spectra modelled on sea states measured off the coast of Norway. These are reviewed below.

#### 3.4.3.1. Ochi & Hubble, 1976

Ochi and Hubble (1976), attempted to develop a systematic method of spectral identification by grouping measured spectra from a data set of 800 measured spectra obtained by a ship borne wave recorder onboard the Ocean Weather Ship “Weather Reporter” at position “J” with coordinates  $53^{\circ} N 18^{\circ} W$ , in the North Atlantic ocean as indicated in Figure 3.13.

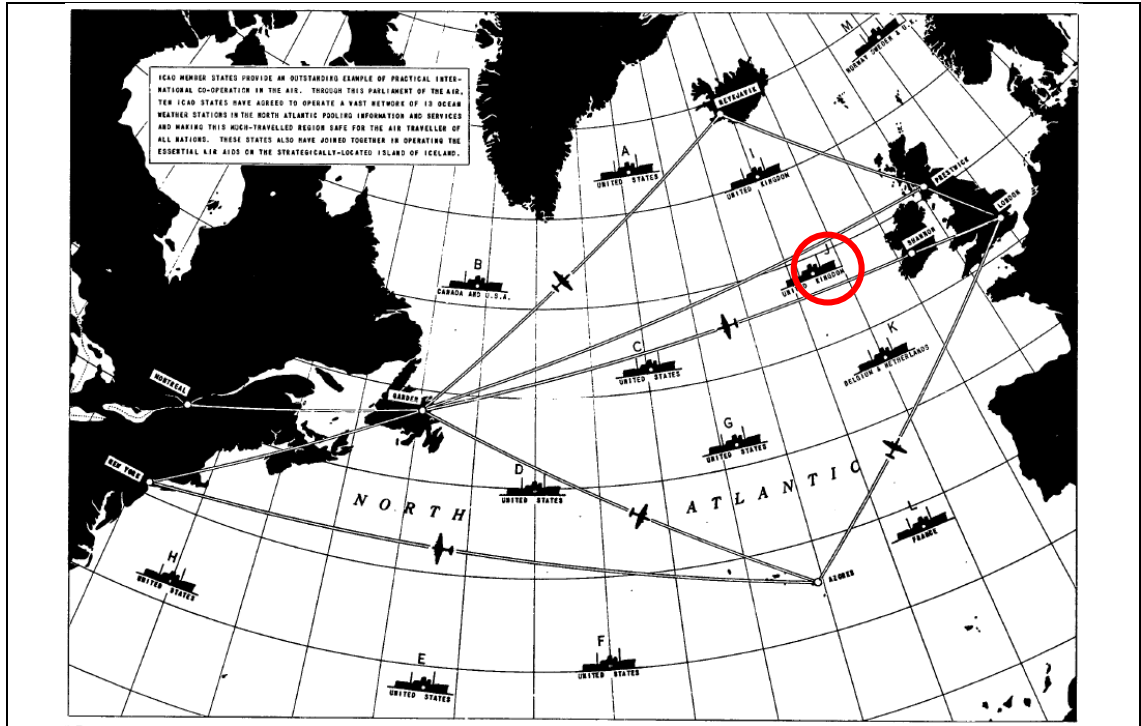


Figure 3.13. Location of Meteorological Observing Stations in the North Atlantic Ocean.

A six parameter representation of ocean waves is made on the 800 observed spectra, and the results are classified into 10 characteristic spectra depending on the severity. Each of the component wave systems can be defined by a three parameter spectrum. Then for each group a statistical analysis is carried out on the parameters taking into account the correlation between them. Finally, the results are presented in a family of spectra including the most probable spectrum expected to occur for a specified sea state as well as the limiting spectral shapes which may occur with a confidence coefficient of 0.95. The values for the six parameters for this set of mathematical spectra are expressed in terms of significant wave height so that a family of spectra for a desired sea severity can be generated (Ochi and Hubble 1976).

Ochi and Hubble (1976), use the Bretschneider form of the wave spectrum equation. This spectrum is then converted to a unit spectrum  $S'(\omega)$  by dividing  $S(\omega)$  by the area,  $m_0$  so that the spectrum has a unit area (Equation 3.46):

$$S'(\omega) = \frac{4B}{\omega^5} e^{-B/\omega^4} \tag{3.46}$$

where  $B$  is as defined in Equation 3.38.

This unit spectrum can be considered as if it were a probability density function, since it is positive, continuous and integrable. In fact, it yields the exponential PDF by letting

$\omega^4 = 1/x$ . Hence, it can be generalised in the form of a new PDF with the additional parameter,  $\lambda$ , which yields the Gamma probability function (Equation 3.47):

$$S'(\omega) = \frac{4}{\Gamma(\lambda)} \frac{B^\lambda}{\omega^{4\lambda+1}} e^{-B/\omega^4} \quad (3.47)$$

Under the assumption that the spectrum is narrow banded,  $S'(\omega)$  may be converted to the dimensional wave spectrum,  $S(\omega)$  which satisfies the condition that the area under the spectrum is equal to  $m_0$ . Then the variance density spectrum becomes Equation 3.48:

$$S(\omega) = \frac{1}{4} \frac{B^\lambda}{\Gamma(\lambda)} \frac{H_s^2}{\omega^{4\lambda+1}} e^{-B/\omega^4} \quad (3.48)$$

where  $B = \left(\frac{4\lambda+1}{4}\right) \omega_p^4$  and  $\omega_p$  is the peak frequency and  $\omega_p = 2\pi f_p$ .

Therefore, the following spectral formulation can be made:

$$S(\omega) = \frac{1}{4} \frac{\left(\frac{4\lambda+1}{4} \omega_p^4\right)^\lambda}{\Gamma(\lambda)} \frac{H_s^2}{\omega^{4\lambda+1}} e^{\left[-\frac{\left(\frac{4\lambda+1}{4}\right)}{\left(\frac{\omega_p}{\omega}\right)^4}\right]} \quad (3.49)$$

The spectrum described by Equation 3.49 has three input parameters; the significant wave height,  $H_s$ , the peak frequency,  $\omega_p$ , and a shape parameter,  $\lambda$ . When  $\lambda = 1$ , Equation 3.49 reverts to the Bretschneider spectral equation and when  $\omega_p = 0.4\sqrt{g/H_s}$  the result gives the Pierson-Moskowitz spectrum.

This spectrum is then applied to both the low frequency and high frequency components of a bimodal spectrum resulting in the identification of six parameters to fully describe the sea state spectrally as shown in Equation 3.50.

$$S(\omega) = \frac{1}{4} \sum_j \frac{\left(\frac{4\lambda_j+1}{4} \omega_{p_j}^4\right)^{\lambda_j}}{\Gamma(\lambda_j)} \frac{H_{s_j}^2}{\omega^{4\lambda_j+1}} e^{\left[-\frac{\left(\frac{4\lambda_j+1}{4}\right)}{\left(\frac{\omega_{p_j}}{\omega}\right)^4}\right]} \quad (3.50)$$

where  $j = 1$  represents the low frequency and  $j = 2$  represents the high frequency components.

A nonlinear least square fitting technique is utilised by which the six parameters can be derived directly from the measured spectra so that the difference between the theoretical and observed spectrum can be minimised. In the case of the peak frequencies, no limit is set for  $\omega_{p_1}$ , However,  $\omega_{p_2}$  has to be greater than  $\omega_{p_1}$  and should not be less than 0.6 rad/s (0.095 Hz). Analysis shows that both peak frequencies obey the normal distribution law.

In general the value of  $\lambda_1$  is much larger than  $\lambda_2$ , however it appears that both follow the gamma probability law.

The authors of this paper went on to derive parameter values for the most probable spectrum for each of the ten levels of severity, with spectra that ranged in significant wave height from  $H_s = 1.22 \text{ m}$  to  $H_s = 13.72 \text{ m}$ . For each of the most probable spectra in each of the ten groups, ten more sets of parameter values were identified that were within the 95% confidence interval of the most probable spectrum, which is presented in the paper.

When the eleven modelled six parameter spectra are plotted for each of the 10 groups of sea state severity the following phenomenon is noticed. For the lower sea states, there is a large variation in the spectral shapes for the same total variance, however this reduces as the wave height increases, and there is very little variation in spectral shape for the last group with a significant wave height of 13.72m. This is generally the case for all sets of wave data, that is, as the wave height increases, the spectrum becomes a single peaked narrow spectrum.

#### 3.4.3.2. *Guedes Soares, 1984*

Guedes Soares (1984) attempted to fit an identified bimodal spectra with a summation of two JONSWAP spectra. Using the JONSWAP spectrum to model the wind sea component was straightforward. To model the swell component of the spectrum it is argued that due to its narrowness, it can also be modelled by the JONSWAP spectrum. The narrowness of the swell component is because as the wave system has travelled over large distances away from its generation source, it loses its high frequency components, which have a lower group velocity. The spectrum therefore becomes much narrower with most of its energy concentrated around its peak.

The double peaked model used, which represents the addition of two JONSWAP spectra, has the following equations as input parameters where the subscript  $s$  indicates swell and  $w$  indicates wind for the significant wave height,  $H_s$  and mean period,  $T_m$  as defined below in Equation 3.51 and Equation 3.52:



$$H_{sw} = H_s \sqrt{\frac{1}{1 + H_R^2}}$$

$$H_{ss} = H_s \sqrt{\frac{H_R^2}{1 + H_R^2}}$$
(3.51)

$$T_{mw} = \frac{1 + \frac{H_R^2}{T_R}}{1 + H_R^2} T_m$$

$$T_{ms} = \frac{T_R + H_R^2}{1 + H_R^2} T_m$$
(3.52)

where the ratios of the component wave height and mean period is given by:

$$H_R = H_{ss}/H_{sw}$$

$$T_R = T_{ms}/T_{mw}$$

The four parameters from Equations 3.51 and 3.52 are then the inputs to the two respective wind and swell JONSWAP spectra. Average values of  $\gamma$ ,  $\sigma_a$  and  $\sigma_b$  for the JONSWAP equation were used initially, however it was found that there was a better fit using a peak enhancement factor of 2. The ratio of the two spectral peaks can be obtained from the following (Equation 3.53):

$$S_R = H_R^2 T_R$$
(3.53)

A correction must be introduced to account for the fact the spectrum is not symmetrical about the peak. Having a double peaked spectrum defined by its four parameters, one first determines the coordinates of the theoretical spectrum at the two peaks and the estimated ratio of the spectral ordinates,  $\widehat{S}_R$ . This value is larger or equal to the value of the spectral parameter  $S_R$ . The value of  $H_R = \sqrt{\frac{K_R S_R}{T_R}}$ , is thus corrected by  $K_R = \widehat{S}_R/S_R$ , and it was found that only two iterations were necessary. When  $S_R$  is equal to zero the double peaked model spectrum reduces to a single peaked JONSWAP spectrum and when the spectral ratio parameter is greater than 1, the result is a swell dominated spectrum.

#### 3.4.3.3. *Torsethaugen & Haver, 2004*

The original Torsethaugen model was established by fitting two JONSWAP shaped models to averaged measured spectra and it was developed from measured seas off the coast of Norway (Torsethaugen 1996). The model parameters were found by fitting a Gamma spectral form to the averaged measured spectra for given classes of sea state. Each sea system is defined by  $H_s$ ,  $T_p$ ,  $\gamma$ ,  $N$  and  $M$  where  $N$  is the negative power of the

high frequency tail and  $M$  is the spectral width parameter. These variables are parameterized in terms of  $H_s$  and  $T_p$  by means of regression analysis and curve fitting. Averaged spectra were established from a broad range of  $H_s$  and  $T_p$ . When utilising a model based on two parameters, on a case-by-case comparison a considerable scatter around the expected shape is observed. The scatter is most clearly pronounced for the low frequency part of the spectrum.

Torsethaugen and Haver (2004), defined a spectral peak period as the distinction between wind and swell dominated sea states is found to be defined by the fully developed sea for the location where  $T_p$  is given by Equation 3.54:

$$T_{pf} = a_f H_s^{1/3} \tag{3.54}$$

If  $T_p \leq T_{pf}$ , the primary peak corresponds to wind sea, otherwise a swell sea. The parameter  $a_f$  is slightly dependent on fetch. Torsethaugen found the following relationships;  $a_f = 6.6$  for a fetch length of 370 km and  $a_f = 5.3$  for a fetch length of 100 km. At first, this spectrum appears very complicated with many parameters that need to be defined such as wind speed, fetch length, and peak enhancement factor. However, some of these parameters only have an effect for low sea states. Torsethaugen and Haver (2004), present empirical parameter values for these variables for use in the simplified model.

The double peaked spectral model gives a parametric description for four types of peaks.

- a) primary wave system generated by a local wind system
- b) primary wave system dominated by swell
- c) secondary wind sea system
- d) secondary swell system

The Torsethaugen and Haver (2004), double peaked spectral model has the following general formulation as described in Equation 3.55:

$$S(f_n) = \sum_{j=1}^2 E_j S_{jn}(f_{jn}) \tag{3.55}$$

where  $f_{jn} = f * T_{pj}$ , and  $E_j = \frac{1}{16} H_{sj}^2 T_{pj}$ .

$E_j$  is used to proportion the energy in the total spectrum according to the primary and secondary component as described by the subscript  $j$ . The modified spectrum for each wave system depends on the four types of peaks as described above. Depending on whether the spectrum is wind or swell dominated,  $E_j$  has a different formulation, however for both systems, the secondary peak is simplified as it does not have a peak enhancement factor. The equations for the spectral form as defined by  $S_{jn}$  is given in Equation 3.56 for  $j = 1$ , the primary wave system and Equation 3.57 for  $j = 2$ , the secondary wave system:

$$S_{1n}(f_{1n}) = \frac{G_0 A_\gamma}{f_{1n}^4} e^{-\frac{1}{f_{1n}^4} \gamma} \exp\left(-\left(\frac{\frac{1}{2}\sigma}{f_{1n}}\right)^2\right) \tag{3.56}$$

where  $G_0 = 3.26$ ,  $A_\gamma = \frac{1+1.1[\ln \gamma]^{1.19}}{\gamma}$ ,  $\sigma$  is defined as in the JONSWAP equation and  $\gamma$  is a modified form of the peak enhancement factor which also has different formulations depending on whether the system is wind or swell dominated.

$$S_{2n}(f_{2n}) = \frac{G_0}{f_{2n}^4} e^{-\frac{1}{f_{2n}^4}} \tag{3.57}$$

To verify the model the author compared the fit to averaged measured spectra from a site off the Norwegian coast. These averaged spectra are presented for four sea states, for low and high wave height and long and short peak periods as described in Table 3.7. The comparison shows that there is a good fit about the peak of the spectra, however for the higher energy sea states, 3 and 4, there are minor deviations from the high frequency tail. Comparisons were also made with the Ochi and Hubble spectrum and selected measured spectra from the Norwegian coast. In all cases, the Torsethaugen and Haver (2004), model showed a better fit to the measured spectra than the Ochi and Hubble (1976), model.

	$H_s$ [m]	$T_p$ [s]	No. of Spectra
Sea State No. 1	2.48	5.3	6
Sea State No. 2	2.59	16.8	14
Sea State No. 3	5.24	9.4	279
Sea State No. 4	5.28	18.5	14

Table 3.7. Sea states used for Torsethaugen model verification.

It was found that for high energy sea states where the significant wave height was greater than 5m, the high frequency tail of the measured spectra tended to fall off faster than  $N = 4$ , as used in the model. Also, for lower sea states the measured secondary wind sea peak appeared to be broader then found by the model (Torsethaugen and Haver 2004). It can

be concluded that due to the amount of parameters involved and that some of these rely on wind speed knowledge and fetch dependence, it is not a trivial exercise to use this model for site specific studies.

#### **3.4.4 Directional Spectra Partition Methods**

In general, it is easier to apply a separation technique to a one-dimensional spectrum as the energy concentrations in the frequency domain can be easily quantified. However, when the directional distribution of energy is taken into account, different techniques are required as it is possible to have the following situation. A single peaked one-dimensional spectrum could in fact be double peaked in the directional domain if the wave systems that share the same frequency components are travelling at different directions.

Portilla, Ocampo-Torres and Monbaliu (2009), gives a summary of some partitioning schemes for two-dimensional spectra. Most of these techniques are based on a scheme devised by Hasselmann *et al* (1996) which is a modification of the Gerling (1992) method for use with SAR data. This technique treats the wave spectrum as an inverted catchment area in the sense of the hydrological concept. The overall catchment is partitioned according to sub-catchments associated with peak energy levels. A further routine is applied to qualify a sub-catchment area and its association with a peak although this part of the process is not straightforward and requires constant calibration of the parameters.

Portilla *et al* (2009) reports that one of the first techniques was developed by Gerling (1992). This algorithm quantifies partitions by identifying the lowest energy threshold at which upper parts of the spectrum get disconnected. These partitions are qualified by determining the integral mean parameters of neighbouring spectral components and subsequent times. A partition is considered significant if it is persistent in time and space.

##### **3.4.4.1 Gerling, 1992**

Gerling (1992) presents an identification method for application to directional spectra. There are three parts to the partitioning scheme, the first identifies the wave systems within the directional spectra, the second verifies legitimate wave systems by their consistency in time and space, and the third part will remove apparent wave systems that were identified in the first step but found to be illegitimate in the second step.

The partitioning technique was developed by utilising the measurements of the LEWEX project, a wave measurement and forecasting project that took place in the Labrador Sea between Canada and Greenland in 1987. The aim of this project was to compare various numerical models, directional buoys and remote sensors (airborne or satellite) in a natural environment expected to produce large seas. The heave, north and east slope from an Oceanor Wavescan buoy was analysed with the Maximum Entropy Method to produce directional spectra. This method was chosen as it produced believable wave systems when compared to the WAM model output which was also part of the LEWEX project.

The first algorithm in the Gerling (1992) partitioning method is the Spectral Partitioning Algorithm (SPA). The SPA partitions the support of the directional spectrum, the non-zero values, into regions that can be attributed to component wave systems. This is achieved through an iterative sequence. Initially a threshold value,  $l$  for the saddle points,  $S$  between local peaks is set. If the magnitude of the saddle points of the spectrum are below the threshold value,  $S < l$ , then the ordinates of the directional spectrum are set to zero,  $S(f, \theta) = 0$ . If the magnitude of the saddle points are greater than the set threshold value,  $S \geq l$ , then a new threshold level is set,  $l_0$  which is equal to the lowest saddle point greater than  $l$ . To improve efficiency the ordinates of the directional spectrum are normalised to integer values from 0 to 255 so that the value of  $l_0$  is an integer value within this range.

When a component wave system has been identified to have ordinates greater than the threshold level, regions,  $R_{i0}$  are defined within the overall spectrum when a region can be bounded by a constant level. The variance of that region is calculated along with its proportion to the total variance of the directional spectrum. This iterative process is now applied to each of the identified regions of the first run, to determine if there are further legitimate regions within the level zero regions,  $R_{i0}$ . This procedure results in a hierarchically structured description of the system, where each region is defined by a proportion of the total variance, and the sum of these proportions equals 1. Statistics are determined for each of the legitimate regions that were identified. The frequency,  $f_{max}$  and direction,  $\theta_{max}$  at the peak of the local maximum of each region as well as the average frequency,  $f_{avg}$  and direction,  $\theta_{avg}$  are recorded.

These statistics are then passed to the Pattern Recognition Algorithm (PEA) for further analysis. This algorithm will identify consistent wave systems within each directional spectrum. This is achieved by comparing the summary statistics found in the SPA step and comparing these to similar results from neighbouring spectra to determine a consistency over time of each identified wave system. Regions that appear in only one directional spectrum may be an indication of noise, and if so, the Pruning Algorithm (PA) can be used to remove weak or spurious regions from the spectrum and subsequently redistribute the variance to other more legitimate regions. In its present form, the PEA is not a completely automatic function and requires the user to give a final determination of a wave systems legitimacy.

This partitioning method was verified by comparing the results of the algorithm to the output of a WAM model that was running for the region. By creating a vector with the length proportional to the variance of that wave system and the angle of the vector equal to the propagation direction, this can be plotted with the modal frequency as the ordinate and with time along the abscissa. With this type of plot the growth and decay, along with the change in direction of the individual wave systems is easily assessed. Another strength of this method is that it does not make any assumptions of the spectral form and therefore the statistics determined are true variables.

#### 3.4.4.2. *Aarnes & Krogstad Review, 2001*

Aarnes and Krogstad (2001) summarise and present various methods to calculate a separation frequency which distinguishes the wind sea contribution of the spectrum from the low frequency swell modes in directional spectra. However, the point is made that for different swell wave systems to be identified, information about the directional properties of the waves need to be taken into account. The authors of this review outline the basic steps of a partitioning system by Hanson and Phillips (2001) which is itself a modification of the Hasselmann method. Wind wave systems are defined by a local wave age criterion where the wave propagation direction is within  $\frac{\pi}{2}$  of the wind direction and the phase speed is less than a certain fraction of the wind speed. Further to this, a wind catchment area is defined and all wind sea peaks within this area is classified as one wind wave system. Swell systems are identified if they fall outside the criteria identifying the wind wave systems, but they are combined as one swell system if the distance between peaks is small compared to the spread and if the saddle point between peaks is greater than a

required energy level. As a final definition of a partition, the total energy in a partition is required to be of a certain magnitude to justify its inclusion as a legitimate wave system.

One of the points made by the authors is the sensitivity of the success of the process to the choice of the parameters for setting the various threshold and qualification procedures. Initially this process of selecting parameters is a tuning exercise, however Aarnes and Krogstad do report what they found to be the best values to use from the experimental work of the EnviWave project from which this report was published.

## 4. OCEAN WAVE SPECTRA

The assessment of WEC response and power production in the marine environment requires the quantification and qualification of many variables. These can be broken down into the localised conditions of the deployment site and the intrinsic nature of the device characteristics. However, a quandary exists in that the influence of the local wave climate will dictate to some extent the response of the device, and so it is as important to consider the measurement of the impinging sea state, as it is to evaluate device motions and forces.

Wave conditions at a proposed test site, at either a benign or a demonstration scale, will be influenced by the following conditions:

- local bathymetry
- wind climate and swell affect
- directional properties

All these issues have an influence that is best described by the spectral shape. With the increase in understanding of wave growth, wave interaction, data collection and analysis techniques; methods have developed which hope to more accurately model the real sea surface and its complexities. Over the last forty years, our understanding of wave spectra has evolved from the one-dimensional single peaked spectrum to the more advanced multi-modal directional spectrum. Along the way, the observational techniques have improved considerably, but also the methods by which complex wave phenomena can be model.

Depending on the instrument used to measure the seaway and the implemented analysis method, the derived information will have certain caveats associated with its use. The main caution is the associated errors with the measurements. Linear theory is a close approximation to stationary wave measurement. For water depths which are regarded as deep water,  $h > \frac{gT^2}{4\pi}$ , simplified equations can be used to determine various measurements of the waves. At the other end of the scale, shallow water approximations need to be taken into account when the following is true,  $h < \frac{gT^2}{40\pi}$ , and the appropriate equations to calculate characteristics such as wave length and phase velocity should be used. This leads to the following range of wave periods that require a higher order other than linear



theory for more accurate results to be determined,  $\sqrt{\frac{40\pi h}{g}} < T < 2\sqrt{\frac{\pi h}{g}}$ . For those wave periods in intermediate water, between shallow and deep water approximations, the various wave parameters need to be determined in full.

If we take for example a water depth of 50m, then the periods that can be dealt with by the deepwater approximations of linear theory are less than 8s. If the wave period exceeds 25.3s at this water depth, then the shallow water equations are required, however this wave period is far outside the expected range of periods that wave energy devices would operate in.

The previous chapter described the various analysis techniques used to derive both non-directional and directional spectra, primarily from surface following data buoys. There is also a lot of options available to define the spectral shape of a seaway for theoretical study and comparison to the measurements. These methods have been derived from empirical studies in the 1950's and 1960's. The three main equations will be discussed here.

#### **4.1. Time Domain Analysis**

Using the data sets described in Section 2.3, various hypotheses can be tested using time domain analysis techniques. Of particular interest is the relationship between the significant wave height derived using zero crossing analysis from the surface elevation time series,  $H_{1/3}$  and by calculating the variance of the time series to determine the significant wave height,  $H_{var}$ . Also of interest is the distributions of the wave heights and surface elevation for a sample of the measured sea states.

##### **4.1.1. Validation of Empirical Results**

The previous section described various methods of obtaining summary statistics with both time and frequency domain tools. Wave energy devices are resonant operators, and so much of the work will be carried out in the frequency domain, however it is important to check the consistency of results by using both methods.

Taking twelve months worth of data from the wave elevation records for the Galway Bay test site (2007) and the exposed Loop Head site (2004), the relationship between these

time domain derived significant wave heights can be investigated as shown in Figure 4.1. These years were chosen because they provided the most complete datasets for both test sites.

The significant wave height ( $H_{var}$ ) calculated from the variance of the time series of the surface elevation is greater than the significant wave height ( $H_{1/3}$ ) calculated as the mean of the highest one third of the waves by about 6%. The Galway Bay data indicates that  $H_{var}$  is 93.4% of the significant wave height derived from the surface elevation,  $H_{1/3}$  while for the deeper site at Loop Head, the percentage is 94.5%, however the correlation between the two significant wave height measures for the two sites is very close to unity indicating that either method of calculation is an acceptable measure.

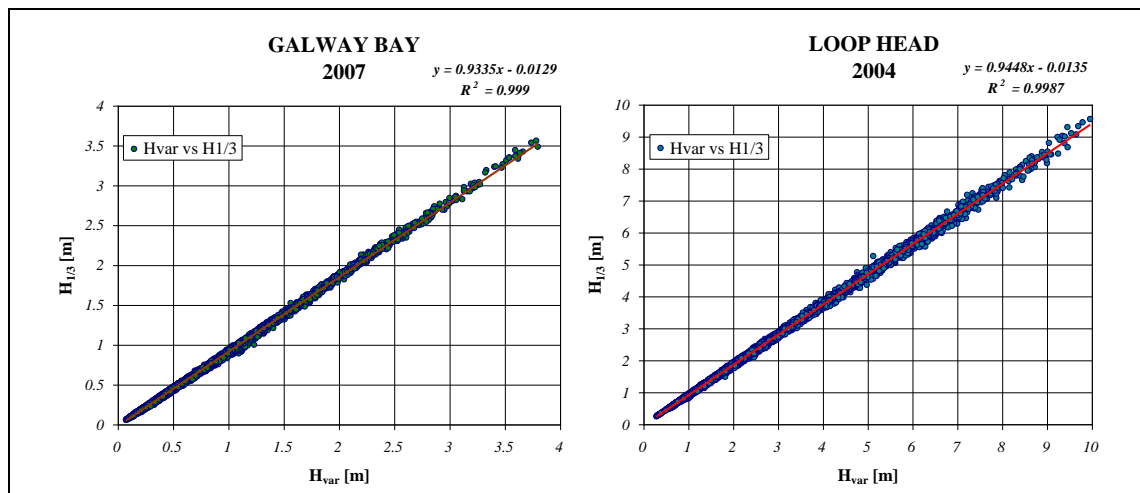


Figure 4.1. Comparison of significant wave height time domain derivation methods.

4.1.2. Statistical Distributions

Figure 4.2 shows two examples from Galway Bay of the distribution of a sample surface elevation record for a low and high sea state. Figure 4.2a has a significant wave height,  $H_s = 1.73m$  and average period,  $T_z = 4.93s$ , while Figure 4.2b has a significant wave height,  $H_s = 3.78m$  and average period,  $T_z = 6.3s$ . The bar chart is the distribution of the surface elevation shown at the top of the plots and the solid line is the theoretical Gaussian distribution for that range of values. Note that the ordinate axes is not the same range for both plots, due to the fact that the Gaussian distribution is a Probability Density function and its integral is equal to unity.

The maximum and minimum elevation levels of the record are used as an indication of the range of values to be used for the Gaussian distribution. This is not necessarily the

same as the maximum wave height,  $H_{max}$ . This range is divided into 100 equal divisions to get the bin size for each record and the surface elevation is sorted accordingly. Note that the bin sizes are not the same for each of the examples. The Gaussian distribution will have a lower probability magnitude for a larger range, as can be seen from Figure 4.2.

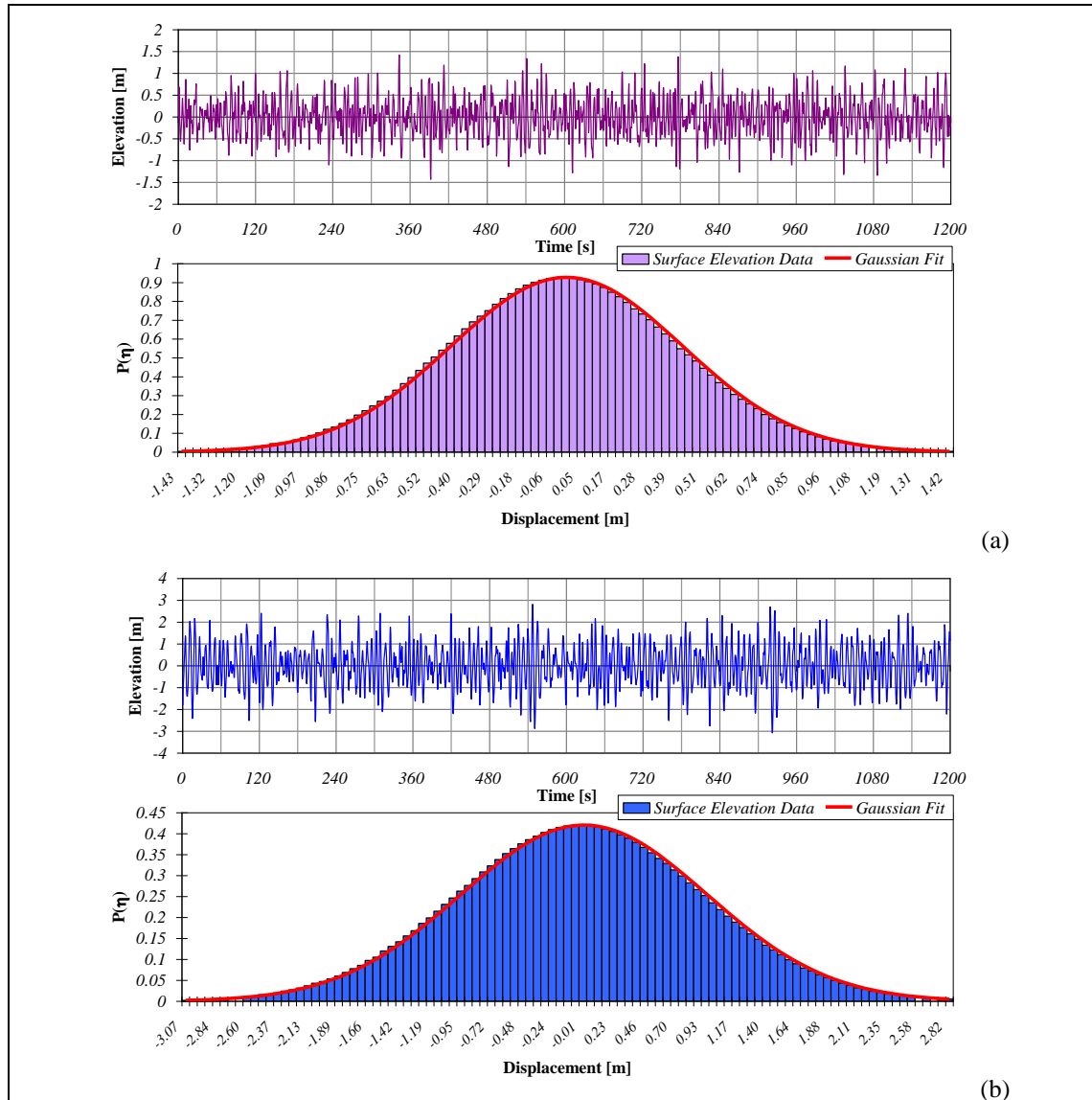


Figure 4.2. Gaussian distribution of two example surface elevation records.

Figure 4.3 shows two examples of the distribution of the zero crossing wave heights of these seaways. These are based on the zero crossing analysis of the surface elevation distributions of the examples in Figure 4.2. For this distribution, the bin sizes are the same. The first irregular wave signal of Figure 4.2a has 242 zero crossing waves and the signal in Figure 4.2b has 186 zero crossing waves. To explain the deviation of the

distribution of the measured seaway to the theoretical Rayleigh fit, the variance density spectra is required and shown in Figure 4.4.

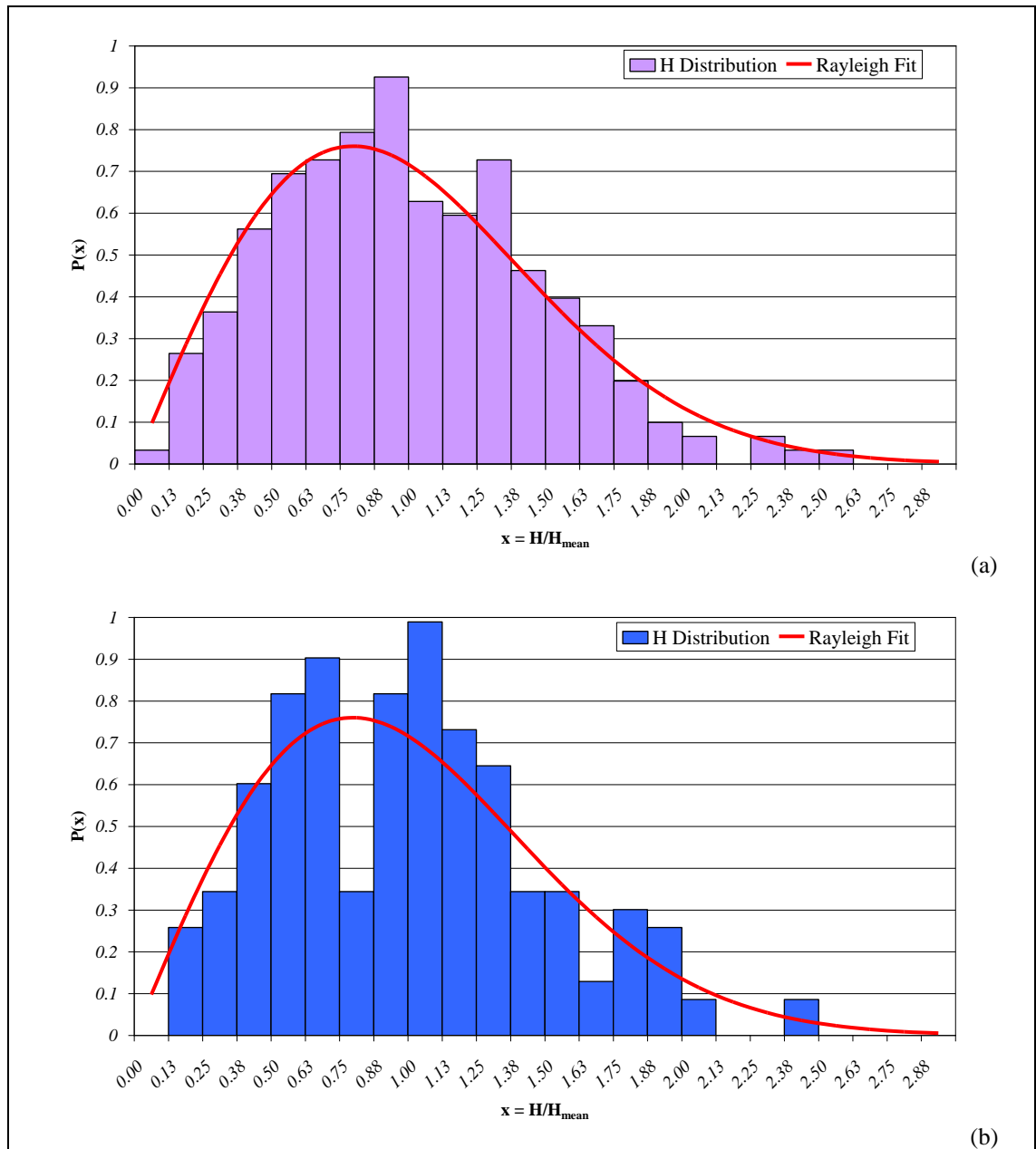


Figure 4.3. Rayleigh distribution of the two example surface elevation records in figure 4.2.

Interestingly, it would appear that the broader spectrum of Figure 4.4, which is a lower energy sea state has a better corresponding Rayleigh distribution of wave heights than the second data set. Longuet-Higgins (1980) indicated that his proposed Rayleigh distribution was found to agree well with many field observations, even though the frequency spectrum may not necessarily be narrow. Figure 4.3b indicates that the Rayleigh distribution does not fit quiet as well, but this may be due to the fact that the spectrum of the corresponding data is in fact too narrow.

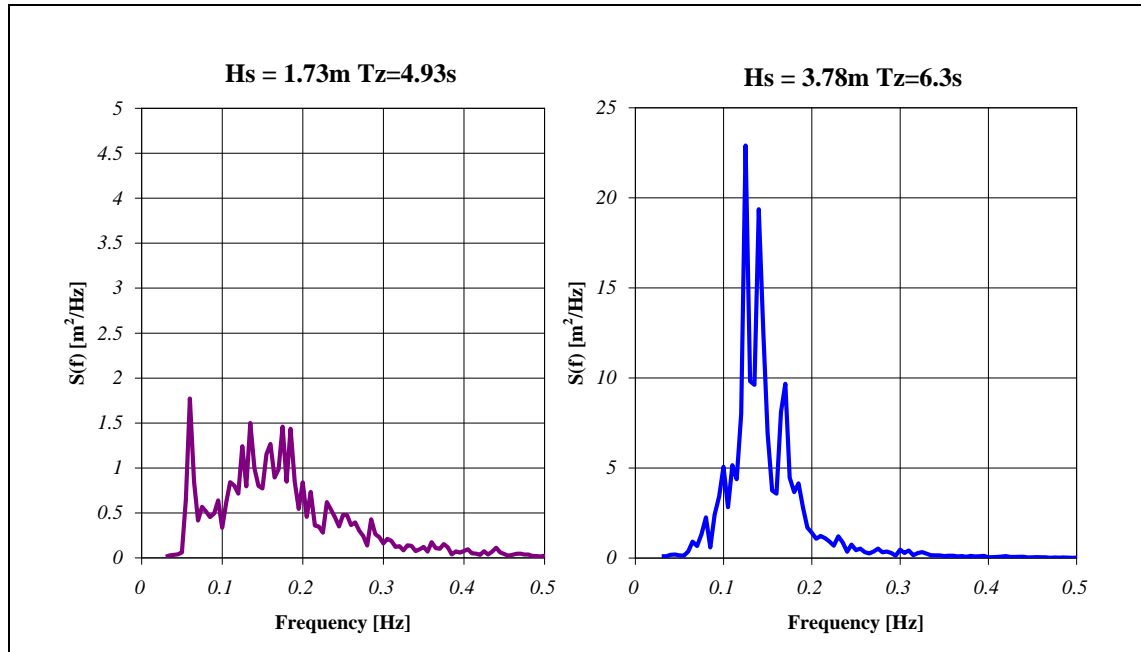


Figure 4.4. The variance density spectrum corresponding to the irregular signals of figure 4.2.

## 4.2. Frequency Domain Analysis

It was indicated in previously that the summary statistics determined from the variance density spectrum are a robust measure of the statistics of the seaway being investigated and that these frequency domain measurements can be verified by similar statistics determined from time domain analysis. Figure 4.5 shows a sample record of a measured surface elevation record and the summary statistics derived from both time and frequency domain analysis.

This particular example is taken from the non-directional buoy located at the Galway Bay wave energy test site. The summary statistics are primarily derived from the variance density spectrum, although checks were carried out for agreement with the time domain analysis. The spectra plotted at the top of the figure are in frequency and period. The blue spectrum indicated by the ‘SP’ notation is the spectral file computed by the DIWAR system and the green spectrum in both plots is calculated by doing an FFT analysis on the surface elevation record. It is clear from the plots that there is good agreement between the buoy output spectrum and the post-processed spectrum. Also plotted in grey is the equivalent Bretschneider spectrum using the significant wave height and peak period as input to the equation.

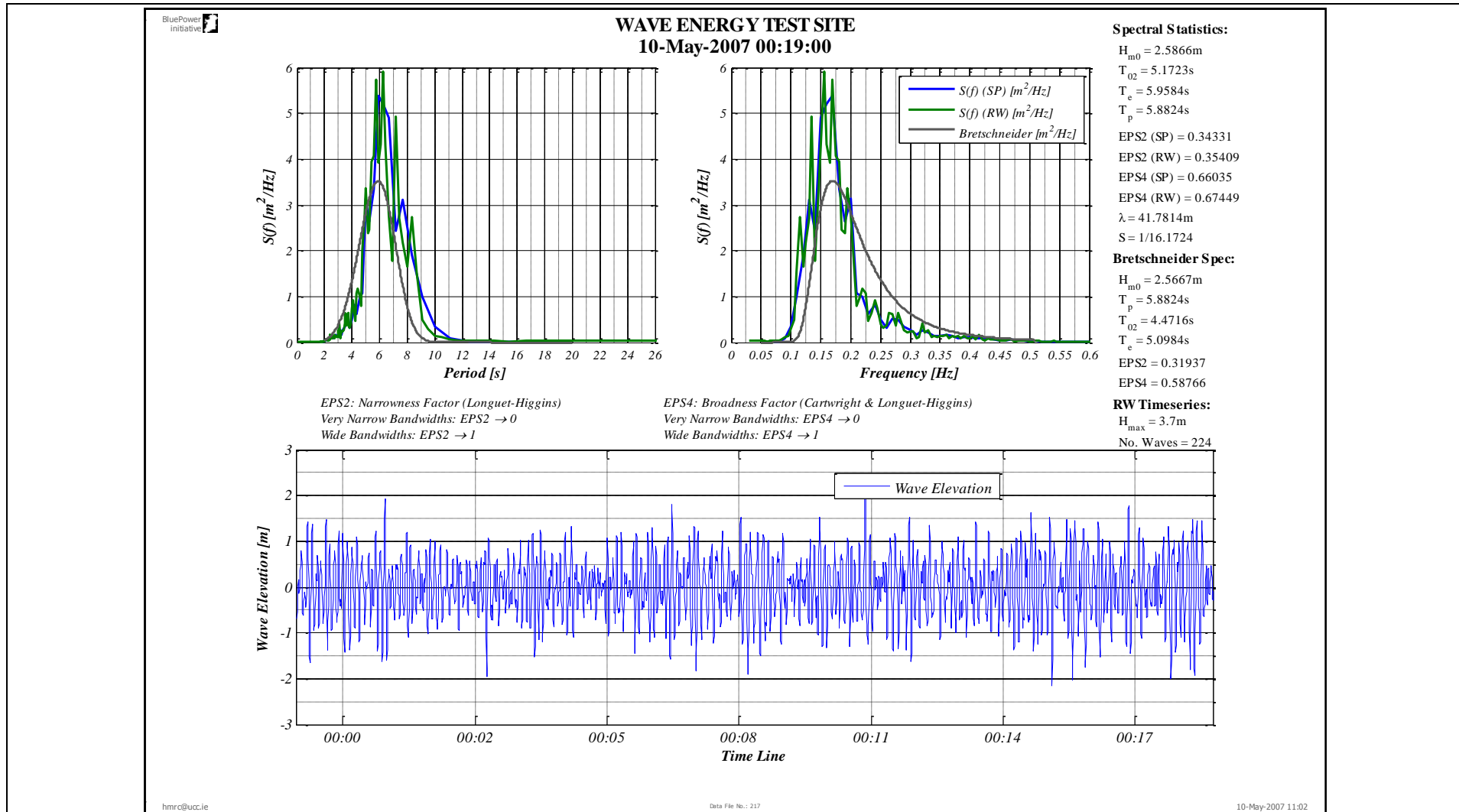


Figure 4.5. Example analysis record of surface elevation measurement.

The analysis that was carried out to produce the plot in Figure 4.5 is conducted on all sea surface records that have passed the Quality Check procedures set out in Section 2.3.3. At the end of each month, the data is compiled to produce plots of the various time and frequency domain summary statistics. Figure 4.6 shows the comparison of the calculated significant wave height,  $H_{1/3}$  and average period,  $T_z$  from the time domain analysis and,  $H_{m0}$  and  $T_{02}$  from the frequency domain analysis for the month of January 2007 for the Galway Bay site. The plots show good agreement which gives confidence in using the spectral analysis derived measures as the primary statistics and this is confirmed by the comparative plots of Figure 4.7.

Referring back to Section 3.2.1, the results from the comparative analysis below indicate a closer approximation (0.998) of the significant wave heights calculated than those reported by Longuet-Higgins (1980), Goda (1988) and Holthuijsen (2007), although this is only for a months' worth of data. The relationship between the time and frequency domain derived average periods is not as close as that for the significant wave height. With the frequency domain variable on the abscissa and the time domain variable on the ordinate axis, a small portion of the measured values are under estimated by the zero crossing method. On closer inspection of Figure 4.6, this discrepancy occurs during the very low energy period from the 22<sup>nd</sup> to the 25<sup>th</sup> day of the month, when the zero crossing algorithm may have had trouble deciphering individual waves for these low energy seas.

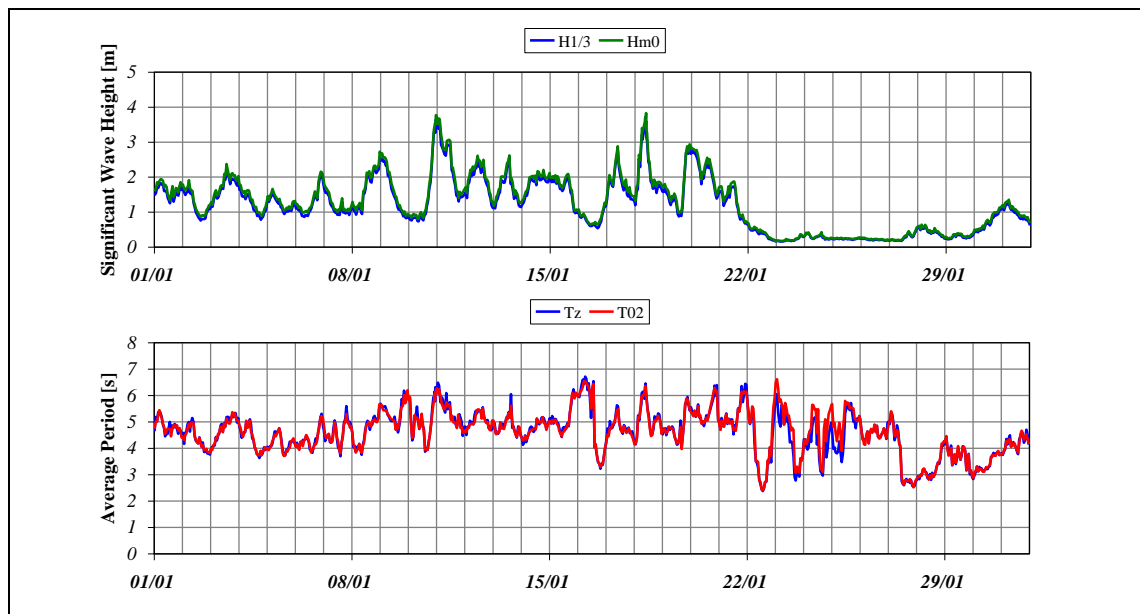


Figure 4.6. Significant wave height and average period from both time and frequency domain analysis for Galway Bay, January 2007.

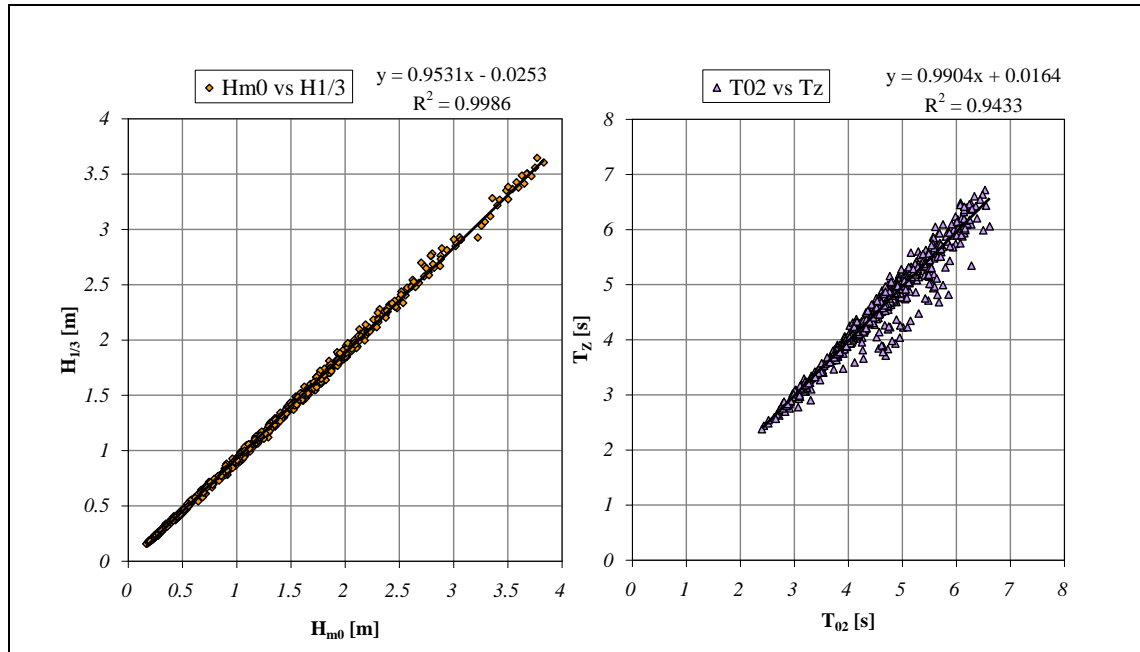


Figure 4.7. Comparison of time and frequency domain derived significant wave height for the data plotted in figure 4.6.

### 4.3. Buoy Measured Summary Statistics

One of the functions of amassing this summary data is to create the occurrence scatter plot for a specific site location. Due to the processes of wave generation and propagation, the percentage occurrence of nearly all scatter diagrams will follow the fully developed steepness line, known as the Pierson-Moskowitz line, to some extent i.e. significant steepness  $s_s = \frac{1}{20}$ .

Figure 4.8 shows the scatter diagrams of a year’s data for the test site in Galway Bay. The site specific nature of the test site is evident from these scatter plots. The semi-enclosed bay location has limited fetch in almost all directions, therefore reducing the magnitudes of the wave heights experienced. In addition, being a semi-enclosed location, waves from the North Atlantic enter the site through the channels north and south of the Aran Islands. This is characterised by the low wave height, long period sea states signifying the swell components. The scatter diagram from the exposed Loop Head site is shown in Figure 4.9 as a contrast to the benign test site. This more exposed site exhibits characteristics of a classical North Atlantic location, with sea states grouped along the fully developed line.



Scatter diagram element sizes of 0.5m by 0.5s were chosen as a reasonable size to segregate the data to form the bi-variate scatter diagram as shown in Figure 4.8. This was taken as the size being proposed by current recommendations such as the DTI Protocol (Smith and Taylor 2007). The form of this equation, when using the temporal parameter,  $T_e$ , is shown in Equation 4.1 (Pitt 2005). Also plotted on these graphs are lines of constant steepness and constant incident wave power ( $P_w$ ) on the right according to the following equation for wave power (Equation 4.2) from Section 3.2.1.1 and using the spectral ratios presented in Table 3.6.

$$P_w = 0.49H_{m0}^2 T_e \text{ [kW/m]} \tag{4.1}$$

$$P_w = 0.59H_{m0}^2 T_{02} \text{ [kW/m]} \tag{4.2}$$

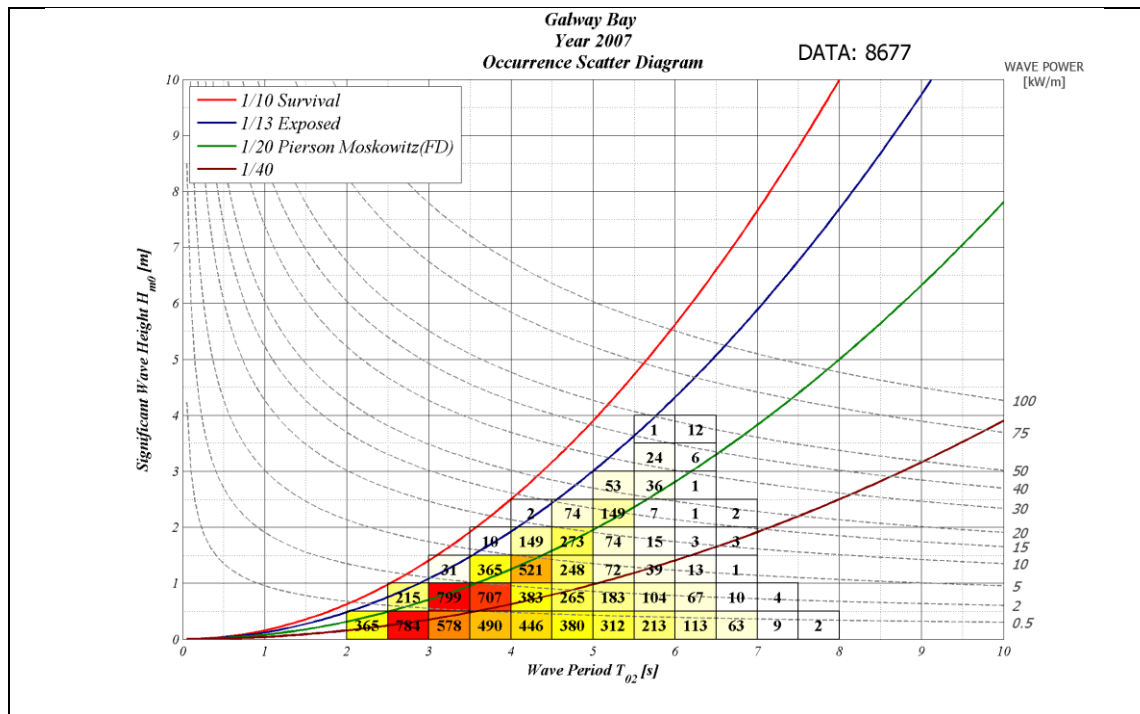


Figure 4.8. Scatter diagram for Galway Bay, 2007 with 99% data.

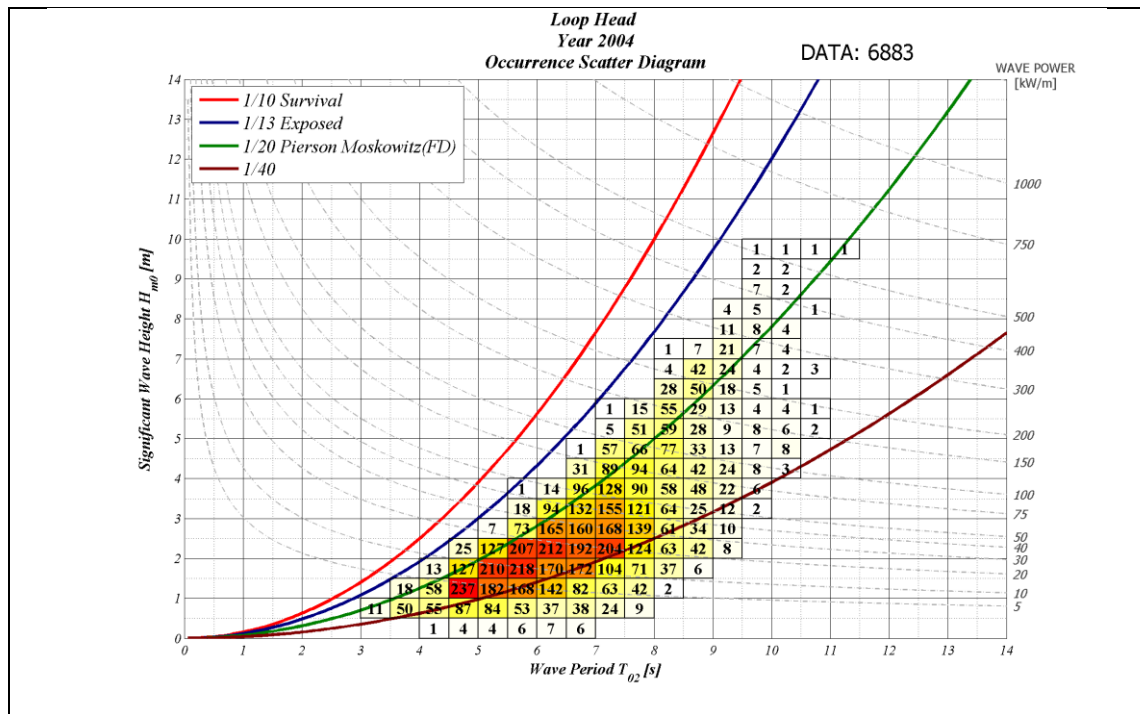


Figure 4.9. Scatter diagram for Loop Head, 2004 with 79% data.

What is interesting to note, and a phenomenon that occurs in many other site investigations is the location of the sea state of most occurrence, or the “hot spot”. The location of the hot spot and the spread of occurrences on the scatter diagram will be site specific, as shown in Figure 4.8 and 4.9. What is also site specific to some extent is the nature of the spectral shapes within each element of the scatter diagram, but this will be discussed in a later section.

Another important point to note from these scatter diagrams is the value that can be gained from collecting and analysing more than one year’s data, when possible and if available. Generally, some years will exhibit stormier conditions than others, which will influence the location of the extreme sea states of the scatter diagram. An example of this is shown in Figure 4.10, which is the scatter diagram for the previous year to Figure 4.8 at Galway Bay. This data set is much reduced with only 54% of available data recorded by the buoy due to technical difficulties experienced on site at the time. However, the data loss was due to the inoperability of the buoy during the summer months, and it is not expected that the addition of this data would have had a major influence on changing the general distribution of occurrences, but only the numerical percentages of the lower sea state elements within the scatter diagram.

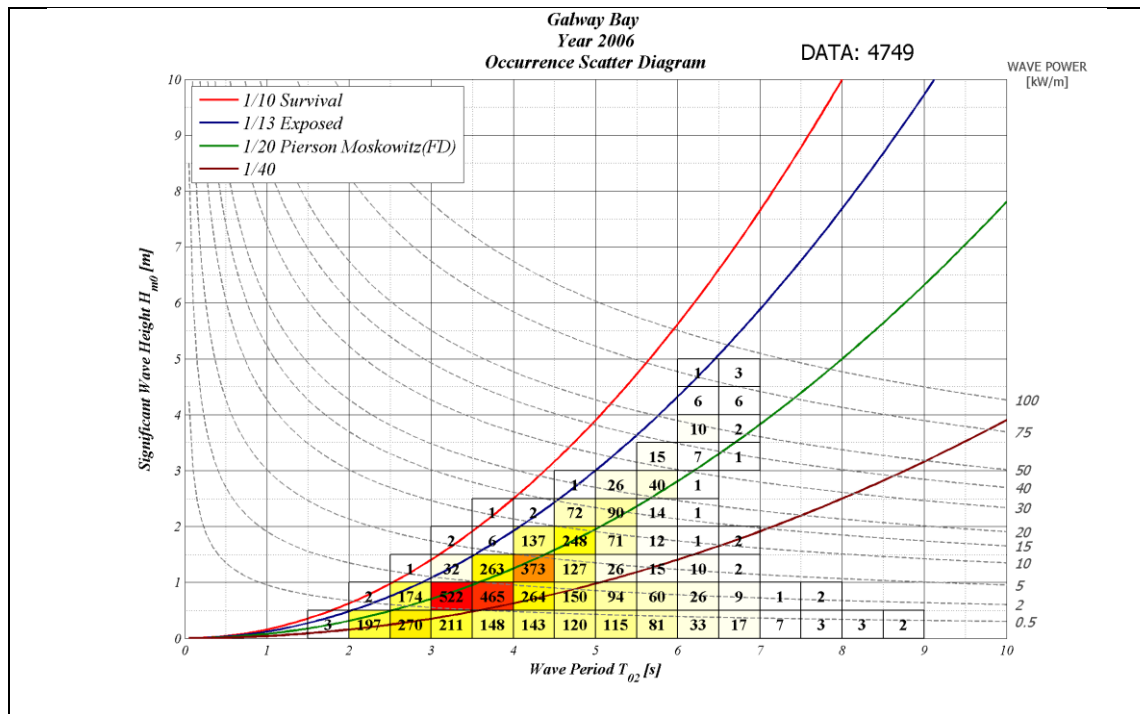


Figure 4.10. Scatter diagram for Galway Bay, 2006 with 54% data.

Of course not only is there variation from year to year, but there will also exist variation throughout the year. By analysing the Galway Bay data in more detail, box plots can be produced to investigate many of the statistics of the site in one plot. Figure 4.11 illustrates the monthly summary statistics for the test site in Galway Bay for the year 2007. This diagram depicts the variability of the significant wave height,  $H_{m0}$  for the twelve months of the year. The solid line follows the trend of the average of the statistics from month to month. The range of the hatched box is the standard deviation  $\sigma = \pm 1$  and the extremes of the vertical lines are the maximum and minimum measurement recorded within that month. This format is carried through to Figure 4.12, for the average wave period,  $T_{02}$ , and for the maximum wave height in Figure 4.13. As expected the plot of the average significant wave height follows the usual trend for northern hemisphere oceans of high sea states in the winter months falling off to calmer summer months. However, the average wave period as shown in Figure 4.12, does not change that significantly throughout the year, staying within the range of approximately one second of the average for that year. These trends were also found in data from other locations and will be discussed in a subsequent section.

Figure 4.13 gives an indication of the survival issues to be considered when deploying a device at the intermediate test site in Galway Bay. The maximum wave height statistics are derived from the height from crest to trough of the largest wave in the surface

elevation data record, defined by the zero down crossing identification method. A deployed device will have to experience wave heights in the region of at least 6m in the winter months, equivalent to approximately 20m waves at full-scale that are not unexpected in storm events in the open ocean.

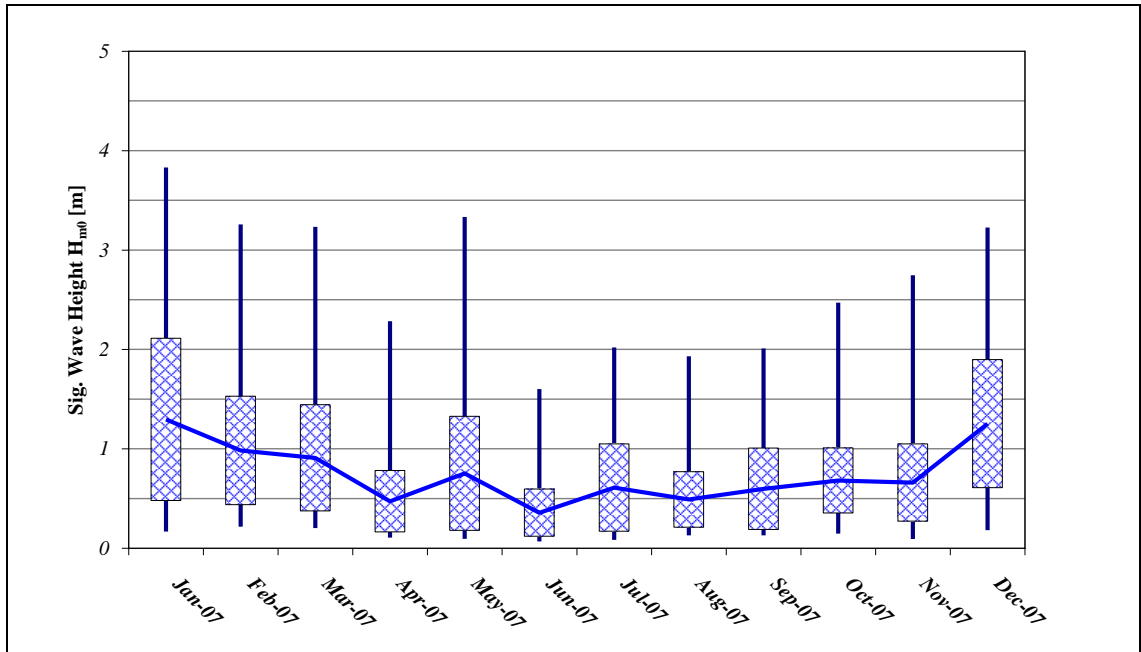


Figure 4.11. Galway Bay  $H_s$  for year 2007.

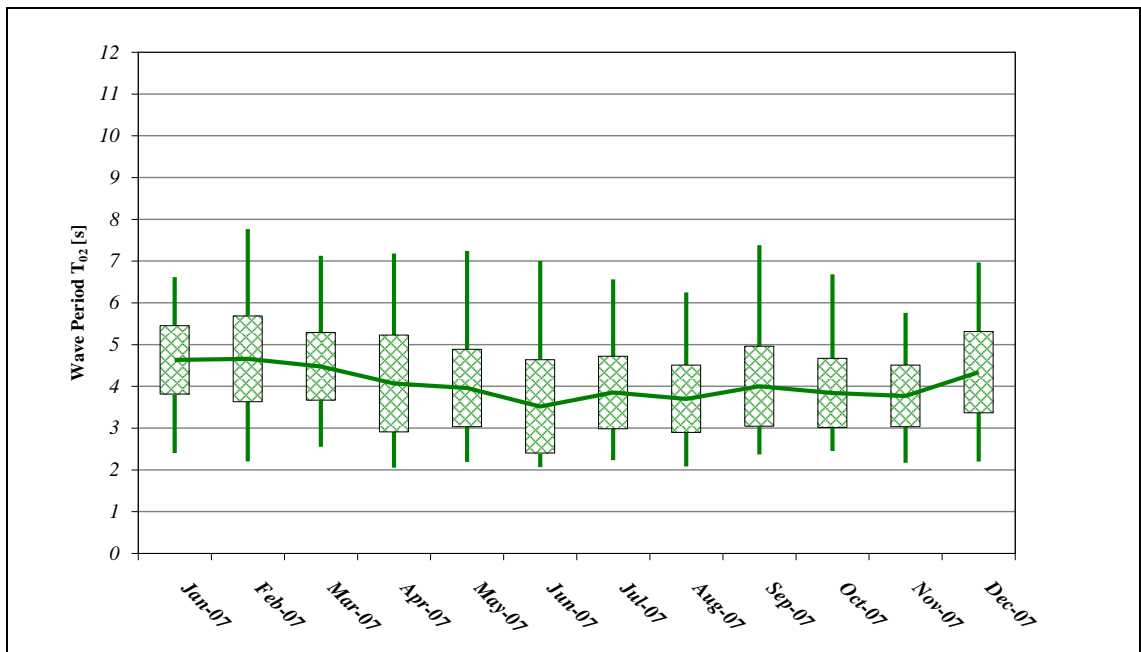


Figure 4.12. Galway Bay  $T_z$  for year 2007.

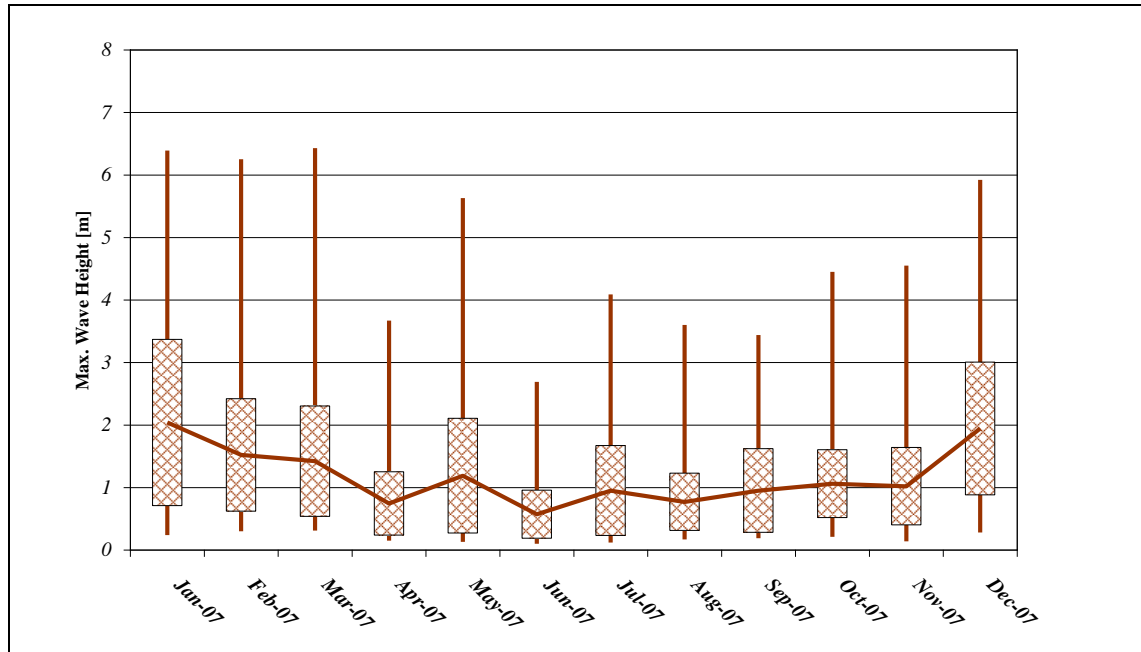


Figure 4.13. Galway Bay  $H_{max}$  for year 2007.

#### 4.3.1. Temporal Variations

During the development path of an ocean energy convertor, some tank testing of the device concept will have taken place at various scales. The common approach taken during this concept appraisal and performance verification stage of technology development is the testing of the device in irregular sea states. These panchromatic seas will be generated from classical spectral distributions, from which device reactions and power production will be estimated. In real sea conditions, however, the average of the measured sea state conforms to these traditional spectra only, and not necessarily to the individual half hourly recorded incident sea spectra. However, in order to develop wave energy in a cost effective manner, there are limitations in terms of time and budget for the testing of these devices in wave basins, therefore the classical spectra are an accepted method to quantify device performance. It also allows for consistency in testing when variables have been changed or when comparison of difference devices is investigated.

Site assessment for device deployment can begin with looking at the available wave data that is available for the region in question. Each method has its advantages and disadvantages. This can include data from wave models such as SWAN or WAM, satellite data, or meteorological buoys that have been in situ over a number of years. The variability of a chosen site can further be broken down into the following divisions:

- year to year,

- season to season,
- month to month,
- day to day,
- hour to hour,
- location to location.

Shown in Figure 1.6 is an idealised map of Ireland and the North Atlantic with ODAS buoy locations. For site investigation work, some of these buoys may seem too remote, but the data from these buoys give a quick and clear indication of the prevailing conditions in the area, as they mostly only give the summary statistics recorded over the hour, not detailed frequency spectra.

#### *4.3.1.1. Monthly Average Trend*

The data supplied by the various buoys off the coast of Ireland as shown in Figure 1.6 is used to assess the variation in significant wave height and average period as a measure of the variability of summary statistics throughout a given year. Plots are produced by normalising the summary data with the lowest month average of the year, which for the northern hemisphere is generally in the summer months. Shown in Figure 4.14 is the variation of the monthly average of the significant wave height to the lowest monthly average for that year. The location of the buoy and the year can be seen in the legend above the graph. It is interesting to note that the average monthly significant wave height,  $H_s$  in winter can be up to four times the magnitude of the minimum summer monthly average. When the average zero crossing period is considered, it is evident from the  $T_z$  ratio which is plotted in Figure 4.15, that there is little change from summer to winter in the monthly averages, both in terms of site-by-site and year by year.

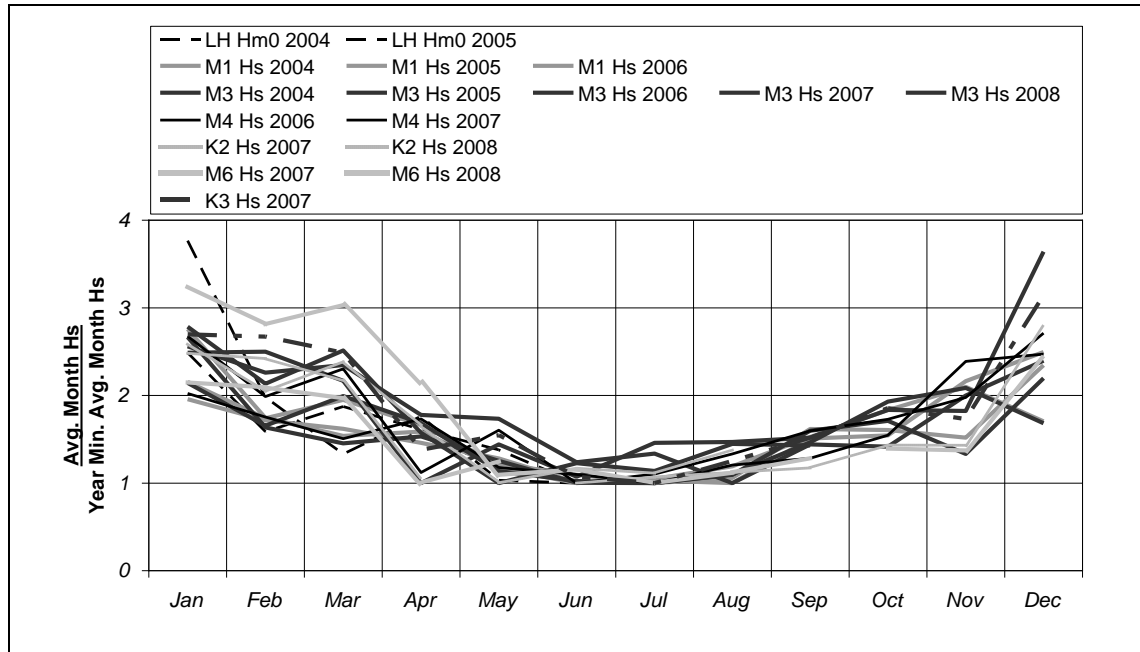


Figure 4.14. Average significant wave height ratio for offshore buoys.

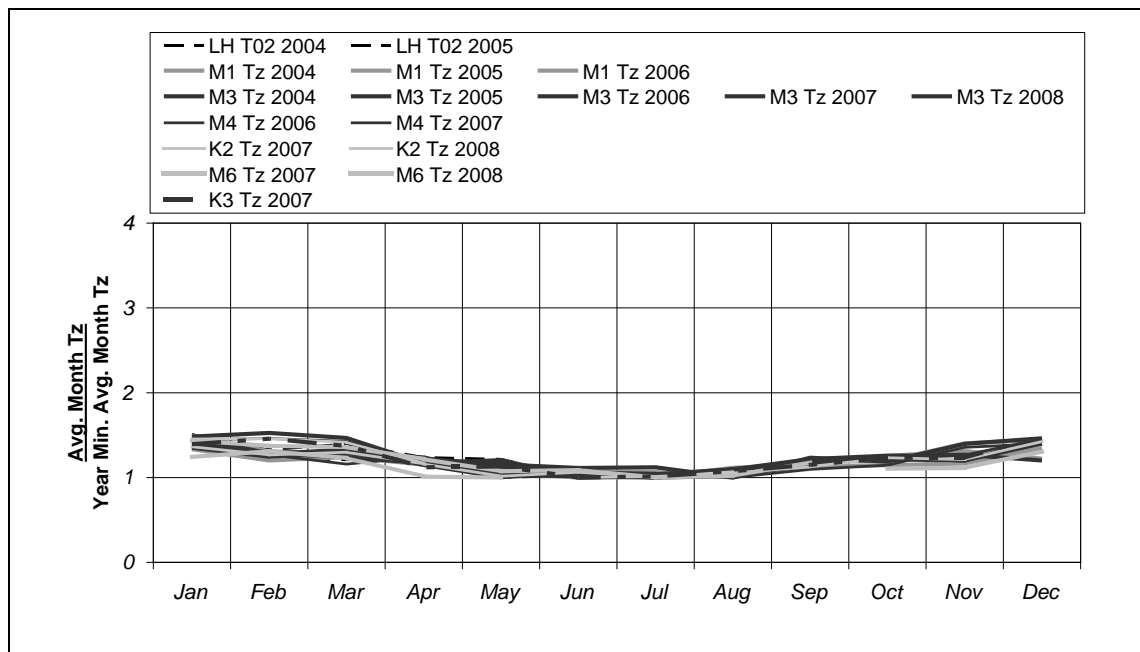


Figure 4.15. Average wave period ratio for offshore buoys.

This indicates that the significant wave height is more variable from year to year and site to site, where as in terms of wave period, which the device will be matched to for a specific site, this quantity does not vary significantly throughout the year. However, it should be noted that these plots only show the variation in the average statistic over the year and not the actual average period or significant wave height, which may be site specific. To assess the site-specific implications from the summary statistics, a more detailed assessment of the site is necessary and the production of a scatter diagram is

required. This will indicate the sea state of most occurrence along with any extremes, or deviations from the norm.

#### 4.3.1.2. Winter/Spring Average Spectrum

The first portion of the Loop Head data analysed was six months of measured surface elevation over the winter/spring period from December 2003 to the end of May 2004. The winter/spring seasons are chosen for investigation as it is expected that in the northern hemisphere this six month period will be the primary period of electrical production from wave energy devices. The initial data depository contained all data files recorded, which included those extra measurements when the significant wave height exceeded a set threshold level and continuous measurement was instigated automatically. If these additional files were included when calculating the occurrence of the scatter diagram, a bias would exist toward the storm seas. To preclude this effect of over measurement, only files that were recorded in the first twenty minutes of each hour are incorporated into the data set for this study.

Over 97% of all possible hourly available data is represented in the scatter plot for the six months of measurement from December 2003 to May 2004. Figure 4.16 shows that the occurrences of sea states centre at a significant wave height,  $H_{m0} = 2m (\pm 0.5m)$  and zero crossing period,  $T_{02} = 6s (\pm 0.5s)$ . The average of all the spectra that occurred in this six-month period is plotted as the blue line with circles in Figure 4.17. This average spectrum is derived by calculating the mean of the spectral ordinates for all the spectra and plotting the result against frequency. There is now the option of fitting an empirical spectral profile to this averaged data set. The Bretschneider spectrum is used due to its flexibility and ease of use with only two input parameters, the total variance and the peak frequency. Using this method an equivalent Bretschneider spectrum is plotted, with the same summary statistics as those derived from the average spectrum. However, different parameters are available to fit the Bretschneider spectrum to the average spectrum.



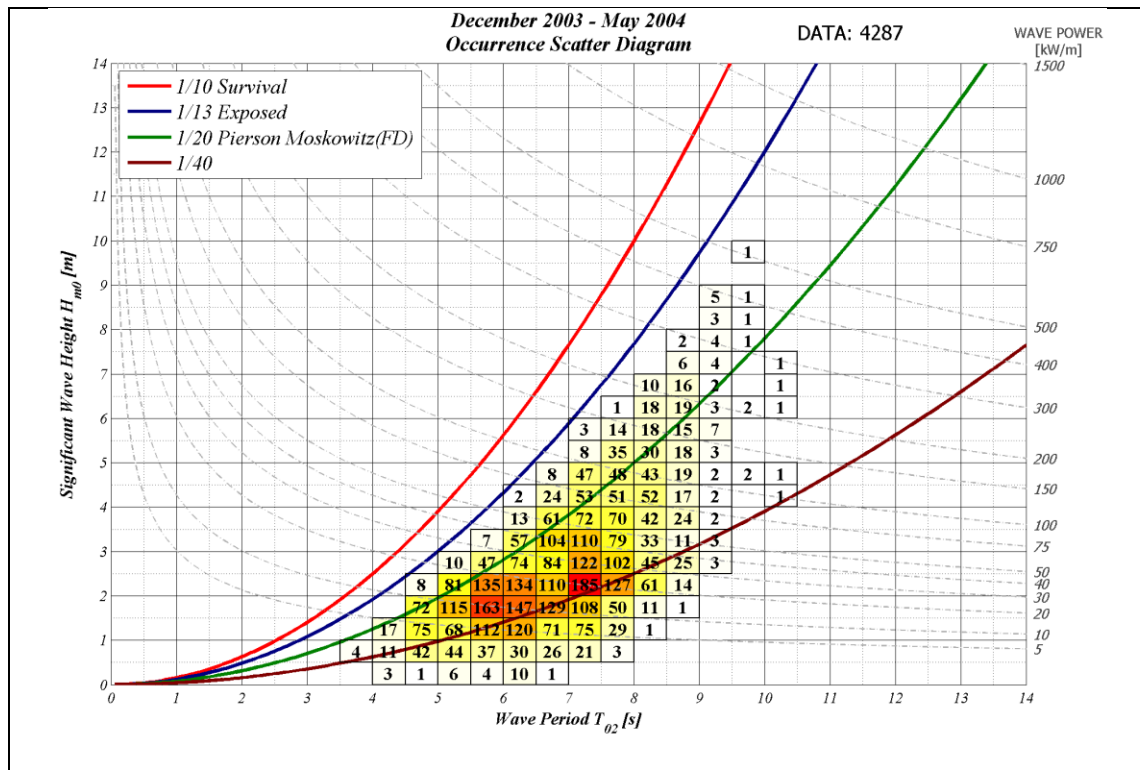


Figure 4.16. Scatter diagram of the combined winter and spring seasons of 2003-2004 for Loop Head.

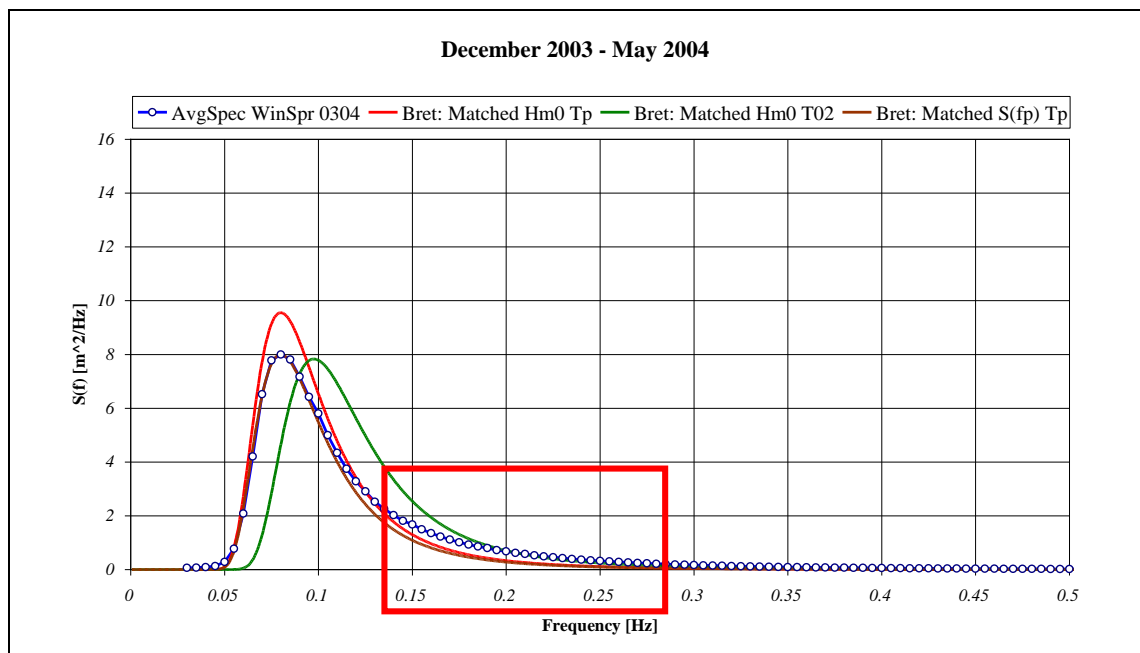


Figure 4.17. Average spectrum and Bretschneider fit of the combined winter and spring seasons of 2003-2004 for Loop Head.

Firstly, the total variance of the average spectrum,  $m_0$  represented by the significant wave height,  $H_{m0}$  and the peak period,  $T_p$  is used as inputs to the Bretschneider equation (*Bret: Matched  $H_{m0} T_p$* ). This results in a close approximation to the average spectrum but with a larger magnitude peak.

The Bretschneider spectrum maintains a constant relationship between the periods, such as the ratio between the average period,  $T_{02}$  and the peak period,  $T_p$ , which is used as the second method of fitting to the average spectrum ( $T_p/T_{02} = 1.406$ ). In this case, the total variance,  $m_0$  and the average period,  $T_{02}$  of the average spectrum are used as the input parameters to the Bretschneider equation. This results in a shift of the fitted empirical spectrum to higher frequencies, clearly shown in Figure 4.17 (*Bret: Matched  $H_{m0} T_{02}$* ). This shift is due to the use of  $T_{02}$ , which incorporates the zeroth and second moments in its calculation. The second moment,  $m_2$ , involves a frequency term raised to the power of two. The average spectrum has a relatively high energy content at frequencies higher than the peak frequency ( $f > f_p$ ), in the area indicated by the box and so this results in a shift of the spectrum.

Finally, as an alternative to the fitting of the empirical spectrum by using summary statistics, the magnitude of the maximum ordinate of the average spectrum,  $S(f_p)$ , was used to fit the Bretschneider spectrum (*Bret: Matched  $S(f_p) T_p$* ). This fitted spectrum will be similar to the previously fitted Bretschneider (*Bret: Matched  $H_{m0} T_p$* ) but to achieve the same  $S(f_p)$  as the average spectrum, the overall variance has to be reduced. The effect of this is also evident in the area of the spectral plots identified by the box in Figure 4.17.

Three methods of fitting the empirical Bretschneider profile to the averaged measured spectra are presented above and plotted. The initial method of using the total variance,  $m_0$  and the peak period,  $T_p$  will continue to be used in further examples in this document, as it retains the overall energy of the target spectrum while its profile is a closer approximation to the measured spectrum.

The same analysis methodology is performed on the second six-month data set of the measurements from the Arch Point location for the period of December 2004 to May 2005. In this instance, approximately 96% of the possible hourly data is available. The scatter diagram for this period is shown in Figure 4.18 and the average spectrum for this period is plotted in Figure 4.19. Figure 4.18 shows that this scatter diagram has a similarly located concentration of occurrences as the previous six months of data shown in Figure 4.16.

The Bretschneider profiles in Figure 4.19 are plotted using the same methods as applied to Figure 4.17. This average spectrum shows the same high frequency energy content characteristic, highlighted by the box as in the previous bi-seasonal average spectrum in Figure 4.17.

From the plots of Figure 4.17 and 4.19, it is evident that the closest fit to the averaged spectrum is the Bretschneider profile defined by the total variance,  $m_0$  and the peak period,  $T_p$  as it maintains the overall energy of the target spectrum and the peaks coincide at the same frequency. This method will be used in further spectral comparisons.

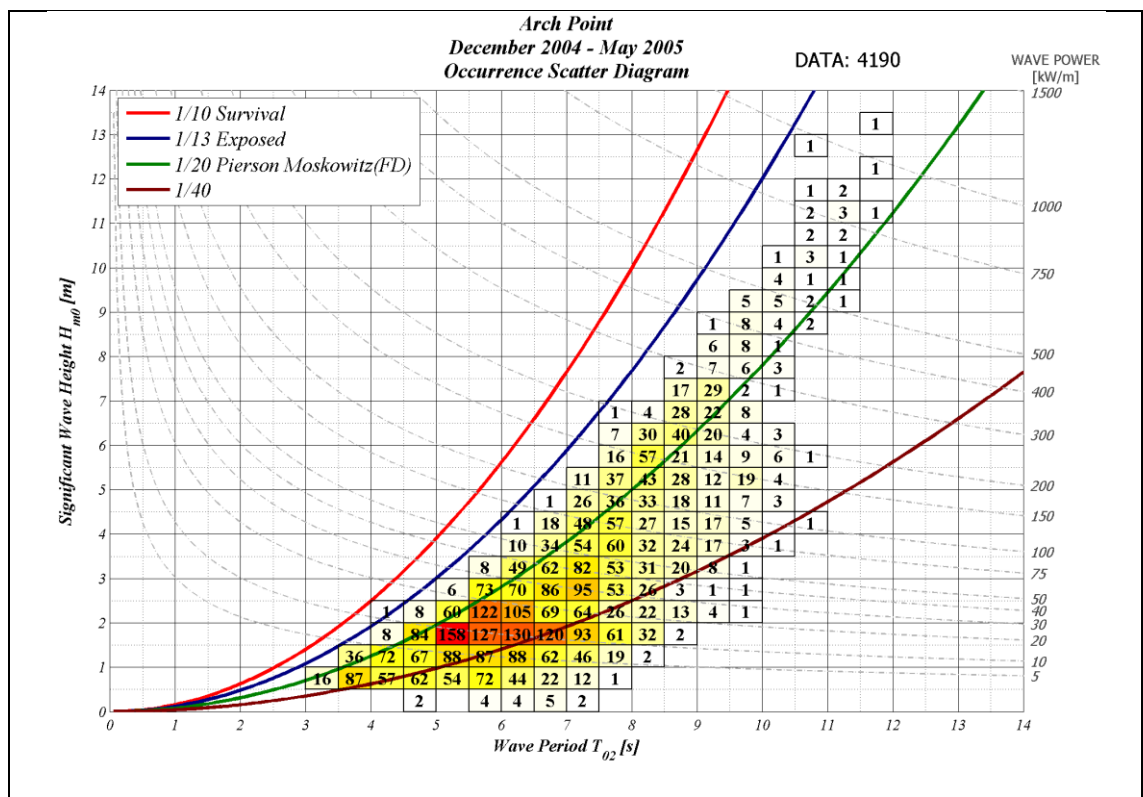


Figure 4.18. Scatter diagram for the period December 2004 to May 2005 at the Loop Head location.

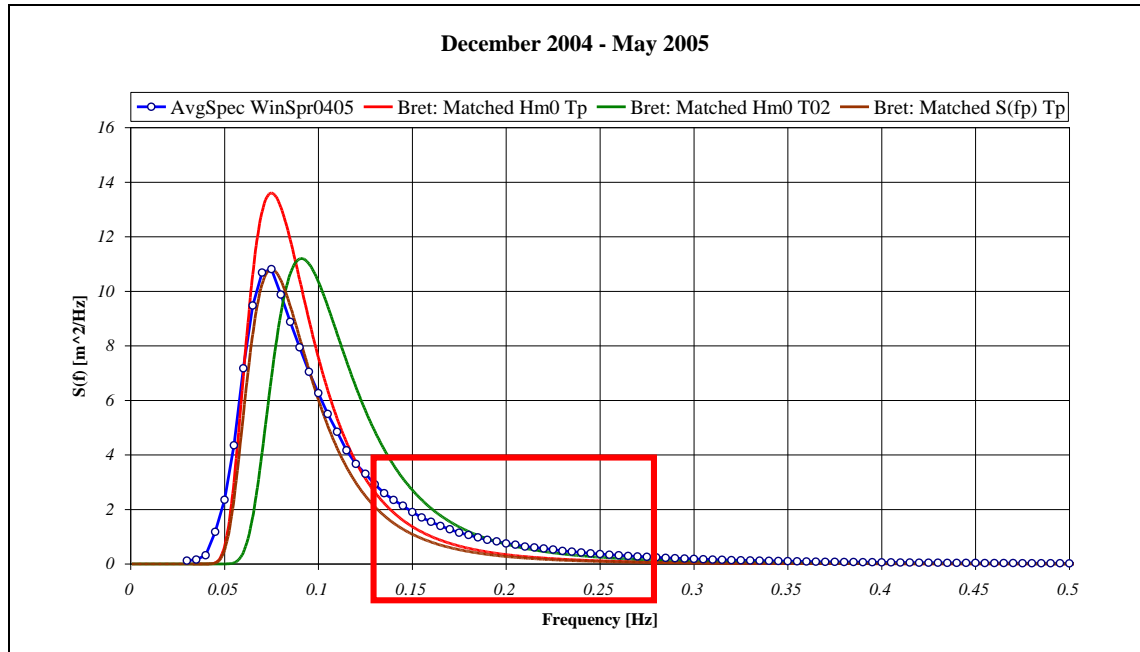


Figure 4.19. Average spectrum and Bretschneider fit of the combined winter and spring seasons of 2004-2005 for Loop Head.

The inherent variability of ocean waves is clearly visible when the Figures of 4.16 and 4.18 are compared as larger sea states are experienced in the winter/spring seasons of 2004/2005. This results in the average spectrum of this data set being larger, as shown in Figure 4.19, the summary statistics of which are shown in Table 4.1.

Data Set	$H_{m0}$	$T_{02}$	$T_e$	$T_p$	Wave Power ( $T_e$ )	Wave Power ( $T_{02}$ )	% Diff $\frac{P(T_e)}{P(T_{02})}$
	[m]	[s]			[kW/m]		%
Dec'03-May'04	2.92	7.30	9.96	12.50	41.61	36.66	11.9
<i>Winter</i> Dec'03-Feb'04	3.08	7.36	10.03	13.33	46.62	41.12	11.8
<i>Spring</i> Mar'04-May'04	2.75	7.22	9.87	11.76	36.57	32.16	12.1
Dec'04-May'05	3.37	7.83	11.00	13.33	61.21	52.38	14.4
<i>Winter</i> Dec'04-Feb'05	4.21	8.30	11.50	14.28	99.88	86.65	13.2
<i>Spring</i> Mar'05-May'05	2.15	6.49	8.99	11.11	20.36	17.67	13.2

Table 4.1. Summary statistics of average spectra for Loop Head location.

The summary statistics that are presented in Table 4.1 are calculated from the spectral moments of the respective averaged spectra of the seasonal data sets, using the equations presented in Table 3.1. The variability of the seasons is evident from the variation of significant wave height. The extreme winter season of 2004/05 is followed by a low spring season, with the winter and spring of 2003/04 positioned between these in terms of magnitude. There is no large variation of the periods of these average spectra.

The primary wave power equation is derived using the energy period,  $T_e$ . The secondary wave power equation, which uses the average period,  $T_{02}$ , has a coefficient based on the ratio of these periods when using the Bretschneider empirical equation. The period statistics derived from the average spectra do not conform to the Bretschneider period ratios, therefore there is an inequality in the wave power calculated using both methods. The percentage difference of these figures is also presented in Table 4.1, which shows that in each case, the wave power calculated from the average period,  $T_{02}$  is on average underestimated by 13%.

#### 4.3.1.3. Seasonal Average Spectra

Four individual seasons make up the two data sets and the summary statistics of the average wave spectrum of each of these seasons are also noted in Table 4.1. To understand the variability of the variance density distribution of these average spectra, a method was required to plot them simultaneously. This was achieved by producing a non-dimensional plot of the spectra, both in terms of the variance density and the frequency range. Figure 4.20 is a log-log graph showing the non-dimensional plots of the average spectra for all four seasons present in the two data sets and the combined two winter/spring seasons. This is not a plot of the variance density distribution, but rather the ratio of each frequency ordinate to the maximum ordinate. The thick grey line is the representative Bretschneider spectrum for all the various input variance densities and peak frequencies. The abscissa represents the non-dimensional frequency where the harmonics of the spectrum are divided by the peak frequency. The ordinate axis as described above is the harmonics non-dimensional variance density of the spectrum divided by the maximum value.

When the Bretschneider spectrum is plotted in this way, the non-dimensional Bretschneider profile is the same irrespective of the input variance or peak frequency, as shown in Figure 4.20. However, this type of plot is only useful to compare the average

measured spectrum with the equivalent Bretschneider since inter comparison of the average spectra is not so clear when the ratios between the peaks is not apparent. The actual average spectra and respective Bretschneider fit are shown in Figure 4.21.

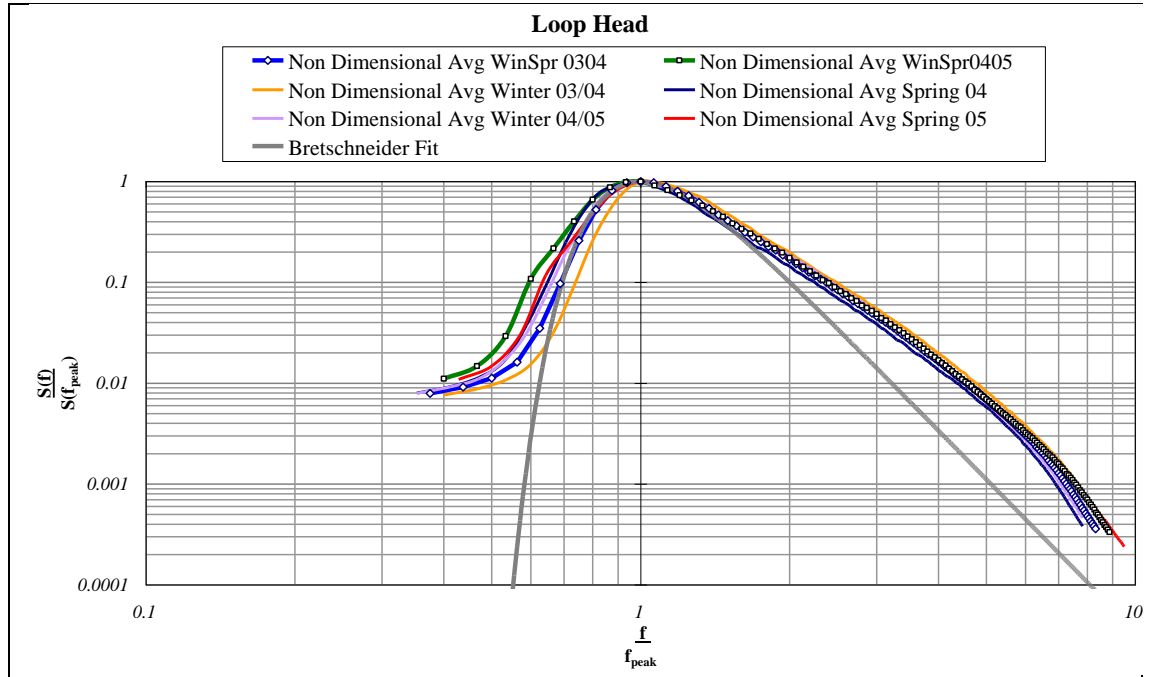


Figure 4.20. Comparison of non-dimensional spectra.

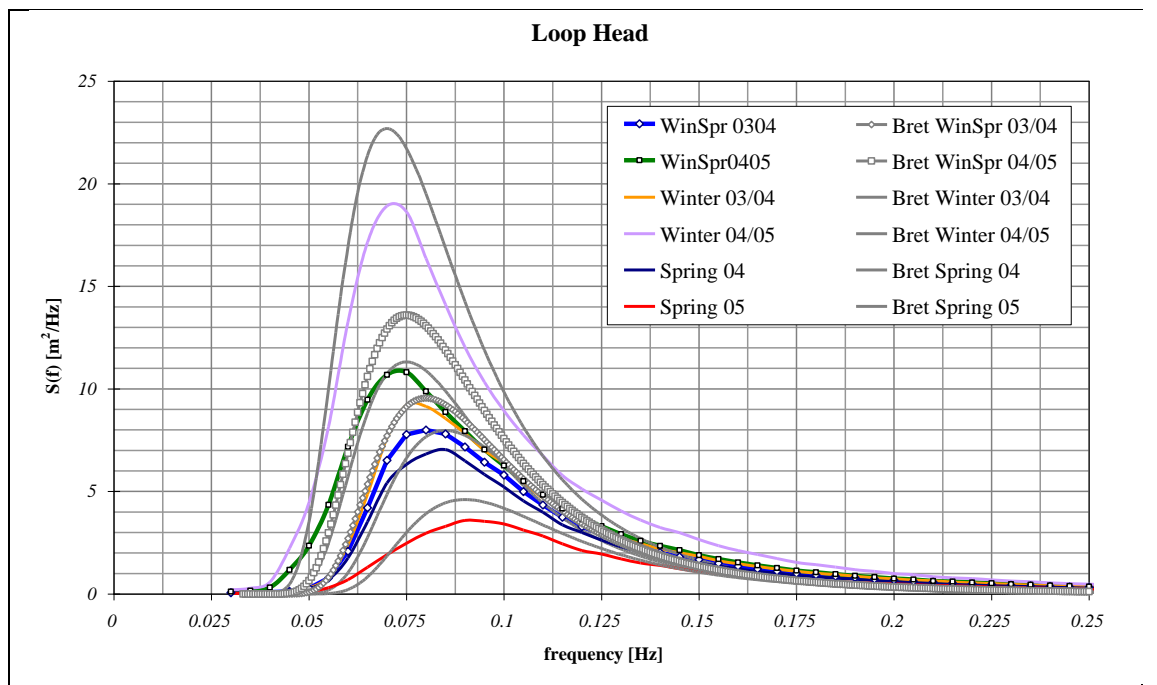


Figure 4.21. Comparison of average spectra and Bretschneider fit.

Examination of Figure 4.20 leads to the following conclusions. This plot indicates that the ratio of the spectrum peak to the ordinates at frequencies higher than the peak

frequency ( $f > f_p$ ) is larger than for a Bretschneider spectrum, and that this ratio is similar for all the seasonal averaged spectra depicted in Figure 4.20. However, the same is not the case at frequencies ( $f < f_p$ ). In this region of Figure 4.20, there appears a greater variation in the ratio of spectral ordinate to peak ordinate which may indicate a greater variability in the contribution of long period components to the spectra considered here.

The seasonally averaged spectra follow the respective Bretschneider profiles reasonably well but over-estimation of the energy around the peak by the Bretschneider equation in comparison to the averaged spectra is balanced out by the underestimation at frequencies greater than 0.125Hz. The measured spectra and their respective Bretschneider equivalent contain the same energy, depicted by the area under the plot lines in these graphs. It appears that the averaged spectra from the measured data is wider than the empirical counterpart.

By breaking down the time scales for further analysis, a greater variation in the distribution of energy in the spectrum becomes apparent. The time scales are separated as follows and ensemble averages of the measured spectra are compared to the classical shape:

- 6 months (Winter & Spring)
- 3 months (Winter)
- 1 month (January)
- 1 Week
- 1 Day

#### 4.3.1.4. Monthly, Weekly & Daily Spectral Averages

To assess the variance density distribution of the average spectra more clearly, they are plotted together. Figure 4.22 shows the average spectra and the fitted Bretschneider for the seasonal and monthly time scales. Figure 4.23 is the same plot but now with non-dimensionalised axes. In general, it can be said that the resultant average spectra are closely related to the Bretschneider equation, and that there is very little variation in the ratios of the spectral ordinate to spectral peak at either side of the peak frequency.

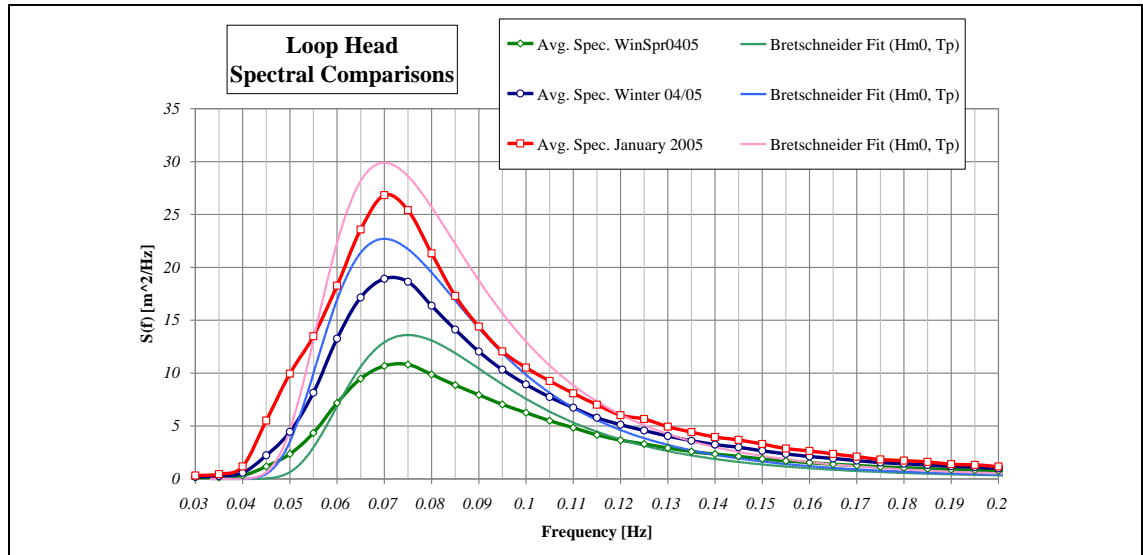


Figure 4.22. Average spectra and Bretschneider fit for seasons and month time scales.

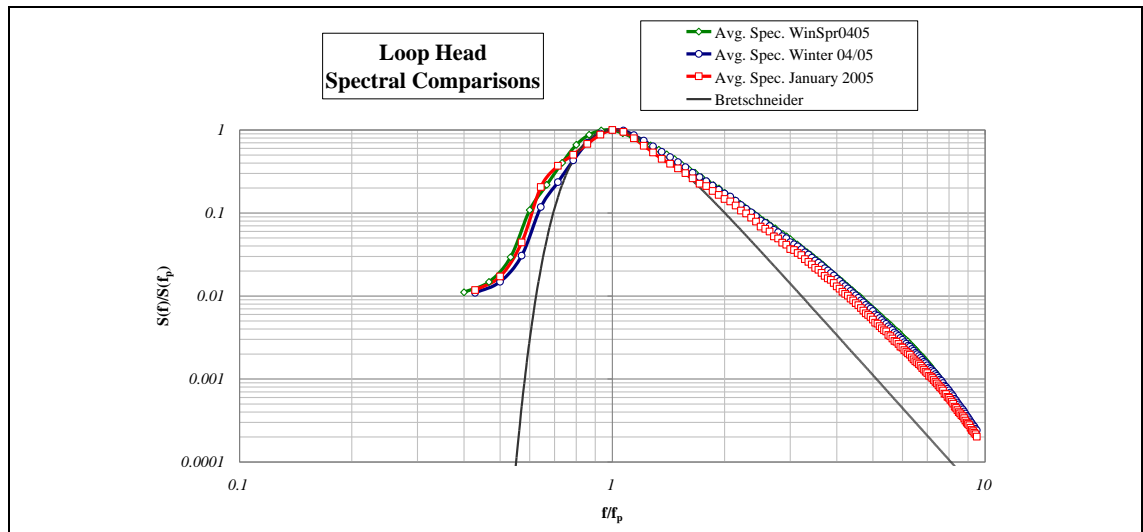


Figure 4.23. Non-dimensional averaged spectra and Bretschneider fits of spectra shown in Figure 4.22.

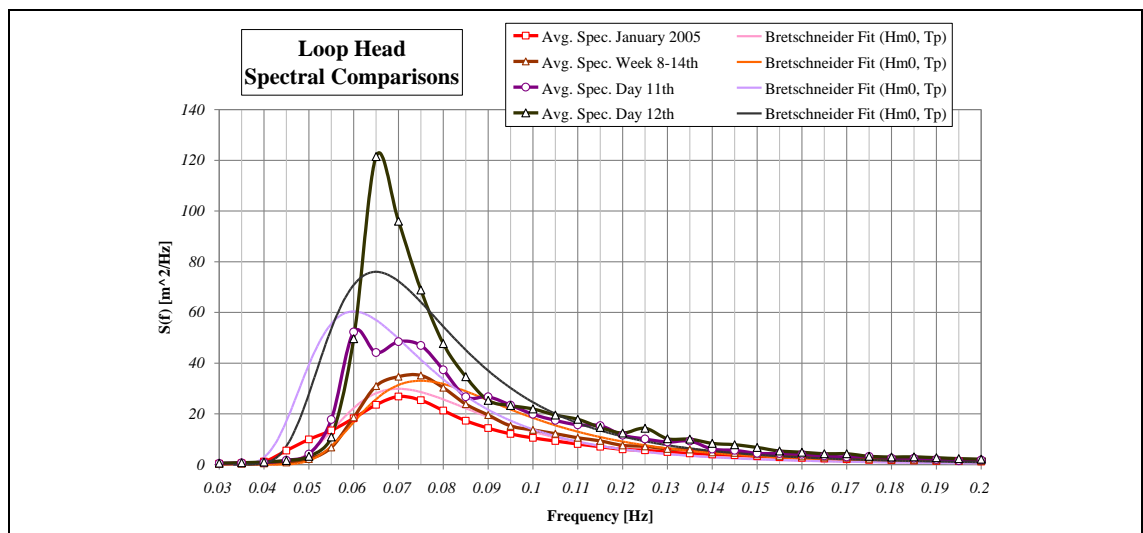


Figure 4.24. Average spectra and Bretschneider fit for month to day time scales.



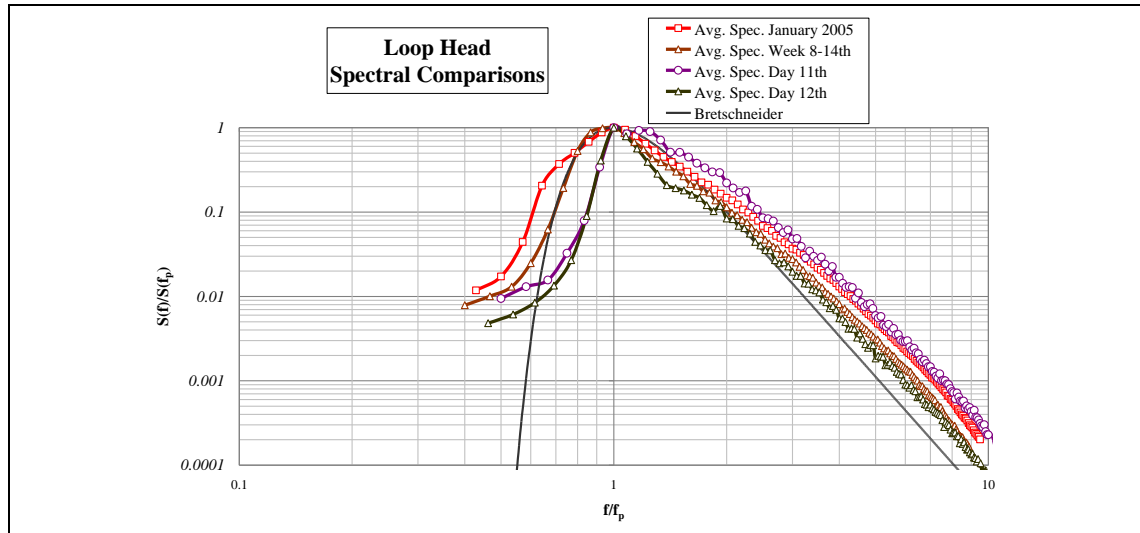


Figure 4.25. Non-dimensional averaged spectra and Bretschneider fits of spectra shown in Figure 4.24.

The next time duration determines the average spectra for one week and for two individual days within the selected month. The average spectra of these particular data sets are shown in Figure 4.24 and in non-dimensional form in Figure 4.25. It is clear from the plots that there is a greater variation in the average spectra at these time scales. Shown previously in Figure 4.21, the monthly average closely resembles a Bretschneider spectrum, however the approximation to a Bretschneider spectrum is lost as the time averaging scales are reduced. Even for two consecutive days, there is a marked difference in the overall spectral shape of the average of the hourly measured spectra. This could have important consequences in the rate of measurement and reporting at a potential deployment site.

4.3.1.5. Daily & Hourly Spectral Averages

To better understand the variation in the two daily averaged spectra shown in Figure 4.24, the individual hourly spectra, daily average spectra and respective Bretschneider fits are plotted in Figure 4.26. The spectra of Day 1 (11<sup>th</sup> January 2005) are shown in Figure 4.26a, while the spectra of Day 2 (12<sup>th</sup> January 2005) are shown in Figure 4.26b. The average spectra over the 24 hour period is plotted with its respective Bretschneider equivalent, along with the hourly individual spectra that were recorded on the respective day. The black lines are not spectra but the bounds of the maximum and minimum spectral ordinate magnitudes.

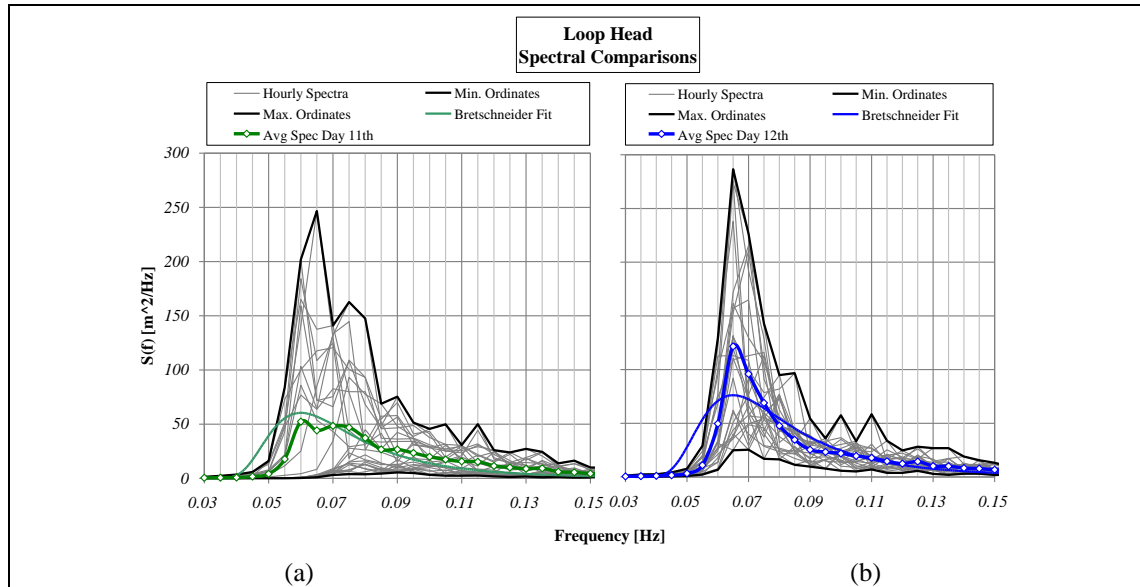


Figure 4.26. Hourly and average spectra with Bretschneider fit for two consecutive days.

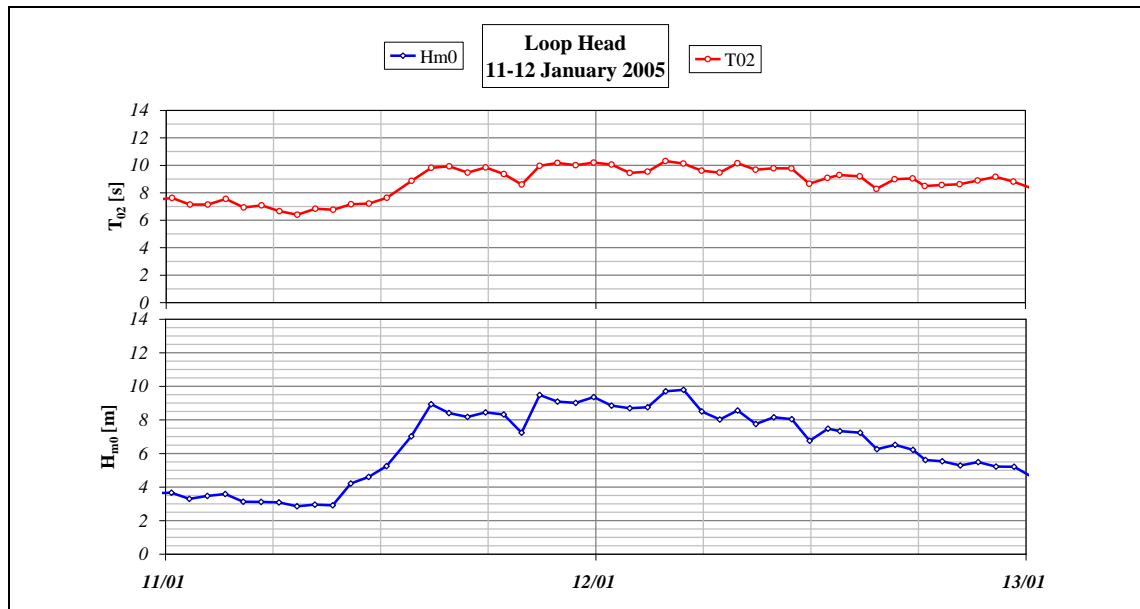


Figure 4.27. Significant wave height,  $H_{m0}$ , and average wave period,  $T_{02}$  for the two consecutive days selected.

The consequent summary statistics of significant wave height,  $H_{m0}$  and average wave period,  $T_{02}$  for these selected consecutive days are shown in Figure 4.27 and it is apparent from this plot the cause of the difference in average spectral shape for the two days. Day 1 has a step change as the significant wave height doubles from below 4m to over 8m. Figure 4.28 is a plot of the wind speed from a meteorological station positioned at Shannon Airport, the closest met station to the site of interest (59km). This shows an introduction into the measurement area of a generating wind in the second half of Day 1, resulting in two distinctive forms of spectra occurring. However, the declining wind

speeds during Day 2 correspond to the wave height levels as the storm abates, leading to similar forms of spectral shape occurring, and therefore a more narrow average spectrum.

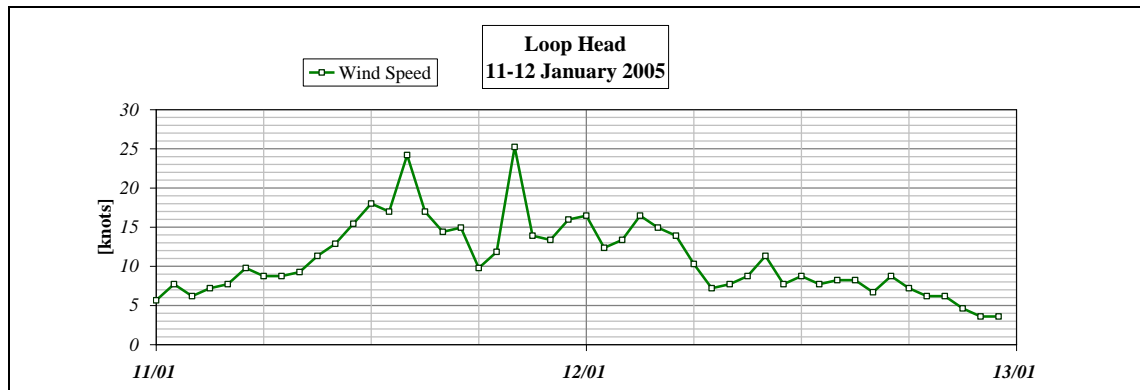


Figure 4.28. Wind speed measured at Shannon land station close to Loop Head.

#### 4.4. Storm Growth & Decay

Having looked at the variation of the spectral shape in terms of time scales, the variation of spectral shape due to changing summary statistics is now investigated. This is conducted by assessing the average spectral shape of all the spectra that reside within certain elements of a scatter diagram. In this instance the size of the scatter diagram elements used are 1m by 1s element sized bins, to increase the number of spectra residing in a scatter diagram component. To investigate this phenomenon, data from the exposed Loop Head site was used.

To assess the change in spectral shape as a storm passes the location of a surface following buoy, a storm event that occurred at the Galway Bay wave energy test site is investigated. Selected spectra, preceding, during and following the storm are compared to the empirical spectral forms.

##### 4.4.1. Iso-Height and Iso-Period

Firstly, the change in shape of the average spectrum as the wave height increases but the period remains constant is investigated. A similar investigation for scatter diagram elements of constant wave height and increasing period is conducted. This is complimented by examining the change in spectral shape along the Pierson-Moskowitz steepness line, a contour in the scatter diagram with constant significant steepness,  $S_s =$

$\frac{1}{20}$ , which is said to indicate the point where sea states are fully developed, as would be experienced during the growth of sea states during a storm event.

Figure 4.29 below shows the bi-variate scatter diagram for the month of December 2003 from Loop Head, which consisted of 100% data coverage for the month. The scatter elements of iso-height with a range of  $2m \leq H_{m0} < 3m$  and iso-period of  $7s \leq T_{02} < 8s$  are indicated by the bounding boxes. These were selected as they both incorporate the element of most occurrences ( $H_{m0}: 2 - 3m, T_{02}: 7 - 8s$ ).

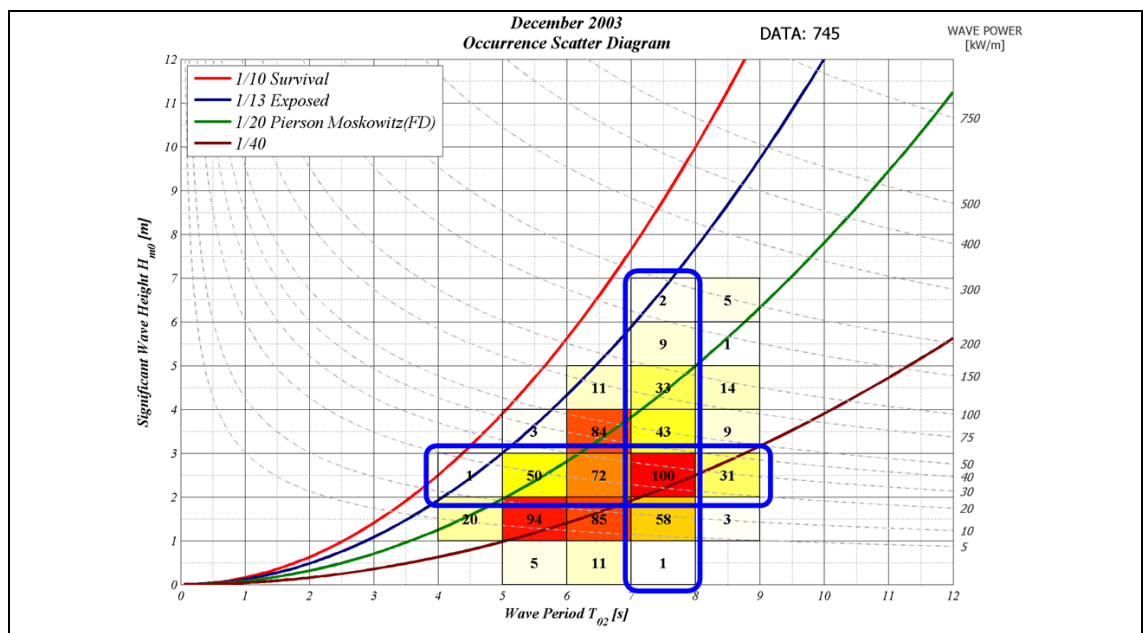


**Figure 4.29. December 2003 scatter diagram for Loop Head.**

Figure 4.30 shows the average spectra and relevant Bretschneider equivalent for the five elements that are contained within the iso-height band of the scatter diagram of Figure 4.29. The Bretschneider fit was calculated from the significant wave height and average period of the resultant average spectrum and not the median points of the scatter diagram elements. The plots are truncated at a frequency of 0.3Hz for convenience as the spectral ordinates that reside from 0.3Hz to the upper frequency limit contain very little energy. The goodness of fit of each of the empirical spectra are clearly visible by inspection.

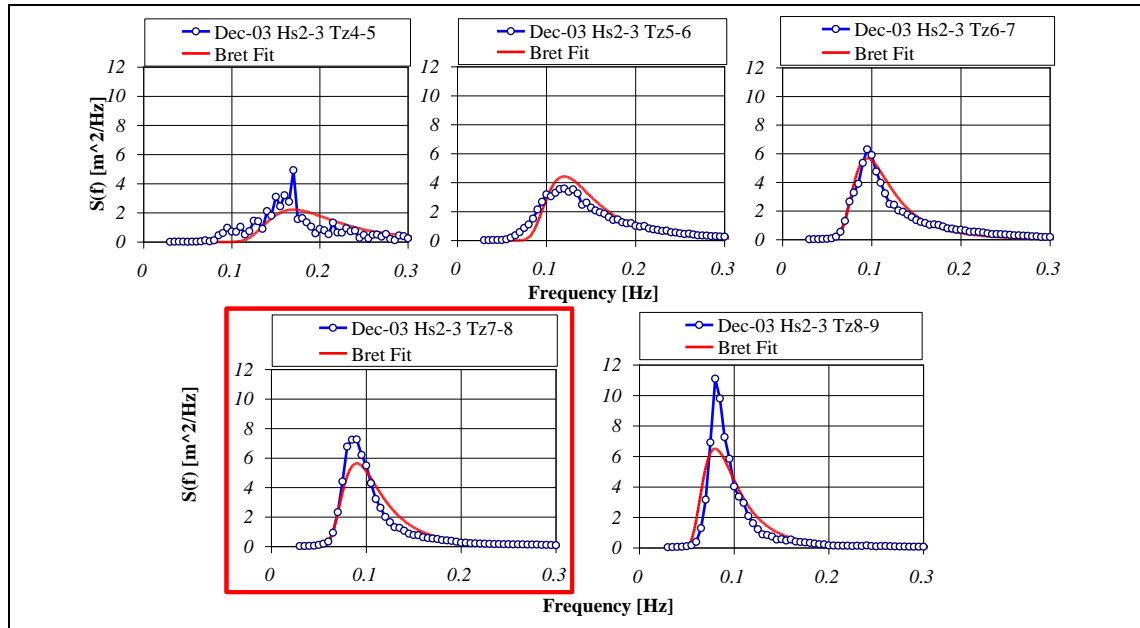


Figure 4.30. Average spectra and Bretschneider fit for iso-height scatter elements of Figure 4.29.

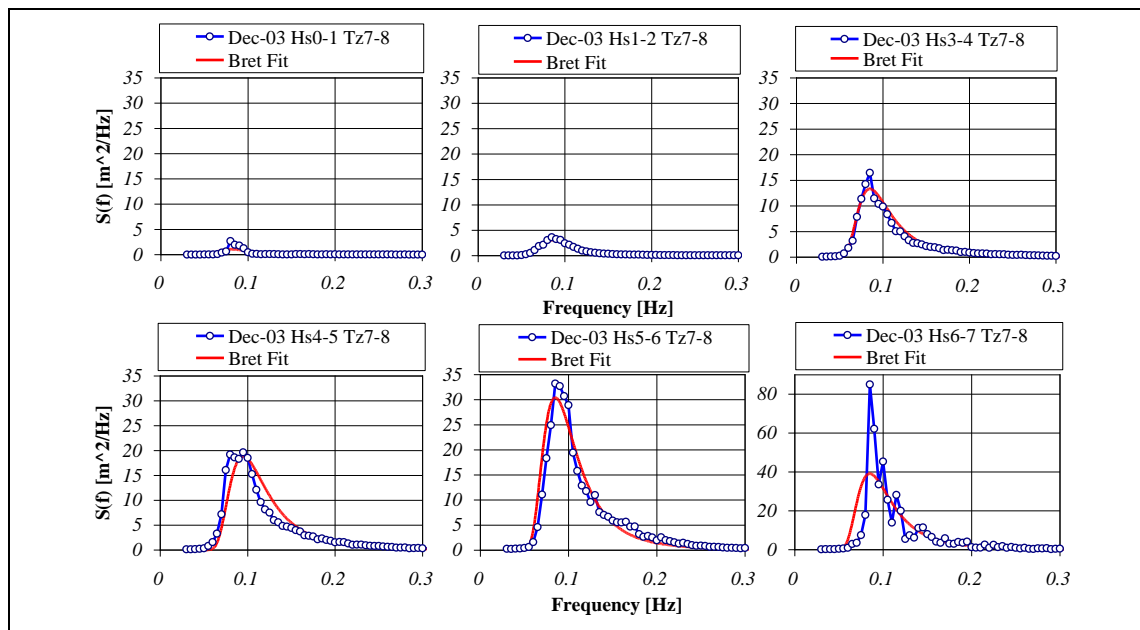


Figure 4.31. Average spectra and Bretschneider fit for iso-period scatter elements of Figure 4.29.

Figure 4.31 shows the average and Bretschneider spectra for each of the iso-period scatter elements indicated in Figure 4.29. The common component of  $H_{m0} : 2 - 3m, T_{02} : 7 - 8s$  to both the iso-period and iso-height is not repeated in Figure 4.31 but outlined in Figure 4.30. Also note that for convenience, the ordinates of the last plot of Figure 4.31 do not have the same scale as the other plots in that figure. From Figure 4.31 it can be argued that the average spectra of each scatter diagram component is a better fit to their equivalent Bretschneider spectra except for the element of  $H_{m0} : 6 - 7m, T_{02} : 7 - 8s$  which may be better approximated by a JONSWAP type spectral shape.

#### 4.4.2. Iso-Steepness

Another investigation that can be performed on the variation of measured spectra, is to look at the scatter diagram components that follow the significant steepness line of  $s_s = 1:20$ . This was investigated for the month of January 2005, again from the Loop Head site. This particular month was selected as it incorporated the highest recorded significant wave height in the duration of the measurement scheme at the Loop Head site. The significant steepness of  $s_s = 1:20$  was chosen as it is an approximation of the steepness of a Pierson-Moskowitz empirical spectrum ( $s_s = 1:19.7$ ), therefore the fitted Bretschneider spectrum to the average spectra would be a close approximation to such a spectrum. The positions of the chosen facets of the iso-steepness are indicated in Figure 4.32 below, the bi-variate scatter diagram for the month of interest. This is the unbiased scatter diagram for the month of January and incorporates 737 measurements, which results in one measurement per hour for 99% of the month.

The average spectra and Bretschneider equivalent for the eight components selected along the iso-steepness line as indicated in Figure 4.32 are plotted in Figure 4.33. Six of the eight averaged spectra are in good agreement with the Bretschneider fit, including those sea states of a severe nature. The reason that some of the sea states selected do not conform to the empirically derived spectra in some instances is due to low levels of occurrence or low wave height.



#### 4.4.3. Storm Progression

At the Galway Bay Wave Energy test site, the largest sea state experienced while an operational data buoy was on site, occurred in December 2006. The twenty minute surface elevation file that contained the largest recorded sea state occurred at the peak of a storm event and equated to a significant wave height,  $H_{m0} = 4.94m$ , an average period,  $T_{02} = 6.9s$ , with a maximum wave height of  $H_{max} = 8.15m$ . A portion of the surface elevation trace recorded by the Datawell Waverider buoy containing the largest individual wave is indicated in Figure 4.34.

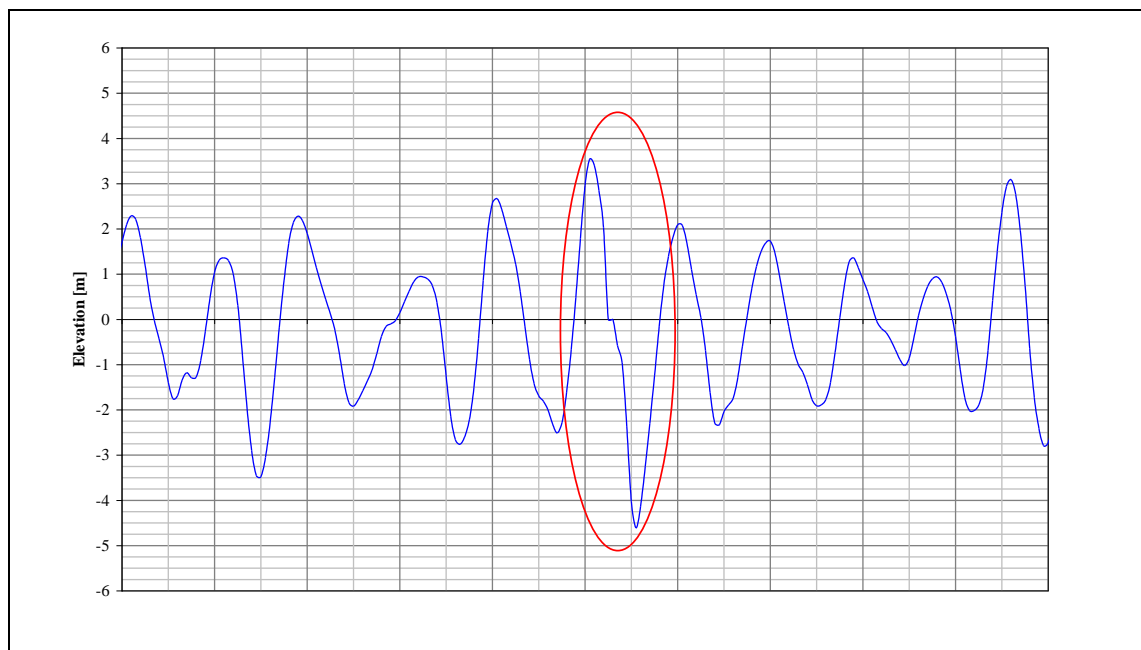


**Figure 4.34. Surface elevation of the largest recorded wave at the Galway Bay Test Site.**

The storm event, from which this maximum wave was measured, grew from a significant wave height of approximately 1.5m to 5m and subsided to 1.5m over a period of 24 hours. This storm progression can be seen in Figure 4.35. Figure 4.36 are the individually derived spectra from twenty minutes of surface elevation data recorded and processed by the data buoy on site in Galway Bay, and indicated by letters (a) to (i) in Figure 4.35. Also plotted is the theoretical Bretschneider spectrum for the same summary statistics, indicated by the broken line.



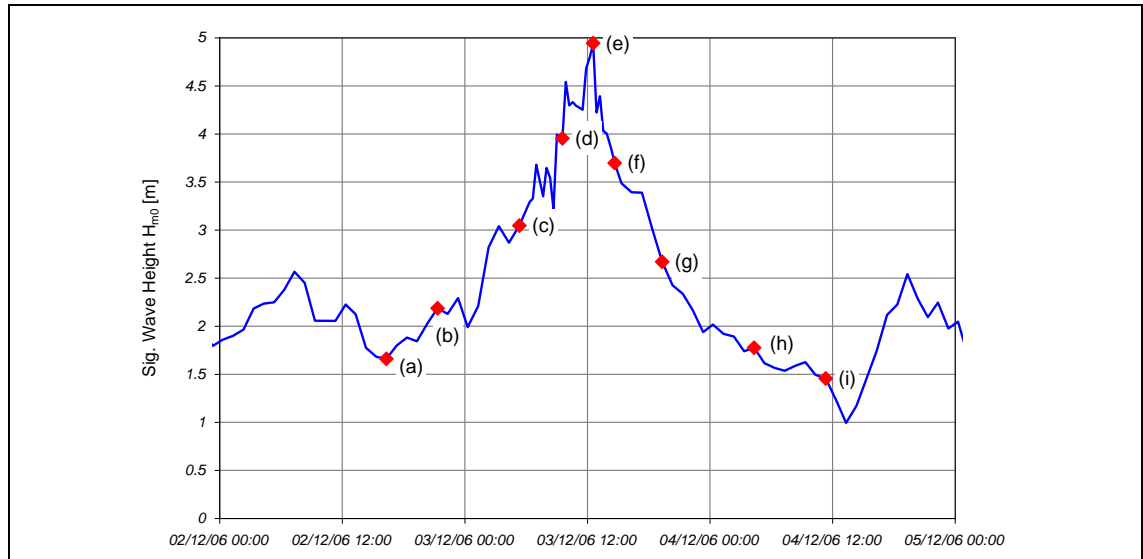


Figure 4.35. Significant wave height time series of the December 2006 storm event for Galway Bay.

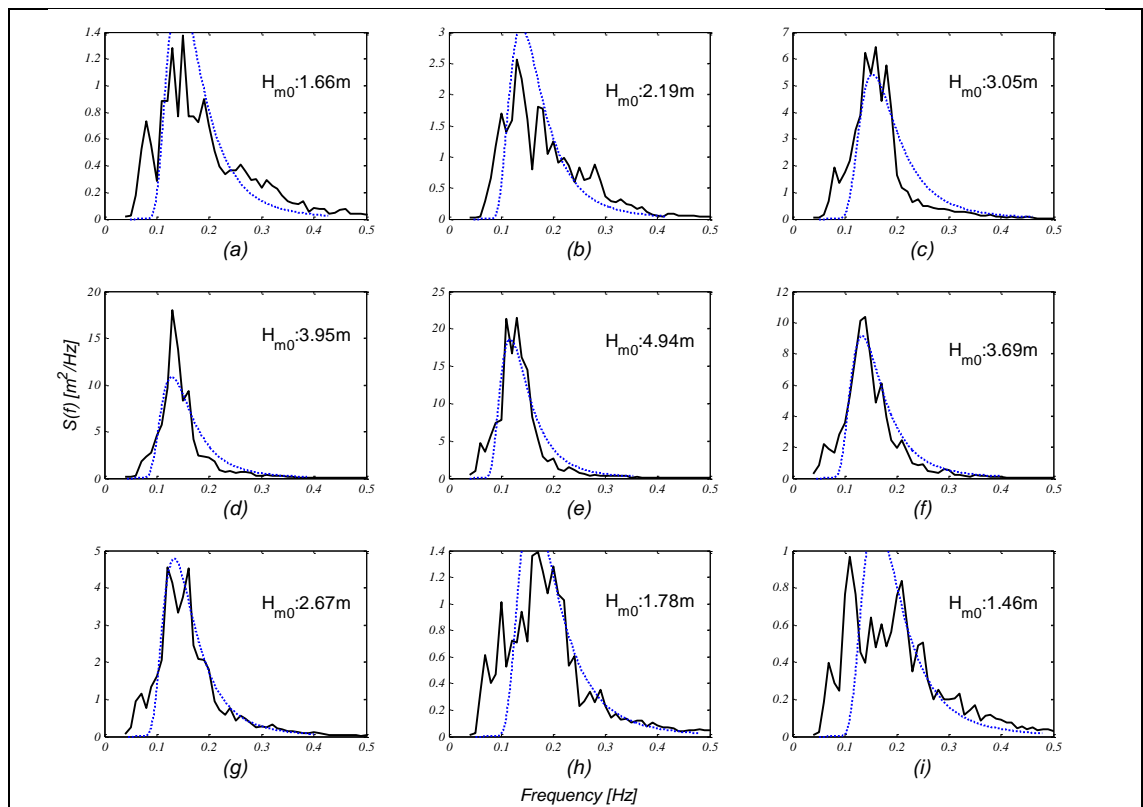


Figure 4.36. Sequence of spectra during the course of a storm event, corresponding to the indicators in Figure 4.35.

Spectra (a), (h) and (i) show evidence of multiple wave systems, such as those that have been identified in previous sections. As the wave height increases, the spectral shape conforms to a more characteristic Bretschneider type shape around the peak of the storm. The central spectrum (e) with a significant wave height of approximately 5m, was recorded at the peak of the passing storm and shows a good fit with the equivalent

Bretschneider empirical equation for spectral distribution. This closeness of fit holds until the wave height falls below  $H_{m0} = 2.5m$ . Note that while the frequency range is constant, to better visualise the spectra in Figure 4.36, the spectral ordinate axis is not constant.

#### 4.5. Spatial Variations

The response of wave energy converter to incident waves govern their operational performance and for many devices, this is highly dependent on spectral shape due to their resonant properties. Resource assessments, device performance predictions and monitoring of operational devices, will often be based on summary statistics and assume a standard spectral shape such as Pierson-Moskowitz, JONSWAP, or other derivatives. Furthermore, these are typically derived from the closest available wave data, frequently separated from the site on scales in the order of 1km. Therefore, variability of seaways from standard spectral shapes and spatial inconsistency between the measurement point and the device site will cause inaccuracies in the performance assessment.

Direct measurements from a wave energy site provide a dataset of the wave field incident on the devices. Prior to deployment, this data is applied to resource assessments and device performance predictions, and during operation, for monitoring of device response and performance (EMEC 2004). The placement of wave sensors around a development will be outside of the immediate proximity of the devices, where they cannot interfere with normal device operation and radiated or reflected waves from the devices do not interfere with measurements. In the protocols for performance assessments of WEC, a minimum separation of 100 metres and a maximum of 1km are proposed. In order to transpose measurements from the measurement site to the devices, it is necessary to quantify any differences in the wave field at the two points. A detailed investigation of the site, including bathymetry or tidal regimes can reveal possible deterministic factors that will affect the wave-field. Such an investigation coupled with modelling sensitivity studies are also advised (Smith and Taylor 2007).

These sensitivity studies can be undertaken in the spatial domain and in the frequency domain. Site specific conditions can influence the energy distribution of a spectrum, especially in areas with locally generated wind seas, due to fetch limited conditions coexisting with the remnants of far distant storms that seep into the investigation area as

swell. For wave energy extraction, knowledge of the sea state spectral components is essential both for power extraction calculations and control issues as this information can be hidden within the historically used summary statistics. By using spatially separated data buoys, confidence can be gained about the measurements at a particular location on site due to the concurrent measurements of the buoys.

**4.5.1. Concurrent Summary Statistics**

Both wave buoys on site in Galway Bay are separated by a distance of 200m and produce two 30 minute surface elevation files every hour. The buoys have different sampling rates, 2.56Hz for the non-directional buoy and 1.28Hz for the directional buoy. The heave displacement of the directional buoy is only considered here as no concurrent directional comparisons can be made. These elevation files are spectrally analysed by a Fast Fourier Transform using the Welch segmenting method, resulting in comparative spectral files. From the variance density spectra, the summary statistics can be derived by computing the moments of the spectrum. Of interest in this study are the significant wave height,  $H_{m0}$ , average period,  $T_{02}$ , energy period,  $T_e$  and peak period,  $T_p$  as defined in Table 4.1.

The following plots (Figures 4.37 to 4.40) depict the measured significant wave height and average period for the four months of concurrent data from Galway Bay. Although the concurrent data is intermittent, there does exist over 2,000 elevation records from each buoy. The maximum significant wave height recorded is 2m, but it must be remembered that this location is a benign test site and suited to device testing of 1/4 scale wave energy converter.

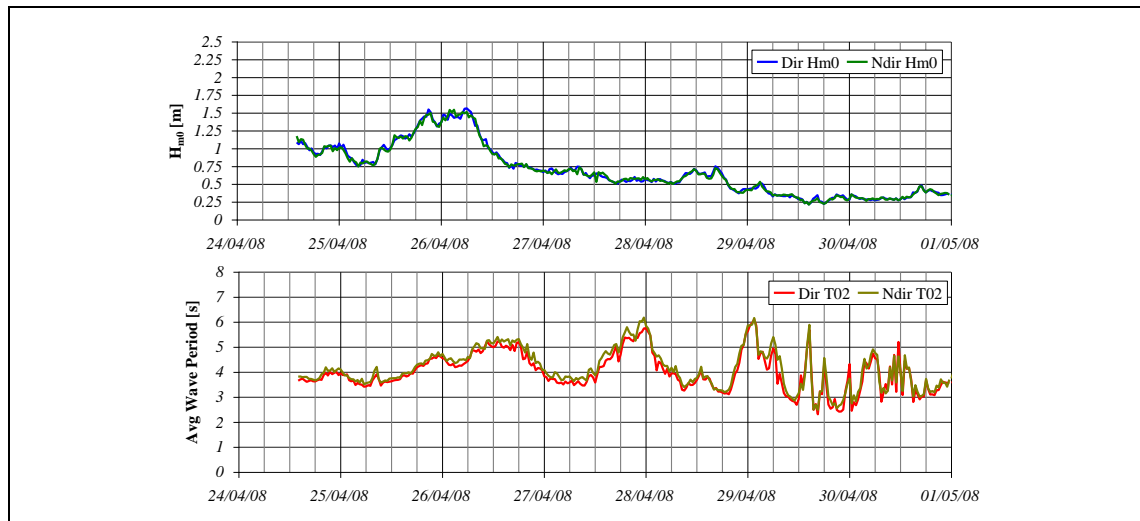


**Figure 4.37. Significant wave height and average period from both buoys, April 2008.**

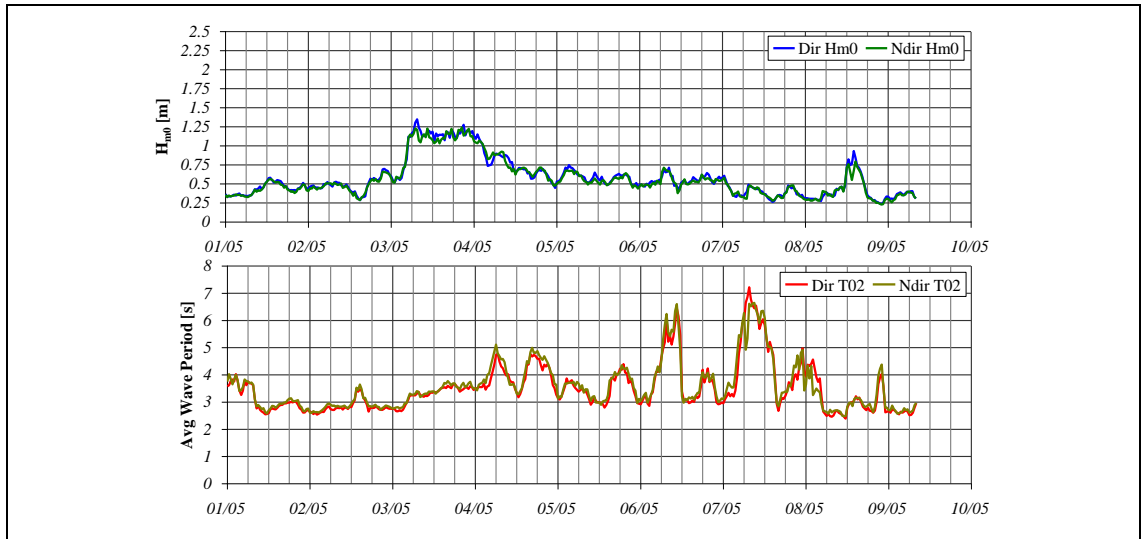


Figure 4.38. Significant wave height and average period from both buoys, May 2008.

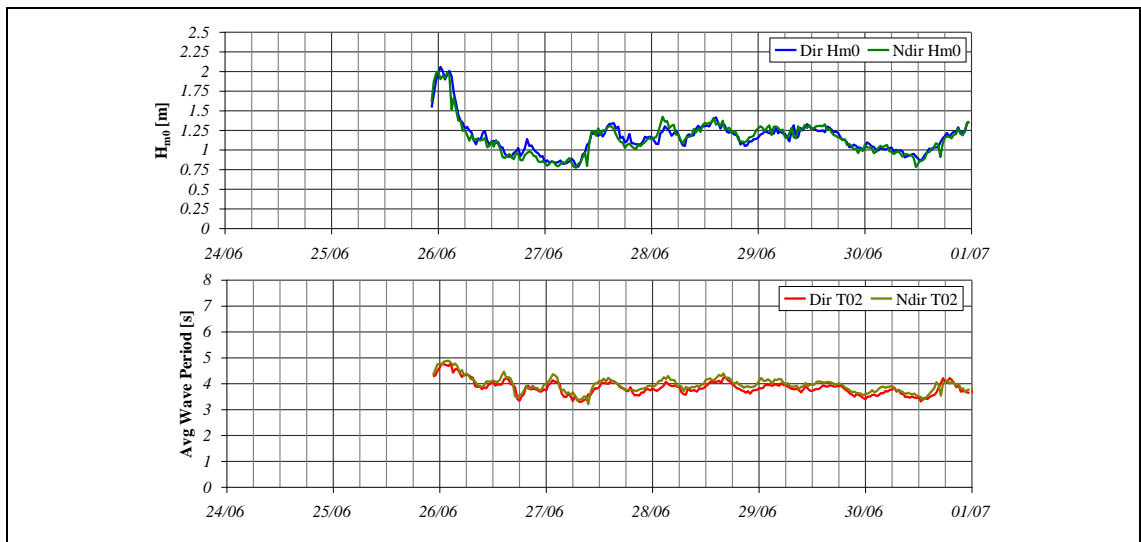


Figure 4.39. Significant wave height and average period from both buoys, June 2008.

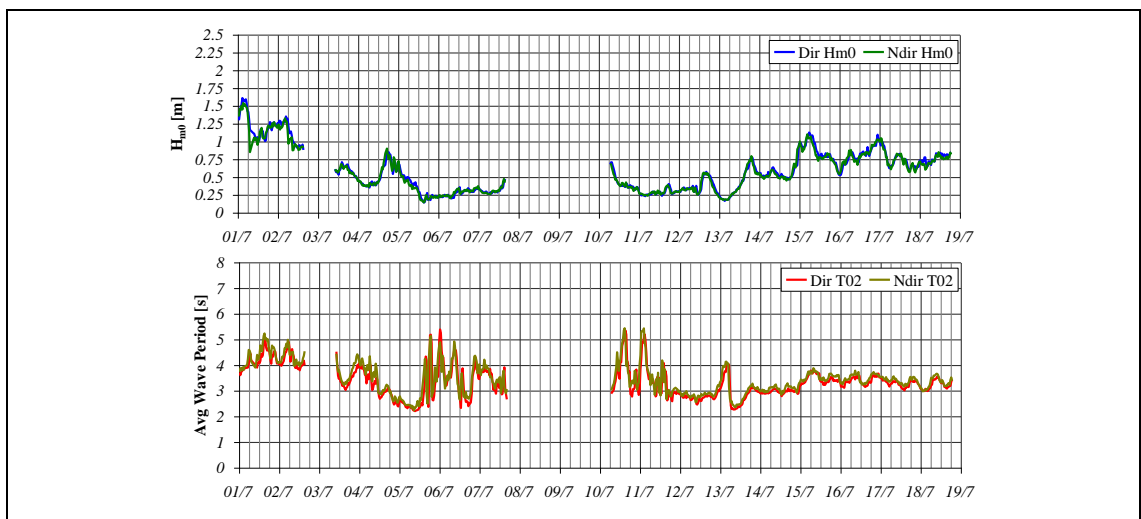


Figure 4.40. Significant wave height and average period from both buoys, July 2008.

An interesting aspect of these plots is the relatively large fluctuations of the average period when the significant wave height is below 0.5m, which is experienced equally by both buoys. This is primarily due to the prevalence of long period swell during times of low wave height. During these events, spectra become bi-modal with two concentrations of energy from the wind and swell systems. As one concentration of energy vies for dominance, the periods, which are influenced by the spectral moments, move from high to low frequencies. Two examples of this are shown in Figure 4.41, a new wind sea in the area of measurement, however this is gone a few hours later as shown in Figure 4.42. In these plots the concurrently measured spectra are shown. The swell system exists in both plots at approximately 0.1 Hz, becoming dominant in Figure 4.42. The wind system at higher frequencies is only evident in Figure 4.41.

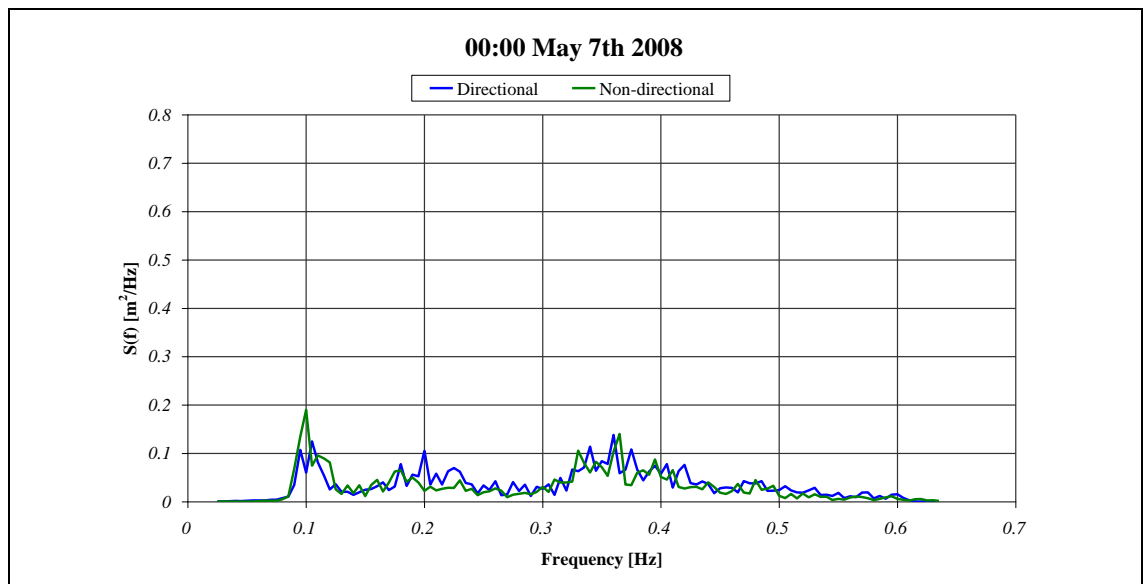


Figure 4.41. Spectra with short average period,  $T_{02}$ .

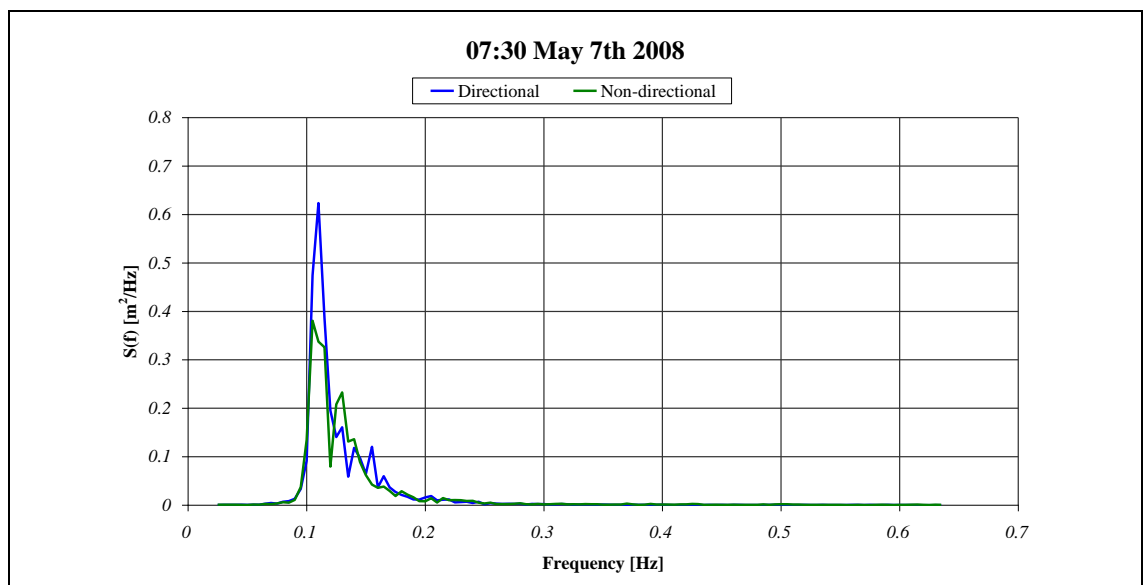


Figure 4.442. Spectra with long average period,  $T_{02}$ .

These plots are the measured spectra from data buoys placed 200m apart. This spacing can be taken as the distance a data buoy would be placed from a wave energy device at a deployment site. These plots indicate that at the time of these concurrent measurements there is very little difference in both the spectra obtained and the summary statistics that are derived from either buoy. This means that the sea state measured by the buoy can be used to compare against the power output of the wave energy device with confidence when these examples are taken into account.

**4.5.2. Regression Analysis**

To further compare the concurrent readings of the data buoys in Galway Bay a regression analysis was conducted on the summary statistics from each surface following buoy. Table 4.2 gives the results of this analysis for the four selected parameters, which are plotted in Figure 4.43. The equation at the top of each plot is the linear fit to the data. The correlation coefficient is given by Equation 4.3 and the covariance is given in Equation 4.4.

$$R = \frac{\Sigma(x - \bar{x})(y - \bar{y})}{\sqrt{\Sigma(x - \bar{x})^2 \Sigma(y - \bar{y})^2}} = \frac{cov}{\sigma_x \sigma_y} \tag{4.3}$$

$$cov = \frac{\Sigma(x - \bar{x})(y - \bar{y})}{n - 1} \tag{4.4}$$

where  $x$  and  $y$  represent the datasets from the two buoys.

Statistic ( $n = 2114$ )	Mean, $\bar{x}$	StdDev, $\sigma_x$	Mean, $\bar{y}$	StdDev, $\sigma_y$	Correlation Coeff, $R$	$R^2$	Covariance $cov$
	<i>Dir</i>	<i>Non-Dir</i>	<i>Dir</i>	<i>Non-Dir</i>			
$H_{m0}$	0.658	0.338	0.648	0.334	0.989	0.978	0.112
$T_{02}$	3.676	0.849	3.801	0.861	0.951	0.904	0.696
$T_e$	5.152	1.206	5.285	1.203	0.970	0.942	1.409
$T_p$	6.387	2.562	6.509	2.510	0.793	0.628	5.100

**Table 4.2. Statistics of regression analysis.**

For the parameters,  $H_{m0}$ ,  $T_{02}$  and  $T_e$  the data from the two buoys fit quiet well. The significant wave height has a correlation coefficient closest to one, suggesting that this parameter has the best fit. The results indicate that  $T_e$  measured from both buoys is closer than that for  $T_{02}$ . With a correlation coefficient of 0.79 for  $T_p$ , this would be regarded as

a poor fit. However, this may be exacerbated by spectra similar to that shown in Figure 4.41.

The contrast in the peak period can be seen in the comparison of the spectra from the directional buoy and the non-directional buoy. Both spectra have peaks of significant magnitude at approximately 0.35 Hz and 0.1 Hz. However, the maximum ordinate for the directional spectrum, from which the peak frequency is obtained, occurs at 0.35 Hz although it is not much greater than the peak at 0.1 Hz. The non-directional buoy spectrum has a clearly identified dominant peak at the 0.1 Hz frequency. There is little difference in the magnitude of many of the spectral ordinates, therefore the maximum ordinate which gives the peak period is an arbitrary measure in some respects.

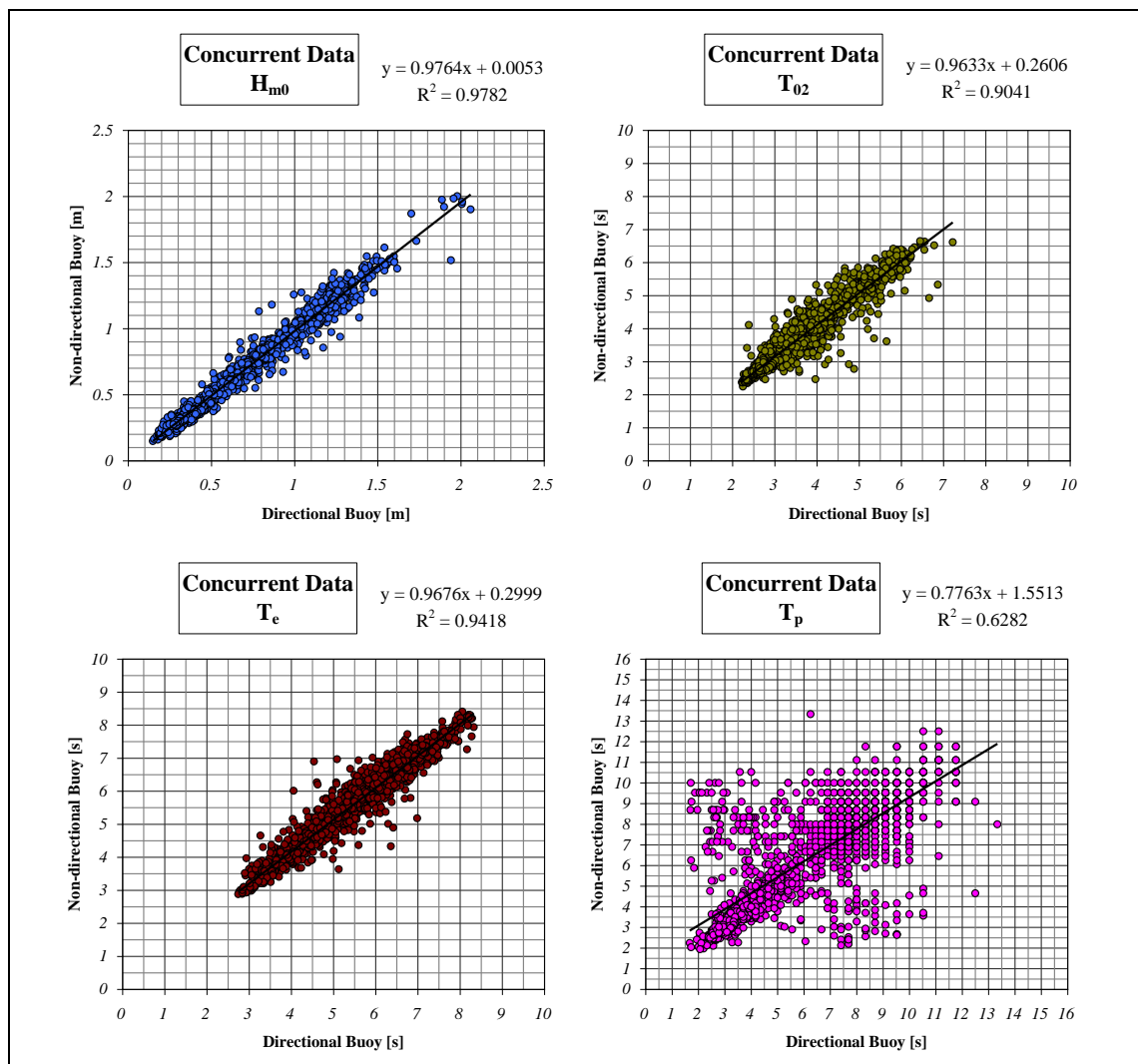


Figure 4.43. Regression analysis of frequency domain parameters.

## 4.6. Bimodal Spectra Identification

The concept of the bimodal spectrum was introduced in an earlier section. This can occur when there is a mixing of the spectral components of a long period swell and a locally generated wind sea at the measurement point. Several methods to model and identify these type of wave spectrum were introduced in Section 3.4 and some of these techniques will be applied here.

### 4.6.1. Application of Separation Methods

The Galway Bay test site is partially sheltered from the Atlantic Ocean by the Aran Islands, and due to this there is a large degree of mixing between the offshore swell and the locally generated fetch limited wind seas. As an attempt to quantify the degree of multi-modal spectra at the wave energy test site some of the simplified search methods were applied to identify legitimate peaks of wind and swell wave systems within primarily non-directional wave spectra measured by the Datawell Waverider buoy on site. Comparison was also made with a similar data set from the more exposed Loop Head Atlantic site. Both sets of spectral data have the same frequency bounds,  $f_{min} = 0.04\text{Hz}$  and  $f_{max} = 0.6\text{Hz}$  with  $\Delta f = 0.01\text{Hz}$  and  $\nu = 18$  degrees of freedom. Both data sets consist of four months over the winter period, December to March, however due to constraints, the Loop head site covers the 2005 to 2006 period while the Galway Bay data set consists of measurements from 2006 and 2007.

#### 4.6.1.1. Constant Separation Frequency

Initially, the simplest method to extract wind and swell data from a spectrum is to choose a suitable frequency at which each spectrum is arbitrarily separated. For an open Atlantic site such as Loop Head, it would be usual to apply a separation at 0.1 Hz to the spectra and work out the high and low energy contributions about this frequency for each spectrum. This is a very crude method and does not allow for qualification of a spectrum to be classed as twin peaked, as it is applied to each spectrum. Therefore no knowledge of the number of double peaked spectra can be gained from the application of this method, only the portion of energy that resides in each spectrum at the high and low frequencies.

Figure 4.44 shows the summary statistics for the month of January from the data set of the Loop Head offshore site. The month of January 2007 was chosen for closer inspection as it contains a large storm followed by a period of calm weather. The significant wave



height plot indicates that the vast amount of energy in the spectra reside above a period of 10s, which was used as the separation period. It is interesting to note that although the significant wave height calculated from the low frequency swell portion ( $f < 0.1\text{Hz}$ ) of the spectra closely follows the overall significant wave height, it is the average period calculated from the portion of the spectra above the separation frequency of  $f_s = 0.1\text{Hz}$  that gives a better approximation of the overall average period of  $T_{02}$ . This is especially evident towards the end of January during the calm period when both the wind portion of wave height and period closely match the overall statistics.

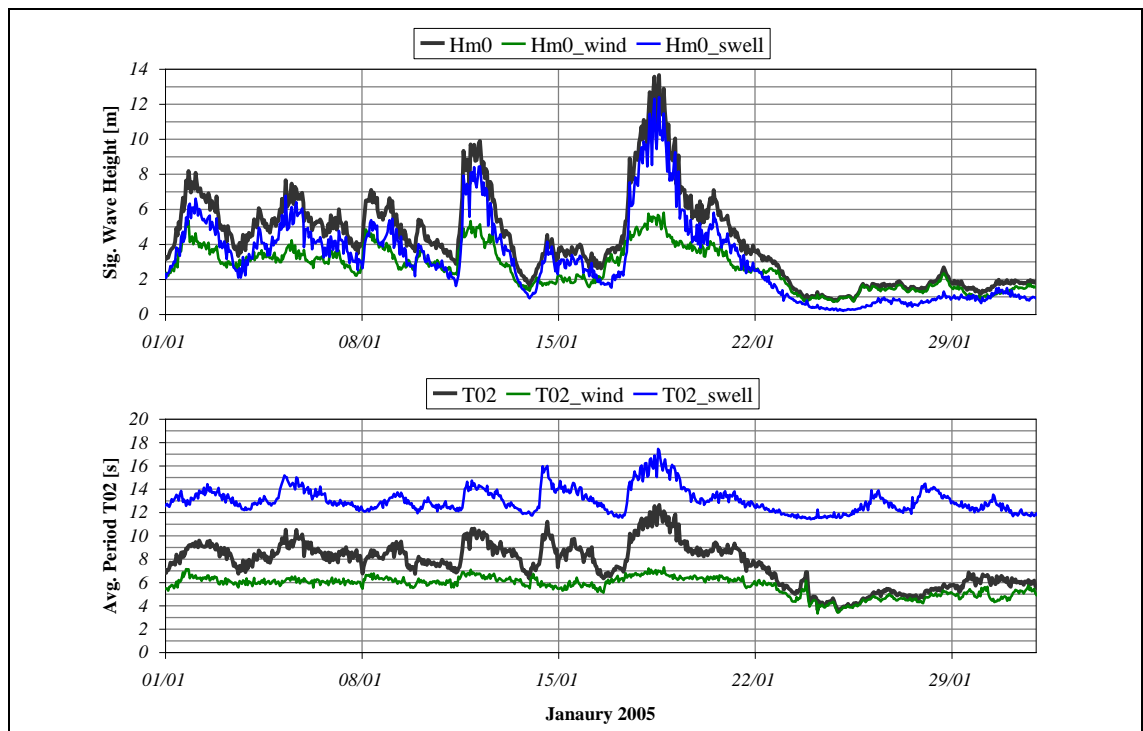


Figure 4.44. Overall and separated summary statistics for January 2005, from Loop Head.

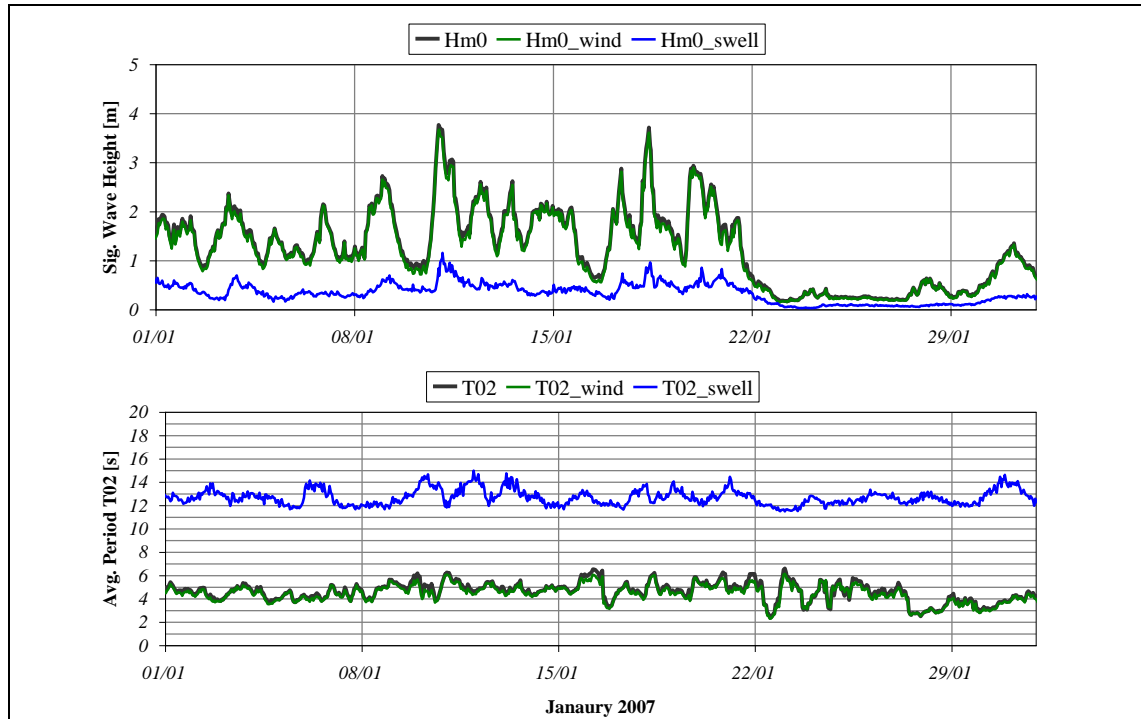


Figure 4.45. Overall and separated summary statistics for January 2007, from Galway Bay.

A similar plot to Figure 4.44 is shown in Figure 4.45, but using the Galway Bay data shows the opposite characteristics of the wave energy test site to an open Atlantic site. At this benign site, the wave conditions are such that it is at the shorter periods that the vast majority of the energy resides. For the month of January shown, the significant wave height calculated from the variance density in the higher frequencies is very close to the overall wave height as there is very little energy at the low frequencies. The case for the average period has a similar trend, where  $T_{02}$  calculated from the short period portion of the spectra closely follows the overall average period, again indicating that in all spectra the majority of the energy resides below the separation period of 10s.

#### 4.6.1.2. Parametric Separation Method

To get an indication of the number of double peaked seas a more intuitive algorithm is required. A simplified method based on parametric rationale is applied to the buoy measured spectra of Galway Bay and the more exposed Loop Head site. The method adopted is based on identifying legitimate peaks of energy in the spectrum, not just variations due to sampling errors. The identification procedure applies the following guidelines to classify legitimate peaks in the spectra:

- i. A peak is classified as legitimate if the centre ordinate in a frequency range of  $\pm 0.055$  Hz is a maximum. The maximum with the largest ordinate is termed the primary peak.
- ii. Secondary peaks qualify as such if the secondary peak magnitude is greater than 20% of the magnitude of the primary peak and the local minimum between the peaks is less than 10% of the magnitude of the primary peak.
- iii. Additional peaks are discounted if they are within 2 seconds of an identified peak larger in magnitude.

The same data sets were used from both sites as in the previous analysis method, that is four months over a winter period, December to March. The multi-peak identification procedure results in an overall average percentage occurrence of approximately 60% of all the spectra exhibiting bimodal features at the Galway Bay site from the winter data set according to the criteria adopted above. This compares to 13% for the more exposed Loop Head test site.

Having applied the partitioning algorithm to both data sets, the results are plotted in Figure 4.46 and Figure 4.47. The dominance of multi-modal seas can be seen in Figure 4.47 in contrast to the Loop Head site. As testament to previous work referred to in earlier sections, the existence of multi-modal seas are only evident at low wave heights for an exposed site. This can be seen in Figure 4.47 after the storm event toward the end of the month.

Linear Wave Theory gives the following relationship (Equation 4.5) for wavelength,  $\lambda$  in intermediate wave depths ( $0.05 < d/\lambda < 0.5$ )

$$\lambda = \frac{g}{2\pi} T^2 \tanh \frac{2\pi d}{\lambda} \quad (4.5)$$

where  $T$  is the wave period and  $d$  is the water depth

This is then approximated for deep water ( $d/\lambda > 0.5$ ), as shown in Equation 4.6

$$\lambda = \frac{g}{2\pi} T^2 \quad (4.6)$$

For the range of water depths that occur at the benign wave energy test site in Galway Bay, the ratio of water depth to wavelength from these two equations have been plotted over a range of wave periods, as shown in Figure 4.48.

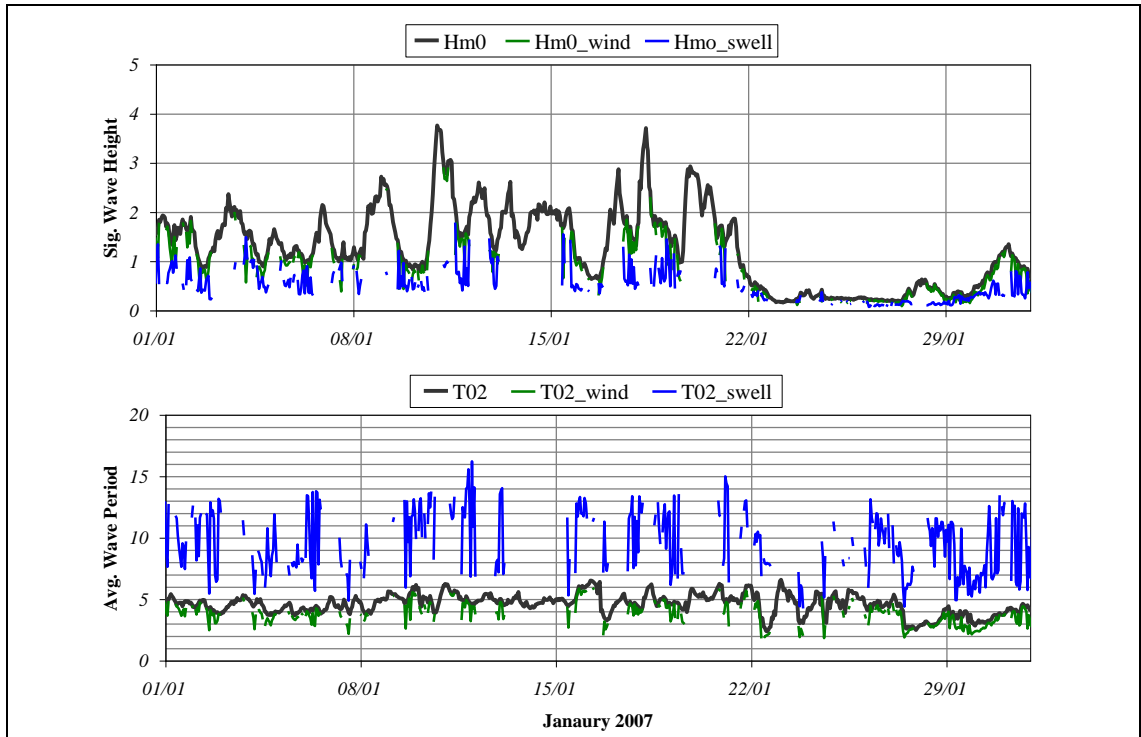


Figure 4.46. Measured and separated statistics for January 2007, Galway Bay.

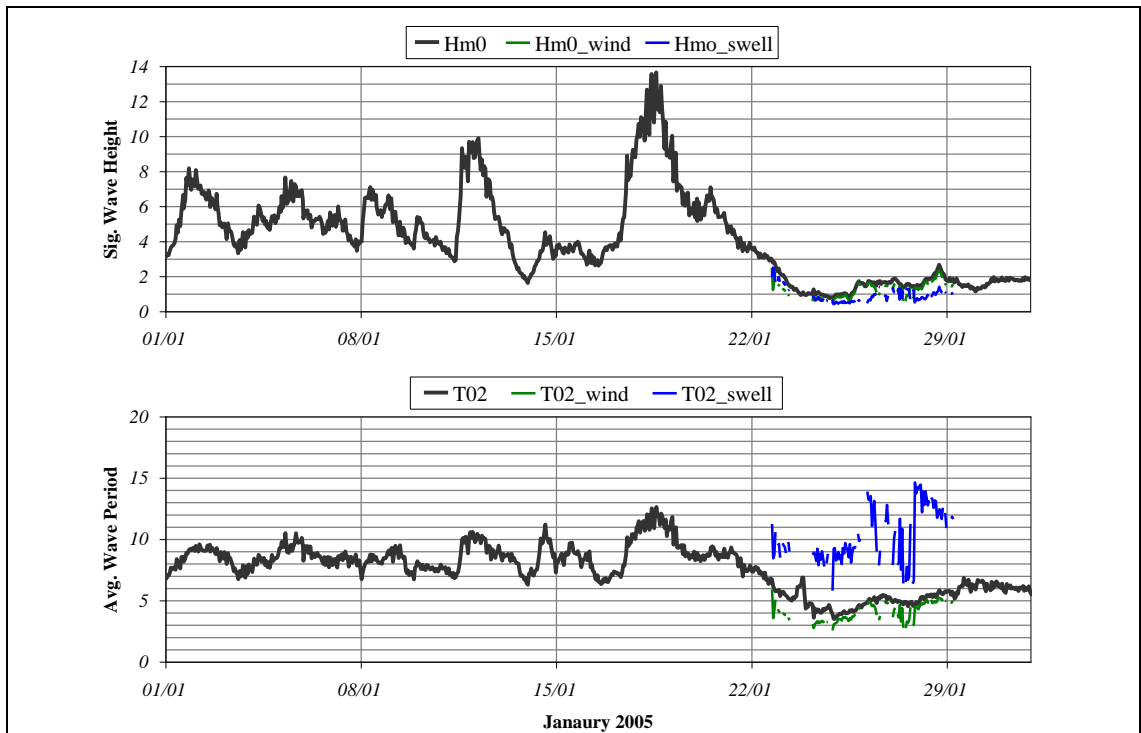


Figure 4.47. Measured and separated statistics for January 2005, Loop Head.

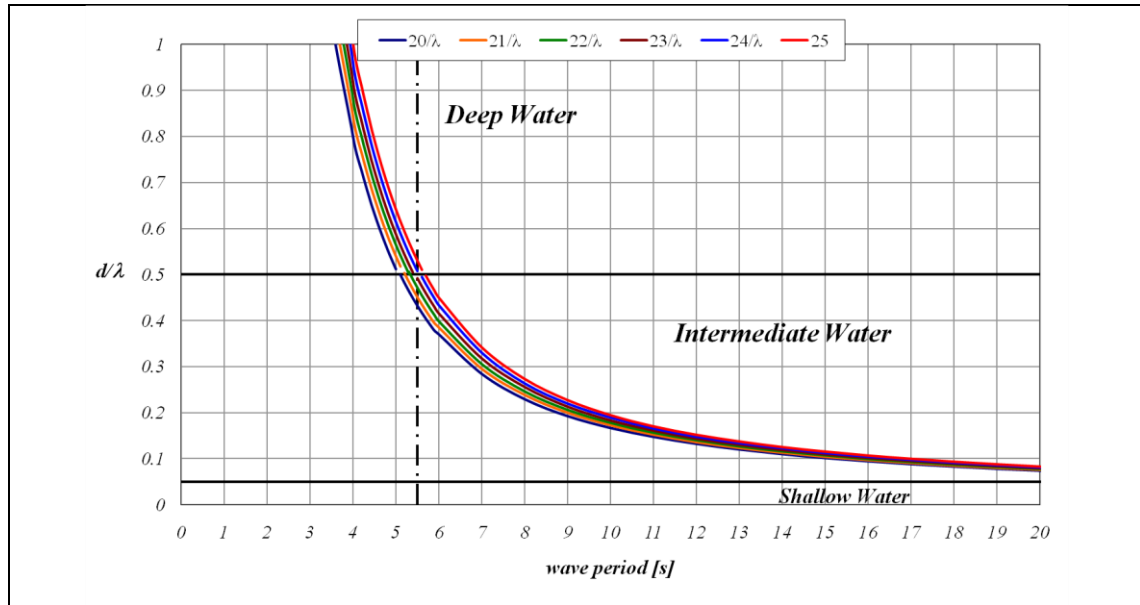


Figure 4.48. Water depth to wavelength ratio for range of water depths over a range of wave periods.

It is clear from Figure 4.48 that a transition occurs at a wave period at which the waves go from deep water ( $d/\lambda > 0.5$ ) to intermediate depth water, determined as being  $T = 5.5s$  over the range of water depths at the test site. The incoming waves with a period of between 5.5s and 20s, start to ‘feel’ the bottom. Waves with a period shorter than 5.5 seconds can be regarded to be in deep water at the test site. Reference to Figure 4.47 that showed the average wave period,  $T_{02}$  for the separated wind and swell wave systems for Galway Bay, indicates that the majority of the wind wave periods are below  $T = 5.5s$  and can be considered to be in deep water. For the periods associated with the swell wave systems identified, these are considered to be in intermediate water depths at the test site.

It is important to note that if the qualifying parameters of the peak identification algorithm were changed or if a larger data set were used when applying the above algorithm, then the percentages of double peaked spectra would also change. In fact, taking nearly a full years worth of data for the Loop Head site, the applied algorithm indicates that 12% of all measured spectra qualify as double peaked. Unfortunately, due to scheduled maintenance on the data buoy, there was no data recorded for the months of July and August, when the sea states would be relatively low, which could have potentially increased the double peaked spectral count. The year’s data set for 2004 in this case accounted for 78.5% of the total available data for that year. Comparing this to the benign test site in Galway Bay for the year 2007, 97% of the hourly data records were measured and of these, 58% are indicated as having two distinct wave systems that conform to the

policy set out in the algorithm being used. The results from the yearly analysis indicate that the four months of winter used are a good indication of the entire year for the Galway Bay site, however a full years worth of data is required for the Loop Head exposed site.

#### 4.6.1.3. Wang & Hwang Bimodal Identification Method

An example of the Wang and Hwang (2001) steepness function method, which was introduced in Section 3.4, is applied first to an idealised single peaked fully developed sea of  $H_{m0} = 4m$  and  $T_p = 10s$  and then to a spectrum with  $H_{m0} = 1m$  and  $T_p = 5s$  as shown in Figure 4.49 with  $\Delta f = 0.01Hz$ . The dashed light line is the steepness function,  $\alpha(f_*)$ , the vertical dashed line is the peak frequency of the steepness function, and the solid vertical line is the separation frequency given by Equation 3.36. For the higher energy spectra in Figure 4.49a, the separation frequency given by this method seems a reasonable estimate, however for the lower energy spectrum (Figure 4.49b) which could be considered to be a wind sea in its own right, the separation frequency given seems to be over estimated.

This method has been applied to two measured wave spectra from the exposed Loop Head site on the west coast of Ireland. These spectra have two evident wave systems as shown in Figure 4.50. The two spectra shown here have the same significant wave height of approximately 2.25m with an average period in the region of 5.5s. It is interesting to note that for both spectra the steepness function,  $\alpha(f_*)$  have the same peak,  $f_m$ , however, the coefficients to work out the separation frequency given by Equation 3.37 do not seem suitable for this data, as it would be expected that the separation frequency in both cases should be less than  $f_m$ .

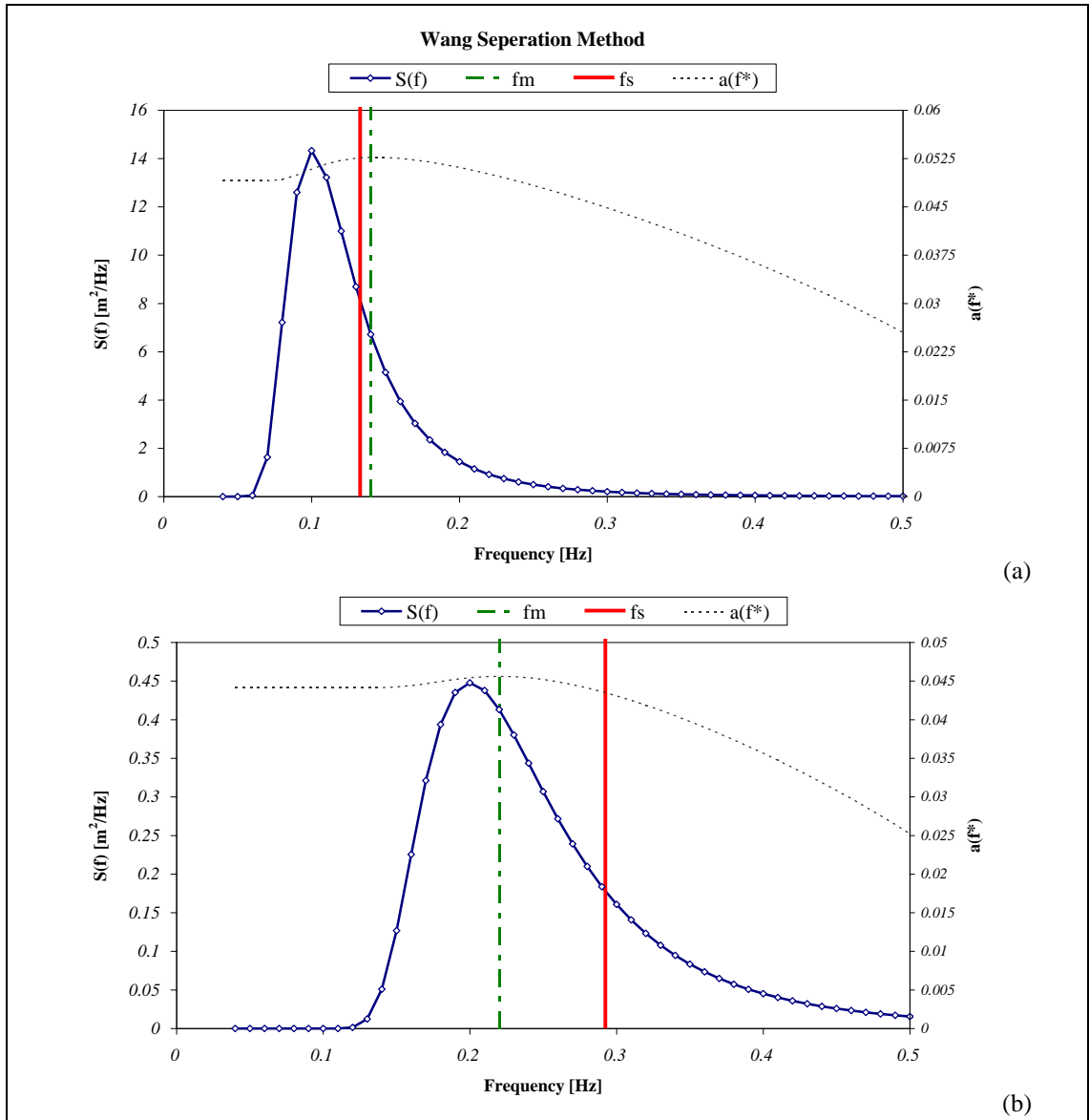


Figure 4.49. Application of steepness function to fully developed spectra.

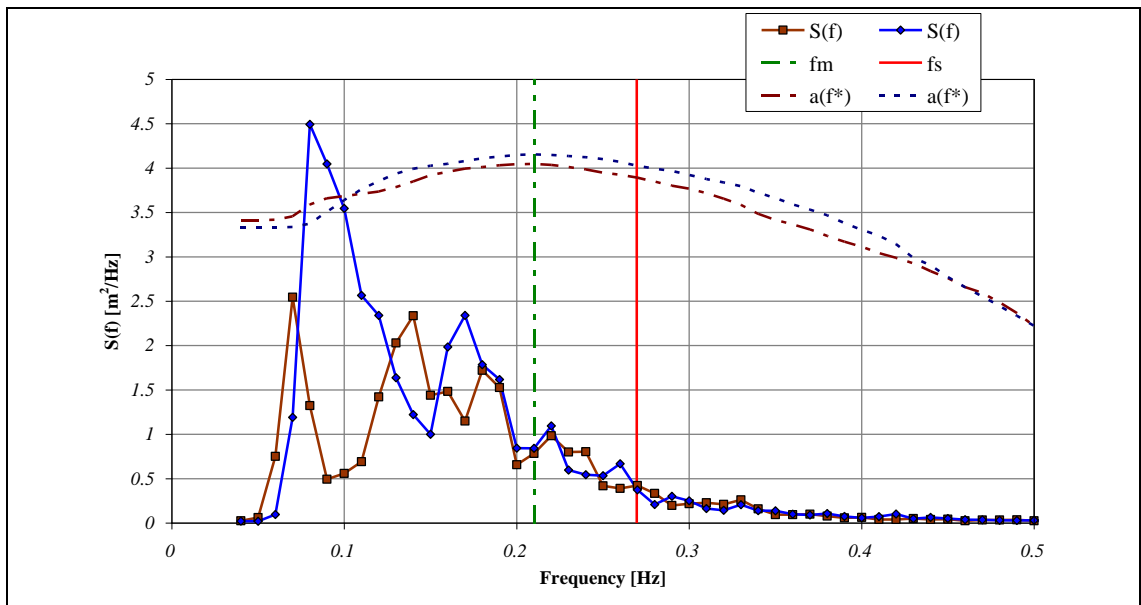


Figure 4.50. Application of steepness function to measured spectra,  $H_{m0} \approx 2.25\text{m}$ ,  $T_{02} \approx 5.5\text{s}$ .

The following limitations are reported by the authors on the use of this method. The steepness function involves the use of the second moment of the wave spectrum, which could be sensitive to noises appearing at the tail end of the wave spectrum. In practice, a cut-off upper-frequency limit between 0.4-0.5Hz is suggested. Due to the use of the upper frequency limits, the proposed steepness method may not work well in low wind conditions, especially in the early hours of wind wave generation when wind-generated waves have little energy and are at higher frequencies than the chosen upper-frequency limit (Wang and Hwang 2001).

Other authors have also indicated shortcomings with this separation method. Portilla *et al* (2009) looked at 1D spectra from two datasets, the first a point in the Pacific off the Mexican coast where geographical and meteorological conditions produce very distinct double peaked spectra due to fetch limited northerly offshore winds in conjunction with open ocean southerly swells. The second data set consists of measured data from the North Sea where there is local wind with occasional swell from the north. By applying the Wang and Hwang function to both data sets of double peaked spectra it is reported that the separation frequency is systematically higher than the splitting frequency which consequently results in swell over estimation, especially during wind sea periods, as also shown by this author in Figure 4.49b.

#### **4.6.2. Consequences of Bimodal Spectra**

An introduction is given in Section 1.4.1.1 of the SWAN numerical modelling package that was used to derive a years worth of hindcast wave data for the wave energy test site in Galway Bay. This data was produced in two forms, the summary statistics and the directional spectrum. From early analysis of the two data sets it became obvious that a difference existed from the summary statistics output by the SWAN model and those obtained by integrating the two-dimensional spectra. This can be seen in Figure 4.51, a comparison of  $H_{m0}$  from both data sets for the month of January 2000. The data set denoted *SWAN Output* is the summary statistics produced by the SWAN model. The data set denoted *Calculated* comes from the integration of the output spectra from the SWAN model.

The SWAN model produces directional spectra at 3 hour time steps, however the summary statistics, denoted *SWAN Output* in this case have a 12 hour time step. It can



be seen from Figure 4.51 that the *Calculated* data is underestimated and is due to the calculation of the spectral moment being limited to the imposed frequency range i.e. 0.0521Hz to 1Hz, in contrast to the calculation of the *SWAN Output* data over the wave spectrum with a diagnostic tail  $f^{-m}$  added to the high frequency cut off. Based on physical arguments the value of  $m$  should be between 4 and 5 (Phillips 1985).

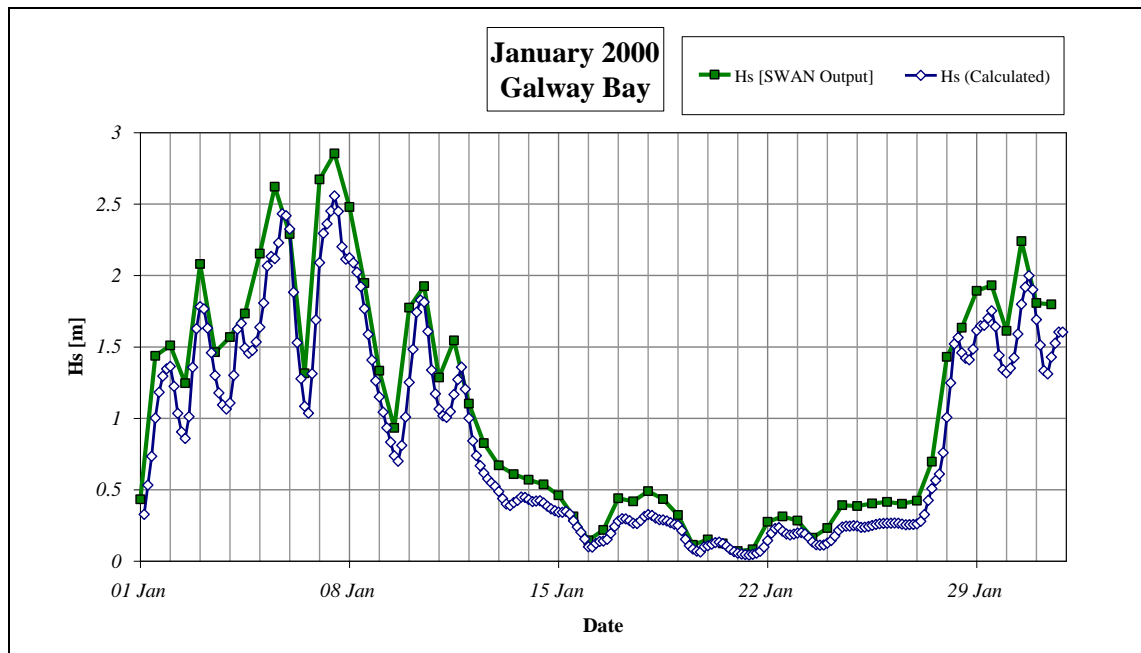


Figure 4.51. Comparison of derived summary statistics from SWAN model for Galway Bay.

Figure 4.52 shows the bi-variate scatter plot of  $H_{m0}$  versus  $T_p$  for both the *SWAN Output*, indicated by the circles and the *Calculated* results, indicated by the diamonds. Due to the difference in the sampling period of the data, there is four times more *Calculated* data than *SWAN Output* data. The peak period is associated with the dominate peak in the spectrum, if more than one wave system exists. This plot gives an indication that two wave systems are being modelled by SWAN. One has the characteristics of a local wind sea with short peak periods associated to the limited fetch, while the other is of longer periods approaching the site from the Atlantic around the Aran Islands. These two systems can be seen as data concentrations, the wind sea on the left and swell sea on the right. One of the data points is selected to further investigate this aspect of the bi-variate plot.

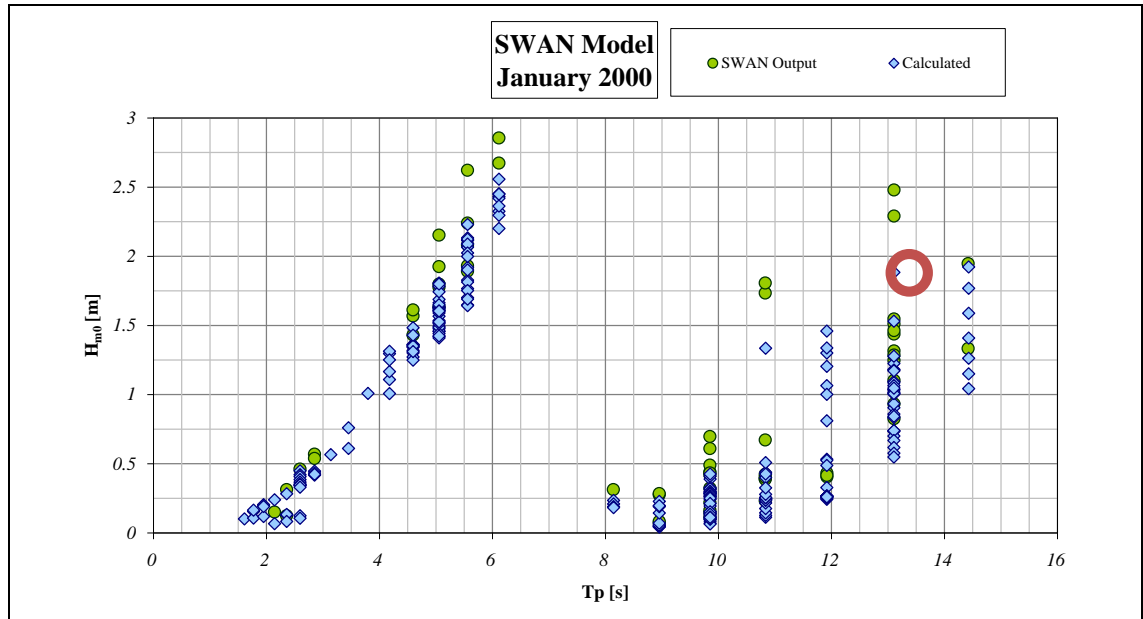


Figure 4.52. Bi-variate scatter diagram of data plotted in Figure 4.51.

The spectrum corresponding to the circled point in Figure 4.52 is shown in Figure 4.53. Quite clearly this is a twin peaked spectrum, however the dominant peak, and therefore the peak period  $T_p$ , is associated with the wave system with least energy in the overall spectrum. The allocation of the peak period with the significant wave height that represents the whole spectrum creates a false impression of the sea state. Therefore, it is dangerous to refer to the summary statistics of un-separated multi-modal seas as is shown in Figure 4.53 as the plot indicates that relatively high wave heights with long periods, and associated higher wave energy content may be experienced at the site. The indicated point in Figure 4.53 should be aligned with a  $T_p$  in the region of 5.5s to 6s.

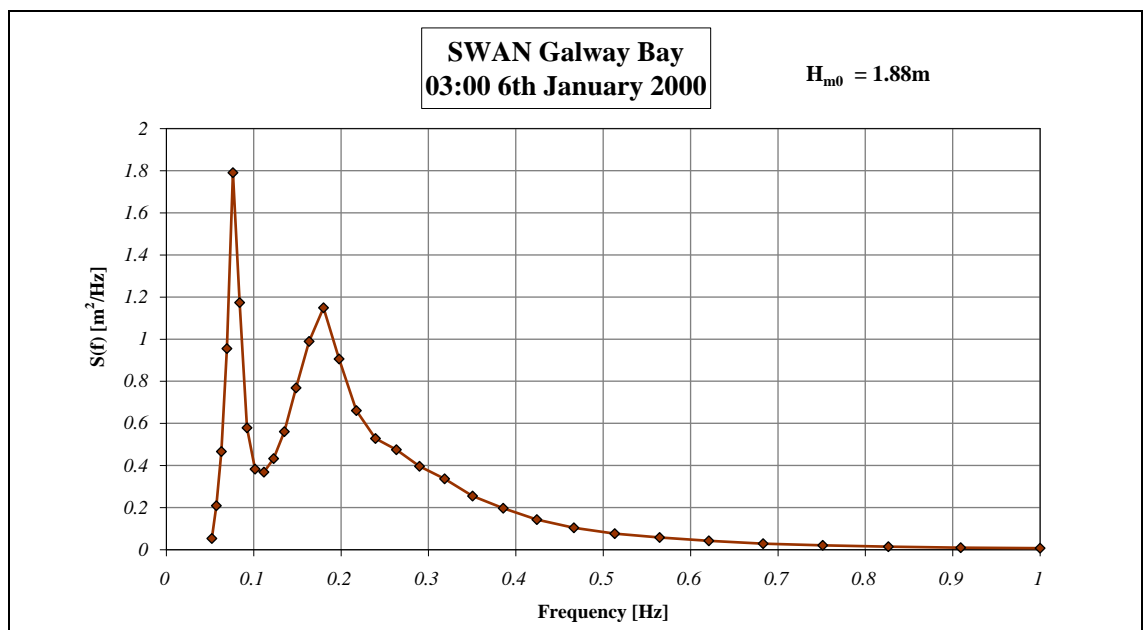


Figure 4.53. One dimensional variance density spectrum for  $H_{m0} = 1.88m$  and  $T_p = 13.11s$ .

Even with the occurrence of double peaked wave spectra, different types occur at the benign wave energy test site. Figure 4.54 shows various one dimensional spectra, produced by the SWAN model, with significant wave height,  $H_{m0}$  and mean wave periods,  $T_{02}$  which are approximately identical, while the only differing statistic is the peak period,  $T_p$ . The spectrum identified as *SPEC1* in Figure 4.54 is a wind dominated spectrum, characterised by a high frequency peak and possibly generated by a wind wave system meeting a low frequency swell system that travelled a considerable distance losing much energy. An example of a swell dominated multi-peak spectrum is presented as *SPEC2*. This spectrum is dominated by a low frequency peak of an older swell wave system which coexists with a wind or a change in wind direction. When the wind subsides, the wave components become uncoupled and the wave system becomes a swell sea. For comparison a uni-modal short period spectrum is presented in Figure 4.54 as *SPEC3*. An equivalent Bretschneider spectrum with similar summary statistics is also plotted as an indication of the empirically derived spectral equations.

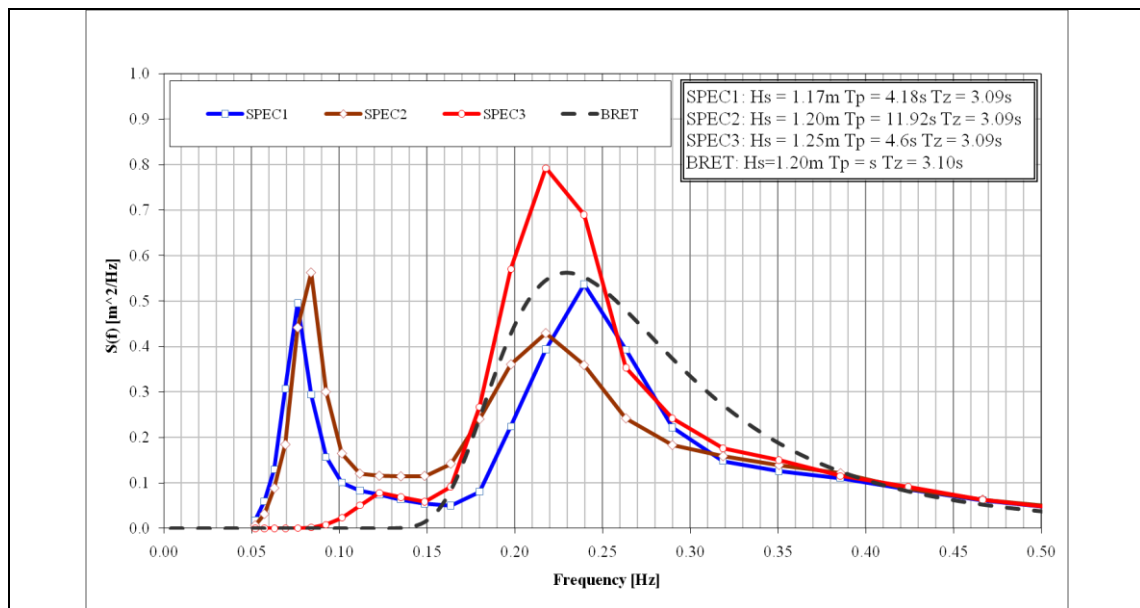


Figure 4.54. Examples of SWAN modelled twin peaked spectra with a single peaked spectrum, all of similar  $H_{m0}$  and  $T_{02}$  statistics.

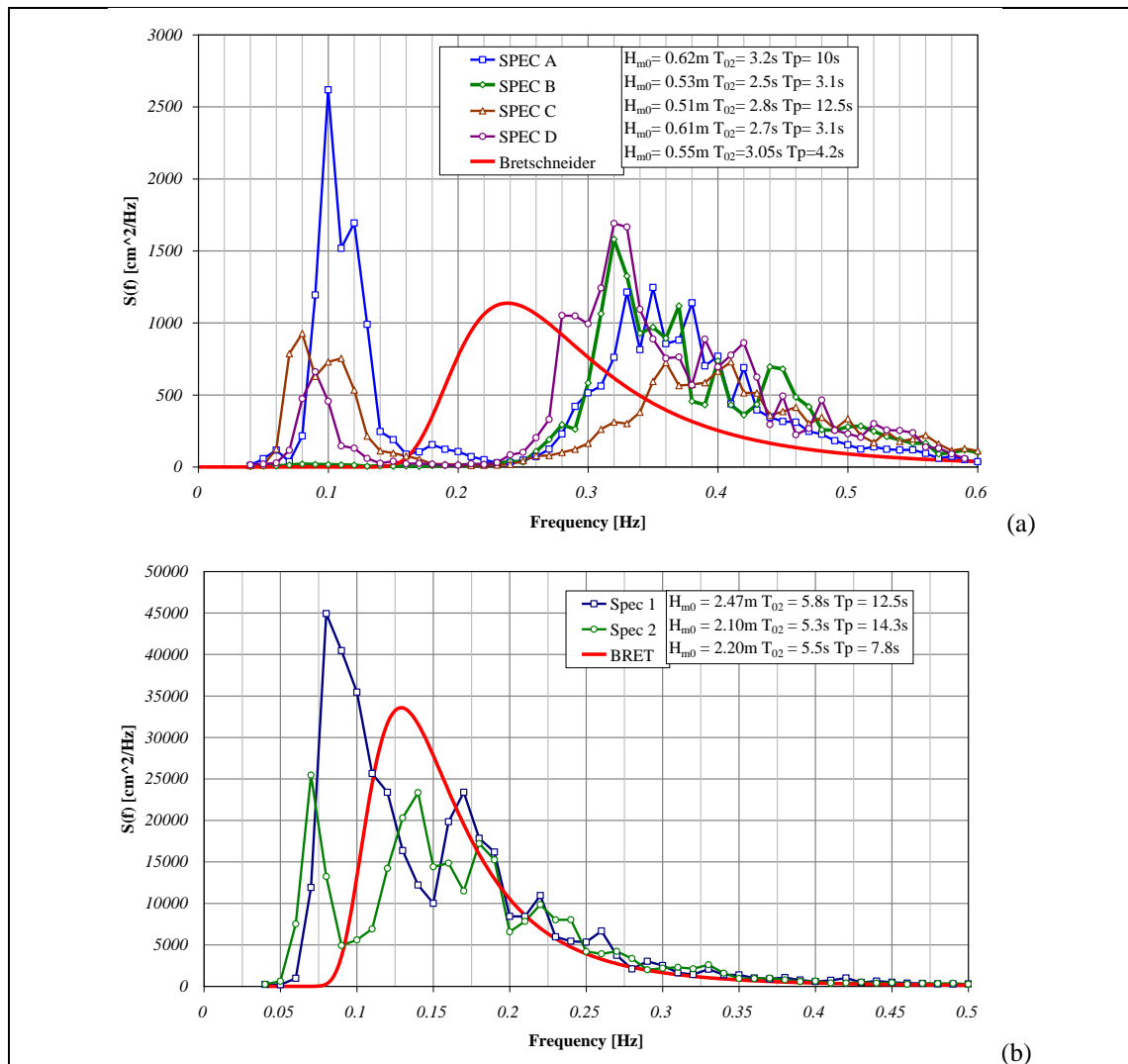


Figure 4.55. Examples of bi-modal spectra from Galway Bay (a) and Loop Head (b).

This phenomenon is replicated by real sea measurements as shown in some examples for both the Loop Head site and the test site in Galway Bay in Figure 4.55. This plot shows that for closely matching significant wave heights and wave periods, the distribution of variance over the frequencies can vary considerably. Superimposed upon these plots is the empirical Bretschneider spectral shape for similar summary statistics. It is easy to imagine that these spectral shapes can coexist within one element of a scatter plot.

It is clear from the above plots that there exists at Galway Bay a significant long period swell element at  $H_{m0} < 1.5m$ . It will be shown later that spectra such as these can have an effect on the power production of a WEC, especially if the resonant period of the device in question coincides with the frequency of the valley of a bimodal spectrum.

#### 4.7. Directional Spectra

Initially, the wave recording buoy on site in Galway Bay was a non-directional Datawell Waverider buoy. Preceding this, the SWAN modelling package was used to provide data for the test site. The two-dimensional spectra produced by the SWAN model was used as an indication of the wave directions present at the test site in Galway Bay. The modelled directional spectrum from the SWAN model is very smooth, therefore the assumption is made that any peak of a required magnitude is legitimate, therefore the identification of the peaks of wave systems is a trivial procedure. An example of a multi-modal directional spectrum is shown in Figure 4.56. This example shows the main swell peak propagating from a direction of  $245^\circ$ , which is Atlantic swell reaching the site from south of the Aran Islands. There are also, what appear to be two wind wave systems with two different propagation directions,  $95^\circ$  and  $245^\circ$ . These correspond to fetch lengths of 27.5 km from the southwest and 16 km from the east respectively (See Figure 1.10), and may be due to a turning wind direction.

The spectrogram of Figure 4.57 is a plot of the one dimensional spectrum derived from the SWAN directional spectrum concurrently for a period of one week. The evolution and decay of energy concentrations in the frequency domain is easily observed. A similar plot was also produced in Figure 4.58 which shows the development of the directional characteristics of the spectra over the same time period of five days in January 2000. Each section perpendicular to the date axis is the integration of the individual two-dimensional spectrum across the frequencies or directions respectively, i.e. the one-dimensional directional spectrum for that time step. The total wave height is less than 0.5m for this period.

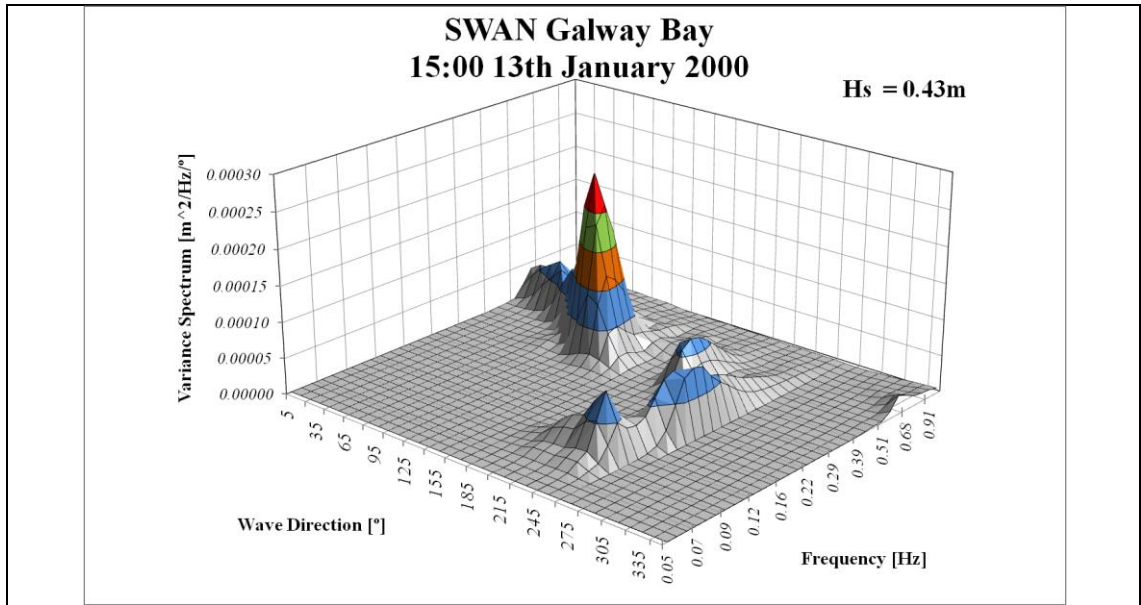


Figure 4.56. Example of multi-modal spectrum from SWAN Model.

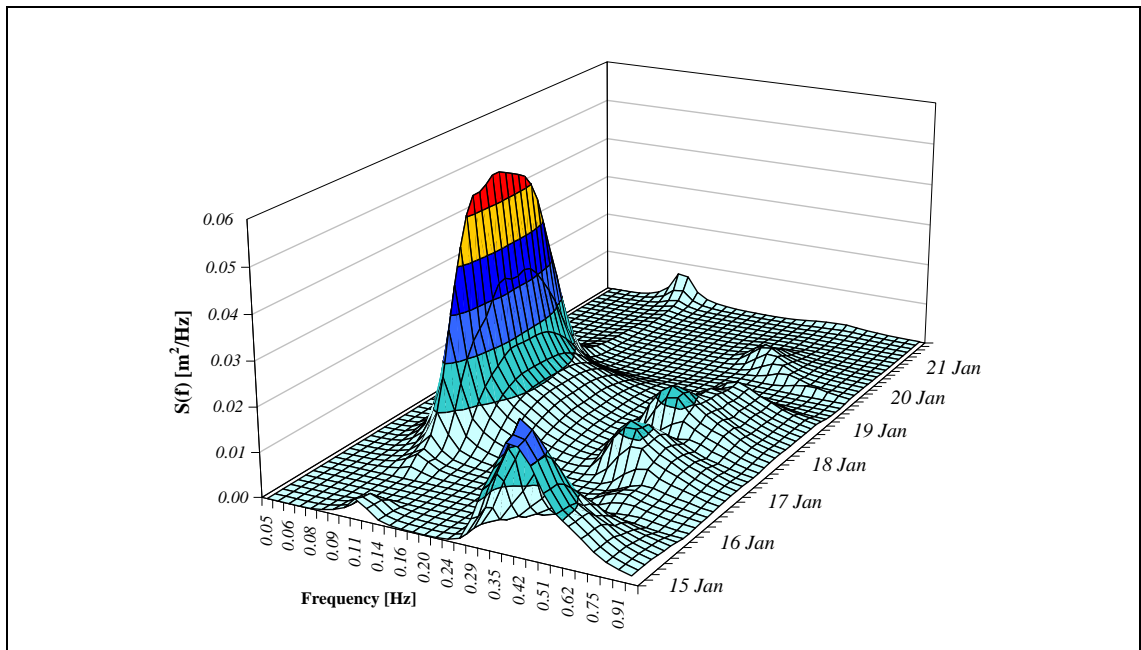
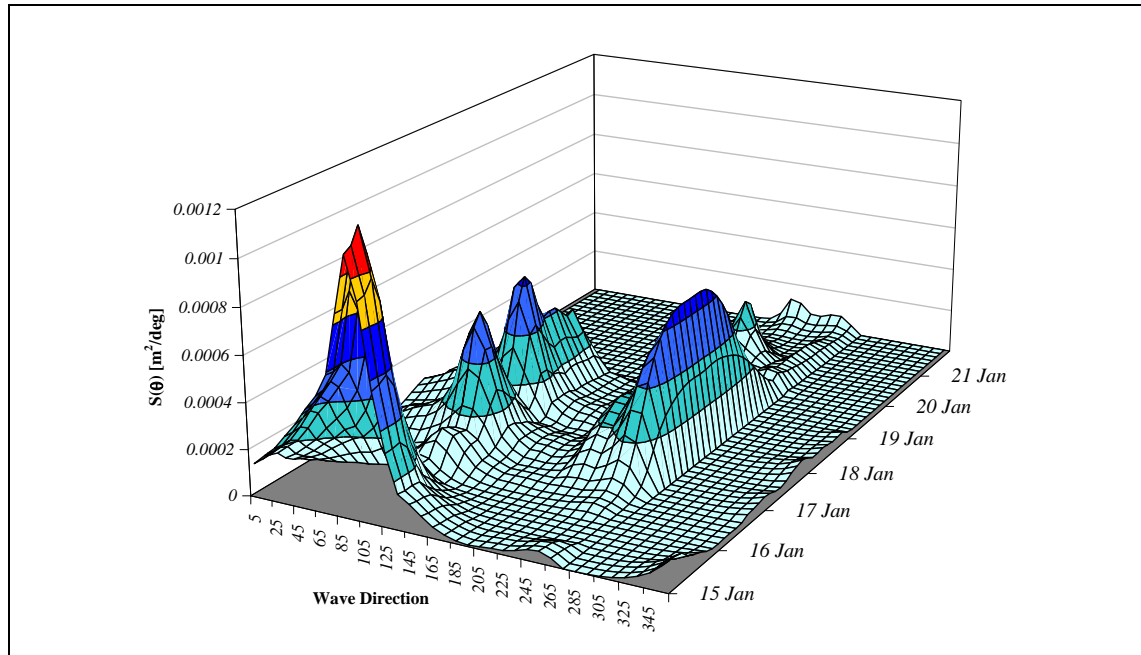


Figure 4.57. Spectrogram of variance density spectra for Galway Bay Test Site SWAN model.



**Figure 4.58. Spectrogram of directions for Galway Bay Test Site SWAN model.**

Reference to Figure 4.57 and Figure 4.58 indicates that for this short duration of a number of days, the origin of the waves at the test site is a combination of two sources, the dominant source being a local wind sea originating from the East and a secondary source with a wave direction of  $245^\circ$  propagating from the Southwest. This secondary source appears to originate offshore and approach the test site through the channel at the south of the Aran Islands. It is clear from both these plots that wave systems exist at the test site concurrently in both frequency and direction.

To understand the bimodality in the frequency domain, an algorithm similar to the preceding section was applied to the derived one dimensional spectra. As the SWAN output spectra are smoother in appearance than measured spectra, a simpler qualification procedure is applied, which is in essence a peak finding task. Again, once the peaks have been identified, the minimum point that exists between them is found and the frequency at which this minimum ordinate exists is used as the separation frequency to derive wind and swell sea state statistics. The results of the application of this method for significant wave height are shown in Figure 4.59 for the month of January 2000 and are quiet similar to the results from the application of the partitioning algorithm to the buoy measured data.

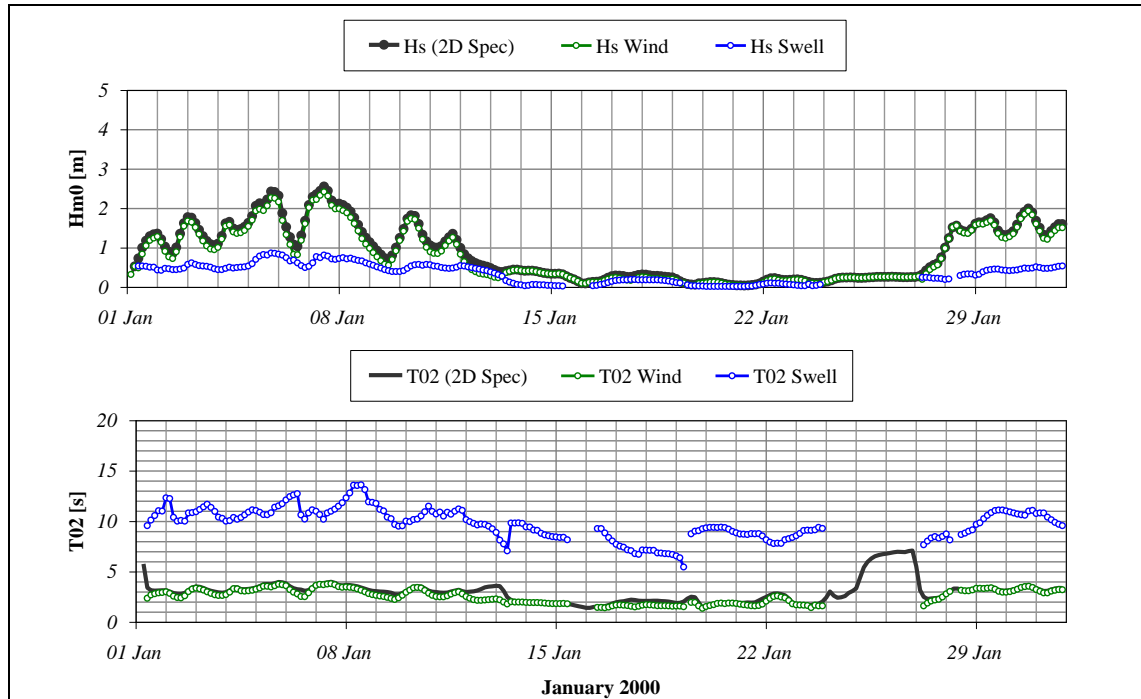


Figure 4.59. Application of separation method to SWAN model spectra.

By assigning the local peaks in each two-dimensional plot, such as that shown in Figure 4.56 with a direction, the wave direction of each peak for each time step in the data can be determined. Secondary peaks are accepted if their ordinate value is greater than 90% of the ordinate of the maximum or primary peak in the two-dimensional spectrum. The occurrence of these peaks is then further broken down into varying ranges of wave heights as shown in Figure 4.60, taking the month of January as an example. The dominant direction that transpires is  $215^\circ$  or south-southwest from the test site. Secondary wave directions propagate from southwest, which is the longest fetch length in Galway Bay (see Figure 1.10) and  $100^\circ$  east-southeast of the Test Site.

Only twelve months of SWAN data was made available for analysis, the month of January was chosen for further inspection as it contained the most energetic seas. Within the hindcast data for the month of January 2000, there are 247 two dimension spectra, and within this data there are 367 legitimate peaks indicating local wave systems. This results in nearly 50% of all January spectra being multi-peaked spectra. When a higher limit on wave height is placed on this data, the number of multi-peak spectra decreases significantly to 10% for all  $H_s > 0.5m$ , and 5% for all  $H_s > 1m$ . By referring to Figure 4.60, more than half the swell  $H_s$  from the separated spectra for January, is less than 0.5m, while no swell exists for  $H_s > 1m$ . From these results, it can be concluded that where the significant wave height exceeds 1m, it is likely that the spectra are single peaked wind



dominated, and for those significant wave heights below 1m, there is a combination in direction and wave source.

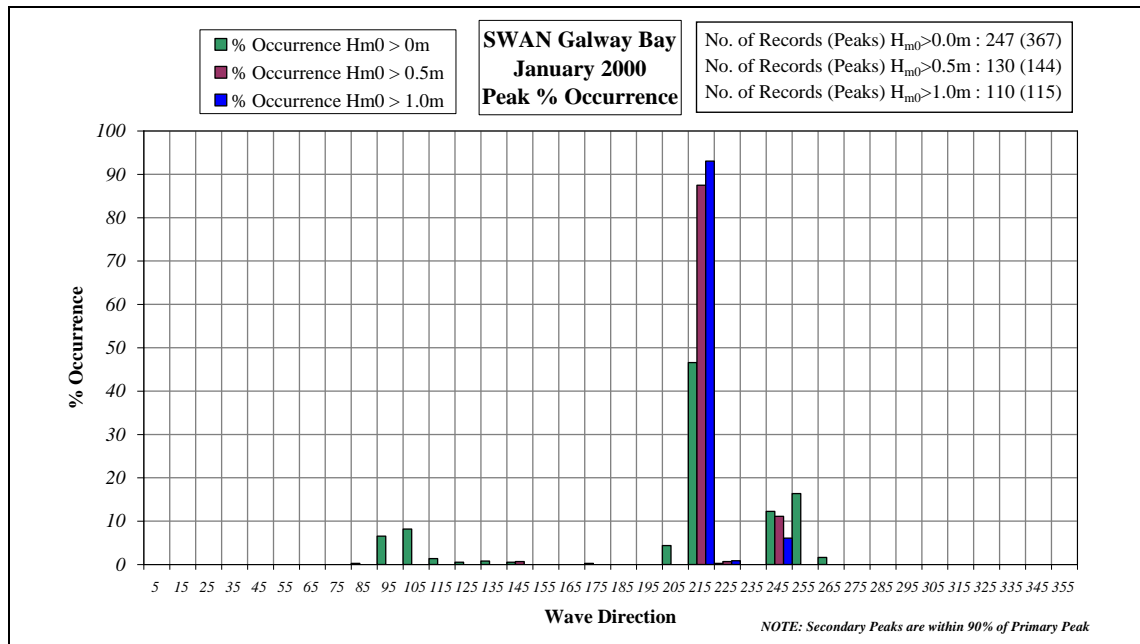


Figure 4.60. Percentage occurrence of wave system peak directions for January 2000, SWAN.

By determining the direction of the local peak in the same way as for Figure 4.60 for the remainder of SWAN model data for the year 2000, and calculating the percentage occurrence, a bi-variate scatter plot of the direction of the local peaks against significant wave height is produced in Figure 4.61. Again, the primary peak direction with 50% of all significant wave systems for the year is 215°, which is through the South Sound, between Inisheer, the southernmost Aran Island and the Clare coastline. The secondary direction is through the North Sound at 255° with 30% of all systems, propagating through the channel from Inishmore to the Galway coastline. The element of most occurrence for the year is 18% and has a propagation direction of 255° and lies between a significant wave height of 0.25m and 0.5m. From this direction, swell seas penetrate into Galway Bay from the open Atlantic Ocean.

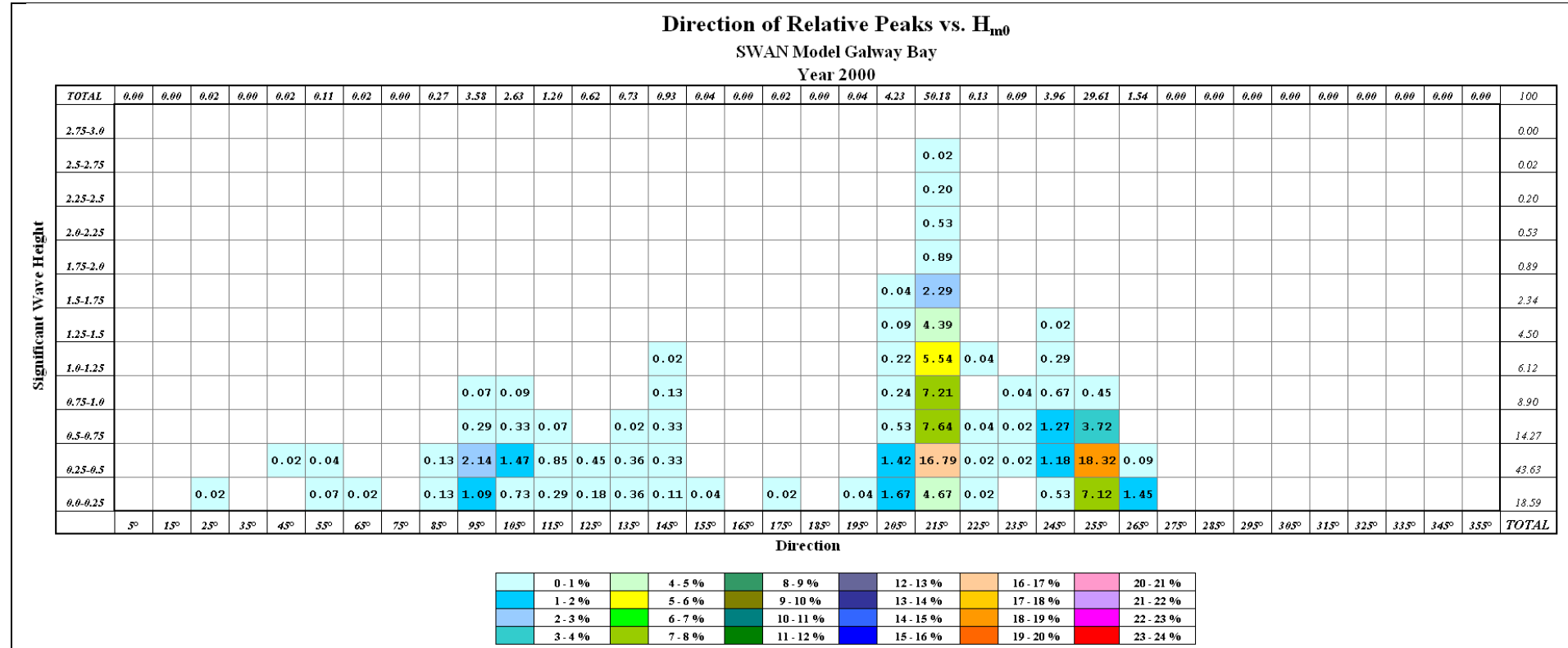


Figure 4.61. Percentage occurrence of direction of local peak wave systems.

## 5. SITE SCALING & WEC INTERACTION

Marine energy extraction is a complex process of which there are many facets. A greater knowledge of a device's working environment is required over the oceanographic standard of summary statistics. This means that near instantaneous measurement of the impacting sea state is necessary to understand the reaction of a wave energy or tidal current device. The primary objective is to quantify the power produced, which can be pneumatic, mechanical and electrical. Of equal importance is the assessment of weather windows for operation and maintenance issues and survival of these machines in severe storm conditions.

For a successful device development path, it is recommended that the development protocols and test schedules advised in documents such as the Irish Development Protocol (Holmes 2003), the DTI Device Performance Protocol (Smith and Taylor 2007) or the EMEC Performance Assessment guidelines (Pitt 2009) are followed. The strategies in these documents will mitigate both the financial and technological risk to the device developer, as they enforce a gradual increase in the size and complexity of the device from concept to commercial product based on Technology Readiness Levels. This is endorsed by the funding bodies and government agencies that have placed decision gates at the conclusion of each phase of testing to determine the success of the previous phase and the viability of moving to the next stage of device development (Sustainable Energy Ireland 2005). Each phase is carried out with guidance from a testing schedule which will be device dependent, and the overall path is termed the development protocol.

In the previous sections the evolution of the spectral shape over spatial and temporal scales was investigated and compared to the empirically derived expectation. The distribution of energy in the frequency domain as well as the contributing factors such as wind or swell seas have been investigated. However, as previously mentioned, the empirical spectra relate closely to the conditions at the measurement location and there exist methods of quantifying the impact that this has on the sea state as it evolves from calm conditions into more energetic seas. For a successful device deployment in real sea conditions, a thorough knowledge of both the incident wave conditions and the excited device reactions is required.

### 5.1. Benign Site Scaling

For an intermediate test site to be a fair representation of full-scale conditions, the sea states measured on site have to conform to the expected sea environment of a potential exposed offshore location. The analysis conducted here compares the Froude scaled seas of the Galway Bay test site at a quarter scale, to those conditions measured at the more exposed North Atlantic location of Loop Head, which would represent full-scale. This comparative exercise cannot be carried out on a sea state by sea state basis, as the inherent randomness of each sea state and the randomness of the associated measurement program or instrument may not give favourable results. Therefore, a more general and overall comparison is required involving an extensive data set over a period of time from a minimum of a season to a number of years.

By using Froude scaling laws and scaling the summary statistics of the recorded measurements, a scaling factor of ( $\lambda \approx 1:4$ ) is used to compare the results from Galway Bay to the measured results from the surface following buoy at Loop Head.

#### 5.1.1. Scalability

As the Galway Bay Test Site was proposed for the quarter scale testing of wave energy devices, it is expected that the sea states in Galway Bay would scale reasonably well to a full-scale exposed site representative of the North Atlantic. For a full-scale device rated as 2MW, a device designed for testing in Galway Bay will be rated at approximately 16kW. This is the case when Froude Scaling is applied, derived below in Equation 5.1 using Table 1.1.

$$Power = \frac{Force \times Distance}{Time} = \frac{kg \frac{m}{s^2} \times m}{s} = \frac{[M][L^2]}{[T^3]} = \lambda^3 \lambda^2 \lambda^{-\frac{3}{2}} = \lambda^{3.5} \tag{5.1}$$

Production of electricity at this magnitude will not justify grid connection or the expense of subsea cables. Instead, it should be possible to equip the device with a scaled power take-off mechanism, simulate grid connection and dissipate the produced power through heat exchangers or a similar system.

To compare the Galway Bay site to that of the North Atlantic, the summary statistics are scaled with Froude similitude laws using a scale of  $\lambda = 1:4$  and then compared to the statistics of the Loop Head site, which can be taken to represent a generic full-scale North

Atlantic deployment site. A representative data set of a winter season from December through to March was used for the Galway Bay site, scaled appropriately and used for this exercise, the results of which can be seen in Figure 5.1. Using the scaling laws described in Section 1.2, the significant wave height is scaled linearly while the wave period is multiplied by the square root of the scale factor.

The background in grey in this scatter plot is the measured hourly data from the surface following buoy positioned at the Loop Head site. Overlaid on this is the combined significant wave height,  $H_{m0}$  and average period,  $T_{02}$  values, scaled to prototype ( $\lambda = 1:1$ ) scale from the Galway Bay test site. It is evident from this graph that the scaled values of the sea states from the Galway Bay site do follow the “fully developed” line of constant significant steepness  $s_s = 1/20$ .

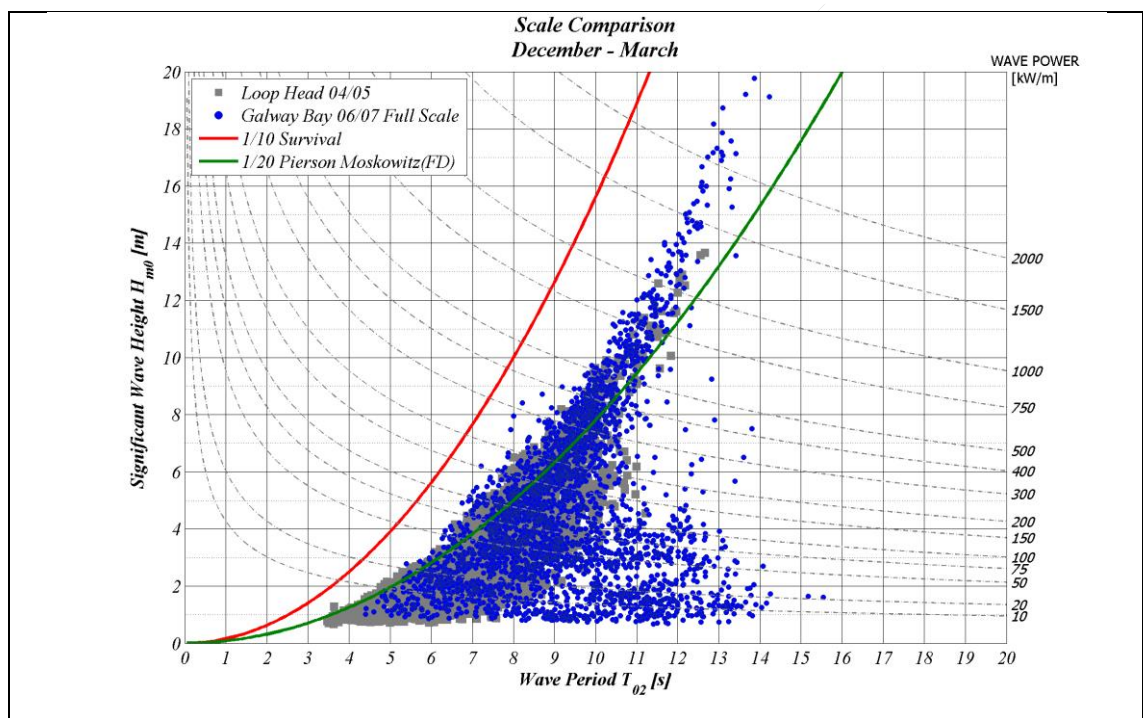


Figure 5.1. Comparison of scaled Galway Bay and Loop Head statistics.

Other than the long period, low wave height sea states that exist in Galway Bay due to the contamination of North Atlantic swell, the Galway Bay sea states scale well to the full-scale site, the extent of which is shaded in the background. However, the maximum significant wave height in the Loop Head data set measured just under  $H_{m0} = 14m$ , in contrast to the scaled Galway Bay data which approaches a significant wave height of  $H_{m0} = 20m$ , which is 43% greater. In a study of the measured significant wave height

from the US Navy's satellite 'Geosat' for the period from November 1986 to October 1989, Carter (1993) found that the 50 year significant wave height for the west coast of Ireland was determined to be approximately 20m as shown in Figure 5.2a. Other studies support this in determining the 50 and 100 year return significant wave height for the North East Atlantic (see Figure 5.2b and 5.2c). This agrees well with the scaled results from Galway Bay.

Focusing on the long period ( $T_{02} > 10s$ ), low wave height ( $H_{m0} < 4m$ ), Galway Bay scaled sea states, there are no occurrences of these type at the exposed Loop Head site. This is primarily thought to be due to the long period swell that reaches the wave energy test site from the Atlantic Ocean. This component of the wave spectrum is approximately full-scale at the wave energy test site, therefore it is not valid to scale this again.

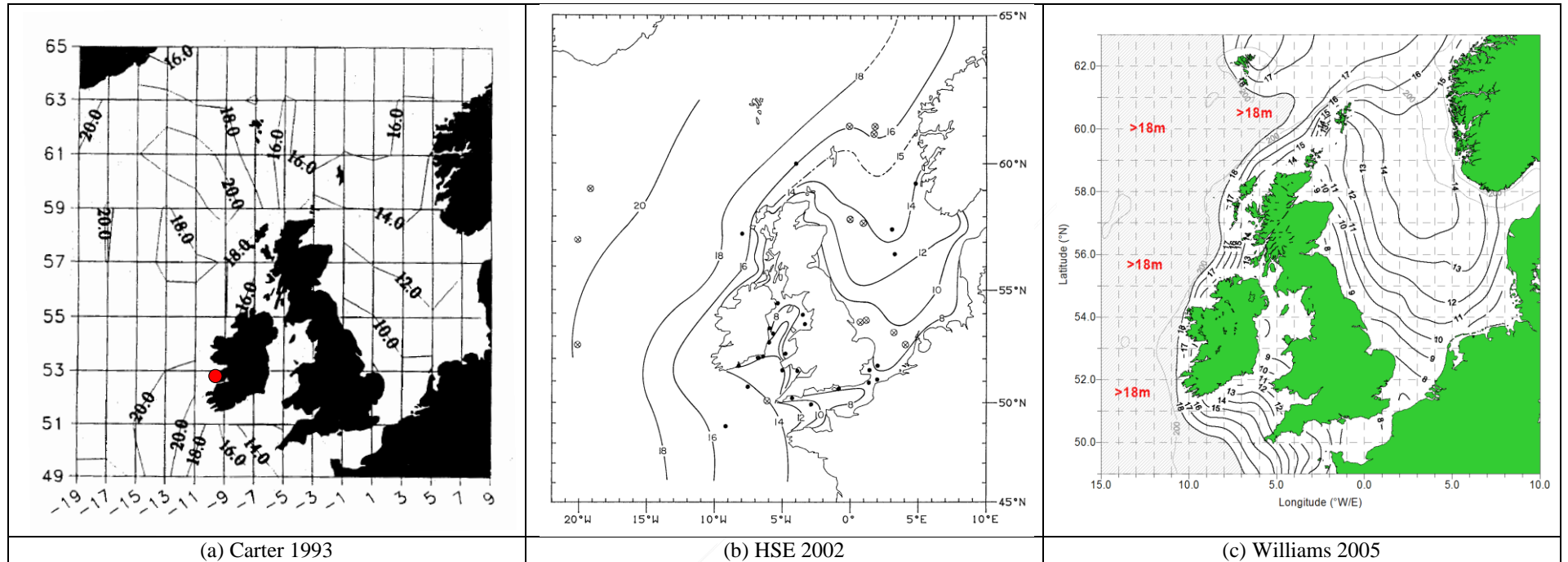


Figure 5.2. 50 year (a & b) and 100 year (c) return values of  $H_s$  for North Atlantic.

## 5.2. Wave Energy Device Interaction

One of the major issues that arises when moving from the early phases of wave energy device development, conducted in hydraulic facilities to initial sea trials is the loss of control of the excitation conditions. This imposition requires that the test programmes and data analysis techniques must be much more rigorous and expansive to ensure understanding and appreciation of the large amounts of information that should be in the process of being generated. This situation exists whether the early sea trials are being conducted at benign medium scale sites (circa  $\lambda \approx 1:4$ ) such as Galway Bay and Nissum Bredning or have advanced to full prototype size exposed locations such as EMEC, or the Portuguese's pilot zone or the many other demonstration sites proposed for the future around Europe.

Phase 3 of the Development Protocol bridges the end of laboratory model testing and the beginning of sea trials. The initial phases of the protocol will have involved controlled laboratory conditions, mostly being a combination of monochromatic trials with idealised irregular seas such as the standard representative formulae for Pierson-Moskowitz, Bretschneider or JONSWAP spectra. The detail of these panchromatic trials are at the discretion of the developer but it is envisaged that they represent all areas of a typical scatter diagram (Forestier et al. 2007). This phase also facilitates the assembly of a multi-disciplinary team to design and build a more realistic power take-off mechanism with all the power electronics and controls inherent with such a design.

In the relative comfort of hydraulic facilities, excitation sea states can be programmed on demand and repeated with reasonable fidelity as required. Besides classical seaways, any mix of wind sea and swell combinations should be possible, producing twin peaked spectra in the frequency domain, directional bi-modality or both simultaneously. Test schedules investigating the various aspects of a WEC design affecting performance can be drawn up and run to a pre-determined timetable. This convenience is not available once at sea and situations must be exploited when they become available. To achieve this control to any degree of satisfaction the appropriate sea state conditions must be identified implicitly. Simply knowing the summary statistics of the conditions is no longer satisfactory due to the variation in shape of the variance density spectrum, as has been shown in previous sections. Knowledge of the excitation forces is essential before understanding of the device response can be expected. As most floating wave energy



converter have a narrow response bandwidth, a high occurrence of twin peaked spectra may not produce the expected power production from the device, especially if resonance falls within the valley between the wind and swell spectral components.

### 5.2.1. Wave Excitation

During the laboratory trials of the OE Buoy, certain sea states were identified for testing the device in a range of conditions. These were represented by the Bretschneider equation and had significant wave height,  $H_s$  and peak period,  $T_p$  as input parameters. These sea states were tested at both the  $\lambda = 1:50$  and  $\lambda = 1:15$  scale trials using an orifice plate to model the PTO mechanism. By measuring the displacement of the water column and air pressure within the plenum chamber, the pneumatic power was calculated.

The scale of the OE Buoy device in Galway Bay was chosen as  $\lambda = 1:2.5$ , as this matched the resonant period of the device to the sea state of most occurrence for a given year. The OE Buoy was stationed on site on Christmas Day, 2006 (Irish Examiner 2008). Soon after that, it experienced the storm that was detailed in Figure 4.45. From the end of December 2006 to May 2007, an orifice plate was used to simulate the power take-off mechanism on the device (see Figure 1.4).

When testing in real conditions a decision has to be made, whether to wait for the environmental conditions that were set out in the testing criteria to occur, or to impose a time limit on the test schedule and to accept whatever sea states that may be realised. Eighteen Bretschneider seas states were tested in the previous two phases of the OE Buoy development and they are presented in Table 5.1, with summary statistics given at the Galway Bay scale of  $\lambda = 1:2.5$ . At best, it would be hoped that during the real sea testing phase, all of the seas states with the summary statistics of Table 5.1 would occur when there was concurrent device data being recorded onboard. The last column in Table 5.1 shows the number of concurrent measurements of device data and sea state data that are an approximate match to the sea states that have been tested in previous phases. Although this is only a small fraction in comparison to the amount of wave data recorded, in total there was 2,052 hourly OE Buoy data files in comparison to 3,685 Waverider buoy hourly records for the period from the end of December 2006 to May 2007. An example of this is shown in Figure 5.3, where the solid line is the buoy measured significant wave height, and the circles represent a concurrent OE Buoy device data file.

Sea State	Significant Wave Height, $H_s$ [m]	Peak Period, $T_p$ [s]	Avg. Period, $T_z$ [s]	No. Concurrent Measurements
B01	0.8	3.6	2.5	-
B02	1.2	4.5	3.2	2
B03	0.4	5.4	3.8	28
B04	1.2	5.4	3.8	59
B05	2.0	5.4	3.8	-
B06	1.2	6.7	4.8	28
B07	2.0	6.7	4.8	65
B08	3.0	6.7	4.8	-
B09	2.0	8.0	5.75	2
B10	3.2	8.0	5.75	4
B11	0.4	9.0	6.4	8
B12	1.2	9.0	6.4	-
B13	2.8	9.0	6.4	-
B14	3.2	9.0	6.4	-
B15	2.0	11.2	8.0	-
B16	0.4	6.7	4.8	38
B17	0.4	8.0	5.75	49
B18	0.8	8.0	5.75	16
Total				103

Table 5.1. Bretschneider sea states.

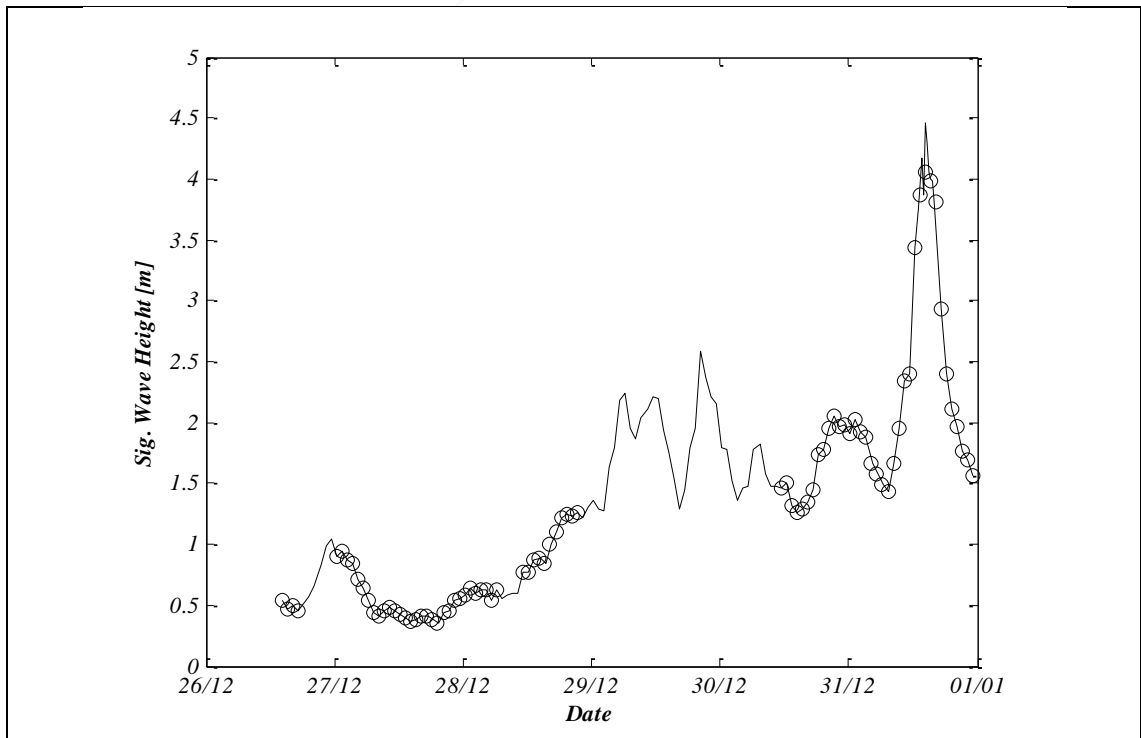
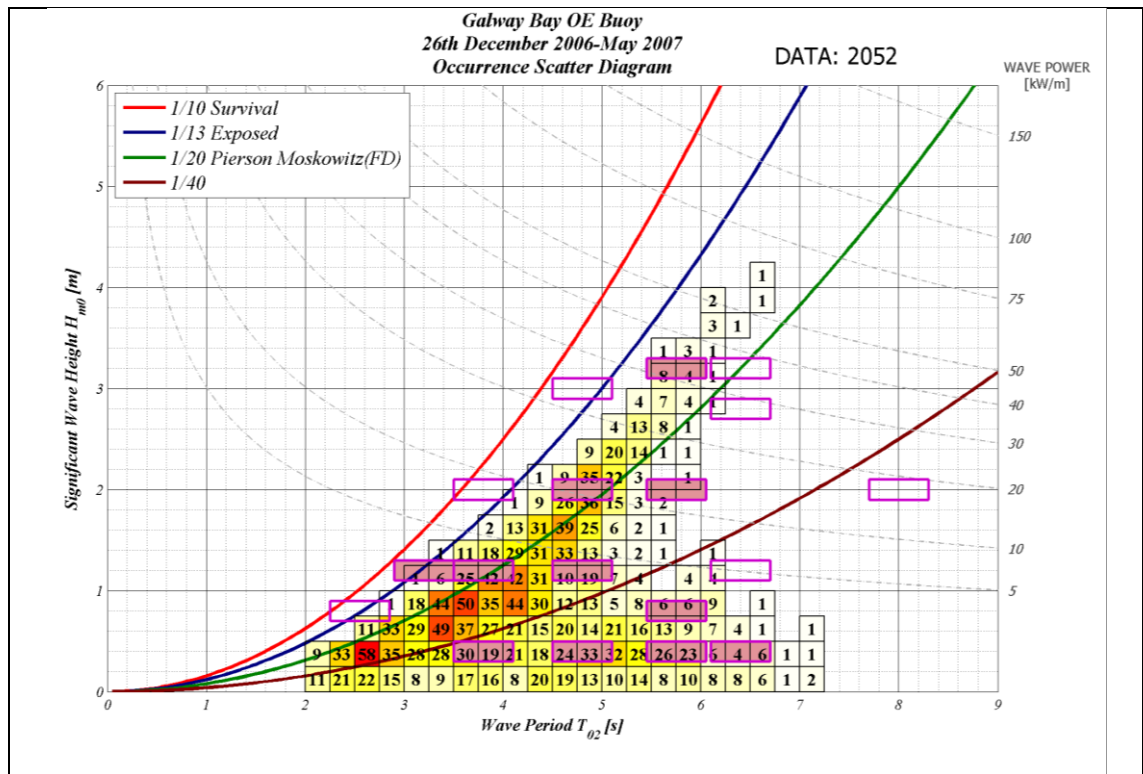


Figure 5.3. Plot of significant wave height, indicating concurrent OE Buoy data records.



**Figure 5.4. Scatter diagram occurrence for OE Buoy deployment in Galway Bay indicating trial sea states.**

Figure 5.4 shows the bi-variate scatter plot for the duration of deployment of the OE Buoy with the orifice plate PTO in Galway Bay. These occurrences relate to when there was both a wave data file and a device output file recorded within the hour, that is the circled data points in Figure 5.3. The eighteen test trial sea states, which were used in previous phases of the development protocol, are marked by the overlain boxes. The extent of the boxes in this plot have centres equivalent to the summary statistics presented in Table 5.1. The extent of the boxes are  $T_z \pm 0.3s$  and  $H_s \pm 0.1m$ . Eleven of the eighteen sea state trial boxes are shaded, indicating that there exists concurrent measured plenum pressure data from the OE Buoy, so that the power output of the device can be compared to the impinging sea state and the scaled results from previous trials.

**5.2.2. Device Power Response**

The power output from the OE Buoy wave energy device is obtained by measuring the instantaneous air pressure within the plenum chamber and using the orifice equation with a coefficient of discharge value that was obtained and verified through the previous phases of testing to calculate the power output. Pneumatic power ( $\mathbb{P}$ ) results from the symbiotic relationship between air pressure ( $\Delta p$ ) and air volume flow ( $Q$ ) through an orifice. When only one of these parameters can be measured, in this case the air pressure

within the plenum chamber, then the orifice equation can be used to determine an estimate of the unmeasured parameter,  $C_d$  (Equation 5.2), or the power output can be calculated directly by using Equation 5.3:

$$C_d = \frac{Q}{a \sqrt{\frac{2 \Delta p}{\rho}}} \quad (5.2)$$

$$\mathbb{P}_p = C_d a \Delta p^{\frac{3}{2}} \sqrt{\frac{2}{\rho}} \quad (5.3)$$

where  $C_d$  is the coefficient of discharge,  $Q$  is the air volume flow,  $a$  is the area of the orifice,  $\Delta p$  is the air pressure within the plenum chamber,  $\rho$  is the density of the air, and  $\mathbb{P}$  is the pneumatic power output, and the subscript  $p$  denotes that the power is derived from the measured pressure only using the discharge equation.

Due to confidentiality issues in relation to the device data, the nominal values of the produced power output of the OE Buoy cannot be published. As a result, the power production figures are normalised to the greatest average power output value obtained from the  $\lambda = 1:15$  scale trials conducted at ECN, Nantes in France. From Table 5.1, sea state *B08*, tested during Phase 2 of the Development Protocol at ECN ( $\lambda = 1:15$ ) produced this maximum average power output value, which is then set as the benchmark of 100% for all subsequent averaged power output values in the comparison below.

Figure 5.5 plots the significant wave height,  $H_{m0}$ , in the top graph, the wave energy flux,  $\mathbb{P}_w$ , on the left hand ordinate axis of the lower graph and the normalised pneumatic power output calculated from the internal air pressure,  $\mathbb{P}_p$ , which is indicated by the diamonds on the right hand ordinate axis of the lower graph, for the first few days of deployment in December 2006. The storm at toward the end of December was the largest experienced by a device in Galway Bay, and the significance of the power produced can be seen in the plot, where it approaches the target value during the storm event.

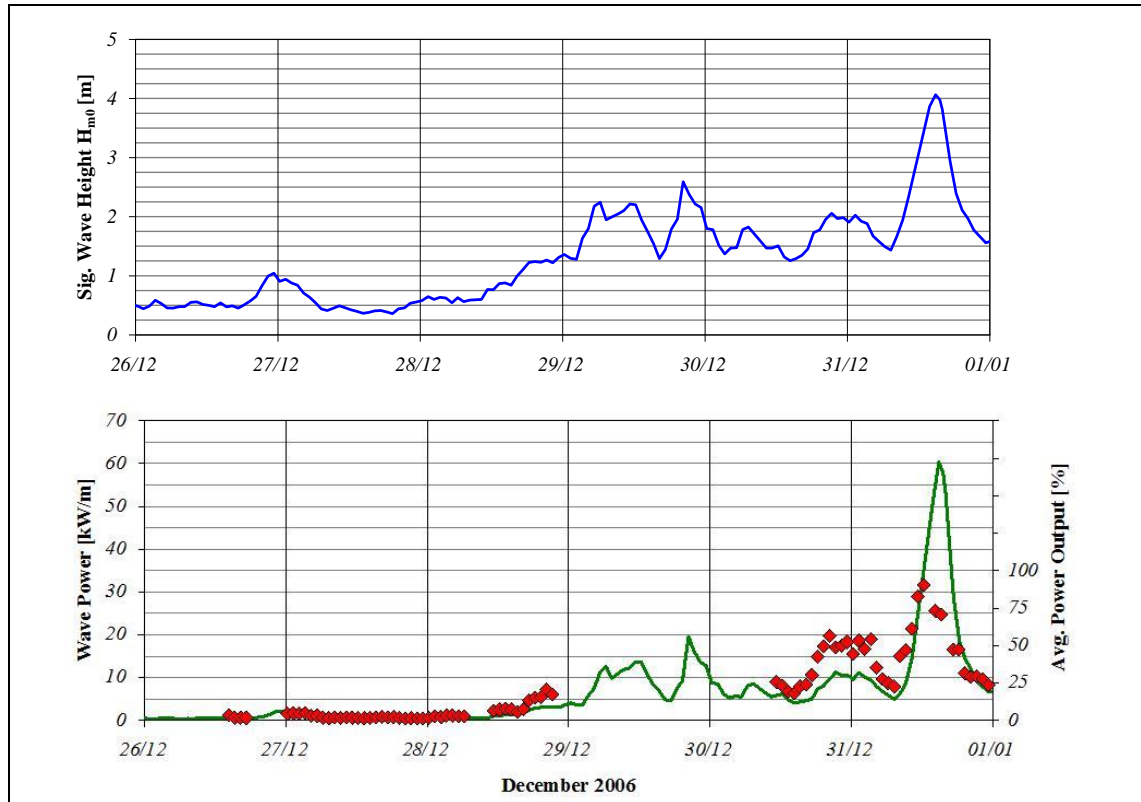


Figure 5.5. Wave height, wave power and average device power output for December 2006.

In order to determine if the device is generating what it is capable of, the results of the previous device development phases are scaled from  $\lambda = 1:50$  and  $\lambda = 1:15$ , to the Galway Bay scale of the device,  $\lambda = 1:2.5$ . However, this can only be achieved for the eighteen sea states described in Table 5.1, which were tested at the laboratory phases. The results of these trials, scaled to Galway Bay and normalised as described above, are shown in Figure 5.6. The sea states that are used as examples in the following section are indicated, along with the benchmark sea state of the *B08* from the ECN trials at 100%. Good agreement was found when a comparison of the power output from each scale was made, although the results from the  $\lambda = 1:15$  ECN trials are slightly higher due to the greater influence of vorticity losses at the smaller scale. This gave the device developers and funding body's confidence to proceed to the next phase at the Galway Bay benign wave energy test site.

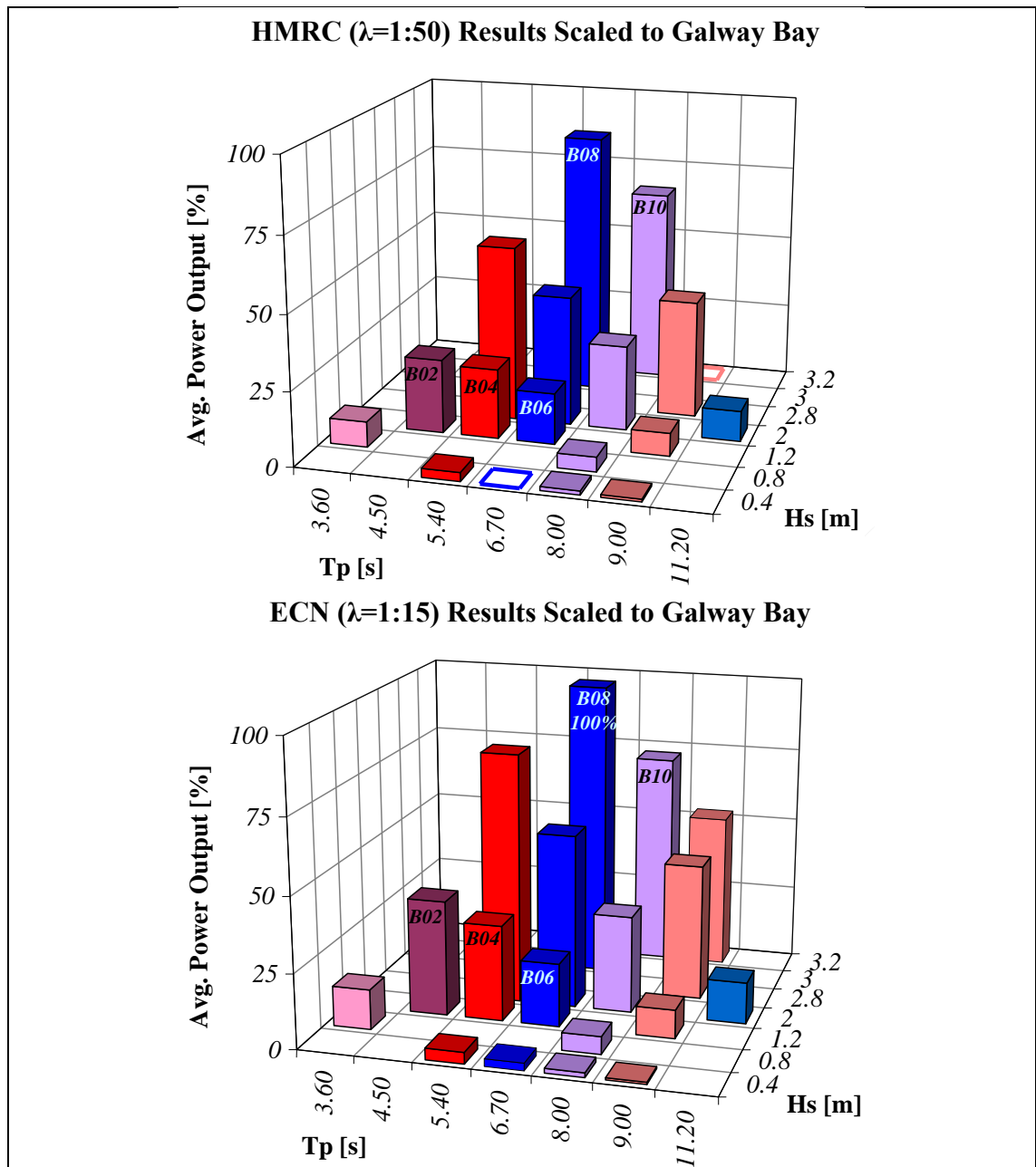


Figure 5.6. Average device power output from Phase 1 and 2 testing scaled to Galway Bay.

The inconsistency in the distribution of the variance density over the frequency range of a spectrum will have varying degrees of influence on the power production of the device. When concentrating on one element of the scatter plots such as those shown in Figure 5.4, it may not always be the case that for the same summary statistics, the spectral frequency distribution will be identical, such as the spectra shown in Figure 4.55. A further complication of the issue is that a device cannot be expected to perform equally due to the variation of the excitation spectra, therefore different power levels will be produced by the device for the same summary statistics. By scaling the previous laboratory trial results to that of the sea trials and comparing the power output, an

understanding of the influence of changing spectral shape can be deduced. This effect is especially exaggerated when the valley between the wind and swell wave system components coincide with the eigen frequency of the device.

In this instance the normalised results from the previous phase of testing is based on the average power output of the individual sea states from Phase 2 of the development protocol. For each of the following examples of sea states, the 100% level of power output is set by using the measured 30 minute average power output of the device from the testing phase at  $\lambda = 1:15$  and scaling the result to the Galway Bay OE Buoy scale of  $\lambda = 1:2.5$ . The variation of the normalised power output from the OE Buoy device in Galway Bay per identified sea state as given in Table 5.2 is then plotted as the histogram.

In the following figures, the concept of a power spectrum is introduced. This spectrum is used to understand the resonant properties of the power take off when excited by the incident wave field. The power spectrum is determined by applying the sign of the pressure signal to the power determined using Equation 5.3. This power signal now oscillates about zero, and is analysed using an FFT algorithm in the same way as the wave signal to produce a power variance density spectrum.

Selected sea states *B02*, *B04* and *B06*, that are indicated in Table 5.1 and by the shaded areas in Figure 5.4 with  $H_{m0} = 1.2m \pm 0.1m$  are represented in Figure 5.7 to Figure 5.9. Each bar of the histogram represents an individual device data record, from which the power output calculated from the instantaneous recorded internal plenum air pressure due to the twenty minute excitation sea state is derived. The number of bars in the histogram for each sea state is the number of sea states that occurred within the respective shaded area of Figure 5.4 and given in Table 5.1 as the number of concurrent measurements. The only parameter that was free to vary is the peak period,  $T_p$ , the values of which increase left to right along the abscissa axis.

As an indication of the variation of the spectral shape for these sea states, the respective spectra for the wave input and device power output, indicated by the hatched bars of the histogram, are also shown in these plots. For each of the three spectra shown in Figure 5.7, the wave spectra, indicated by the heavy blue line has the same ordinate axis scale on the left of the individual plots, however as the first wave spectrum produces more

power, the power spectrum, indicated by the lighter red line with the ordinate axis on the right of each plot, has a larger scale for this than for the other two. The ordinate values of the device power spectrum are not plotted due to confidentiality. The equivalent Bretschneider, which would have been the input sea state tested at the earlier phases to produce the 100% benchmark is also shown. It is clear from the variation of the wave spectral shapes why the device produces different power levels. The second and third wave spectra are very similar, being very narrow with large magnitude peaks, but it is the wider first wave spectrum that produces the greater power output.

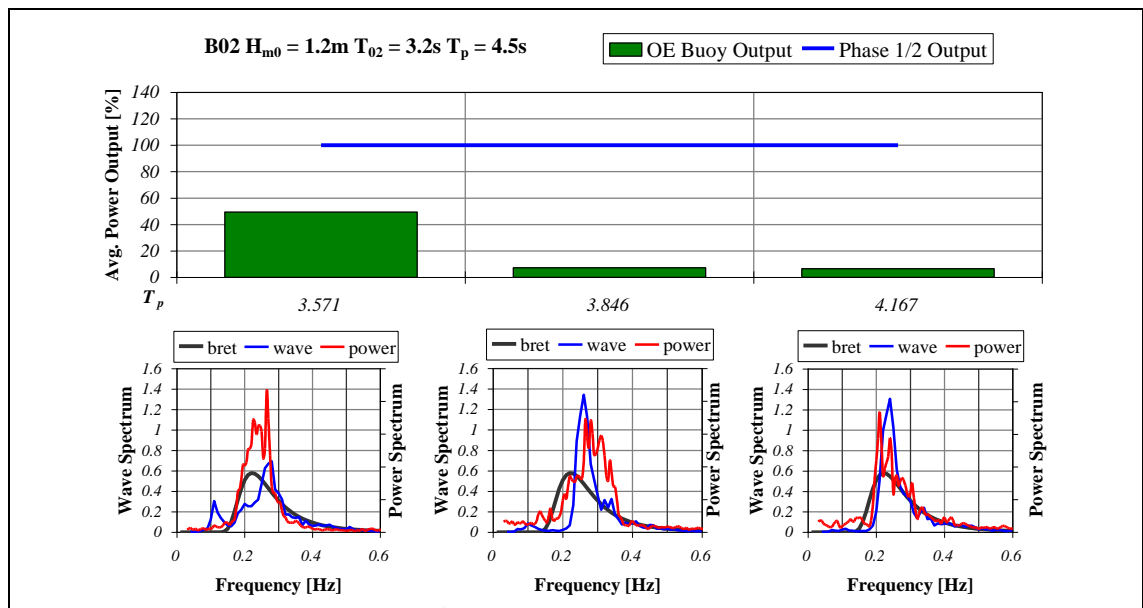


Figure 5.7. Device power output for selected sea state  $B02: H_{m0} = 1.2m \pm 0.1m,$   
 $T_{02} = 3.2s \pm 0.3s.$

Figure 5.8 shows a similar plot for another sea state with the same significant wave height but for a longer period than the previous example. This sea state,  $B04$  resides on the fully developed line, therefore it experiences the second most occurrences of recorded power output. Again, the variation in power output from the device can be seen and some examples of the wave and power spectra are shown for the indicated power outputs in the histogram. Note that the power spectra do not exhibit the same scale. One of the extreme cases of power level variation is shown in the first example of the spectral forms in this figure. Due to the well-defined double peaked spectrum and the valley between the two wave systems coinciding with the resonant frequency of the device, only 5% of the power output that would be expected to be produced by an equivalent spectrum with similar significant wave height and average period and defined by the Bretschneider equation is achieved.



The final example for this significant wave height is shown in Figure 5.9. As with the previous examples, the same characteristics of the power output due to the frequency distribution of the input wave spectrum can be seen. Again, the power spectra scale is not consistent throughout this plot. When the wave spectral shape is close to the target spectrum, or when the variance density ordinates at the resonant frequency of the device are high, the average power output of the device approaches the target level for that sea state.

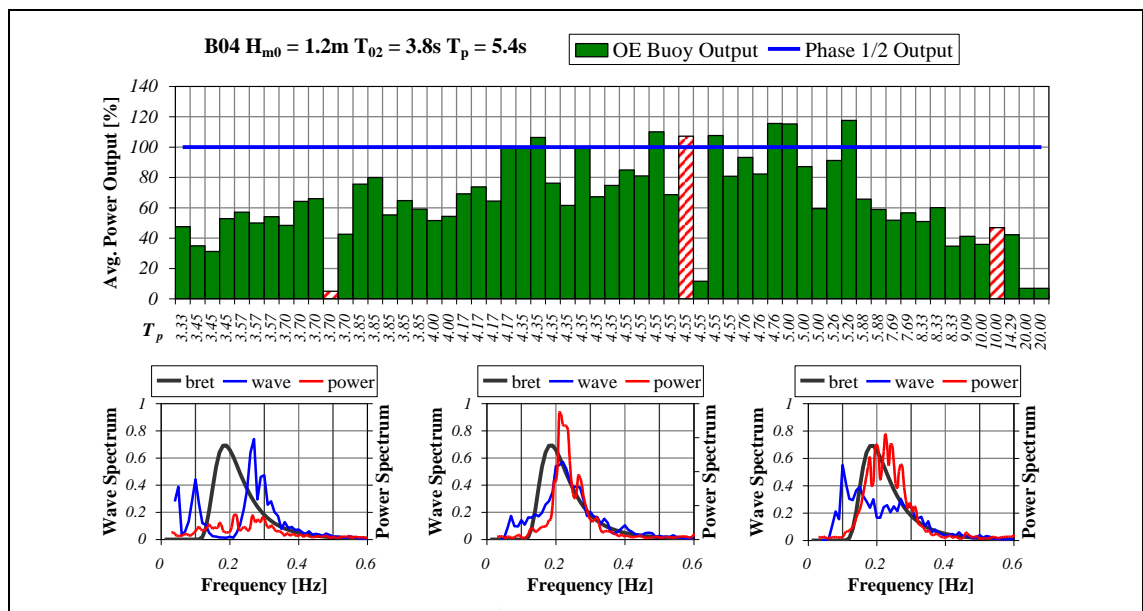


Figure 5.8. Device power output for selected sea state B04:  $H_{m0} = 1.2m \pm 0.1m$ ,  $T_{02} = 3.8s \pm 0.3s$ .

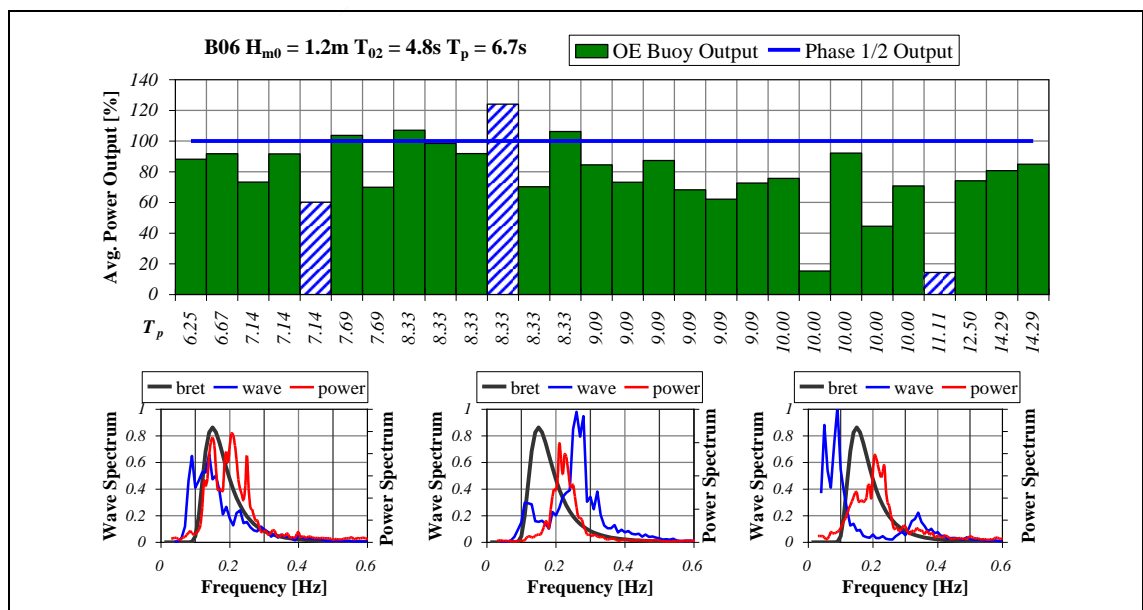


Figure 5.9. Device power output for selected sea state B06:  $H_{m0} = 1.2m \pm 0.1m$ ,  $T_{02} = 4.8s \pm 0.3s$ .

Floating wave energy devices respond to a very narrow frequency range unless they have multi-resonant components or a control strategy is implemented to enhance the power capture of the device. The frequency response of the OE Buoy is evident from inspection of the Power Response Amplitude Operator (RAO) of the device, which is derived from Equation 5.4 with units of power per meter of wave height elevation:

$$\text{Power RAO} = \sqrt{\frac{\text{Power Variance Spectrum}}{\text{Wave Variance Spectrum}}} \text{ [kW/m]} \quad (5.4)$$

The Power RAO for the example sea states of Figure 5.7 to Figure 5.9 are shown in Figure 5.10. The order of the examples in the legend of each plot relates to the selected elements of the histogram in each of the figures above. The Power RAO from the above equation is normalised so that the maximum value at resonance has a value of unity. The Power RAO can be used to indicate the resonant frequency of the device. The large magnitude values at the very low and high frequencies are due to division of small numbers and can be expected when using sea states with short characteristic periods. The peak of each of the RAOs reside at the resonant frequency of the device and it is at this frequency that the level of energy in the incident sea state will dictate the power production of the device. The RAO plot with the highest ratio of unity is not necessarily the sea state that produced the most power of the three examples, but where the ratio of the incident wave spectrum to the output power spectrum at the resonant frequency is largest. Inspection of Figure 5.10 combined with Figures 5.7 to 5.9 indicates that when the variance density of the wave spectrum at the resonant frequency is lower than that indicated by the Bretschneider equivalent, then the power output of the device will be lower than the expected benchmark and vice-versa.

The variation of the frequency distribution of the wave spectrum tends to vary less as the significant wave height increases. Evidence of this is shown in Figure 5.11, which shows the histogram of power output and some selected spectra for one of the storm seas, B10. In the case of the three spectral examples shown, the wave spectra are a close match to the expected empirical solution and the power output is within 25% of the target power output for each matching sea state that occurred.

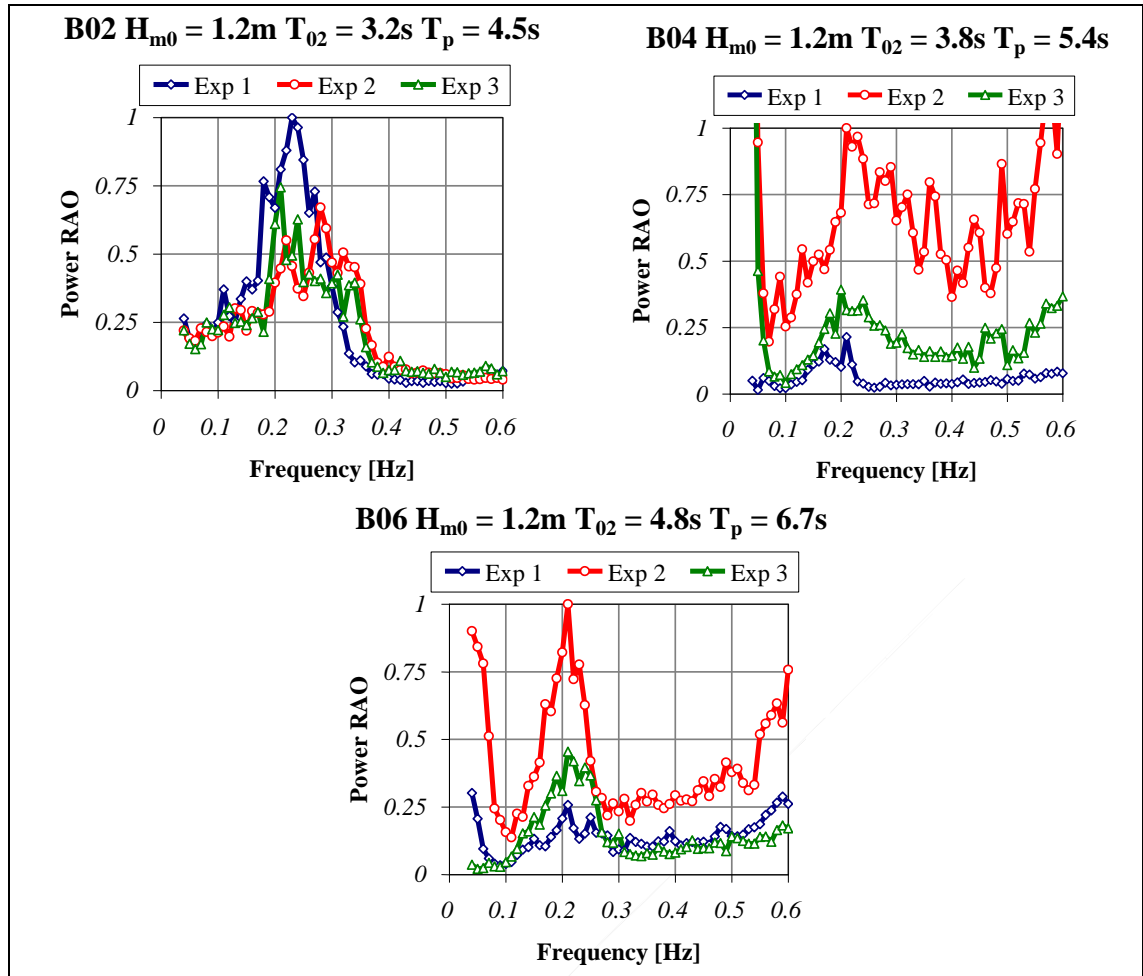


Figure 5.10. Power RAO for sea states B02, B04, and B06.

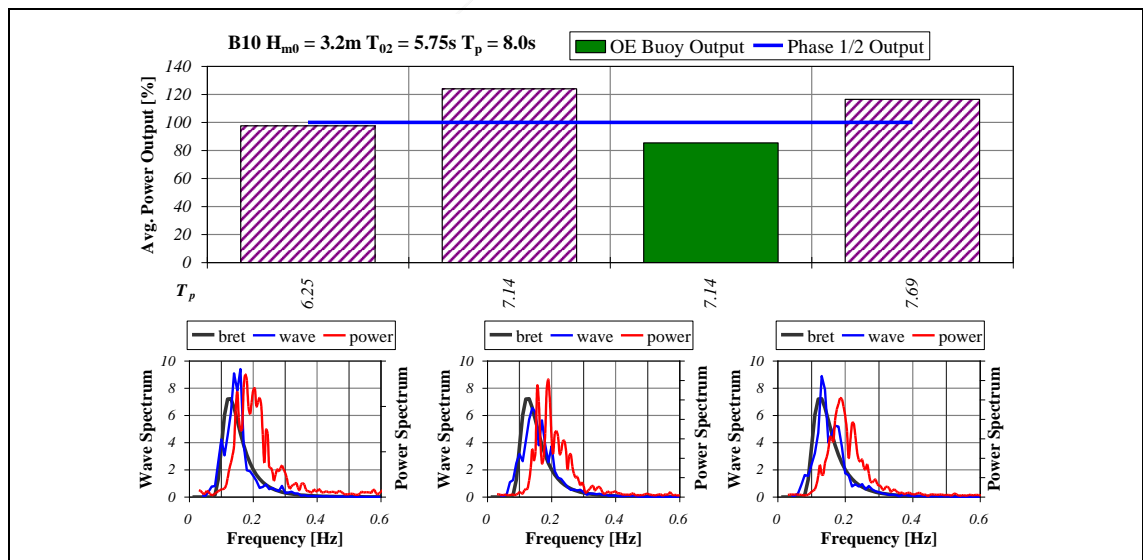


Figure 5.11. Device power output for selected sea state with  $H_{m0} = 3.2m \pm 0.1m$ ,  $T_{02} = 5.75s \pm 0.3s$ .

Figure 5.12 shows the Power RAO plot for the storm seas given in Figure 5.11. Although the first example of Figure 5.11 has the largest magnitude RAO, this sea state does not

produce the largest power output of the examples shown. The peak of the RAO plots occur at the resonant frequency of the device, and the combination of the incident and output spectra at the resonant frequency produce the magnitude of the peaks at that frequency.

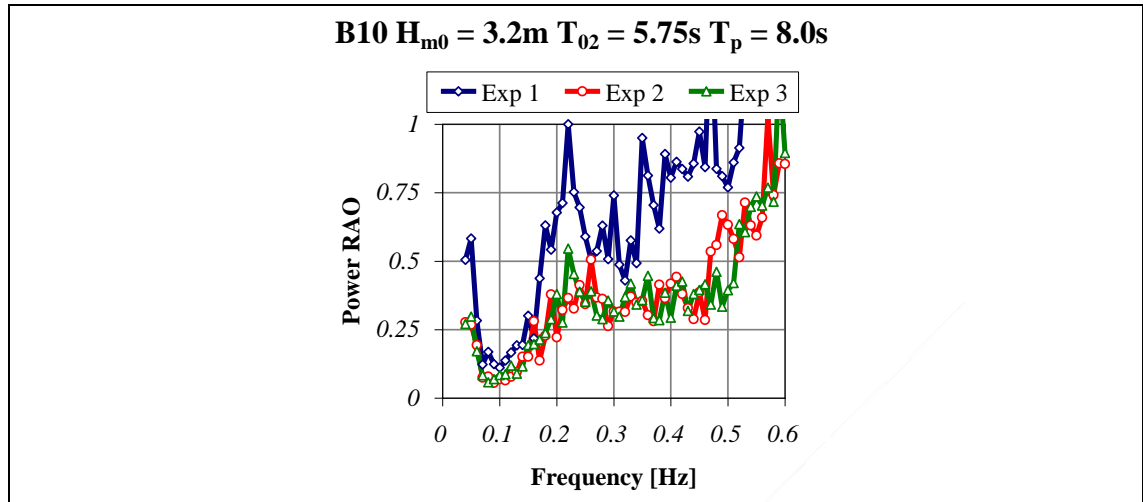


Figure 5.12. Power RAO for storm sea state B10.

The device normalised average power outputs that are depicted by the histograms for the sea states listed in Table 5.1 are used to determine how closely the device scales to the previous phases of the development protocol. An indicative power output per sea state is achieved by normalising the average power output of each sea state from Galway Bay to the Phase 2 benchmark ( $\lambda = 1:15$ ) and the resulting bar chart is plotted in Figure 5.13 along with the ECN results repeated from Figure 5.6 for direct comparison. The bar chart elements that are outlined are of those sea states that did not occur in Galway Bay during the six-month testing schedule.

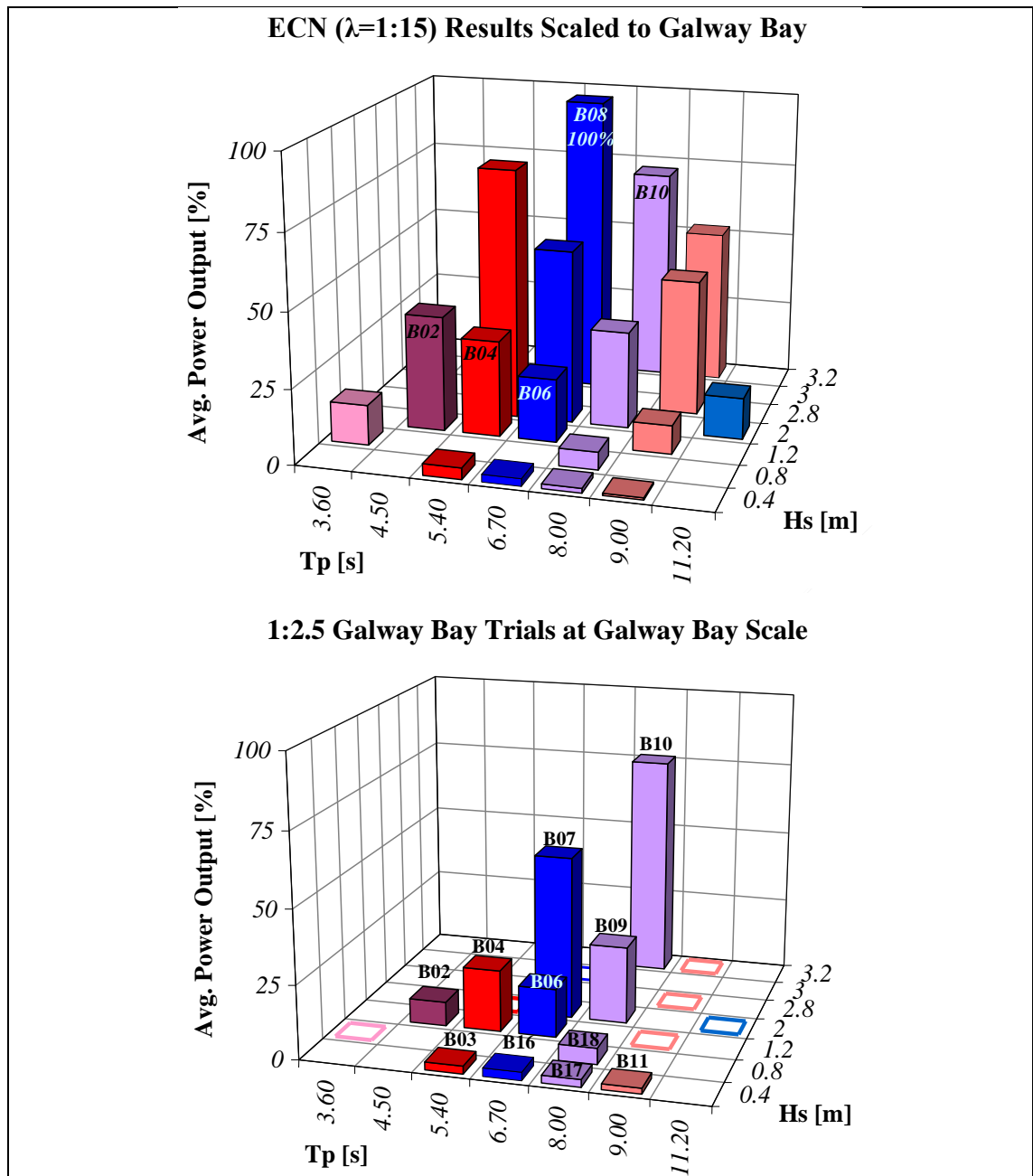


Figure 5.13. Normalised power output of  $\lambda=1:15$  ECN trials and results from Galway Bay.

For those sea states with  $T_p = 6.7s$  and  $8s$  in Figure 5.13, the average device power output scales quite well to the previous phases of testing, however for those sea states with a shorter peak period, but also a lower significant wave height, there is a significant difference in the levels of power output. This is due to the larger variation in the wave variance density spectrum that defines these sea states as shown above, especially with the results of the investigation of the sea state spectral properties that gave similar summary statistics to B02 in Figure 5.7. This gives an indication of the differences that can be experienced at real sea deployment sites when there is no longer control over the

input wave conditions and the device power output may not be at expected or estimated levels.

The individual normalised average power outputs of the 2,052 device power output files that were measured concurrently with the sea states are plotted on the left of Figure 5.14. Each one of the data points in this plot represents a twenty minute record. To the right of this figure, is the same plot but with the expected normalised power outputs from the previous trials at ECN, scaled to Galway Bay, and overlaid as a surface. Any points represented by the stem plot that is visible above the surface are device power outputs that exceeded the expected level that was set and verified from previous phases of testing.

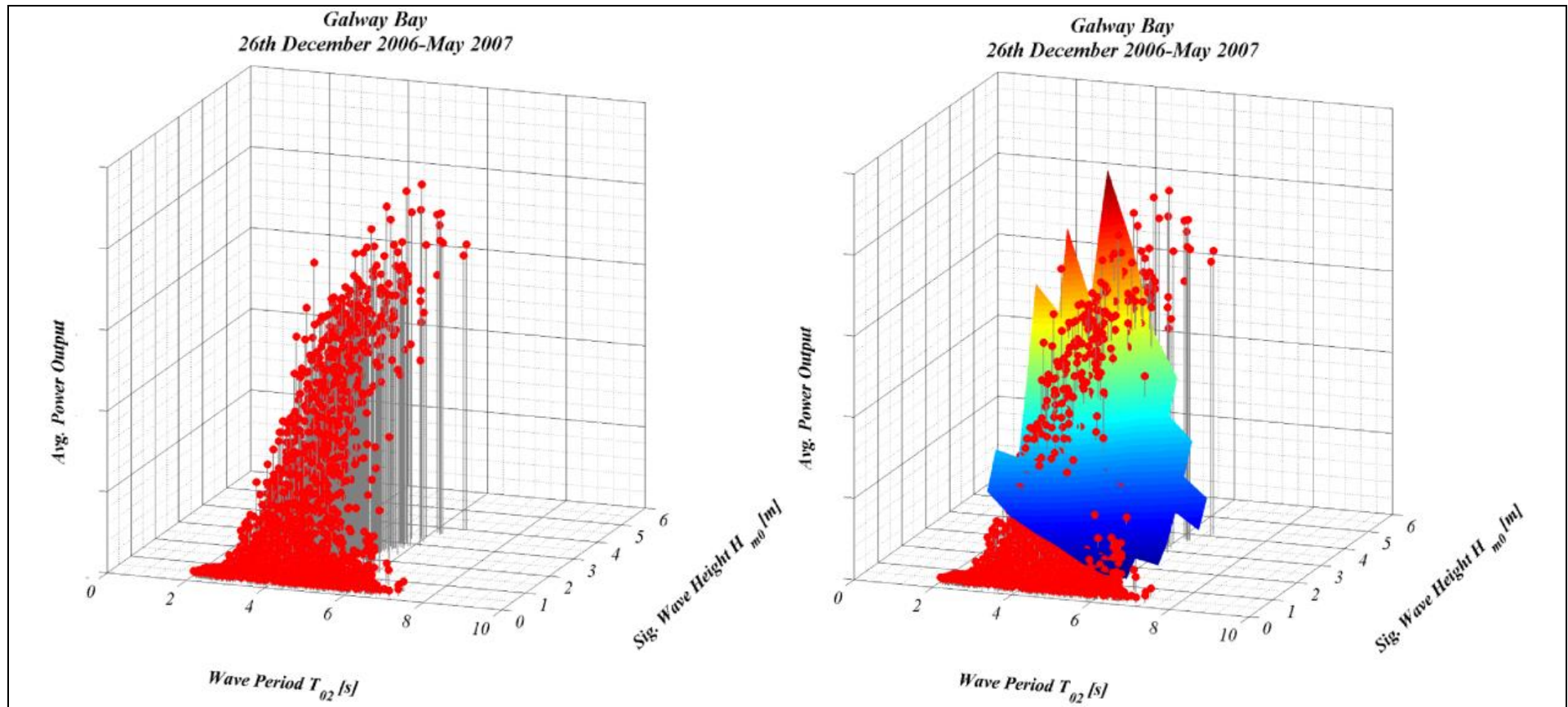


Figure 5.14. Average Power Output of OE Buoy in Galway Bay (left) and Surface of Expected Power Output Level from Previous Phase Testing (right).

As a final conclusion, the power map of the OE Buoy device, using the results from the previous phase ECN trials, and scaled to Galway Bay, is shown in Figure 5.15. This is achieved by fitting polynomials along the significant wave height and peak period axes to achieve a correlation close to one. Two examples are given in Equation 5.5 for  $H_{m0} = 1.2m$  and in Equation 5.6 for  $T_p = 8s$ .

$$\begin{aligned} & \text{All } T_p @ H_{m0} = 1.2m: \\ & y = 0.1555x^2 - 3.7107x + 23.003, R^2 = 0.9974 \end{aligned} \tag{5.5}$$

$$\begin{aligned} & \text{All } H_{m0} @ T_p = 8s: \\ & y = -0.2369x^3 + 2.4695x^2 - 0.0832x + 0.0246, R^2 = 1 \end{aligned} \tag{5.6}$$

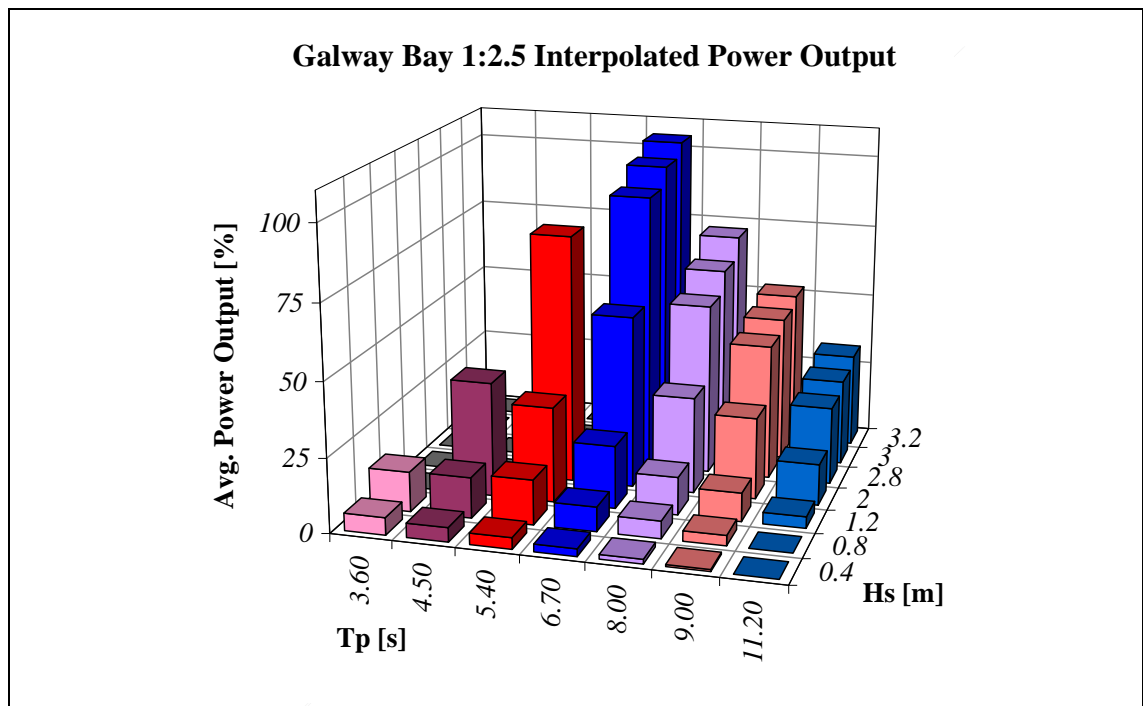


Figure 5.15. Interpolated target average power output for OE Buoy at the Galway Bay test site.

Note that the highest power outputs predicted from the interpolation exercise exceed the benchmark value as set from the results of the Phase 2 trials at ECN, Nantes. This final step allows all the relevant elements of the scatter diagram to be filled in with power output values. These figures can then be applied by the development team of the device to various different potential deployment locations and a power map can be produced. This power map will give an estimate of the likely power production of the device at various suitable sites.



### 5.2.3. Long Period Excitation

Up to the point of putting a device out in the test site in Galway Bay, the developer will have followed the Development Protocol and have completed Phase 1 and 2 which are laboratory controlled trials of monochromatic and panchromatic seaways, over a frequency range matched to the power production potential of the device (Holmes 2003). Typically, panchromatic trials are conducted for a range of seaways defined by a theoretical spectral shape and varying in both magnitude and period limited only by the constraints of the facilities equipment. Due to this, the highest peak period tested would be in the region of 15-20s at prototype scale.

For most floating WECs, especially oscillating water columns, the primary body motion of concern would be the heave of the device, which in most cases will match that of the resonant period of the power take-off of the device. For the heave motion, the Response Amplitude Operator (RAO) will become 1 [ $\text{m}^2/\text{m}^2$ ] in periods greater than 15s at full-scale, where the floating device no longer heaves relative to the water surface.

In the case of other motions, for most floating devices the pitch period is specified to be at a long period, well outside the power production range of the device. Figure 5.16 shows the pitch RAO for two different wave energy converter, both of which have an RAO above 30s at prototype scale. Identification of these devices is not possible due to confidentiality concerns. This scenario is acceptable for open ocean sites where the prototype device would be deployed and the energy content of spectra above 30s are extremely low. However, for deployment in Galway Bay, periods in the region of 15-18s at the quarter scale test site equate to 30-35s at prototype scale. Figures in Section 4.6 indicated that, after multi-modal spectra have been identified and separated into wind sea and swell wave systems, seaways with average wave periods at these periods do occur, although they do have significant wave heights less than  $H_s < 1.5\text{m}$ . Therefore, it would be expected that a device in Galway Bay might experience excitation in a degree of freedom of motion, which at full-scale may rarely occur.

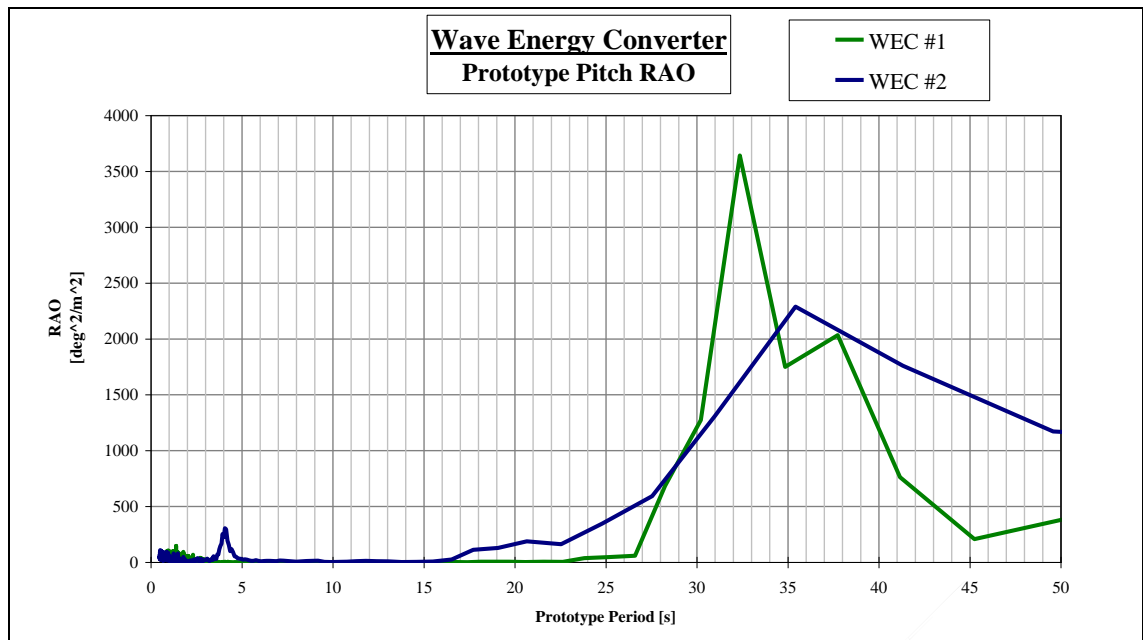


Figure 5.16. Pitch RAO's for two floating devices at full-scale.

Long wave periods such as these would not have been tested in the previous phases of the Development Protocol, and it is not expected that a prototype device will experience these periods at an exposed offshore site. Therefore, this phenomenon is unique to the test site in Galway Bay, or a similar site which experiences fetch limited wind seas with offshore swell. Developers need to be aware of this phenomenon and try to understand the consequences of it for their device in terms of any device access or survival issues that may arise, but more likely in terms of access for maintenance and/or data retrieval, as it is more an inconvenience at this particular scale rather than a long term issue of device stability.

## 6. DISCUSSION & CONCLUSION

The main aim of this work was to assess the measurement and analysis techniques that are available to wave energy device developers and to then apply those techniques that were found to be relevant to WEC development. The instrumentation that can be used to acquire detailed wave data and the methods to assess the suitability of a particular site for wave energy extraction and device deployment from the data was addressed. Emphasis was placed on using surface following buoys for both directional and non-directional measurement. The analysis techniques presented are the current industry standards and their applicability and drawbacks have been presented.

### 6.1. Discussion

There are a variety of methods that can be utilised to provide information of the wave conditions at a particular site of interest. These range from manned observation to *in situ* instrumentation to remote sensing techniques. Within the sub-category of floating buoys, there are large meteorological buoys for atmospheric data capture, smaller surface following buoys primarily designed for wave measurement and sacrificial drift buoys which are used to measure and understand currents on an oceanic scale. Due to the availability of a large amount of data, the Datawell Waverider buoys were selected for further investigation, although there are other industrially accepted designs available. The fundamental component of these directional and non-directional buoys are delicate and would not be as robust as other solid state instrumentation, however, a proven track record in reliability has been established since their commercial availability in the 1970's.

The data used throughout has come from two locations. The major data set was provided by the Marine Institute from their quarter scale wave energy test site in Galway Bay. This benign site is within a semi-enclosed bay on the west coast of Ireland where it experiences fetch limited wind seas combined with long period swell from the Atlantic. The secondary site was located off the west coast of Ireland at Loop Head, Co. Clare. This is a more exposed North Atlantic site and proved useful for complimentary analysis in terms of full-scale comparisons to the intermediate site of Galway Bay.

However, gathering wave climate data is just the beginning of the measurement and analysis process. Buoy measurements can be used as ground truth indicators for various

third generation numerical prediction models. The readings of these instruments have to be quantified and qualified before usage and publication. This verification process is conducted in both the time and frequency domain, where results from one domain can be used to compliment and qualify results from the other domain. Standards exist for time domain analysis (IAHR 1986), however there are various options available to the analyst when operating in the frequency domain.

One of the fundamental tools that is utilised in the frequency domain is the Fast Fourier Transform. Based on the assumption that the recorded surface elevation signal is the superposition of sinusoidal waves of harmonic frequencies and random phase, the time domain signal can be converted to a distribution in the frequency domain, from which various parameters can be calculated. This type of transform is an important element of wave energy analysis as most WECs are resonant in nature and respond to the frequency components of the excitation sea state. However, proper use of these tools will only provide appropriate results once the advantages and limitations of their application are understood. The analysis techniques in the frequency domain can be further embellished for application to the analysis of directional spectra. Various parametric methods are available to the user although a definitive algorithm is a product of the accuracy required and the application of the results garnered.

For comparison to the results of the analysis of measured waves, several empirical studies have been conducted that define a variance density distribution in the frequency domain. These accept various summary statistics of the wave field as inputs, all of which can be further modified to incorporate directional aspects. These spectral definitions are used at hydraulic testing facilities at the concept appraisal stage of device development to give an indication of the power production abilities of the device, along with design loads. It was shown that these empirical equations also hold true for long-term averages of measured spectra, both at a benign sea test site and a more exposed offshore Atlantic location.

It was found that there is a large variation in the variance density spectral shape when comparing short-term averages or individual spectra to empirical formulae. This can usually be quantified by the combination of wind sea and swell wave systems, which coexist at the measurement site. The level of coexistence was quantified for both the wave

energy test site in Galway Bay and the more exposed location. Several methods are available to separate spectra into their respective systems, and there exist several models for defining such multi-modal spectra.

The suitability of the Galway Bay wave energy test site as a Phase 3 benign site was investigated by comparing the wave climate to that of the exposed site off the west coast of Ireland. This site can be assumed to be an approximation of a Phase 4 demonstration site. The measured data from both the installed wave buoys and the SWAN numerical model were considered and analysed. Outside of the existence of low wave height, long period swell that encroaches the benign test site around the Aran Islands from the Atlantic, the statistics suggest that the test site represents the North Atlantic reasonably well at a quarter scale, making it suitable for Phase 3 testing of floating wave energy devices.

Finally, an assessment was conducted on the performance of a floating wave energy device at the aforementioned benign site in Galway Bay. The device utilises a simplified power take-off mechanism, and the results were compared to the two previous phases of the device development protocol at different scales. Due to the spectral variation of the incident wave fields previously mentioned, a variation of the expected power output also exists, however it can be directly attributed to the amplitude of the harmonic excitation of the wave field.

## **6.2. Conclusion**

Various analysis tools have been presented here along with their method of application and suitability of use, especially concerning the understanding of the wave climate in terms of floating wave energy devices and power extraction. Small floating surface following buoys are found to be the most suitable instruments for data recording in the harsh marine environment due to their robustness and longevity, but also due to the large knowledge base that exists on their use and application. Other measurement methods such as satellite and ADCPs can be utilised but the data coverage and ease of deployment are a major advantage for floating buoys.

It was shown that the Fast Fourier Transform is an adequate and accepted method of achieving the spectral components of a surface wave record, and although more

sophisticated methods are available, the applicability and efficiency of the algorithm suggest that it will be the industry standard for the time being. The application of the FFT to wave records was discussed and the various methods of appeasing the associated errors were presented, such as tapering and windowing. There is still some debate as to the appropriate analysis method for directional spectra, however if there is a greater accuracy required in this respect, other measurement instrumentation may be a more suitable solution, such as gauge arrays or ADCPs, rather than surface following buoys.

The three most common empirical spectral models were presented with a history of their definition and some comments on the parameters that can be derived. It would seem from the investigation presented here that the Bretschneider spectral equation is suitable for modelling long term average sea states, of scales ranging from a month to a year. However, for the application or modelling of individual spectra, it would be more appropriate to apply a JONSWAP spectrum, or if appropriate a bi-modal spectrum, such as Torsethaugen and Haver (2004), both defined by suitable parameters. Ideally, spectra that represent the actual deployment site derived from measurements should be used in device development work, however, this is not always feasible given time and budget constraints on start up wave energy companies. It was also concluded that the use of bi-modal spectra is only necessary at low wave heights, as the measured spectral distribution conforms to the single peaked empirical equations during storm seas. The importance of the identification of bimodal seas was also highlighted, both in terms of the characterisation of a site and the potential influence of such a spectrum on the power production capabilities of a wave energy device.

One of the most important aspects of this study is that in terms of wave energy analysis, the overall summary statistics of the sea state is not adequate for wave energy as important information is hidden in the frequency distribution of the spectrum. The transmission of summary statistics from floating buoys was a compromise between battery life and transmission limitations. However, as technology improves, the surface elevation record and subsequent variance density spectrum should be the minimum requirement when the data is to be used for wave energy technologies. As WECs are resonant devices, knowledge of the frequency spectrum is of fundamental importance. It was shown that there is variability in the ratios of the various wave period parameters of individual sea

state spectra and that the empirical models should only be used as a guide or an indication of long term site characterisation.

The majority of the data used in this study was recorded and processed by Datawell buoys installed at the Galway Bay wave energy test site. This site is provided as a Phase 3 testing facility, the first experience that device developers will have with their device in real sea conditions. The suitability and Froude scalability of this site as a quarter scale test site was investigated. Although there is a higher than expected degree of bimodality at the test site, the wind sea component of the spectra are indeed a quarter scale of the North Atlantic. This was confirmed by comparing the summary statistics from the test site to that of an exposed site off the west coast of Ireland, a location that may be suitable for full-scale deployment in the future.

The analysis tools that were discussed and investigated throughout this work were applied to the power output of a floating WEC, Ocean Energy Ltd OE Buoy in Galway Bay. This device is at approximately quarter scale and follows the development of the device through two previous phases of development at hydraulic facilities at smaller scales. The results of these preceding trials were used for comparison to the power output from the Galway Bay device, and good agreement was found. Due to the variability of the input wave spectrum in comparison to the empirical models used in previous phases of testing, there is an inherent variability in the device power output from previous test phases, which was quantified. The concept of the Power RAO was introduced to identify the resonant frequency of the power take off of the WEC, which can then be compared to the peak frequency of the incident wave field to understand in greater detail the power output levels for a designated sea state. The importance of wave measurement and comparative analysis of the device power output with the wave spectral input is clear as there can be large variations within a defined sea state defined by summary statistics, both in the spectral shape of the wave spectrum and the average power output of the device. It is expected that this will occur during all real sea trials.

## REFERENCES

- Aarnes, J. E. and H. E. Krogstad. 2001. "Partitioning Sequences for the Dissection of Directional Ocean Wave Spectra: A Review."
- Alves, J. H. G. M. and I. R. Young. 2003. "On Estimating Extreme Wave Heights using Combined Goesat, Topex/Poseidon and ERS-1 Altimeter Data." *Applied Ocean Research* 25(4):20.
- Aranuvachapun, S. 1987. "Parameters of JONSWAP spectral model for surface gravity waves--II. Predictability from real data." *Ocean Engineering* 14(2):101-115.
- Axys Technologies Inc. 2005. "Triaxys Directional Wave Buoy User Manual."
- Barrett, S. 2005. "Offshore Wave Energy Devices: Model Testing of the Backward Bent Duct Device (B2D2)." In Dept. Civil Engineering. Cork: University College Cork.
- Benoit, M. 1992. "Practical Comparative Performance Survey of Methods used for Estimating Directional Wave Spectra from Heave-Pitch-Roll Data." In *Coastal Engineering, 1992 : Proceedings of the 23rd International Conference on Coastal Engineering*, ed. Billy L. Edge. Venice, Italy: American Society of Civil Engineers.
- Benoit, M., P. Frigaard and H. A. Schaffer. 1997. "Analysing multidirectional wave spectra: A tentative classification of available methods." In *IAHR Seminar Multidirectional Waves and their Interaction with Structures*. San Francisco.
- Bergdahl, L. 2009. "Comparison of measured shallow-water wave spectra with theoretical spectra." In *8th European Wave and Tidal Energy Conference*. Uppsala, Sweden.
- Bergdahl, L. and P. McCullen. 2003. "WaveNet F2: Development of a Safety Standard for Wave Power Conversion Systems." In *Results from the work of the European Thematic Network on Wave Energy*, ed. European Community.
- Booij, N., R. C. Ris and L. H. Holthuijsen. 1999. "A Third Generation Wave Model for Coastal Regions Part I: Model Description and Validation." *Journal of Geophysical Research* C4(104):7649-7666.
- Bouws, E., H. Günther, W. Rosenthal and C. L. Vincent. 1985. "Similarity of the wind wave spectrum in finite depth water 1. Spectral form." *Journal of Geophysical Research-Oceans* 90(C1).
- Bracewell, R. N. 1999. *The Fourier Transform and Its Applications*. 3<sup>rd</sup> Edition: McGraw Hill.
- Bretschneider, C. L. 1959. "Wave variability and wave spectra for wind-generated waves." Beach Erosion Board US Army Corps of Engineers.
- Bretschneider, C. L. 1963. "A one-dimensional gravity wave spectrum." In *Ocean Wave Spectra*, ed. United States Naval Oceanographic Office: Prentice-Hall.
- Carter, D. J. T. 1982. "Estimation of Wave Spectra from Wave Height and Period." Institute of Oceanographic Sciences.
- Carter, D. J. T. 1993. "Estimating Extreme Wave Heights in the NE Atlantic from GEOSAT Data." In *Offshore Technology Report, OTH 93 396*. ed. HSE.
- Cartwright, D. E. 1963. "The use of directional spectra in studying the output of a wave recorder on a moving ship." In *Ocean Wave Spectra*, Prentice Hall, Englewoods Cliffs, N.J.
- Cochran, W. T., J. W. Cooley, D. L. Favon, H. D. Helms, R. A. Kaenel, W. W. Lang, G. C. Maling, D. E. Nelson, C. M. Rader and P. D. Welch. 1967. "What is the Fast Fourier Transform." *IEEE Trans. on Audio and Electracoustics* AU-15(2):11.



- Cruz, J. and C. Elkinton. 2009. "Task 2.1.2: Wave Energy Technology Review." In Oregon Wave Energy Trust Utility Market Initiative. Pacific Energy Ventures.
- Cummings, W. E., S. L. Bales and D. M. Gentile. 1981. "Hindcasting waves for engineering applications." In Proc. of the Int. Sym. on Hydrodynamics in Ocean Engineering. The Norwegian Institute of Technology, Trondheim.
- Datawell BV. 1992. "Operation and Service Manual for Waverider." Harleem, Netherlands.
- Datawell BV. 2001. "History of Datawell."
- Datawell BV. 2007. "Datawell Waverider Reference Manual." Datawell BV.
- Dean R. G. 1965. "Stream function representation of non-linear ocean waves." *Journal of Geophysical Research* 70(18).
- Dept. Communications Marine & Natural Resources. 2005. "Ocean Energy In Ireland." Dept. Communications, Marine & Natural Resources.
- DNV. 2008. "Certification of Tidal and Wave Energy Converters." In *Offshore Service Specification DNV-OSS-312*, ed. Det Norske Veritas.
- Donelan, M. and W. J. Pierson. 1983. "The Sampling Variability of Estimates of Spectra of Wind-Generated Gravity Waves." *Journal of Geophysical Research* 88(C7):12.
- Draper, L. 1963. "Derivation of a Design Wave from Instrumental Records of Sea Waves." In *Proceedings of ICE*.
- Draper, L. 1986. "Additional Visual Wave Observations in Scottish Waters 1976-1985: Supplementing Data Presented in IOS Report No. 29, 1976."
- Earle, M. D., K. E. Steele and D. W. C. Wang. 1999. "Use of advanced directional wave spectra analysis methods." *Ocean Engineering* 26(12):1421-1434.
- Elgar, S. 1987. "Bias of Effective Degrees of Freedom of a Spectrum." *Journal of Waterway, Port, Coastal and Ocean Engineering* 113(1):77-82.
- EMEC. 2004. "Performance Assessment for Wave Energy Conversion Systems in Open Sea Test Facilities." European Marine Energy Centre.
- EMEC. 2009. "Nursery Sites." In Press Release <http://www.emec.org.uk/nursery-sites/>
- Forestier, J. M., B. Holmes, S. Barrett and A. W. Lewis. 2007. "Value and Validation of Small Scale Physical Model Tests of Floating Wave Energy Convertors." In *7th European Wave and Tidal Energy Conference*. Porto, Portugal.
- Foerstall, G. Z. 1978. "On the statistical distribution of wave heights in a storm." *Journal of Geophysical Research* 83.
- Frigaard, P., M. Brorsen and J. P. Kofoed. 1997. "PADIWA: A Package for Directional Wave Analysis." *Hydraulics & Coastal Engineering Laboratory*, Aalborg University.
- Gerling, T. W. 1992. "Partitioning Sequences And Arrays Of Directional Ocean Wave Spectra Into Component Wave Systems." *Journal of Atmospheric And Oceanic Technology* 9:15.
- Gerritzen, P. L. 1993. "The Calibration of Wave Buoys." In *Calibration of Hydrographic Instrumentation*. Reading, UK. The Hydrographic Society.
- Goda, Y. 1988. "Statistical variability of sea state parameters as a function of a wave spectrum." *Coastal Engineering in Japan* 29(1):39-52.
- Guedes Soares, C. 1984. "Representation of Double-Peaked Sea Wave Spectra." *Ocean Engineering* 11(2):185-207.

- Guedes Soares, C. 1991. "On The Occurrence Of Double Peaked Wave Spectra." *Ocean Engineering* 18(1/2):167-171.
- Guedes Soares, C. and M. C. Nolasco. 1992. "Spectral Modeling of Sea States With Multiple Wave Systems." *Journal of Offshore Mechanics And Arctic Engineering* 114(4):278-284.
- Gulev, S. K., V. Grigorieva, A. Sterl and D. Woolf. 2003. "Assessment of the reliability of wave observations from voluntary observing ships: Insights from the validation of a global wind wave climatology based on voluntary observing ship data " *J. Geophys. Res.* 108(C7).
- Hanson, J. L. and O. M. Phillips. 1999. "Wind Sea Growth and Dissipation in the Open Ocean." *Journal of Physical Oceanography* 29(8):1633-1648.
- Hanson, Jeffrey L. and Owen M. Phillips. 2001. "Automated Analysis of Ocean Surface Directional Wave Spectra." *Journal of Atmospheric And Oceanic Technology* 18(2):277-293.
- Hasselmann, K., D. J. Olbers, T. P. Barnett, E. Bouws, H. Carlson, D. E. Cartwright, K. Enke, J. A. Ewing, H. Gienapp, D. E. Hasselmann, P. Kruseman, A. Meerburg, P. Muller, K. Richter, W. Sell and H. Walden. 1973. "Measurements of wind-wave growth and swell decay during the Joint North Sea Wave Project (JONSWAP), *Ergänzung zur Deut.*" *Deutschen Hydrographischen Zeitschrift* 12:1-95.
- Hasselmann, S., Hasselmann, K., Allender, J. H. and Barnett, T. P. 1985. "Computations and parameterisations of the nonlinear energy transfer in a gravity-wave spectrum, Part II: parameterisations of the nonlinear energy transfer for application in wave models." *J. Phys. Oceanogr.* 15
- Hasselmann, S., C. Bruning, K. Hasselmann and P. Heimbach. 1996. "An improved algorithm for the retrieval of ocean wave spectra from synthetic aperture radar image spectra." *J. Geophys. Res.* 101(C7):15.
- Holmes, B. 2003. "Ocean Energy: Development & Evaluation Protocol." ed. HMRC.
- Holmes, B. 2007. "Sea And Swell Spectra." ed. HMRC: Marine Institute.
- Holmes, B. 2009. "WAVEPLAM State of the Art Analysis." ed. WAVEPLAM.
- Holmes, B. and S. Barrett. 2007. "Sea & Swell Spectra." In 7th European Wave & Tidel Energy Conference. Porto, Portugal.
- Holthuijsen, L. H. 2007. *Waves in Oceanic and Coastal Waters*: Cambridge University Press.
- Houmb, O. G., E. Due. 1978 "On the occurrence of wave spectra with more than one peak." *Int Report Norwegian Institute of Technology, Trondheim.*
- HSE. 2002. *Wave Parameters – Supporting Document to ‘Offshore Installations: Guidance on Design, Construction and Certification – Environmental Considerations’ Offshore Technology Report OTH 89 300.*
- Hwang, P. A., N. E. Huang and D. W. Wang. 2003 "A note on Analysing Nonlinear and Nonstationary Ocean Wave Data." *Applied Ocean Research* 25:7.
- IAHR. 1986. "List of Sea State Parameters." ed. IAHR. Brussels: International Association for Hydraulic Research.
- Irish Examiner. 2008. "Eco Energy Company Rides on a Wave of Success." In *Irish Examiner*. Cork: Irish Examiner.
- Isobe, M., K. Kondo and K. Horikawa. 1984. "Extension of MLM for Estimating Directional Wave Spectrum." In *Proc. Symp. on Description and Modelling of Directional Seas*. Denmark.
- ITTC. 1999. "ITTC Symbols and Terminology List." ed. Bruce Johnson.

- Joosten, H. P. 2006. "Directional Buoys and Their Elastic Mooring." In IOS.
- Khan, J. and G. S. Bhuyan. 2009. "Ocean Energy: Global Technology Development Status." ed. IEA-OES.
- Liu, P. C. and T. A. Kessenich. 1976. "IFYGL Shipboard Visual Wave Observations vs Wave Measurements." *Journal of Great Lakes Research* 2(1):10.
- Longuet-Higgins, M. S. 1952. "On the statistical distribution of the heights of sea waves." *Journal of Marine Research* 11:245-266.
- Longuet-Higgins, M. S. 1980. "On the distribution of the heights of sea waves: Some effects of nonlinearity and finite band width." *Journal of Geophysical Research* 85(C3).
- Longuet-Higgins, M. S. 1986. "Eulerian and Lagrangian aspects of surface waves." *Journal of Fluid Mechanics* 173:683-707.
- Lygre, A. and H. E. Krogstad. 1986. "Maximum Entropy Estimation of the Directional Distribution in Ocean Wave Spectra." *Journal of Physical Oceanography* 16:9.
- Marine Institute. 2009. "INFOMAR, [www.infomar.ie](http://www.infomar.ie)."
- Massel, S. R. 2001. "Wavelet analysis for processing of ocean surface wave records." *Ocean Engineering* 28(8):31.
- Massey, B. 1998. *Mechanics of Fluids*. 7th Edition: Stanley Thornes Ltd.
- MatLab Support. 2008. "Using FFT to obtain simple spectral analysis plots." Tech-Notes 1702.
- Meindl, A. 1996. "Guide to Moored Buoys and Other Ocean Data Acquisition Systems." eds. Data Buoy Cooperation Panel and World Meteorological Organisation.
- Nwogu, O. U., E. P. D. Mansard, M. D. Miles and M. Isaacson. 1987. "Estimation of directional wave spectra by the maximum entropy method." *Proc. Wave Analysis and Generation in Laboratory Basins*:363-376.
- Ochi, M. K. and E. N. Hubble. 1976. "Six Parameter Wave Spectra." In 15<sup>th</sup> Coastal Engineering Conference. Hawaii.
- Oltman-Shay, J. and R. T. Guza. 1984. "A data-adaptive ocean wave directional-spectrum estimator for pitch and roll type measurements." *Journal of Physical Oceanography* 14(11).
- Pawka, S. S. 1983. "Island Shadows in Wave Directional Spectra." *Journal of Geophysical Research* 88(C4):12.
- Pelamis Wave Power. 2008. "World's First Commercial Wave Power Project goes live." In Press Release: <http://www.pelamiswave.com/archive0908.html>.
- Phillips, O. M. 1958. "The equilibrium range in the spectrum of wind-generated waves." *Journal of Fluid Mechanics* 4(4):426-434.
- Phillips, O. M. 1985. "Spectral and statistical properties of the equilibrium range in wind-generated gravity waves." *Journal of Fluid Mechanics* 156:505-531.
- Pierson, W. J. and L. Moskowitz. 1964. "A proposed spectral form for full-developed wind sea based on the similarity law of SA Kitaigorodskii." *J. Geophys. Res* 69(24):5181-5190.
- Pitt, E. G. 2005. "Estimating power from wave measurements at the European Marine Energy Centre (EMEC) test site." *Applied Wave Research*.
- Pitt, E. G. 2009. "Assessment of Performance of Wave Energy Conversion Systems." In *Marine Renewables Energy Guides*, EMEC.

- Portilla, Jes, Francisco J. Ocampo-Torres and Jaak Monbaliu. 2009. "Spectral Partitioning and Identification of Wind Sea and Swell." *Journal of Atmospheric And Oceanic Technology* 26(1):107-122.
- Rayleigh, L, 1880. "On the stability or instability of certain fluid motions." *Proc. London Mathematics Society* 11.
- Rodriguez, G. and C. Guedes Soares. 1999. "A Criterion For The Automatic Identification Of Multimodal Sea Wave Spectra." *Applied Ocean Research* 21:5.
- Rodriguez, G., C. Guedes Soares and U. Machado. 1999. "Uncertainty Of The Sea State Parameters Resulting From The Methods Of Spectral Estimation." *Ocean Engineering* 26:991-1002.
- Smith, G. and J. Taylor. 2007. "Preliminary Wave Energy Device Performance Protocol." Dept. of Trade & Industry.
- Stewart, R. H. 2005. "Introduction to Physical Oceanography."
- Stokes, G. G. 1847. "On the theory of oscillatory waves." *Transactions of the Cambridge Philosophical Society* 8.
- Sustainable Energy Ireland. 2005. "Ocean Energy in Ireland." In Dept. Communications, Marine & Natural Resources.
- Torsethaugen, K. 1996. "Model for a doubly peaked wave spectrum." SINTEF report STF22 A96204
- Torsethaugen, K. and Haver, S. 2004. "Simplified Double Peak Spectral Model For Ocean Waves." In 14<sup>th</sup> International Offshore And Polar Engineering Conference, ed. ISOPE. Toulon, France: ISOPE.
- Tucker, M. J. 1957. "The analysis of finite length records of fluctuating signals." *British Journal of Applied Physics* 8(4):6.
- Tucker, M. J. and E. G. Pitt. 2001. *Waves In Ocean Engineering*: Elsevier.
- United Kingdom Hydrographic Office. 1980. "Admiralty Chart Galway Bay No. 1984."
- Wang, D. W. and P. A. Hwang. 2001. "An Operational Method for Separating Wind Sea and Swell From Ocean Wave Spectra." *Journal of Atmospheric And Oceanic Technology* 18:11.
- Welch, P. 1967. "The use of fast Fourier transform for the estimation of power spectra: A method based on time averaging over short, modified periodograms." *Audio and Electroacoustics, IEEE Transactions on* 15(2):70-73.
- Williams, M. O. 2005. "Wave Mapping in UK Waters." In *Research Report*, ed. HSE.

## **APPENDIX A: Datawell Output Files**

# Directional & Non-Directional Datawell Wave Measurement Buoys, Galway Bay Test Site.

## Introduction

The Marine Institute Wave Energy Test site was commissioned in March 2006. However, since November 2005 a Datawell 0.7m diameter non-directional wave measuring buoy (*Waverider FL*) has been on station recording the wave elevation and associated spectral quantities. Toward the end of April 2008, a Datawell directional buoy was added (*Waverider MkIII*). Both buoys transmit over HF radio to the Marine Institute headquarters in Rinville, Galway. Since the addition of the directional buoy to the test site in Galway Bay, both buoys are now being processed by Datawell's RfBuoy module. This has changed the format of the non-directional buoy data files, although the file extensions remain the same. Further information is available from the Datawell website ([www.Datawell.nl](http://www.Datawell.nl)).

The naming convention of the buoy data files are as follows:

BuoyName } YYYY-MM-DD**T**HH**h**mm**Z** . file extension

where:

- YYYY* is the year
- MM* is the month
- DD* is the day
- HH* is the hour
- mm* is the minute

**T** denotes time segment of file name, **h** denotes the hour part and **Z** denotes the time zone, i.e. Greenwich Mean Time.

The monthly historical files are named as follows:

*BuoyName* } YYYY-MM . file extension

Data files identified by  $\$$  e.g. *BuoyName*  $\$$  } YYYY-MM-DD**T**HH**h**mm**Z** . file extension are indicative of Buoy produced files. These files are calculated onboard by the buoy processor, are sent over the HF radio link with a timestamp derived from the receiving

time at the PC. Data files without the **\$** are computed by the receiving PC. This also applies to the historical files.

**NB:** With the new Waves21 Datawell system the timestamp of the **.1RW** and **.RAW** wave elevation files corresponds with the **FIRST** data point of the file. This is different to the old DIWAR system of the non-directional buoy.

### Waveriderfl Non-Directional Buoy Data Files

Wave elevation file:                    **...1rw [cm]**

At least 30min of wave elevation data sampled at a frequency of **2.56Hz** ( $\geq 4608$  data points). Units are in centimetres.

Spectral file:                            **...\$}....1sp [cm<sup>2</sup>/Hz]**

The file contains one column of 61 data values containing some summary statistics and spectral density at a resolution of 0.01Hz in the following order:

136.4	$H_s$ [cm]
3.74	$T_{02}$ [s]
11879	Maximum Spectral Density [cm <sup>2</sup> /Hz]
50.127	Spectral Density at 0.03Hz
↓	
69.746	Spectral Density at 0.60Hz

Each file is the non-directional spectrum of 256 data points of the **RW** file data. The buoy transmits a spectral data file every 225 seconds. The spectrum is derived from the Fourier analysis of a 200 second signal of wave elevation. This is stored by the receiving computer and can be identified by the dollar sign (**\$**) in the file name.

Time series statistics file:                    **....1wv [varied]**

This file contains the summary statistics derived from a Zero Down-crossing Analysis of the time series in the **RW** file. The first character sequence is the time and date, i.e. **YYYY-MM-DDTHH:mm:ss.sssZ**. The remaining numbers in the top line are as follows:

- Percentage data of **RW** file without error,
- Maximum wave height, [cm]

- Period corresponding to maximum wave height, [s]
- Average wave height of the highest 10<sup>th</sup> of the waves, [cm]
- The average period of the highest 10<sup>th</sup> of the waves, [s]
- Average wave height of the highest 3<sup>rd</sup> of the waves, [cm]
- The average period of the highest 3<sup>rd</sup> of the waves, [s]
- The average wave height from the entire time history, [cm]
- The average period of the entire time history,  $T_z$ , [s]
- EPS4, spectral width parameter, calculated from the number of maxima and minima that occurred: for a random process the ratio of the number of peaks to the number of zero-up crossings is estimated by:  $N_{cross}/N_{peaks} = \sqrt{(1 - EPS4^2)}$
- Number of waves,

The subsequent lines have column headers as follows:

```
Ordinal Pointer,
Crest Displacement [cm],
Trough Displacement [cm],
Corresponding Period [s]
```

The **Ordinal Pointer** column is the rank of the wave heights where 1 is the highest wave in the time series. It is in order of occurrence of the wave in the time series.

```
2008-07-
01T02:00:02.985Z,100%,221,3.98,178.53,4.56,140.98,4.56,92.97,4.03,0.621,446
345, -9, -39, 2.591
45, 25, -74, 7.427
22, 27, -81, 11.287
88, 31, -54, 5.654
297, 0, -41, 2.687
381, -17, -37, 1.905
```

Wave Statistics Historical File: ....**hiw** [varied]

This file is updated half hourly and generated monthly. Each line contains the data from the first row of the **.1wv** file.

Spectral Data Historical File: ...**\$}**....**his** [varied]

This file contains the summary statistics generated from the spectral files (...**\$}**....**1sp**). Each file contains 19 columns of data with the following column headers:



- Time stamp (same as spectral file time stamp),
- Peak Period ( $1/f_p$ ), [s]
- ~~Peak Direction~~ (Directional Buoy Only)
- ~~Peak Spread~~ (Directional Buoy Only)
- $T_{02}$ , Average Period,  $\sqrt{\frac{m_0}{m_2}}$  [s]
- $H_{m0}$ , Significant Wave Height,  $4\sqrt{m_0}$  [cm]
- $T_I$ , Integral Period, the average period ( $T_{02}$ ) of the integral of the record  $(\sqrt{\frac{m_{-2}}{m_0}})$  [s]
- $T_1$ , (also  $\bar{T}$ ) Mean Period,  $(m_0/m_1)$  [s]
- $T_c$ , Crest Period,  $\sqrt{\frac{m_2}{m_4}}$  [s]
- $T_{dw2}$ ,  $\sqrt{\frac{m_1}{m_1}}$  [s]
- $T_{dw1}$ ,  $\sqrt{\frac{m_{-1,2}}{m_0}}$  [s]
- $T_{pc}$ , Calculated Peak Period,  $\frac{m_{-2}m_1}{m_0^2}$  [s]
- $\nu$  (nu), spectral bandwidth parameter,  $\sqrt{\left(\frac{T_1}{T_{02}}\right)^2 - 1}$  or  $\sqrt{\left(\frac{m_0m_2}{m_1^2}\right) - 1}$ ,  $\nu \rightarrow 0$ : very narrow bandwidths, PM spectrum  $\nu = 0.425$
- $\epsilon$  (eps), spectral bandwidth parameter,  $\sqrt{1 - \left(\frac{T_c}{T_{02}}\right)^2}$  or  $\sqrt{1 - \left(\frac{m_2^2}{m_0m_4}\right)}$ ,  $\epsilon \rightarrow 0$ : narrow bandwidths
- QP, Goda's Peakedness Parameter,  $2\frac{m_{1,2}}{m_0^2}$
- $S_s$ , Significant Steepness,  $\frac{2\pi H_{m0}}{gT_{02}^2}$ , PM Spectrum (fully developed)  $\approx 0.05$
- ~~$T_{ref}$ , Reference Temperature [°C], (Directional Buoy Only)~~
- ~~$T_{sea}$ , Sea Surface Temperature [°C], (Directional Buoy Only)~~
- ~~Battery Status, range (Alves and Young 2003), 0 = 0-6 weeks, 7 = 61 weeks or more, (Directional Buoy Only)~~

Spectral Moment Definition: 
$$m_n = \sum_{f=0}^{f=\infty} S(f) f^n \delta f$$

$$m_{n,2} = \sum_{f=0}^{f=\infty} S(f)^2 f^n \delta f$$

### WaveriderMkIII Directional Buoy Data Files

Wave elevation file:                   ... .raw [cm]

Four columns of data are titled as follows:

Status,  
Heave,  
North,  
West

Status is a quality indicator of the displacement values.

0	Correct
1	Repaired
>2	Irreparable

**Heave, North, and west** are the filtered, double integration of the onboard buoy accelerometers. At least 30min of wave elevation data is sampled at a frequency of **1.28Hz** ( $\geq 2304$  data points). Units are in centimetres. Refer to the Datawell Manual for a more in depth explanation of their derivation.

Buoy spectral file:                   ... .spt [m<sup>2</sup>/Hz]

1	Transmission Index				
139	Hs [cm]				
3.704	T <sub>02</sub> [s]				
1.05E+00	Maximum S(f) [m <sup>2</sup> /Hz]				
24.95	Reference Temperature [°C]				
14.85	Sea Surface Temperature [°C]				
7	Battery Status				
0.29625	Vertical Accelerometer Offset [m/s <sup>2</sup> ]				
-0.0375	X Accelerometer Offset [m/s <sup>2</sup> ]				
-0.0625	Y Accelerometer Offset [m/s <sup>2</sup> ]				
278.4	Compass Heading [°]				
67.5	Magnetic Field Inclination [°]				
	Normalised				
Freq	Spectrum	Direction	Spread	Skewness	Kurtosis
[Hz]	[m <sup>2</sup> /Hz]	[°]	[°]	[-]	[-]
0.025	5.12E-05	117.2	71.5	-0.64	1.52
.	.	.	.	.	.
0.58	1.67E-02	188.4	57.4	-1.04	1.79

Above is a representation of the spectral file sent by the Datawell directional buoy every 30 minutes. The start of the file is comprised of twelve data values covering various statistics and indicators as listed with their respective units. Following this, there are 6 columns comprising of 64 data values. The frequency range goes from 0.025Hz to 0.01Hz inclusive with a spacing of 0.005Hz and continues from 0.11Hz to 0.58Hz with a frequency spacing of 0.01Hz. The spectrum is normalised by the Maximum Spectral Density so that the normalised spectrum has a maximum value of 1m<sup>2</sup>/Hz.



A hexadecimal file containing all the spectral file information corresponding to the buoy. This file is not easily decoded without the Datawell Waves21 software suite.

Wave Statistics Historical File:      ...**.hiw** [varied]

This file is updated half hourly and generated monthly. Each line contains the data from the first row of the 30 minute wave statistics file (**.wvs**).

Spectral Data Historical File:      ...**.his** [varied]

This file contains the summary statistics generated from the spectral files (**.spt**). Each file contains 19 columns of data with the following column headers:

- Time stamp (same as spectral file time stamp),
- Peak Period ( $1/f_p$ ), [s]
- Peak Direction, the direction at  $f = f_p$ ,
- Peak Spread, the directional spread at  $f = f_p$ ,
- $T_{02}$ , Average Period,  $\sqrt{\frac{m_0}{m_2}}$  [s]
- $H_{m0}$ , Significant Wave Height,  $4\sqrt{m_0}$  [cm]
- $T_I$ , Integral Period, the average period ( $T_{02}$ ) of the integral of the record  $(\sqrt{\frac{m_{-2}}{m_0}})$  [s]
- $T_1$ , (also  $\bar{T}$ ) Mean Period,  $(m_0/m_1)$  [s]
- $T_c$ , Crest Period,  $\sqrt{\frac{m_2}{m_4}}$  [s]
- $T_{dw2}$ ,  $\sqrt{\frac{m_1}{m_1}}$  [s]
- $T_{dw1}$ ,  $\sqrt{\frac{m_{-1,2}}{m_0}}$  [s]
- $T_{pc}$ , Calculated Peak Period,  $\frac{m_{-2}m_1}{m_0^2}$  [s]
- $\nu$  (nu), spectral bandwidth parameter,  $\sqrt{\left(\frac{T_1}{T_{02}}\right)^2 - 1}$  or  $\sqrt{\left(\frac{m_0m_2}{m_1^2}\right) - 1}$ ,  $\nu \rightarrow 0$ : very narrow bandwidths, PM spectrum  $\nu = 0.425$

- $\epsilon$  (eps), spectral bandwidth parameter,  $\sqrt{1 - \left(\frac{T_c}{T_{02}}\right)^2}$  or  $\sqrt{1 - \left(\frac{m_2^2}{m_0 m_4}\right)}$ ,  $\epsilon \rightarrow 0$ : narrow bandwidths
- QP, Goda's Peakedness Parameter,  $2\frac{m_{1,2}}{m_0^2}$
- $S_s$ , Significant Steepness,  $\frac{2\pi H_{m0}}{gT_{02}^2}$ , PM Spectrum (fully developed)  $\approx 0.05$
- TRef, Reference Temperature [ $^{\circ}\text{C}$ ],
- TSea, Sea Surface Temperature [ $^{\circ}\text{C}$ ],
- Battery Status, range [0,7], 0 = 0-6weeks, 7 = 61 weeks or more.

Spectral Moment Definition:  $m_n = \sum_{f=0}^{f=\infty} S(f) f^n \delta f$

$$m_{n,2} = \sum_{f=0}^{f=\infty} S(f)^2 f^n \delta f$$

Spectral Data Historical File:      **...\$}...his [varied]**

This file contains the summary statistics generated from the spectral files (**...\$}...spt**). Each file contains 19 columns of data with the same column headers as the other **.his** files.

GPS Location File:                      **...GPS.txt**

When the directional buoy communicates at the start of the 30 minute cycle, its latitude and longitude position are recorded. This is also when the files receive their timestamp. In conjunction with the Waves21 software, this is used as a check that the buoy is still on station. The file consists of four columns of data:

```
Timestamp,
Status,
Latitude,
Longitude.
```

2008-04-24T11:39:00.000Z,	3,	53.22771,	-9.27201
2008-04-24T12:08:59.999Z,	3,	53.22758,	-9.27158
2008-04-24T13:38:59.999Z,	3,	53.22748,	-9.27143
2008-04-24T14:09:00.000Z,	3,	53.22742,	-9.27139
2008-04-24T15:08:59.999Z,	3,	53.22730,	-9.27128

The GPS Status column gives an indication of the probability that the buoy is still within its calculated swept area. This swept area is defined within Waves21 by the water depth and the length of mooring of the buoy. The status score is based on the assumption that the GPS positions obey a bi-variate normal distribution. The probability that the buoy is within the defined swept area is expressed as a Z score, known from 1D normal distributions. The Z scores are as follows:

Status (Z)	Probability
3	99.7%
2.5	98.8%
2	95.4%
1.5	86.6%
1	68.3%

**NOTE 1: To Calculate Energy Period Te from .HIS Files**

$$T_e = \frac{m_{-1}}{m_0}$$

$$T_{dw2} = \sqrt{\frac{m_{-1}}{m_1}} \quad T_1 = \frac{m_0}{m_1}$$

$$T_e = \frac{(T_{dw2})^2}{T_1} = \frac{m_1/m_1}{m_0/m_1} = \frac{m_1}{m_0}$$

**NOTE 2: Data Files Produced by RfBuoy Module**

<b>.HXV</b>	30min	HEX	All RXD Output of HEX values
<b>.RAW</b>	30min	Dec	All Displacement Data
<b>.1RW</b>	30min	Dec	All Displacement Data
<b>\$ .SPT</b>	200sec	Dec	Spectral Data (Non-directional)
<b>\$ .1sp</b>	100sec	Dec	Spectral Data (Directional)
<b>.SPT</b>	1600sec	Dec	Spectral Data (Directional Only)
<b>.WVS</b>	30min	Dec	Wave Statistics
<b>.SPD</b>	4min	HEX	Buoy Produced Spectra
<b>.HIS</b>	Monthly	Dec	Historical PC Spectral Data
<b>\$ .HIS</b>	Monthly	Dec	Historical Buoy Spectral Data
<b>GPS (.txt)</b>	Daily (30min)	Dec	All Transmitted GPS Positions

Buoy computed Spectra      ***Sitename\$}2004-12.his***

PC computed Spectra        ***Sitename}2004-12.his***

Non-Directional Buoy

Every 100s (256 data points) used to compute spectrum with resolution 5mHz to 0.64Hz, written to (...**\$}**...**.1sp**) file.

RfBuoy uses PC real time clock, files have round time labels.

Buoy produced spectral files have random time labels, when data has been received from the buoy by the PC.

## APPENDIX B: Published Papers

### *Papers by Author*

Barrett, S. N., B. Holmes and A. W. Lewis. 2007. "Scalability of a Benign Wave Energy Test Site." In 7th European Wave and Tidal Energy Conference. Porto, Portugal.

Barrett, S. N., B. Holmes and A. W. Lewis. 2008. "Monitoring of Seaway Variability on WEC Performance." In 2nd International Conference on Ocean Energy. Brest, France.

Barrett, S. N. and A. W. Lewis. 2008. "Ireland's Quarter Scale Wave Energy Test Site." AGMET. Dublin, Ireland.



# Scalability of a Benign Wave Energy Test Site

S. Barrett, B. Holmes, A.W. Lewis

Blue Power Initiative  
 Hydraulics & Maritime Research Centre,  
 University College Cork,  
 Ireland.  
 E-mail: hmrc@ucc.ie

## Abstract

A benign quarter scale test site for floating wave energy devices has been provided off the west coast of Ireland in a semi-enclosed coastal bay, partially sheltered from the Atlantic by the Aran Islands. It is expected the provision of this site will encourage developers to progress to Phase 3 of the Ocean Energy: Development & Evaluation Protocol. The site characteristics have been determined from a hindcast model using the 3rd generation wave model SWAN for the year 2000, and a non-directional wave recording buoy in situ since the test site's inception in late 2005. Analysis of this data has shown that there are high occurrences of twin peak spectra, comprising a local fetch limited wind sea and a long period swell which approaches the site around the Aran Islands from offshore. The method that identifies and separates these multi-modal wave generation systems into their constituent processes will be presented in this paper. Through the application of this method the wind and swell sea components will be presented in various forms to engender a thorough knowledge of the conditions at the test site.

Phase 3 of the Development Protocol bridges the end of laboratory model testing and the beginning of sea trials. As completion of the previous two phases is a prerequisite for the use of the test site, this paper explores several considerations that WEC developers will need to take into account. Phase 1 and 2 of the protocol will have involved controlled laboratory conditions, mostly being a combination of monochromatic trials with idealised irregular trials such as the standard representative formulae for JONSWAP or Pierson-Moskowitz spectra. As most floating wave energy converters have a narrow response bandwidth, a high occurrence of twin peaked spectra may not produce the expected power production from the device, especially if resonance falls within the valley between the wind and swell spectral components. What effect will a long period swell occurring at the test site have on the motions of the device, and particularly the power output?

Finally, this paper will look at the scalability of the conditions at the benign test site and compare these to a fully exposed site off the west coast of Ireland which would be typical for full scale prototype deployment.

**Keywords:** Wave Spectra, Wave Energy Test Site, Wave Buoy, Twin-Peaked Spectra.

## Nomenclature

$H_{m0}$	= significant wave height, $4\sqrt{m_0}$
$m_n$	= $\sum f^n S(f) \Delta f$
$T_p$	= peak period
$T_{02}$	= average period, $\sqrt{m_0/m_2}$
$T_e$	= energy period, $m_{-1}/m_0$
$T_z$	= average zero-crossing period
$\Delta\theta$	= change in direction
$\Delta f$	= change in frequency
$N$	= number of spectral frequencies
$f_i$	= frequency component at index $i$
$f_{high}$	= high frequency limit
$f_{low}$	= low frequency limit
$f_l$	= low frequency spectral component
$f_h$	= high frequency spectral component
SP	= wave buoy spectral output file

## Introduction

The Galway Bay Wave Energy Test Site was established jointly by the Marine Institute and Sustainable Energy Ireland under Phase 1 of the Ocean Strategy for Ireland which focuses on development by supporting product R&D and research facilities [1]. This Development Strategy was submitted to government to ensure that ocean energy will be in a strong position to be part of the renewable energy mix in the future. A benefit of this will be the development of Irish expertise and technologies to achieve a leading export industry for ocean energy devices.

The Marine Institute and Sustainable Energy Ireland, agencies of the Irish Government Department of Communications, Marine and Natural Resources obtained a foreshore licence for a 37 hectare site defined by four navigational buoys on the corners, 1.5 miles off the Spiddle coast in Galway Bay as shown in Fig. 1. The site has a minimum depth of 21m, with a spring tidal range of 4.5m and a neap tidal range of 1.9m. Both the flood and ebb tidal stream is approximately 1 knot in an east west direction [2]. This provides developers with an instrumented, legal test site and the prospect to progress to Phase 3 of the Development and Evaluation Protocol for Ocean Energy Devices with a device in the region of a 1/4 scale of the prototype [3]. This phase of the protocol presents developers with the final opportunity to quickly and inexpensively acquaint themselves with their device in real sea conditions. One benefit at this scale is the relatively low power production. For a full scale device rated as 2MW, a device designed for testing in Galway Bay will be rated at approximately 16kW. Production of electricity at this magnitude will not justify grid connection or the expense of sub-sea cables and a consequent quick release system for safety. Instead it should be possible to equip the device with a scaled power take-off

mechanism, simulated grid connection and dump the produced power through heat exchangers.

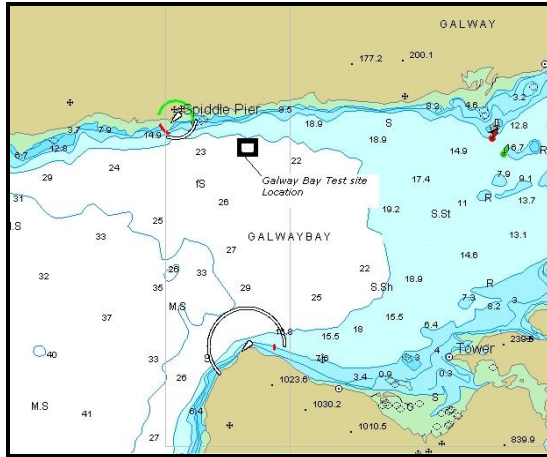


Figure 1: Location of Marine Institute Wave Energy Test Site.

## 1 Numerical Model

To investigate the wave conditions and the sites' suitability as a wave energy test site, a year's data was obtained in hindcast from a numerical wave model. This model was implemented by the Marine Institute for the full year of 2000.

The computer model used to obtain hindcast data for the test site was **SWAN** (Simulating Waves Nearshore), which is a package developed at Delft University [4]. SWAN predicts wave conditions, primarily in shallow water coastal areas, lakes or estuaries from user defined wind, bottom and current conditions. SWAN is a third generation wave model based on the energy balance equation.

The SWAN model is based on a spatial grid that extends from Oranmore, Galway at 8° 54' W to 10° 56' W and from Liscannor Bay, Co. Clare at 52° 49' N to Slyne Head, Co Galway at 53° 28' N. This covers an area of approximately 2,774 square nautical miles. The grid units are in kilometres with grid nodes at 2km spacing. The focus of interest is the Wave Energy Test Site as indicated in Fig. 2 at a grid location of (112.530, 46.037). The test site falls within the bounds of four grid nodes of the SWAN model and so the output data is interpolated from these grid nodes.

The output data from the SWAN model was supplied to the HMRC for analysis in two forms, the summary statistics comprising of significant wave height ( $H_{m0}$ ), spectral peak period ( $T_p$ ), spectral mean period ( $T_{02} \approx T_z$ ) and the mean direction of propagation of the waves in degrees.

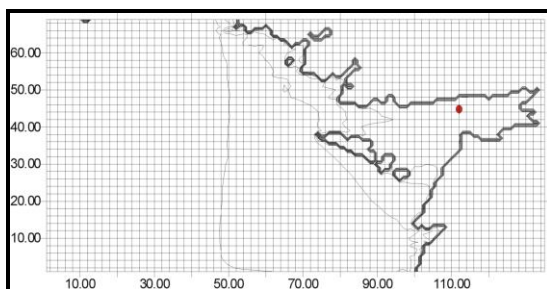


Figure 2: SWAN Model Spatial Grid.

This data is provided for the twelve months of 2000 at 12 hour intervals at midnight and noon. The second output file is the 3 dimensional non-stationary coordinate file from the SWAN model. This file contains the 3 dimensional variance density spectrum, at every three hours for the entire year of 2000 for the chosen grid point. The 3 dimensional data is integrated across 32 frequencies and 36 directions for which the variance densities are supplied.

The variance densities are truncated by SWAN to integer values. A factor is provided for each data set to obtain the correct values of the variance densities. The unit of the variance density is then [ $m^2/Hz/deg$ ]. By integration across frequency or direction, the 1 dimensional variance spectra may be obtained. The spectrum in the model is separated with a constant directional resolution ( $\Delta\theta$ ) of  $10^\circ$  and a constant relative frequency resolution ( $\Delta f/f$ ) of 0.1. The directional resolution is defined by the user as the number of subdivisions of the  $360^\circ$  of a circle. The frequency resolution is defined by the high and low discrete frequencies and the number of frequencies in this range. The frequency resolution is defined by Equation 1, where N is the number of frequencies. This method of discretisation results in a frequency range from 0.0521Hz to 1Hz where  $f_{i+1}=1.1f_i$ .

$$\Delta f = \left( \left( \frac{f_{high}}{f_{low}} \right)^{1/N-1} - 1 \right) f \quad \text{Eq. 1}$$

The spectral moments can then be calculated for each data set for the 1 dimensional spectrum, and in turn the significant wave height and mean spectral period may be obtained. The peak period is defined as the inverse of the peak frequency at which the peak of the spectrum occurs and is determined by a search algorithm which allocates the period corresponding to the maximum spectral ordinate in the spectrum.

From early analysis of the two data sets it became obvious that a difference existed from the summary statistics output by the SWAN model and those obtained by integrating the 3 dimensional spectra. This can be seen in Fig. 3, a comparison of  $H_{m0}$  from both data sets for the month of January 2000. The data set denoted **SWAN Output** is the summary statistics produced by the SWAN model. The data set denoted **Calculated** comes from the integration of the output spectra from the SWAN model. The Calculated data is underestimated and is due to the calculation of the spectral moment being limited to the frequency range i.e. 0.0521Hz to 1Hz, in contrast to the calculation of the SWAN Output data over the wave spectrum with a diagnostic tail  $f^{-m}$  added to the high frequency cut off. Based on physical arguments the value of  $m$  should be between 4 and 5 [5]. Further information on this is available in the SWAN manual.

Fig. 4 shows the bi-variate scatter plot of  $H_{m0}$  versus  $T_p$  for both the SWAN Output and the Calculated results. This plot gives an indication that two wave systems are being modelled by SWAN. One has the characteristics of a local wind sea with short peak periods associated to the limited fetch, while the other is of longer periods approaching the site from the Atlantic around the Aran Islands. These two systems can be seen as data concentrations, the wind sea on the left and swell sea on the right.

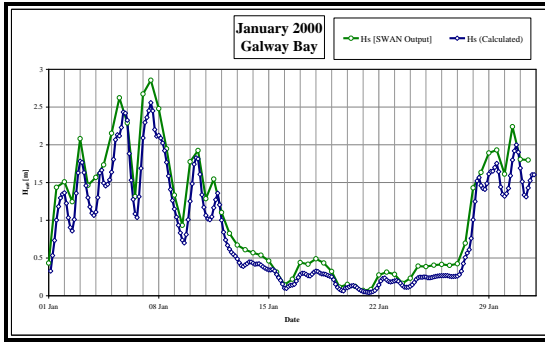


Figure 3: Significant Wave Height ( $H_{m0}$ ), January 2000.

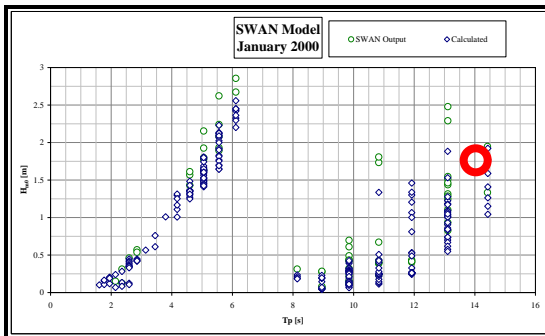


Figure 4:  $H_{m0}$  versus  $T_p$ , January 2000.

The corresponding spectrum of the circled point in Fig. 4 is shown in Fig. 5. Quite clearly this is a twin peaked spectra, however the dominant peak is associated with the smaller proportion of the variance of the spectrum, thereby creating a mismatch between the peak period and the significant wave height. Therefore it is dangerous to refer to the summary statistics of unseparated multi-modal seas as is shown in Fig. 4 as the plot indicates that relatively high wave heights with long periods should be expected at the site. The indicated point in Fig. 4 should be aligned with a  $T_p$  in the region of 5.5s to 6s.

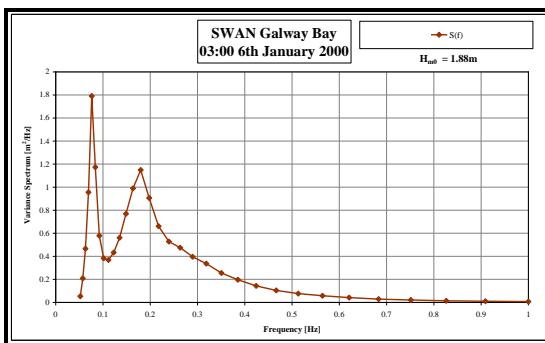


Figure 5: 1-D Spectrum for  $H_{m0}$  1.88m and  $T_p$  13.11s.

Even with the occurrence of double peaked wave spectra, different types occur. Note that in Fig. 6 which are one dimensional spectra from the SWAN model, the significant wave height and mean wave periods are approximately identical, and that the only differing statistic is the peak period. One type of spectrum may be dominated by a high frequency peak. Such spectra may have been generated by a low frequency swell system that travelled a considerable distance losing much energy before meeting a wind wave system. Such

a spectrum is known as a wind dominated spectra and is identified as SPEC 1 in Fig. 6. Spectra dominated by a low frequency peak may have been generated by a wind or a change in wind direction which creates a system of short period waves that coexist with the older swell wave system. When the wind stops, the wave components become uncoupled and the wave system becomes a swell sea. An example of a swell dominated multi-peak spectrum is presented as SPEC 2 in Fig. 6. For comparison a uni-modal spectrum is also presented in Fig. 6 as SPEC 3.

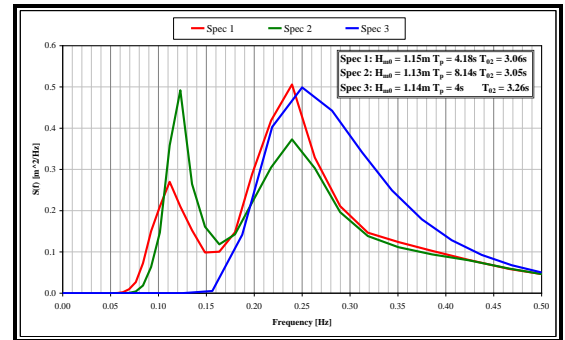


Figure 6: Examples of SWAN model twin peaked spectra with a single peaked spectrum, all of similar  $H_{m0}$  and  $T_{02}$  statistics.

A twin peaked spectrum is defined by two concentrations of energy density separated by a valley or trough. By locating this valley in each spectra and assigning its position along the frequency axis as the separation frequency for that spectra, the wind and swell component of the spectra could be more accurately calculated. The results of the algorithm used are shown in Fig. 7-9. Fig. 7 shows a time trace for the month of January of the separated Wind and Swell  $H_{m0}$  for the test site.

The corrected bi-variate scatter plots for both the wind and swell are shown in Fig. 8 and Fig. 9 for the full twelve months of 2000 from the integrated 3 dimensional spectral output. These plots show that the swell component of  $H_{m0}$  does not exceed 1 m for the entire year, in contrast to the situation indicated by Fig. 4.

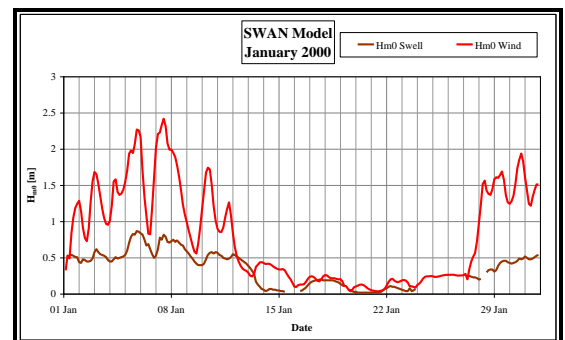


Figure 7: Separated Wind and Swell  $H_{m0}$ , January 2000

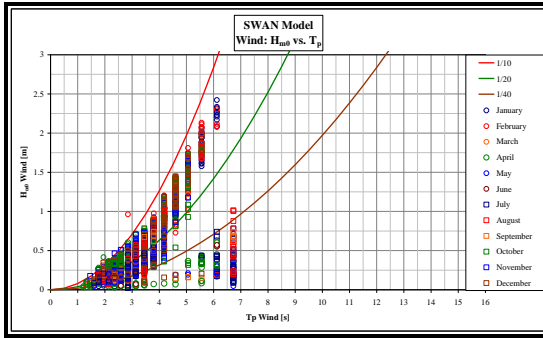


Figure 8: Wind  $H_{m0}$  versus  $T_p$ , for all 2000.

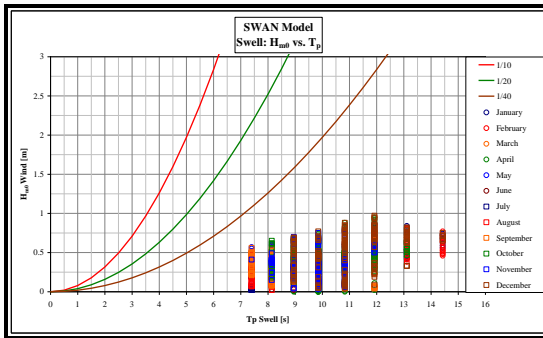


Figure 9: Swell  $H_{m0}$  versus  $T_p$ , for all 2000.

## 2 Hindcast Wave Direction

The wave recording buoy on site in Galway Bay is a non-directional Datawell Waverider buoy and so the 3 dimensional spectra produced by the SWAN model will be used as an indication of the wave directions present at the test site in Galway Bay. An example of a 3 dimensional spectra is shown in Fig. 10. This example shows a twin peaked sea state both in frequency and direction with the main swell peak coming from a direction of  $245^\circ$ , which is originating on the leeward side of the Aran Islands and having a fetch of 27.5km. The shorter period secondary peak is from the south east of the test site over a restricted fetch of approximately 20km.

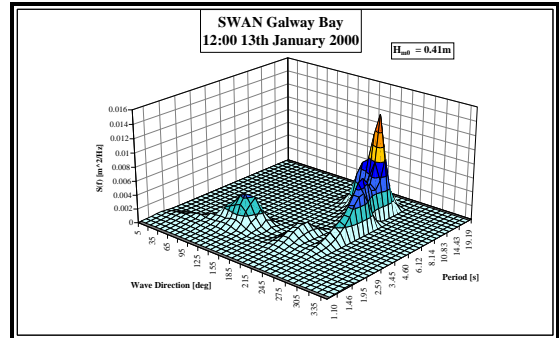


Figure 10: Multi-modal 3 dimensional spectrum.

The spectrogram of Fig. 11 shows the combined directional spectrum for each time step for a period of five days in January 2000. Each section perpendicular to the date axis is the integration of the individual 3 dimensional spectrum across the frequencies, i.e the 1 dimensional directional spectrum for that time step. The total wave height is less than 0.5m for this period. Fig. 11 shows that for this duration, the origin of the waves at the test site is a combination of two sources, the dominant source being a local wind sea originating from the East and a secondary source with a wave direction of  $255^\circ$ . This secondary source appears to originate offshore and approach the test site to the north of the Aran.

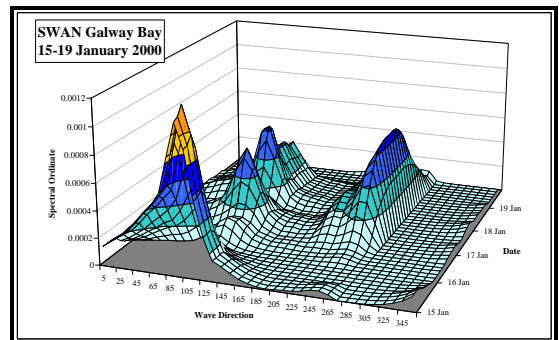


Figure 11: Spectrogram of directional spectra,  $H_{m0} < 0.5m$ .

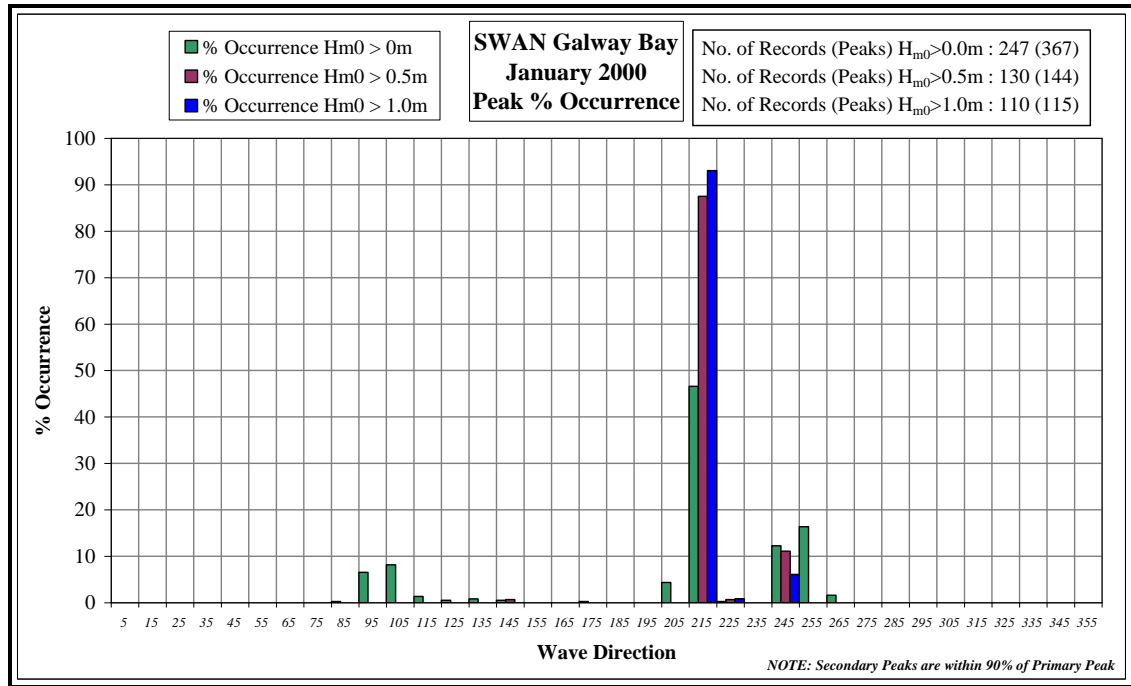


Figure 12: Peak Spectral Directional distribution, January 2000.

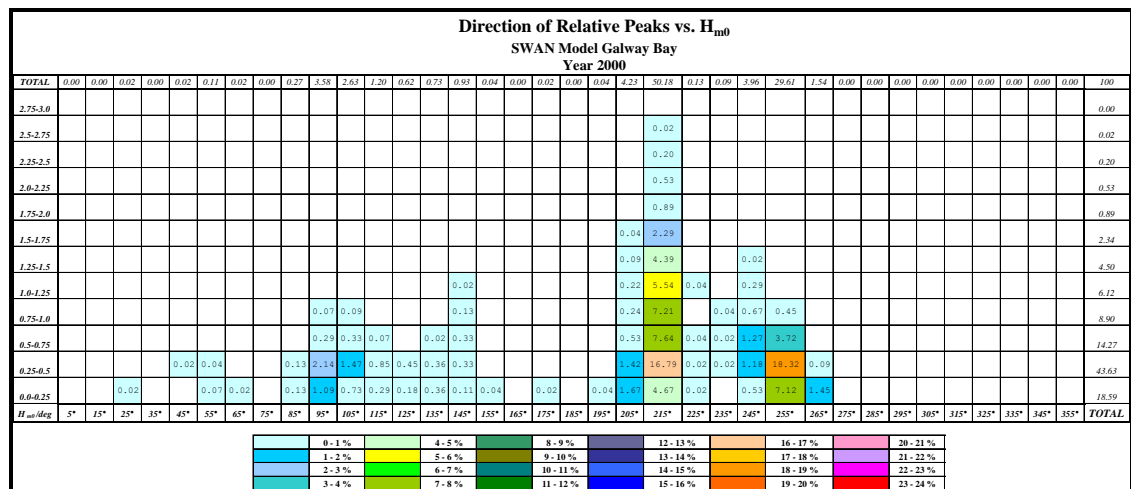


Figure 13: Peak Directional Distribution versus Significant Wave Height for year 2000.

By assigning the local peaks in each 3 dimensional plot as shown in Fig. 10 with a direction, the wave direction of each peak for each time step in the data can be determined. Secondary peaks are limited to within 90% of the ordinate of the primary peak in the 3 dimensional spectrum. The occurrence of these peaks is then further broken down into varying ranges of wave heights as shown in Fig. 12 for the month of January. The dominant direction that transpires is 215° or South South West from the test site. Secondary wave directions are from South West from the Aran Islands which is the longest fetch length in Galway Bay and 100° East from Kinvarra, East South East of the Test Site. For the month of January there is data for 247 time steps, and from this data there are 367 peak directions. This results in nearly 50% of all January spectra being multi-peaked spectra. When a lower limit on wave height is placed on this data, the number of multi-peak spectra drops significantly to 10% for all wave heights greater than 0.5m Hs, and 5% for all wave heights greater than 1m Hs. By referring to Fig. 7, more than half the swell H<sub>m0</sub> from the separated spectra for January, is below 0.5m, with no swell H<sub>m0</sub> existing

greater than 1m. By combining the results from both Fig. 7 and Fig. 12, it can be concluded that where the significant wave height exceeds 1m, it is likely that the spectra are single peaked wind dominated, and for those significant wave heights below 1m, there is a combination in direction and wave source.

By determining the direction of the local peak in the same way as Fig. 12 for the remainder of 2000, and calculating the percentage occurrence, a bi-variate scatter plot of the direction of the local peaks against significant wave height is produced in Fig. 13. Again, the primary direction with 50% of all significant wave heights is 215°, which is through the South Sound, between the Aran Islands and the mainland. The secondary direction is through the North Sound at 255° with 30% of all wave heights, propagating through the channel north of the Aran Islands. Significant wave heights between 0.25m and 0.5m with a direction of 255° occupy the greatest occurrence of 18%. Along these directions, swell seas penetrate into Galway Bay from the open Atlantic Ocean. As can be shown with linear theory, these swell waves will be reduced in height as they diffract around the Aran Islands.

### 3 Measured Data

To provide measured values of the conditions at the test site, a non-directional recording buoy was placed at the South East corner of the test site in mid-November 2005. Fig. 14 shows the Datawell Mark 1 buoy, which has a diameter of 0.7m, on site in Galway Bay.



**Figure 14:** Galway Bay Test Site Waverider Buoy.

The water surface elevation is transmitted onshore at a frequency of 2.56Hz to a data processing unit. The data is recorded for a 20 minute period every hour. The recorded data is analysed in both the time and frequency domain, and the resulting output is saved along with the 20 minute history of the wave surface elevation. These files are then made available to the HMRC for further analysis.

Initially the data from the Datawell post processing unit is verified independently by spectral analysis and zero-crossing analysis of the surface elevation data record. The post processed spectral file is achieved by spectrally analysing overlapping blocks of the 20 minute data file. The frequency resolution of the overall spectrum is achieved by averaging the block spectra of 256 data points, giving a  $\Delta f$  of 0.01Hz.

In mid-October 2006, the wave recording buoy was redeployed onsite after scheduled maintenance. Since that time there has been virtually 100% data retrieval.

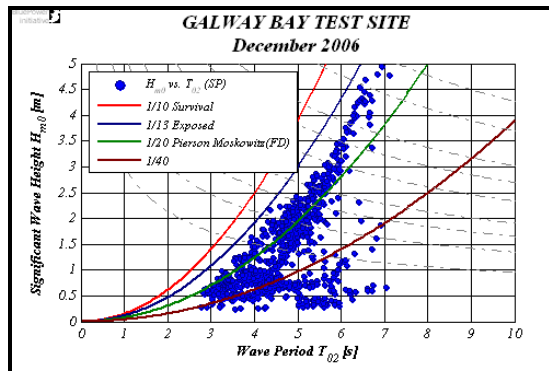


**Figure 15:** Scatter Plot for December 2006 ( $H_{m0}$  vs.  $T_{02}$ )

December 2006 was a particularly stormy month with the test site experiencing the biggest wave conditions recorded at the site. A scatter diagram for the month can be seen in Fig. 15. The highest significant wave height of 4.94m with a maximum wave height of over 8m and with the following periods,  $T_{02} = 6.9s$ ,  $T_e = 8.3s$  and  $T_p = 7.7s$  occurred at midday on the 3<sup>rd</sup> December. This is comparable to a 1 in 50 year storm.

From initial investigation it became clear that the majority of spectra where the significant wave height is greater than 2m are single peaked spectra and this was confirmed through analysis of the shape of the spectra. Some examples of measured double peaked spectra can be seen in Fig. 16.

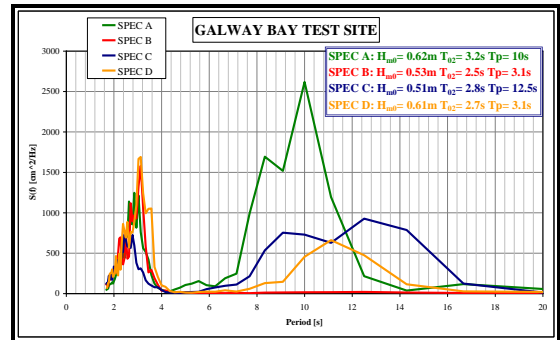


**Figure 16:** Examples of measured multi-peaked spectra.

Fig. 17 shows the results of separating the spectra by identifying multiple peaks. This was achieved by imposing the following conditions on a peak in the frequency spectrum.

- Firstly a local peak was identified as the maximum value in the range of its three closest neighbouring values.
- The biggest magnitude of these local peaks was identified as the primary peak.
- Once the primary peak was identified, secondary peaks were qualified both in the magnitude and temporal regime.
- A secondary peak had to have a magnitude greater than 15% of the primary peak and its corresponding period had to be outside the range of  $\pm 3$ seconds of the primary peak period.
- The same temporal restriction was put in place for a tertiary peak but from subsequent analysis this was not needed.

The legend  $H_{m0}$  vs.  $T_p$  (SP) indicates the significant wave height calculated over the entire spectral width versus the dominant peak period as provided by the post processed data file from the Datawell system.  $H_{m0}$  vs.  $T_p$  (Single Pk) are those spectra that after applying the separation conditions were found to have a single peak.  $H_{m0}$  vs.  $T_p$  (lf) and  $H_{m0}$  vs.  $T_p$  (hf) are the separated spectra in their high and low frequency components. The significant wave height for these separated spectra are calculated over the frequency range limited by a separation frequency that exists between the two peaks.

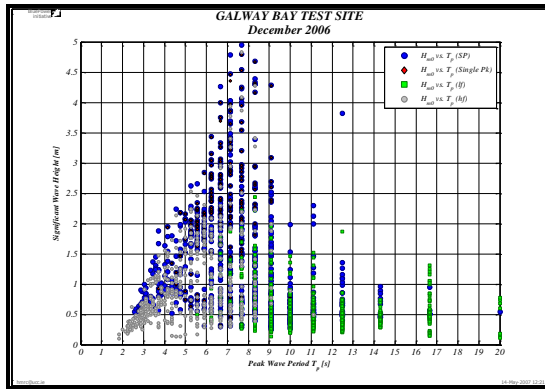


**Figure 17:** Comparison of measured and separated spectra for a scatter plot of  $H_{m0}$  vs.  $T_p$  for December 2006.

From analysis of Fig. 17, for the month of December 2006, it was found that 65% of the observed spectra have double peaks, where the secondary peak is greater than 15% of the magnitude of the primary peak. Fig. 18 shows the same method applied to the measured data for the month of February 2007. February was a calmer month with 63% of the recorded significant wave height being less than 1.0m in comparison to 45% for December 2006. As a result 80% of the spectra for February 2007 have a double peak as defined by the separation method employed. This higher occurrence of twin peaked seas for a month that had lower wave heights indicates that for storm conditions in Galway Bay, the resultant spectra for higher wave heights are single peaked and closely follow the theoretical shapes for such storm conditions.

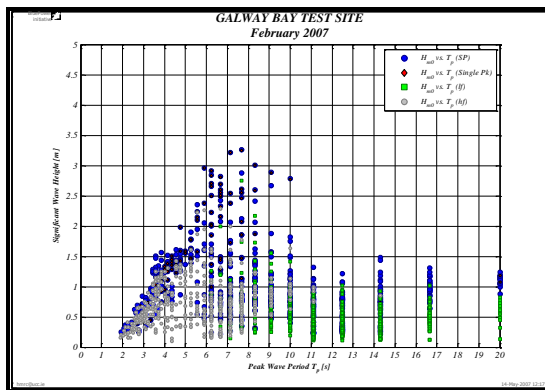


**Figure 18:** Comparison of measured and separated spectra for a scatter plot of  $H_{m0}$  vs.  $T_p$  for February 2007.

As the waverider buoy in place at the test site is non-directional, assumptions of the wave direction can only be taken from the SWAN model referred to earlier. However a directional buoy has been commissioned and will be operational by Autumn 2007.

As a final comparison Galway Bay data of a winter to spring period (December-May) for the year 2006/07 was scaled to full scale using a scale of 1/4 for comparison to a location off the western seaboard of Ireland. Two winter-spring periods of offshore data are used in the comparison covering December-May 2003/04 and 2004/05. The offshore data is from a non-directional waverider buoy in 50-60m of water depth at a full exposed site.

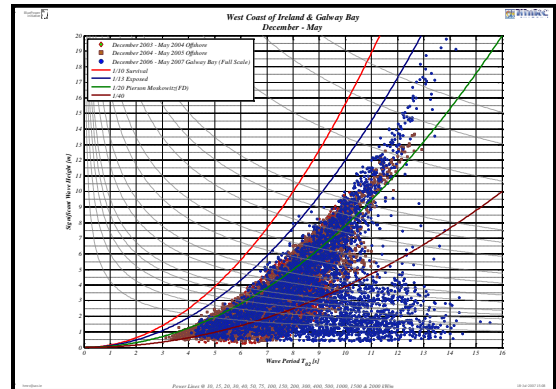


**Figure 19:** Comparison of measured Offshore Data and Galway Bay Data for a scatter plot of  $H_{m0}$  vs.  $T_p$  for December – May for three years (Offshore:03/04 & 04/05, Galway Bay 06/07).

The resulting plot in Fig. 19 shows how well the Galway Bay Test Site scales to offshore conditions. However the longer period low wave height swell at the test site does not exist at an offshore exposed location as can be seen in Fig. 19 at periods greater than 10s and wave heights less than 3m. Once the WEC developer is aware of this extra consideration in terms of unravelling collected WEC data it should not be a problem.

#### 4 Excitation Frequencies

Up to the point of putting a device out in the test site in Galway Bay, the developer will have followed the Development Protocol as shown in Fig. 20, and have completed Phase 1 and 2 which are laboratory controlled trials of monochromatic and panchromatic seaways, over a frequency range matched to the power production potential of the device. Typically panchromatic trials are conducted for a range of seaways defined by a theoretical spectral shape and varying in both magnitude and period limited only by the constraints of the facilities equipment. Due to this, the highest peak period tested would be in the region of 15-20s at prototype scale.

<b>PHASE 1: VALIDATION MODEL</b>		
<i>Concept</i>	<i>Performance</i>	<i>Optimisation</i>
<b>PHASE 2: DESIGN MODEL</b>		
<ul style="list-style-type: none"> <li>Final Design</li> <li>Accurate PTO</li> <li>Designed Mooring System</li> </ul>		
<b>PHASE 3: PROCESS MODEL</b>		
<i>Laboratory Tests</i>	<i>Sea Trials</i>	
<b>PHASE 4: PROTOTYPE</b>		
<b>PHASE 5: DEMONSTRATION</b>		

**Figure 20:** Phases of the Ocean Energy Development & Evaluation Protocol.

For most floating WEC's, the primary body motion of concern would be the heave of the device, which in most cases will match that of the resonant period of the power take-off of the device. For the heave motion the Response Amplitude Operator (RAO) will become 1 [ $m^2/m^2$ ] in periods greater than 15s where the floating device no longer heaves relative to the water surface.

In the case of other motions, for most floating devices the pitch period is specified to be at a long period, well outside the power production range of the device. Fig. 21 shows the pitch RAO for two different

wave energy converters, both of which have an RAO above 30s at prototype scale which is acceptable for open ocean sites where the prototype device would be deployed and occurrences of seaways at periods above 30s are extremely rare.

However for deployment in Galway Bay periods of 30-35s at prototype scale equate to 15-18s at the quarter scale test site. Fig. 17 and Fig. 18 indicate that seaways at these periods do occur, although they do have significant wave heights less than 1.5m. For December 2006, 13% of the seaways recorded have peak spectral components greater than 14s, and for February 2007 that figure more than doubles to 27%, most of which are the low frequency component of a twin peaked spectra.

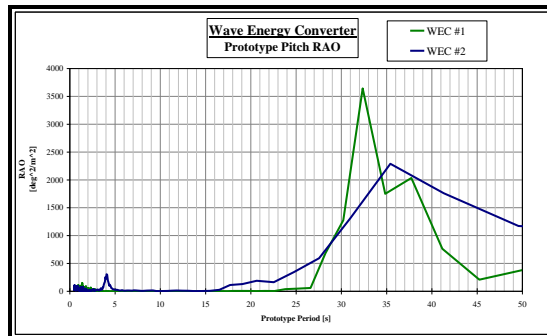


Figure 21: Pitch RAO's of two different WEC's at Prototype Scale.

As periods in this region would not have been tested in the previous phases of the Development Protocol, and it is not expected that a prototype device will experience these periods at an exposed offshore site, this phenomenon is unique to the test site in Galway Bay. Therefore developers need to be aware of this phenomenon and try to understand the consequences of it for their device in terms of any survival issues that may arise but more likely in terms of access for maintenance and/or data retrieval.

## 5 Conclusions

The Marine Institute/Sustainable Energy Ireland Wave Energy Test Site in Galway Bay on the west coast of Ireland has been home to ¼ scale devices and operational for over twelve months and has been extremely beneficial to wave energy converter developers.

The provision of an instrumented and legal test site has enabled developers to effortlessly move from controlled laboratory conditions in Phase 1 & 2 of the Development Protocol, to their first experience of real seaway conditions and its accompanying problems, difficulties and insights. The definition of this third phase of the protocol is to investigate physical properties that were not easily modelled at smaller scales and to realistically model the power take-off of the device. It will also be the developer's first experience of realistic mooring in real conditions and Phase 3 will establish the seaworthiness and survivability of the device.

It has been shown that the test site scales very well to an exposed offshore location, however realisation of the existence of long period swell at the test site is needed.

The identification of twin peaked seas in both the numerical model results and the measured data arm the developer with a greater knowledge of the site characteristics and therefore be able to take necessary precautions when designing the device to the correct scale to match the conditions at the site and to learn as much as possible from the trials duration.

## Acknowledgements

This work was funded under the Marine Institute's Blue Power Initiative through the National Development Plan Strategic Marine RTDI Programme, Submeasure 3.2, Project OE/04/01.

## References

- [1] Dept. Communications, Marine & Natural Resources. *Ocean Energy in Ireland*. 2005.
- [2] Admiralty Chart, *Galway Bay*, No. 1984, Hydrographic Office.
- [3] Hydraulics & Maritime Research Centre, *Development & Evaluation Protocol for Ocean Energy Devices*. Marine Institute, 2003.
- [4] N. Booij, I.J.G. Haagsma, L.H. Holthuijsen, A.T.M.M. Kieftenburg, R.C. Ris, A.J. van der Westhuysen, M. Zijlema. *SWAN Cycle III version 40.41 User Manual*. Delft University of Technology, The Netherlands, 2004.
- [5] O.M. Phillips. Spectral and Statistical Properties of the Equilibrium Range in Wind Generated Gravity Waves. *J. Fluid Mechanics*, 156: 505-531, 1985.



# Monitoring of Seaway Variability on WEC Performance

Sean BARRETT

Brian HOLMES

Dr. Tony LEWIS

Hydraulics & Maritime Research Centre,  
University College Cork,  
Ireland

## Abstract

One of the major issues that arise when moving from the early phases of wave energy device development conducted in hydraulic facilities to initial sea trials is the loss of control of the excitation conditions. This imposition requires that the test programmes and data analysis techniques must be much more rigorous and expansive to ensure understanding and appreciation of the large amounts of information that should be in the process of being generated. This situation exists whether the early sea trials are being conducted at benign medium scale sites (circa  $\lambda \approx 1/4$ ) such as Galway Bay and Nissum Bredning or have advanced to full prototype size exposed locations such as EMEC, or the Portuguese's pilot zone or the many other demonstration sites proposed around Europe for the future.

The real sea is inherently unpredictable, so device developers have to take into serious consideration a number of factors. One of these is the accurate measurement of the impinging ocean waves if any unravelling of how this affects the device performance is to be expected.

In the relative comfort of hydraulic facilities excitation waves can be programmed on demand and repeated with reasonable fidelity as required. Besides classical seaways any mix of sea and swell combinations should be possible, producing twin peaked spectra in the frequency domain, directional bi-modality or both simultaneously. Test schedules investigating the various aspects of a WEC design effecting performance can be drawn up and run to a pre-determined timetable. This convenience is not available once at sea and situations must be exploited when they become available. To achieve this control to any degree of satisfaction the appropriate sea state conditions must be identified implicitly. Simply knowing the summary statistics of the conditions is no longer really satisfactory. Knowledge of the excitation forces is essential before understanding of the response can be expected.

This paper aims to look at some of the aspects, in relation to both resource and engineering that must be addressed when considering body response and power production of wave energy converters at sea. The expected electrical output supply of a device can be considerably different when the concurrent sea state is of the form of a multi-modal sea. This is especially the case if an energy trough exists between the wind sea and swell components that coincides with the eigen frequency of the device. Juxtapose to this, greater energy may be derived in a narrow banded JONSWAP type sea state when the peak harmonic occurs at the

resonant period of the primary degree of freedom (e.g. heave) of the device.

## 1. INTRODUCTION

Today the wave energy industry is at its most exciting period to date. Government and public opinion is changing and becoming more favourable with the realisation that wave energy has a realistic chance of becoming a serious part of the renewable energy mix. The evidence of this exists in the numerous test sites being commissioned around Europe and the large funding schemes being offered by member state governments. Examples of this include the €26million put in place by the Irish government and the Scottish governments Saltire Prize of £10million, a challenge prize for advancements in wave and tidal energy.

Another indication of an emerging industry can be found in the number of bodies involved in certification and standardisation. Two groups at the forefront of this initiative are Det Norske Veritas (DNV) [1] and the International Energy Agency – Ocean Energy Systems (IEA-OES). There are many others involved in drafting recommended practises and standards and these will eventually be incorporated into the International Electrotechnical Commission Technical Committee (TC114), "Marine Energy – Wave, Tidal and other water current converters".

Tangible proof of the existence of a potentially successful industry are the pioneering devices being deployed, primarily as single devices, and then in arrays, to supply electricity to the grid. However, for an industry to be successful and profitable there has to be competition. This can only be achieved by device developers following the standards and protocols set in place by interest groups as mentioned above. For that to happen, testing in the real sea environment is a necessary challenge en route to product development. And it is best that this occurs at a benign site where the conditions of extreme events are of a manageable level, and that conditions for device access are more favourable. Then, when carried out according to the guidelines put in place, device development can be a rewarding and erudite experience, especially in hindsight!

Two sites are chosen as test cases for further examination in this paper, a site located in Galway Bay, and an exposed site off Loop Head, on the west coast of Ireland. The Galway Bay site is a designated large scale benign test site for WEC, and the Loop Head site is an example of a prototype deployment site. Table 1 shows the characteristics of each site.

Table 1: Test Case Site Characteristics

TEST CASE	Galway Bay (GB)	Loop Head (NS)
Water Depth	23m	50m
Location	Semi-enclosed Bay	Exposed Atlantic

## 2. FROM THE LAB TO THE SEA

Structured guidelines on WEC testing exist and are being formalised, consisting of a phased approach from small laboratory models of increasing size and complexity to initial sea going vessels to the final demonstration device. This device evolution procedure is now being adopted by funding agencies as both an indication of the developer’s commitment to mitigate financial and engineering risk and as a tool to assist in the distribution of funds.

The recommended development process is one which consciously and continuously adjusts to the improving technical database of the device being developed. Restricting early investigations to the essential elements helps maintain flexibility during the very fluid stages at the beginning of any design programme [2].

The initial phases of the protocol will have involved controlled laboratory conditions, mostly being a combination of monochromatic trials with idealised irregular seas such as the standard representative formulae for Pierson-Moskowitz, Bretschneider or JONSWAP spectra (See Figure 1). The detail of these panchromatic trials are at the discretion of the developer but it is envisaged that they cover all areas of a typical scatter diagram [3].

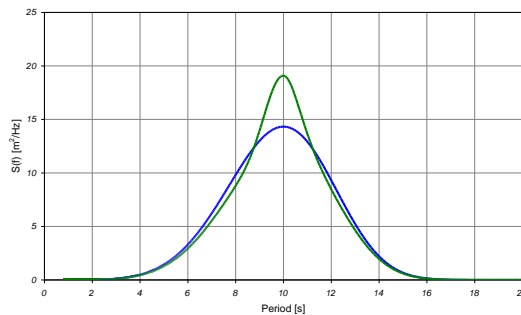


Figure 1. A Pierson Moskowitz Spectrum,  $H_{m0} = 4m$ ,  $T_p = 10s$ ,  $T_{02} = 7.131s$ . Corresponding JONSWAP Spectrum,  $H_{m0} = 4m$ ,  $T_p = 10s$ ,  $T_{02} = 7.331s$ , Peakedness Parameter = 1.5

The benign sea trial phase presents developers with the final opportunity to quickly and inexpensively acquaint themselves with their device in real sea conditions. It can also be used as a guide on the complexities of manufacture and as a yard stick for survivability, which if successful will instil confidence in the product. By implementing Froude scaling a model of the concept at this phase ( $\lambda \approx 1/4$ ) can be built relatively cheaply in comparison to the prototype, and does not require large operational vessels for towing, installation and access.

One benefit at this scale is the relatively low power production. Take for example a full scale demonstration device rated at 2MW. A device designed

for testing at a quarter scale site will be rated at approximately 16kW. This will not justify grid connection and it is possible to equip the device with a scaled power take-off mechanism, simulated grid connection and dissipate the produced power through some resistive load.



Figure 2. Scaled Air Turbine on the OE Buoy.

This phase also facilitates the assembly of a multi-disciplinary team to design and build a more realistic power take-off mechanism with all the power electronics and controls inherent with such a design. Figure 2 shows Ocean Energy Ltd. OE Buoy device. The model shown here with a scaled version of an air turbine on board is installed and operating at a benign seaway test site in Ireland.

The OE Buoy has been on station at the Irish quarter scale wave energy test site in Galway Bay since the end of 2006. Another Irish owned device, Wavebob, has also spent an impressive amount of time at sea in Galway Bay with a reduced scale device (See Figure 3). Experience learned at the test site has been invaluable to the developers in terms of device dynamics and also the real issues of operation, maintenance and access in the sea environment. Both devices have completed their first instalments at the test site and are preparing for a second duration of testing incorporating further elements into the on-site testing regime.



Figure 3. Installation of the Wavebob Device at the Galway Bay Test Site.

Barrett *et al* [4] reported on the suitability of the chosen location in Galway Bay as a benign wave energy test site. The site has two wave measurement instruments, a

Datawell Waverider MkIII directional buoy and a Datawell Waverider MkI non-directional buoy.

Surface elevation, frequency distribution and summary statistics are provided as output variables by the Datawell processing system. Data quality check procedures are put in place by HMRC to verify the summary statistics and frequency spectra by analysing the surface elevation both in the time and frequency domain.

### 3. MONITORING VARIABILITY

The assessment of WEC response and power production in the marine environment requires the quantification and qualification of many variables. These can be broken down into the localised conditions of the deployment site and the intrinsic nature of the device characteristics.

However, a quandary exists in that the influence of the local wave climate will dictate to some extent the response of the device, and so it is as important to consider the measurement of the impinging sea state as it is to evaluate device motions and forces.

Wave conditions at a proposed test site, at either a benign or demonstration scale, will be influenced by the following conditions:

- local bathymetry
- wind climate and swell affect
- directional properties

In parallel to this the device characteristics, which are excited by the incident wave climate have an almost independent influence on body motions but to a lesser extent:

- PTO (damping) loads
- Mooring design
- Arrays (device interaction, reflections)

Although the device characteristics will be design specific, dependant on hull dynamics and PTO type, the various aspects listed above will have varying effects, which should have been investigated (if possible) in the laboratory trials of the previous phases. An investigation of these topics is outside the scope of this paper.

#### 3.1. Sea State Variability

Site assessment for device deployment can begin with looking at the available wave data that is available for the region in question. Each method has its advantages and disadvantages, which are well published. This can be data from wave models such as SWAN or WAM, satellite data, or meteorological buoys that have been in situ over a number of years. However this paper concentrates on the presence of data buoys to provide the required data.

The variability of a chosen site can further be broken down into the following divisions:

- year to year,
- season to season,
- month to month,
- day to day,
- hour to hour,

- location to location.

Shown in Figure 4 is an idealised map of Ireland and the North Atlantic with ODAS buoys indicated. For site investigation work, some of these buoys may seem too remote, but the data from these buoys give a quick and clean indication of the prevailing conditions in the area, as they mostly only give the summary statistics recorded over the hour, not detailed frequency spectra.

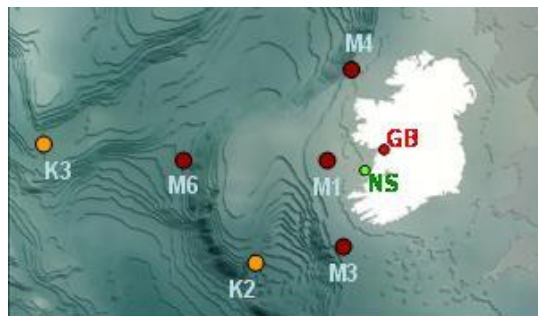


Figure 4. Location of Offshore Buoys along the Irish Coast. (GB: Galway Bay. NS: Nearshore)

By analysing the past records of the data buoys off the coast of Ireland (see Figure 4) and plotting a normalised graph of the ratio between the wave heights and periods recorded in the summer months to those in the winter months, it can be shown that the average significant wave height ( $H_s$ ) can be up to four times the magnitude of the summer average (Figure 5a), where as for the average zero crossing period ( $T_z$ ) ratio (Figure 5b) there is little change from summer to winter.

However, it should be noted that these plots only show the variation in the average statistic over the year and not the actual average period or significant wave height which may be site specific.

To asses the site specific implications from the summary statistics, a scatter diagram is produced, which indicates the sea state of most occurrences along with any extremes, or deviations from the norm.

#### 3.1.1. Scatter Diagrams

One of the functions of amassing this summary data is to create the percentage occurrence scatter plot. Due to the processes of wave generation and propagation, the percentage occurrence of nearly all scatter diagrams will follow the fully developed steepness line, known as the Pierson-Moskowitz line, to some extent i.e. significant steepness = 1/20.

Figure 6 shows the scatter diagrams of a years data for the two test cases indicated in Table 1, a semi-enclosed bay (GB in Figure 4), and an exposed Atlantic site (NS in Figure 4).

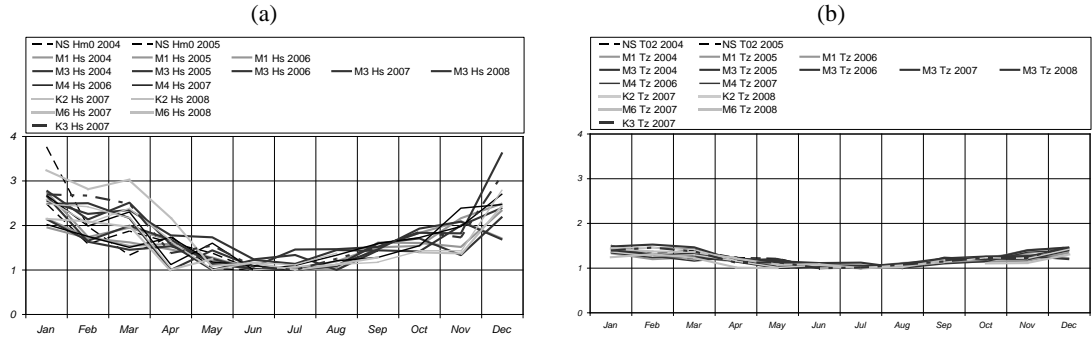


Figure 5. Significant Wave Height Ratio and Average Period Ratio for Offshore Buoys (see Figure 4)

What is interesting to note, and a phenomenon that comes up in many other site investigations is the location of the sea state of most occurrence, or the “hot spot”. As indicated from Figure 5, although most sites will follow a similar trend over the year i.e. from winter to summer comparisons, the location of the hot spot will be site specific, as shown in Figure 6. What is also site specific is the nature of the spectral shapes within each element of scatter diagram which will be examined further in a later section.

Another important point to note from these scatter diagrams is the value of collecting more than one year’s data if available. Specifically, in the Loop Head (NS) plots (b & d) of Figure 6, there is significant variation in the event of extreme sea states from year to year. For

this case the extreme events vary by 4m from one year to the next.

For true extreme analysis, where the 50 or 100 year storm will need to be investigated, these will only be available from hindcast numerical models (e.g. ERA-40) which have been calibrated against available data buoy measurements.

Of course not only is there variation from year to year, but there will also exist variation within the year as shown in Figure 5 for all the data buoys in Figure 4. By taking the case of the Galway Bay (GB) site in more detail, box plots can be assessed to investigate many of the statistics of the site in one plot.

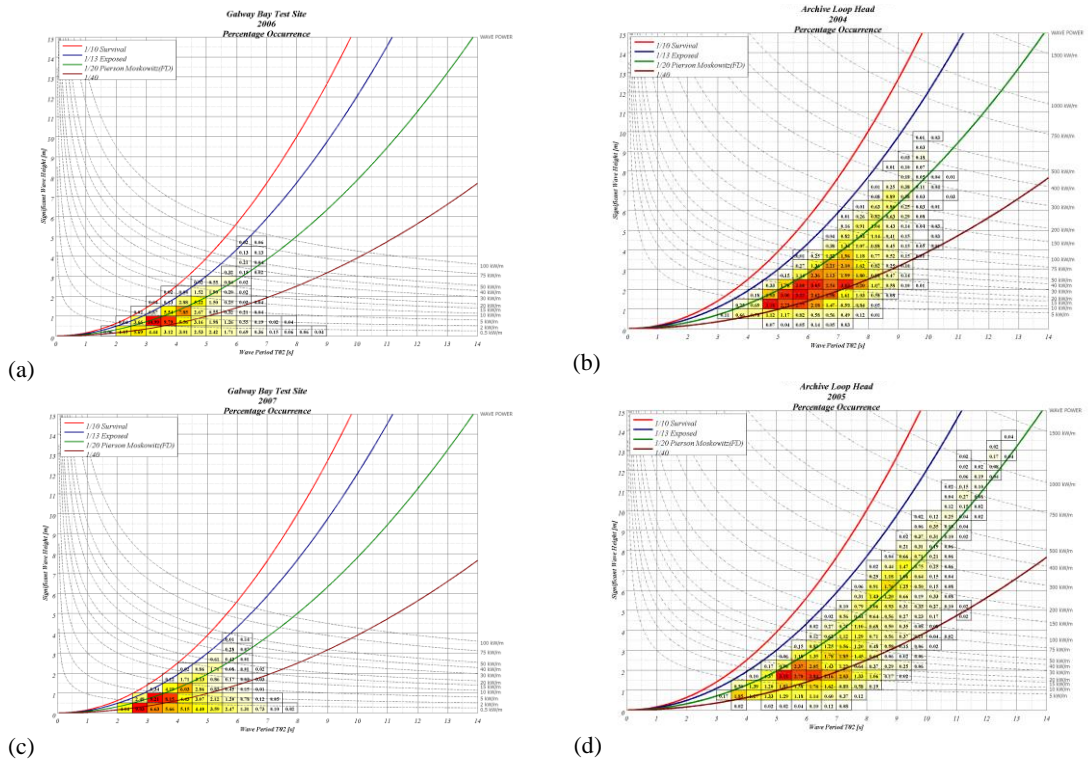


Figure 6. Scatter diagrams of the two test cases, Galway Bay (a & c) and Nearshore (b & d), as depicted in Figure 4.

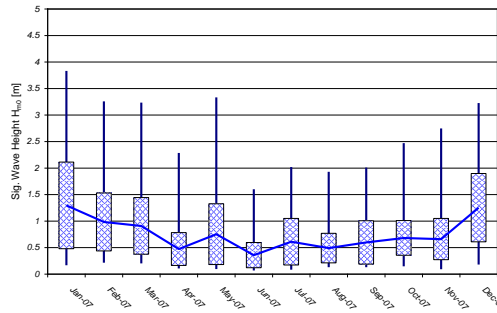


Figure 7. 2007 Monthly Averages, Standard Deviations, Minima and Maxima of Significant Wave Height,  $H_{m0}$ .

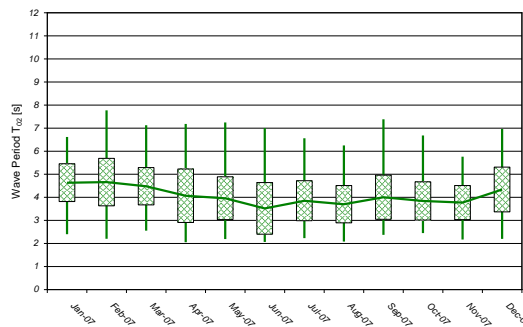


Figure 8. 2007 Monthly Averages, Standard Deviations, Minima and Maxima of Average Wave Period,  $T_{02}$ .

3.1.2 Summary Statistics

Figure 7 illustrates the monthly summary statistics for the test site in Galway Bay for the year 2007, which is a diagram of the variability of the significant wave height,  $H_{m0}$  for the twelve months of the year. The solid line running from month to month is the average statistics from month to month.

The extent of the hatched box is  $\pm 1$  standard deviation and the extremes of the vertical lines are the maximum and minimum statistic for that month. This format is carried through to Figure 8, the average wave period,  $T_{02}$ .

As expected the plot of the average significant wave height follows the usual trend of high sea states in the winter months falling off in the calmer summer months. However the average wave period as shown in Figure 8, does not change that significantly across the year, staying within the range of approximately one second of the average for that year.

Figure 9 gives an indication of the survival issues to be considered when deploying at the test site. The maximum wave height statistics are derived from the height from crest to trough of the largest wave in the surface elevation data record. As is evident from the plot, a deployed device will have to experience wave heights in the region of at least 6m in the winter months, equivalent to approximately 20m waves at full scale which are not unexpected in storm events in the open ocean.

In fact the largest sea state experienced at the test site occurred in December 2006. This twenty minute record occurred at the peak of a storm event and provided a

significant wave height,  $H_{m0}$  of 4.94m, an average period,  $T_{02}$  of 6.9s, with a maximum wave height of 8.15m. A section of the surface elevation trace containing the largest individual wave is shown in Figure 10.

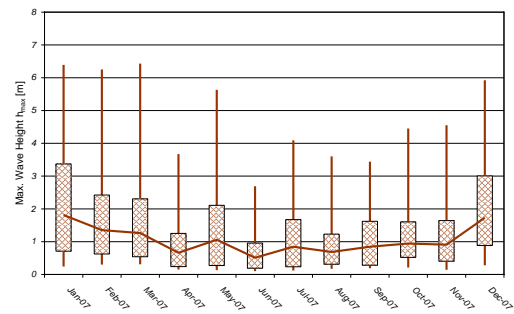


Figure 9. 2007 Monthly Average, Standard Deviation, Minimum and Maximum of the Maximum Wave Height,  $H_{max}$ .

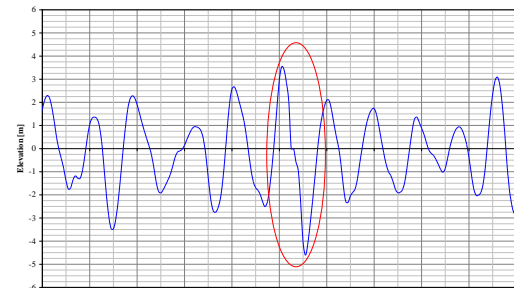


Figure 10. Surface Elevation of the Largest Recorded Wave at the Test Site.

3.1.3 Spectral Variation

The storm event described in the previous section grew from a significant wave height of approximately 1.5m and subsided to 1.5m over a period of 24 hours. This progression can be seen in Figure 11. The markers indicated by letters (a) to (i) are of selected spectra for visual inspection in Figure 12. The double integrated accelerations from the buoys are passed through several data quality check layers, and Fourier analysed. In this way the frequency spectrum can be derived.

Also plotted is the theoretical Bretschneider spectrum for the same summary statistics, indicated by the broken line. As the wave height increases the spectral shape conforms to a more characteristic Bretschneider type shape around the peak of the storm.

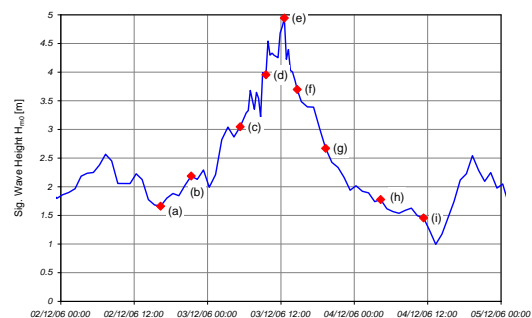


Figure 11. Significant Wave Height Time Series of the December Storm Event for Galway Bay

However it is not a phenomenon exclusive to the Galway Bay test site. Figure 13 shows two spectral plots, as examples from the exposed site at Loop Head which also include independent long period swell components in the frequency makeup. What should be noted from this exercise is that bimodality can exist at both exposed and benign sites, but to lesser and greater

extents respectively, again depending on site specific conditions. Finally, note that in both Figure 12 and 13, the scales change for the ordinates of the spectral plots.

Through the use of directional monitoring equipment, the source of this bimodality can be identified.

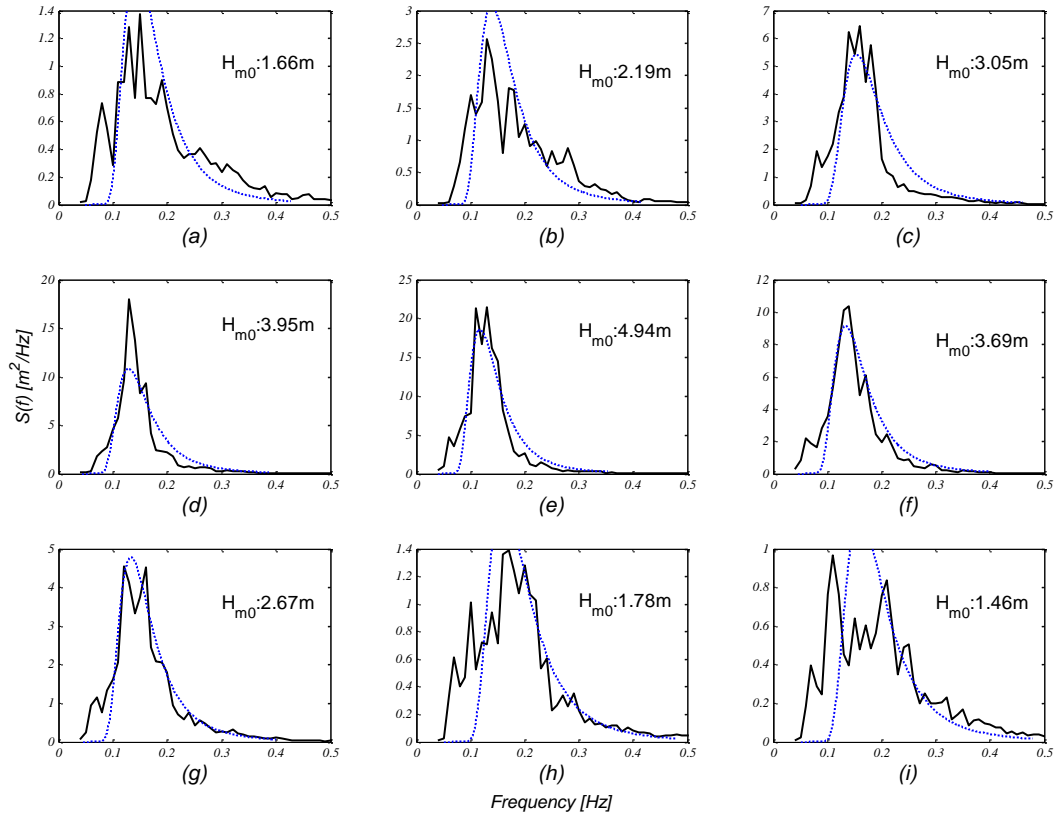


Figure 12. Sequence of Spectra During the Course of a Storm Event, Corresponding to the Indicators in Figure 11.

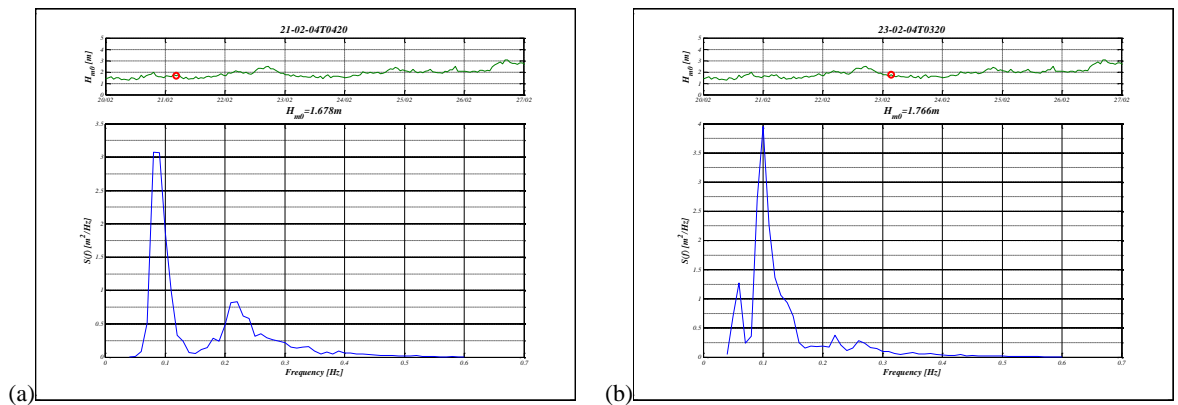


Figure 13. Bimodal Spectra from Exposed Site

Bimodality in a sea state arises when an old sea is in the area of interest and a local wind sea interacts with it in the following ways:

- growth of a local wind field
- decay of a local wind field
- change in direction of a local wind field

For benign test sites, swell components need important consideration due to Froude scaling. For a quarter scale site, a swell with a peak energy at 12s implies an

excitation at full scale of 24s. This will need careful consideration as device response at these long periods may not have been investigated at the laboratory phase of development.

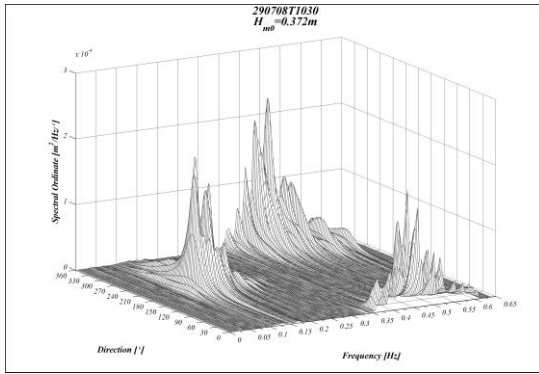


Figure 14. Bimodal spectra with wind and swell from differing directions.

Figure 14 depicts such a sea state with the swell component approaching from the west and a local wind sea developing from the north. In the case of the directional buoy, the Maximum Likelihood Method (MLM) is used to partition the spectrum into frequency and direction [5, 6].

Again it is important to note that these effects are most visible in low sea states, such as the one shown in Figure 14. Directionality aspects of a location could have implications in relation to mooring loads and also windage effects for devices with some freeboard. Other issues of this type include current effects on device with considerable draft.

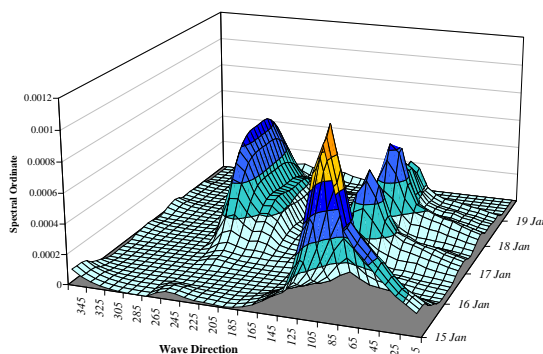


Figure 15. Directional Spectrogram over a number of days.

As can be seen from Figure 15, the directional properties of the Galway Bay site are made up of the local wind sea, and the long period swell which primarily approaches the test site from a south west direction. This implies that care should be taken with the interpretation of 1D spectra, as two distinct directional components of the sea state, that share the same harmonic components, may plot as a single peaked spectrum, and inversely, a twin peaked spectra in one dimension may have wind and swell energy concentrations that have different or similar directional vectors. This can be a feature of a site such as Galway Bay, however, this is generally only in low sea conditions ( $H_s < 1.5m$ ).

The measurement buoy located at the exposed site was not capable of directional measurement so no results can be presented on that sites directional makeup, emphasising the importance of deploying the correct instruments for the required need.

### 3.1.4. Spatial Variation

Spatial homogeneity is also an issue concerning wave energy especially in the case of wave measurement for device array interaction. These issues are currently being investigated at deployment parks such as Wavehub.

Figure 16 shows the concurrent measurement of significant wave height from the Galway bay test site, from two Datawell buoys, over a period of two weeks. These buoys were located within 200m of one another, and prove spatial homogeneity over this range.

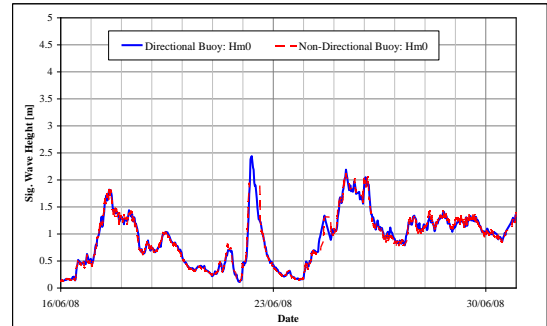


Figure 16. Concurrent Measurements,  $H_{m0}$

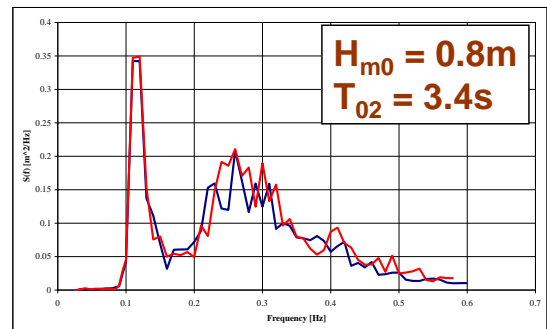


Figure 17. Concurrent Measurements,  $H_{m0}$

At the spectral level, this consistency also exists, as can be seen by the example in Figure 17. There seems very little difference in the spectral plots over this distance of 200m, which should give confidence in the deployment of a measurement buoy within this range of the WEC. However, for the implementation of active control, where to measure the surface elevation is still an issue for further research.

### 3.1.5. WEC Performance Fluctuation

The wave measuring buoys at the Galway Bay Test Site transmit real-time data to the Marine Institute Headquarters by high frequency radio over a distance of 20km. Both raw and processed data is transmitted and further post-processing is done by the receiving module [7]. This data is then made available to the HMRC via an FTP site for further analysis and verification.

In the same way the instantaneously measured power output from the wave energy device is obtained, unrectified and Fourier analysed to obtain a corresponding power spectrum to the excitation wave spectrum. This would also have been possible in the laboratory phases of the testing to get reference values

of the power production capability of the device being tested.

The wave input spectral shape in the tank testing facilities would most likely have been based on an empirical frequency distribution such as Bretschneider, Pierson-Moskowitz, JONSWAP or many others. Input parameters of variance/wave height and period allowed the testing of the device in realistic sea states of varying wave height and period.

However at sea, when concentrating on one element of the scatter plots such as those shown in Figure 6, it may not always be the case that for the same summary statistics, the spectral frequency distribution will be identical. This can be seen in some examples shown in Figure 18 that for closely matching significant wave heights and periods, the distribution of variance over the frequencies can vary considerably. Superimposed over this plot is the theoretical spectral shape of similar summary statistics. It is easy to imagine that these spectral shapes can coexist within one element of a scatter plot.

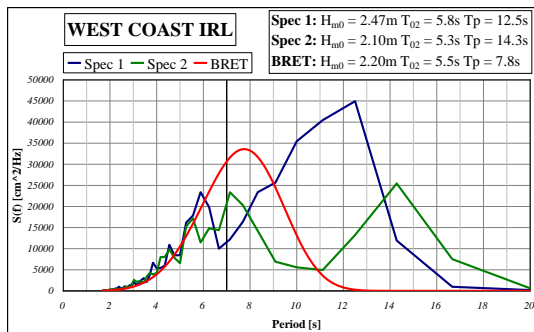


Figure 18. Spectral Shape Variation at the Loop Head site.

This change in spectral shape can be attributed to a variation in the energy input by the wind, an incoming long period swell, or even a change in direction of the local wind as described in this paper.

The inconsistency in the distribution of the variance over the frequency range will have varying degrees of influence on the power production of the device. By scaling the previous laboratory trial results to that of the sea trials and comparing the power output, an understanding of the influence of changing spectral shape can be deduced.

This effect is especially exaggerated when the valley between the wind and swell frequency components coincide with the eigen frequency of the device. In cases such as these, the power production can be reduced by as much as 95% of the expected value from previous trials. Figure 19 shows the measured and theoretical spectra for the summary statistics given. Also shown is the percentage of the expected power output actually produced.

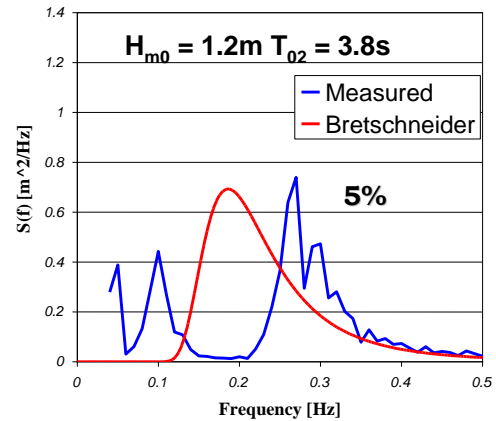


Figure 19. Comparison of Theoretical and Measured Spectral Shape and the Influence on Reduced Power Production.

Juxtapose to this situation is the comparison of the power output when the excitation spectrum exceeds the theoretical input spectrum in Figure 20. In this case more power is derived from the device due to its resonant qualities coinciding with the concentration of variance at specific frequencies.

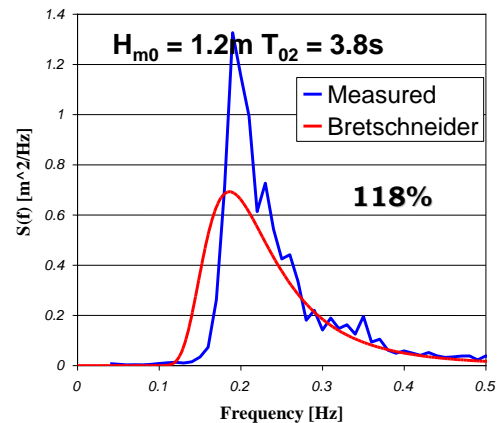


Figure 20. Comparison of Theoretical and Measured Spectral Shape and the Influence on Improved Power Production.

It should also be noted that the two examples presented here (Figure 19 and 20) are for the same sea state that was tested in the facilities ocean basin. This similar trend follows through to varying extents for other sea states tested. Figure 21 shows that for a different element of the scatter diagram with a significant wave height of 2m and peak period of 6.7s, the variation of the power output, still varies but to a lesser extent. This is due to the spectral shape conformity as the wave height increases.

In this plot 100% indicates the expected power output of the device from laboratory trials in the previous phases of testing, and the bar chart signifies the power produced as a percentage of that figure from real sea conditions.



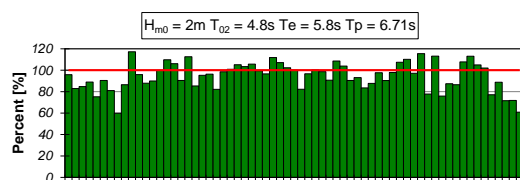


Figure 21. Summary of the Variation in Expected Power Output for a Sea State

#### 4. CONCLUSION

This paper discusses the issues of variability of firstly a sites wave conditions over a number of time scales, but also over a spatial distance. The impact of this wave input variability on the device performance is presented.

One of the important factors to consider before deployment of a device in the real sea is the accurate and appropriate measurement of environmental conditions both on and off the device. Depending on the level of accuracy required a decision is needed on the position of the measurement buoy in relation to the device, and amount of data recorded, i.e. wind speed and direction, waves and currents, etc.

It has been shown that at both a benign test site and at an exposed Atlantic deployment site that instances of twin peaked seas can occur, however these are only ever an issue for low sea state conditions, and their regularity is a site specific consequence.

Finally, the importance of the joint measurement of wave conditions and device performance has been indicated. Without this knowledge false conclusions of the working ability of a wave energy device could be construed, especially when lower than expected device performance is solely due to the incident wave field.

#### 5. ACKNOWLEDGEMENTS

This work was funded under the Marine Institute's Blue Power Initiative through the National Development Plan Strategic Marine RTDI Programme, Submeasure 3.2, Project OE/04/01.

#### 6. REFERENCES

1. Bittencourt Ferreira, C., *Certification of Marine Energy Converters: The Experience so Far*. Journal of Offshore Mechanics And Arctic Engineering, 2008. **130**.
2. Holmes, B. and S. Barrett, *Structured Development Programmes Mitigate Engineering & Financial Risk*, in *10th World Renewable Energy Congress*. 2008: Glasgow, Scotland.
3. Forestier, J.M., et al., *Value and Validation of Small Scale Physical Model Tests of Floating Wave Energy Converters*, in *7th European Wave and Tidal Energy Conference*. 2007: Porto, Portugal.
4. Barrett, S., B. Holmes, and A.W. Lewis, *Scalability of a Benign Wave Energy Test Site*, in *7th European Wave and Tidal Energy Conference*. 2007: Porto, Portugal.
5. Young, I.R., *On the Measurement of directional Wave Spectra*. Applied Ocean Research, 1994. **16**: p. 12.
6. Isobe, M., K. Kondo, and K. Horikawa, *Extension of MLM for Estimating Directional Wave Spectrum*, in *Proc. Symp. on Description and Modelling of Directional Seas*. 1984: Denmark. p. 15.
7. Datawell, *Datawell Waverider Reference Manual*. 2007, Datawell BV.

# IRELANDS ¼ SCALE WAVE ENERGY TEST SITE

**S. BARRETT, A.W. LEWIS**

*Blue Power Initiative,  
Hydraulics & Maritime Research Centre,  
University College Cork, Ireland.*

## INTRODUCTION

A benign quarter scale test site for floating wave energy devices has been provided by the **Marine Institute** in conjunction with **Sustainable Energy Ireland** and the **Department of Communications, Energy and Natural Resources**.

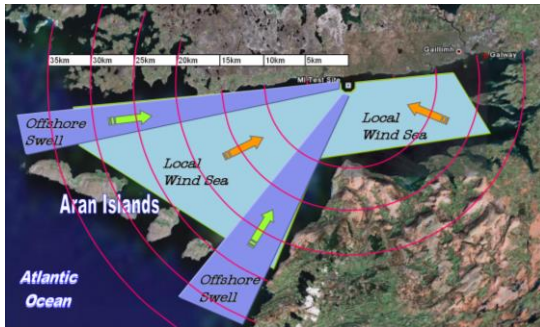


Figure 1. Test Site Location

The site is located on the west coast of Ireland in Galway Bay off the Spiddal coast (Fig. 1). It has a mean water depth of 23m and a tidal range of 4m. It is expected the provision of this site will encourage developers to progress to Phase 3 of the **Ocean Energy: Development & Evaluation Protocol**. The recent announcement of over €26M in targeted funding from 2008 to 2011, shows the Government's belief that Ocean Energy will play a significant part in a future Renewable Energy mix.

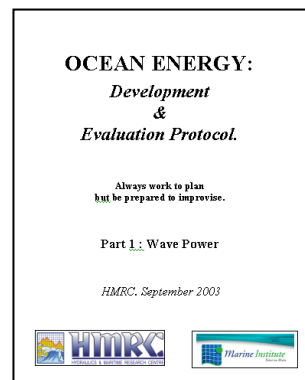
Part of the funding initiative announced by Minister Ryan includes a new National Ocean Energy facility in Cork, a full scale grid connected wave energy test site at an exposed site, an Ocean Energy Prototype Fund and a dedicated Ocean Energy Development Unit as part of Sustainable Energy Ireland. Also announced was a feed-in-tariff of €0.22 per kWh under the REFIT scheme for Wave Energy.

***"We are investing in order to create jobs. We are investing in order that we have clean, cheap and domestically produced energy. I believe that we can be***

***a world leader in renewable energy. We start today with the Oceans."***

Minister Eamon Ryan, 15<sup>th</sup> January 2008.

Phase 3 of the **Development Protocol** bridges the end of laboratory model testing and the beginning of sea trials. Completion of the previous two phases is a prerequisite for the use of the test site.



Phase 1 and 2 of the protocol will have involved controlled laboratory conditions, mostly being a combination of monochromatic trials with idealised irregular trials such as the standard representative formulae for JONSWAP or Pierson-Moskowitz spectra.

Phase 3 of the protocol presents developers with the final opportunity to quickly and inexpensively acquaint themselves with their device in real sea conditions. One benefit at this scale is the relatively low power production.

For a full scale device rated as 2MW, a device designed for testing in Galway Bay will be rated at approximately 16kW due to Froude scaling. Production of electricity at this magnitude will not justify grid connection or the expense of sub-sea cables and a consequent quick release system for safety. Instead it should be possible to equip the device with a scaled power take-off mechanism, simulated grid connection and dump the produced power through heat exchangers.

## SITE CONDITIONS

To investigate the wave conditions and the sites' suitability as a wave energy test site, a year's data was obtained in hindcast from a numerical wave

model. This model was implemented by the Marine Institute for the full year of 2000.

The computer model used to obtain the hindcast data for the test site was **SWAN** (*Simulating WAves Nearshore*), which is a package developed at Delft University. SWAN predicts wave conditions, primarily in shallow water coastal areas, lakes or estuaries from user defined wind, bottom and current conditions. SWAN is a third generation wave model based on the energy balance equation.

The SWAN model is based on a spatial grid that extends west from Oranmore and from Liscannor Bay, Co. Clare to Slyne Head, Co Galway. This covers an area of approximately 9,500 square kilometers, 600km<sup>2</sup> of which covers the area of Galway Bay. The grid units are in kilometres with grid nodes at 2km spacing. The focus of interest is the Wave Energy Test Site and it falls within the bounds of four grid nodes of the SWAN model and so the output data is interpolated.

The output data from the SWAN model was supplied to the HMRC for analysis in two forms, the summary statistics comprising of significant wave height ( $H_{m0}$ ), spectral peak period ( $T_p$ ), spectral mean period ( $T_{02} \approx T_z$ ) and the mean direction of propagation of the waves in degrees but also the 3 dimensional spectra.

Results from the SWAN analysis showed the existence of two distinct wave systems in Galway Bay. One has the characteristics of a local wind sea with short peak periods associated to the limited fetch, while the other is of longer periods approaching the site from the Atlantic around the Aran Islands. An example of this confused sea state can be seen below (Fig. 2).

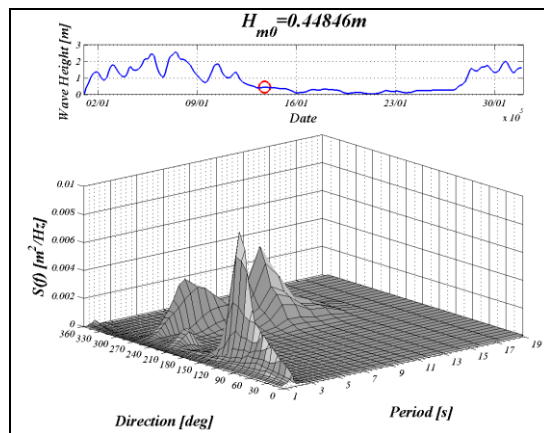


Figure 2. Bimodal Directional Spectrum

At present a directional Waverider Buoy is being commissioned on site to verify the directional spectra from the numerical model. The post-processed output from this buoy will give the

summary statistics but also the 3 dimensional spectra in both frequency and direction.

To provide measured values of the conditions at the test site, a non-directional recording buoy was placed at the South East corner of the test site in mid-November 2005. It is a Datawell Mark 1 buoy, which has a diameter of 0.7m, and outside of a scheduled maintenance period there has been virtually 100% data retrieval.

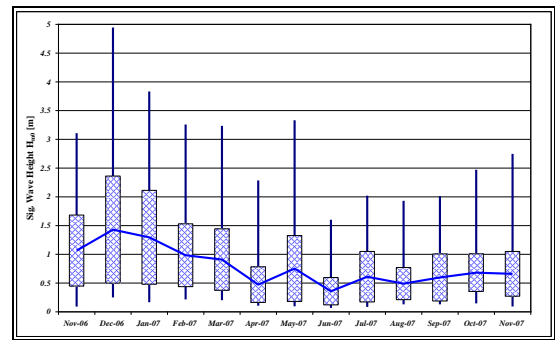


Figure 3.  $H_{m0}$  Statistics

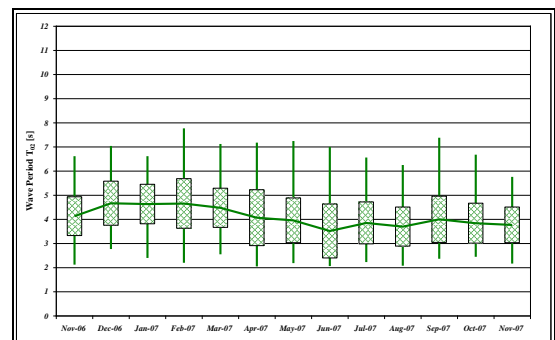


Figure 4.  $T_{02}$  Statistics

The two box plots are the monthly statistics over a year of significant wave height,  $H_{m0}$  and average wave period  $T_{02}$  (Fig. 3 & 4). A sea state with the largest  $H_{m0}$  of 4.94m, a maximum wave height of over 8m and the following periods,  $T_{02} = 6.9s$ ,  $T_e = 8.3s$  and  $T_p = 7.7s$  were recorded at midday on the 3<sup>rd</sup> December 2007. This is comparable to a 1 in 50 year storm for the site.

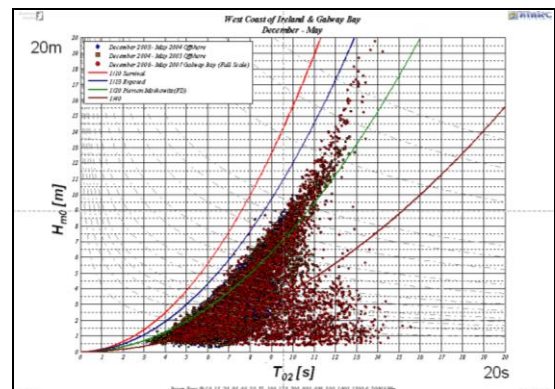


Figure 5. Scatter Diagram

As a final comparison, Galway Bay data of a winter to spring period (December-May) for the year 2006/07 was scaled to full scale using a scale of one quarter for comparison to a location off the western seaboard of Ireland. Two winter-spring periods of offshore data are used in the comparison covering December-May 2003/04 and 2004/05. The offshore data is from a non-directional waverider buoy in 50-60m of water depth at a full exposed site.

The plot shows how well the Galway Bay Test Site scales to offshore conditions (Fig. 5). However the longer period swell with low wave height at the test site can be seen in the area of the plot where the period is greater than 10s and the wave height less than 4m at prototype scale. This is the influence of the swell wave system in Galway Bay that is a unique feature of the test site but does not translate to a prototype site. Once the developer is aware of this extra consideration in terms of unravelling collected device data it should not be a problem. Some examples of measured double peaked spectra can be seen below.

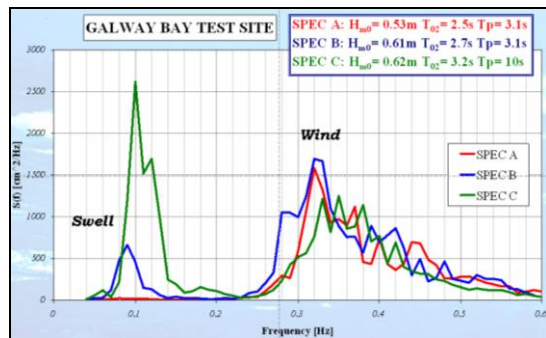


Figure 6. Bimodal Spectra

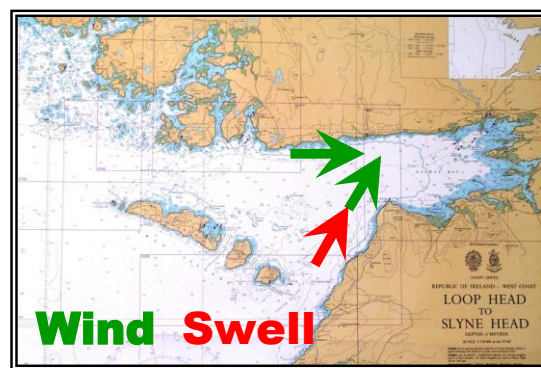


Figure 7. Wave System Directions

However, further investigation showed that this long period swell did not become an issue when the significant wave height is greater than 1.5m on site. In these storm conditions the spectra are single peaked and follow the empirically derived spectral shapes such as JONSWAP or Bretschneider.

## DEVICES AT GALWAY BAY

Wavebob Ltd



OE Buoy Ltd.

Two Irish Wave Energy developers, **Wavebob** and **Ocean Energy Ltd**, have spent an impressive amount of time at sea in Galway Bay with reduced scale devices. Experience learned at the test site has been invaluable to the developers in terms of device dynamics and also the real issues of maintenance in the sea environment.

Both devices have completed their first instalments at the test site and are preparing for a second duration of testing incorporating further elements into the on-site testing regime.

Two of the more general issues that developers have had to come to terms with at the test site are directionality and bi-modal spectra which have been discussed.

Up to the point of putting a device out in the test site in Galway Bay, the developer will have followed the Development Protocol, and have completed Phase 1 and 2 which are laboratory controlled trials of monochromatic and panchromatic seaways, over a frequency range matched to the power production potential of the device. Typically panchromatic trials are conducted for a range of seaways defined by a theoretical spectral shape and varying in both magnitude and period limited only by the constraints of the facilities equipment. Due to this, the highest peak period tested would be in the region of 15-20s at prototype scale.

For most floating WEC's, the primary body motion of concern would be the heave of the device, which in most cases will match that of the resonant period of the power take-off of the device. For the heave motion the Response Amplitude Operator (RAO) will become unity in very long period where the floating device no longer heaves relative to the water surface. In the case of the other motions, the pitch period will be at the high end of the period

range, well outside the power production of the device.

The influence of bi-modal spectra will also have an effect on the power output of the quarter scale device. The graphic below shows two examples of double peaked seas that share similar summary statistics. The red line is the expected power output spectra from the testing conducted in the previous phases of the development protocol for a typical wave energy device.

As can be seen from the figures above there is a significant reduction in power output from the device due to the minimum excitation in the region of the resonant frequencies. This has led developers to be wary of the summary statistics of the sea conditions at the test site and the necessity of the investigation of the spectral shape to explain device results.

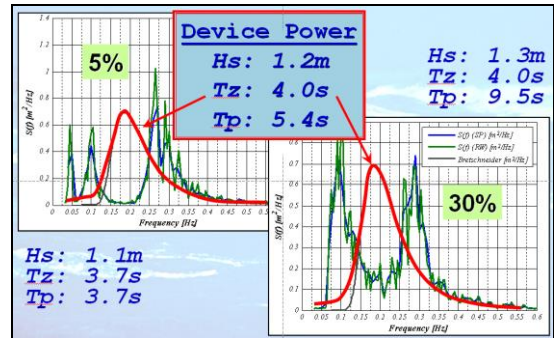


Figure 8. Power Production Spectra